THEORETICAL AND NUMERICAL MODELING OF ANISOTROPIC DAMAGE IN ROCK FOR ENERGY GEOMECHANICS

A Dissertation
Presented to
The Academic Faculty

by

Hao Xu

In Partial Fulfillment
of the Requirements for the Degree
Doctor of Philosophy in the
School of Civil and Environmental Engineering

Georgia Institute of Technology
December 2014

THEORETICAL AND NUMERICAL MODELING OF ANISOTROPIC DAMAGE IN ROCK FOR ENERGY GEOMECHANICS

Approved by:

Dr. Chloé Arson, Advisor
School of Civil and Environmental Engineering
Georgia Institute of Technology

Dr. Seth Busetti
Geostructural Group
ConocoPhillips

Dr. David Frost
School of Civil and Environmental Engineering
Georgia Institute of Technology

Dr. Christian Huber
School of Earth and Atmospheric Sciences
Georgia Institute of Technology

Dr. Carlos Santamarina
School of Civil and Environmental Engineering
Georgia Institute of Technology

Dr. Frederick Chester
Department of Geology and Geophysics
Texas A & M University

Date Approved: July 2014

To my dear wife,

Chen Cheng,

thanks for your support.

Thanks for accompanying with me.

I'm looking forward to the new life with you at next place.

ACKNOWLEDGEMENTS

I am grateful to my advisor Dr. Chloé Arson, who guided me during my Ph.D. studies. Thanks for her encouraging, persistence and tutoring on my research. I very appreciate all your support. I want to acknowledge my Ph.D. thesis committee members: Dr. J. Carlos Santamarina, Dr. J. David Frost, Dr. Christian Huber, Dr. Fred Chester and Dr. Seth Busetti, for their spending time on reviewing my dissertation and providing valuable comments and suggestions.

I want to acknowledge Texas A&M University and Georgia Institute of Technology for providing supercomputer and software to assist my research, and ConocoPhillips funding for my Ph.D. studies. Thanks Texas A&M to accept me as a Ph.D. student, so I can start my fantastic oversea study journey. Lawrence Livermore National Laboratory is a great place, providing me with a wealth of excellent experience learning through the internship.

I also like to thank the help I had received from the students from Georgia Tech and Texas A&M, especially, Cheng Zhu, Yuze Zhang, Congpu Yao, Mengtian Wang and Philip Van Ruitenbeek. I am very enjoying the time discussing hydraulic dynamics with Zhenlei Yang. I look forward to working together more in the future.

Finally, I would like to thank my wife, Chen Cheng, for her endless support and love. I am particularly indebted to my parents. I hope you are happy and healthy in China.

TABLE OF CONTENTS

LIST OF TABLES

LIST OF FIGURES

SUMMARY

Rock is widely distributed in earth's crust. It is the material that constitutes geothermal energy storage facilities, non-conventional oil and gas reservoirs, nuclear waste disposals. Cracking can be originated by changes of the natural environment (tectonic processes, erosion or weathering) or by engineering activities (stress relaxation, drilling, mining, building overburden), which changes the microstructure inside the rock. Stress paths with uniaxial tension or triaxial compression result in different kinds of failure mechanisms (tensile failure or shear failure), which alter rock strength and induce anisotropy of rock elastic properties. Previous engineering applications utilized Linear Elastic Fracture Mechanics (LEFM), which ignores microstructure changes and strength degradation of the rock that occur crack coalescence and subsequent propagation of larger fractures. Therefore, LEFM models cannot be used to predict the damage zone surrounding the crack tip before the fracture extension. In this thesis, the framework of Continuum Damage Mechanics (CDM) is used to develop a constitutive model which can close the gap between microcrack initialization and fracture propagation due to the damage accumulation.

This work presents a modeling framework for anisotropic crack propagation in rock, in conditions of stress typical of geological storage and oil and gas extraction. Emphasis is put on the prediction of the damage zone around cavities and ahead of pressurized fracture tips. After reviewing the theory of Fracture Mechanics and the thermodynamic principles of Continuum Damage Mechanics (CDM), an original model of anisotropic damage, the Differential Stress Induced Damage (DSID) model, is formulated. Drucker-Prager yield function is adapted to make the damage threshold depend on damage energy release rate and to distinguish between tension and compression strength. Flow rules are derived with the energy release rate conjugate to damage, which is thermodynamically consistent. The positivity of dissipation is ensured by using a nonassociate flow rule for damage, while nonelastic deformation due to damage is computed by an associate flow rule. Stress paths

simulated at the material point illustrate damaged stiffness and deformation variations in classical rock mechanics tests. The maximum likelihood method was employed to calibrate and verify the DSID model against stress-strain curves obtained during triaxial compression tests, uniaxial compression tests and uniaxial tension tests performed on clay rock and shale. Logarithmic transformation, normalization and forward deletion allowed optimizing the formulation of the DSID model, and reduce the number of damage constitutive parameters from seven to two for clay rock. The DSID model was implemented in ABAQUS Finite Element (FE) software. The iterative Newton-Raphson scheme was adapted in order to account for the non-linearities induced both by pre-damage and damage-induced deformation. FE simulations of laboratory tests capture size and intrinsic anisotropy effects on the propagation of damage in rock. Smeared DSID zones representing shale delamination planes avoid some convergence problems encountered when modeling discontinuities with debonded contact surface elements. FE simulations of tunnel stress relaxation, fracture propagation and borehole pressurization were performed to illustrate the evolution of the damage zone and the impact on energy dissipation, anisotropy of deformation, and loss of stiffness. Fracture propagation in rock was also simulated by using various techniques, including the DSID model in FE, a Cohesive Zone Model (CZM) and the Extend FE Method (XFEM).

Future work will focus on coupling the propagation of fractures with the evolution of the damage process zone, and on the transition from continuum damage to discrete fracture upon crack coalescence.

CHAPTER I

INTRODUCTION

1.1 Rock damage propagation in energy geomechanics

At present, 85% of the energy power consumed in the world is produced by fossil fuel combustion [123, 131], which has raised increasing interest in renewable energy technologies, non-conventional oil and gas reservoirs, and nuclear power. Innovative nuclear fuels and reactors depend on the economical and environmental impacts of waste management [283]. Disposals in mined geological formations are viewed as potential consolidated storage facilities before final disposition [45]. Different stress paths (e.g., biaxial tension or triaxial compression) during underground construction result in different kinds of failure mechanisms (e.g., tensile failure or shear failure), which alter rock strength and induce anisotropy of rock elastic properties. Crack propagation in rock can be originated by these engineering activities (stress relaxation, drilling, mining, building overburden), or by changes of the natural environment (tectonic processes, erosion or weathering).

In many energy geotechnical applications such as carbon dioxide sequestration [289], disposal of nuclear waste [35, 38, 103, 154, 167, 208, 223, 294], storage of compressed air and natural gas [33, 65, 148, 248, 256], and extraction of geothermal energy [23, 291, 293, 296], stress concentrations result from the displacement of the boundaries of a large discontinuity (typically: a cavity, a tunnel, a well bore, or a hydraulic fracture), which originates microcracks [113, 303]. Underground laboratories were used to characterize rock mechanical, acoustic, and hydraulic properties in the stress relaxation Damaged Zone [186, 253, 268]. Laboratory scale assessment of rock mechanical damage combined loading and unloading cycles with acoustic emissions, flow tests, porosimetry and/or imaging [32, 58, 124]. Thermomechanical damage was assessed by performing temperature-controlled mechanical loading cycles, by conducting a heating phase followed by a mechanical loading, or by performing a heating phase followed by a relaxation period. Most of the published experimental results

focus on rock compressive strength [300].

1.2 Propagation of damage in rock during injection and withdrawal

Carbon capture and storage technologies are thought of as potential technologies that could reduce greenhouse effects. The efficient short-term injection and the stable long-term geological storage of carbon dioxide depends on complex hydro-chemo-mechanical interactions that take place in the formation, including water acidification, mineral dissolution, and stress and volume changes [82]. It was found by [82] that CO_2 injected at high pressure would induce fluid driven fractures and trigger displacements along preexisting faults. Water acidification in the presence of CO_2 enhances mineral dissolution and alters the sediment fabric by the chemical reaction with clay minerals. Rock damage as a result of the propagation of open mode discontinuities (mechanical) and dissolution of the rock matrix (chemical), are therefore key issues in carbon capture [60, 83, 119, 230].

Hydraulic fracturing is the pressurized injection of fluids in underground formations to enhance native permeability and to create conductive pathways, which allows natural hydrocarbons to flow more freely from rock pores to the surface and increases the extraction rates. Previous studies of hydraulic fracturing by [4, 228] focus on the computation of stress around the borehole. Related models are based on the theory of elasticity [216, 251, 205]. The geometry of the borehole and the crack patterns surrounding the well bore are the dominant factors that influence stress concentrations. The new fracture pattern generated during pressurization determines the area of the surfaces created by injection, which form the interface between the fluids and the rock mass. Analytical solutions and numerical models did not consider the degradation of stiffness or the change in rock strength around the propagating fracture. It was established that hydraulic fracture propagation is accompanied by the development of a damaged zone around the tip [49, 237]. Micro-cracks induced around the primary fracture soften the material, which makes it easier to propagate the hydraulic fracture and also enhances rock permeability. Modeling rock damage during the process of hydraulic fracturing is still an open issue [7, 74, 91]. The geometry of crack patterns is affected not only by the geometry of the hydraulic fracture, but also by other

factors, such as the type of the fluids injected, the geological conditions, the in situ tectonic stress. Predicting the actual geometry of the crack pattern in the field is challenging, and laboratory experiments are still lacking to validate models of anisotropic damage around hydraulic fractures. The non-uniform distribution of processes that contribute to micro-crack propagation makes it difficult to upscale damage evolution.

1.3 Scope of this research work

The objective of this research work is to model damage propagation in rock subject to conditions of stress typical of geological storage and oil and gas extraction. An original Continuum Damage Mechanics (CDM) model is proposed, in which rock softening (i.e. loss of stiffness) and the accumulation of irreversible deformation due to residual crack opening evolve differently in tension and compression. The Finite Element Method is employed to simulate the evolution of the damage process zone around cavities, fractures and pressurized boreholes. A review of damage and fracture propagation models in rocks is presented in Chapter 2. Chapter 3 sets the thermodynamic bases, details all the assumptions made in the DSID model, and presents two model calibration methods. The technical aspects of the Finite Element implementation are presented in Chapter 4. Simulation results are presented in Chapter 5, which includes a sensitivity analysis performed on a single element at the integration point, a series of Finite Element analyses of laboratory tests, and several examples of reservoir geomechanics problems. Chapter 6 explains on-going exploratory work on the theoretical and numerical modeling of multi-scale crack propagation in rocks.

CHAPTER II

LITERATURE REVIEW OF DAMAGE AND FRACTURE MODELS IN ROCKS

2.1 Rock Discontinuities at Multiple Scales

Rocks present discontinuities at multiple scales. Figure 1 provides an overview of shale heterogeneities. Fracture propagation at any single scale can be predicted within the framework of fracture mechanics. A stress concentration zone around crack tip is given by the mathematical calculation [226]. Fracture mechanics is very efficient in predicting the propagation of isolated cracks that do not interact with each other: crack propagation occurs when the local stress at the tips exceed a critical value. Computations are more complicated if crack interaction and crack coalescence are accounted for. In Continuum Damage Mechanics (CDM), subsets of cracks are defined as "damage". The following section provides an overview of the modeling strategies available at the micro-, meso- and macro- scales defined Figure 2. In the following, we use the micro-scale to designate defects that range from 10^{-6}m to 10^{-2}m in size, the meso-scale for cracks that range between 10^{-3}m and 100m in size, and the macro-scale for the discontinuities that are 10^{-2}m to 10^{3}m in size (e.g., geological faults, hydraulic fractures).

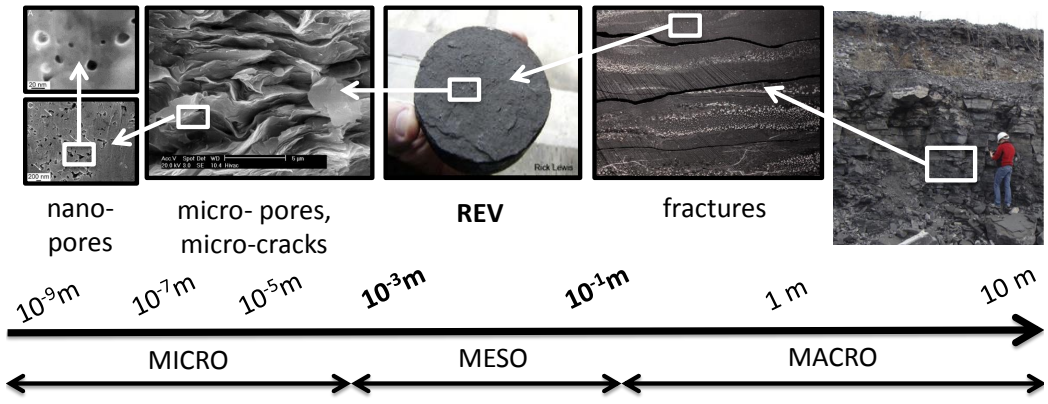

Figure 1: Discontinuities in shale at multiple scales

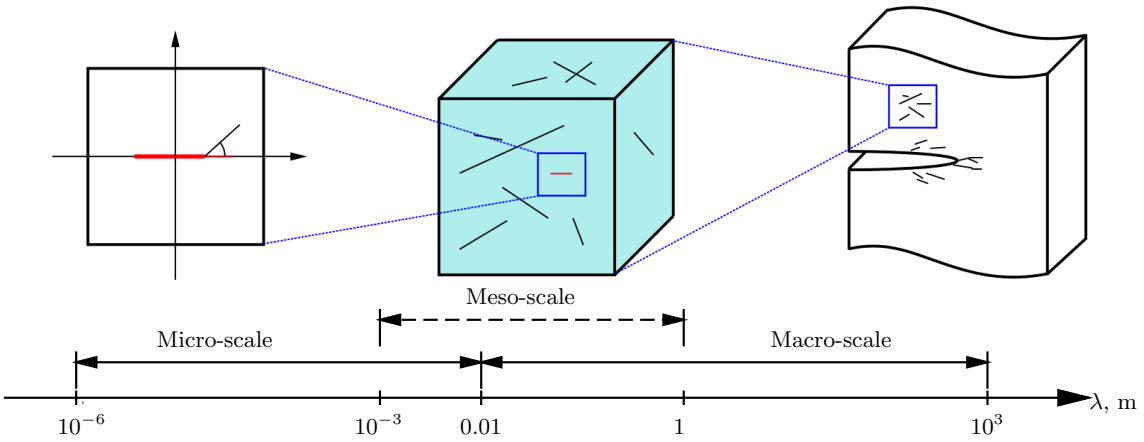

Figure 2: Discontinuities at multiple scales: definitions.

2.1.1 Micro-scale

The non-uniform distribution of micro-cracks is one reason of the heterogeneous properties of rock when looking into the micro-scale. Conversely, the heterogeneity of the lithology can also induce complex micro-crack distributions. The density, size and geometry of cracks are important model parameters, used to predict mechanical anisotropy prior to failure [207, 206]. Phenomenological models allow predicting the energy dissipated during crack growth, and the mechanisms that govern crack propagation and orientation. In order to model the change in size, orientation and shape of individual cracks, it is necessary to employ a micro-mechanical framework (more details are provided in Section 6.1). For instance, crack growth in mode I is predicted by using Griffith criterion: crack length is work-conjugate to the "energy release rate", in which the work is the product of energy release rate by the change in crack length [9, 280]. The crack propagates unstably if the energy release rate exceeds the critical threshold depending on stress concentration factors. Micromechanical processes are generally valid up to the point of crack coalescence, if the linked fractures exceed the scale of the local representative elementary volume (REV) [187].

2.1.2 Meso-scale

Mesoscopic models were proposed in order to avoid having to model the geometry of each discontinuity, and to predict the influence of subsets of micro-cracks on the mechanical

properties of a Representative Elementary Volume (REV) [163]. The REV is the critical size, below which a physical property is non-uniform in the material; while above this size, the variable is uniformly distributed in the volume considered. For the same material, the size of the REV can be various for different properties (The REV for stiffness or permeability may be at different size). Homogenization schemes are often formulated so as to ensure the statistical homogeneity of the stiffness tensor or the stress field [156]. Figure 3 illustrates the definition of the REV for one specific property.

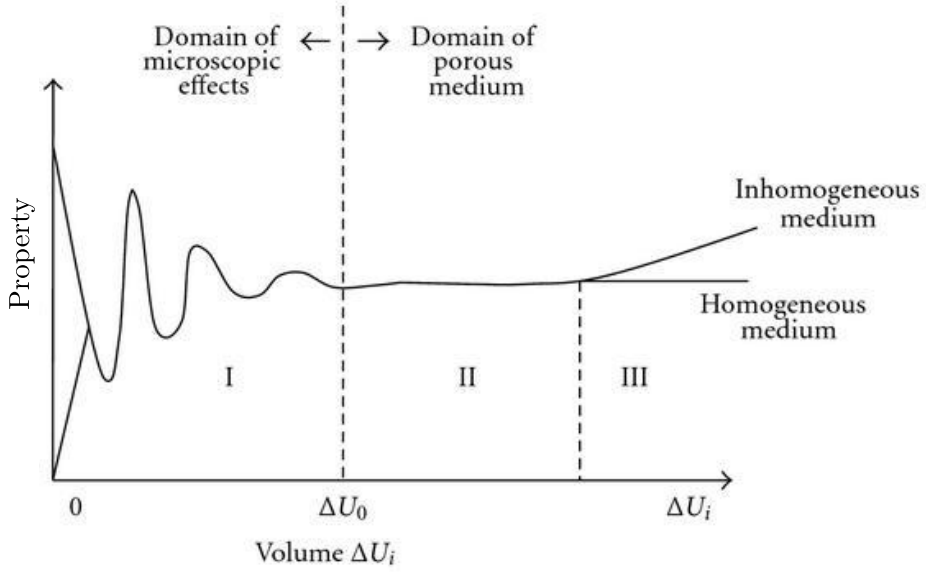

Figure 3: Definition of the Representative Elementary Volume (REV). Modified from [29, 39].

At the meso-scale, the rock is treated as a continuum solid medium, and cracks are modeled indirectly, through their effects on stiffness, porosity, and permeability. In Continuum Damage Mechanics (CDM), the damage evolution law can be obtained by upscaling a microscopic fracture mechanics model. For instance, the model proposed by Swoboda & Yang [261] allows relating microscopic energy release rates to mesoscopic stress for a finite number of crack sets characterized by the crack radius and by the vector normal to the crack plane. Swoboda & Yang's framework can be extended to relate the mesoscopic stress to the statistical distributions of micro-crack size and orientation. Oda [206] and Lubarda & Krajcinovic [174] related the density and orientation of micro-cracks to a mesoscopic

fabric tensor. Cowin [68] related the fabric tensor to the elastic stiffness tensor without resorting to any sort of homogenization scheme. Maleki & Pouya [183] found an empirical statistics-based relationship between Oda's fabric tensor [206] and the mesoscopic permeability tensor, and also related the fabric tensor to the CDM damage tensor. Some authors used CDM models to account for the presence of micro-cracks ahead of fracture tips and relate Linear Elastic Fracture Mechanics (LEFM) parameters, such as the fracture toughness and the stress intensity factors (at the macro-scale), to continuum damage (at the meso-scale) [274]: instead of depending on real stress, properties of the undamaged matrix are functions of "effective stress", defined as the stress that would be developed in a fictitious undamaged REV to store the same deformation energy as the damaged REV subject to real stress. This relatively simple modeling assumption allows deriving "damaged toughness", and other damaged LEFM parameters simply by substituting the elastic properties of the intact (undamaged) rock mass by the damaged elastic properties. The position of the crack tip and the stress field can then be predicted by using the resulting LEFM equations, modified to account for damage.

2.1.3 Macro-scale

When crack sets concentrate in narrow zones or if one fracture is much larger than the REV size, continuum models of fractures become inappropriate. At the macro-scale, LEFM is often utilized to analyze critical states of the material, but it mainly focuses on isolated discontinuities (Figure 2). Fracture propagation is predicted by solving partial differential equations coupling fracture length and aperture to pressure. The analytic solution has been studied by Germanovinch [106, 107, 198, 108]. Several numerical methods may be employed, mainly the Finite Element Method (FEM), the Extended Finite Element Method (XFEM) and Cohesive Zone Models (CZM) [51], and Boundary Element Methods (BEM). However, in all of these methods, fracture nucleation and intersection are impossible to predict, so the expected (approximate) position of the fracture has to be postulated. Other models of hydraulic fracture propagation are based on fluid mechanics and fluid dynamics [108, 74, 231]. In particular, the lubrication theory can be used to predict the movement of

fracture tips [231]. The main limitation of the lubrication theory is that the weakening of the solid part of the rock by fluid pressurization is not taken into account.

2.2 Fracture Models

2.2.1 Fracture Mechanics Review

2.2.1.1 Griffith's Crack Propagation Theory

In Griffith's theory, a crack extends if the potential energy release rate gets larger than the material surface energy at the cracks faces. For illustrative purposes, let us consider a REV subjected to a stress σ_0 in the far field, and containing a line crack of length $2a$, as illustrated in Figure 4. The local stress at the crack faces is noted σ.

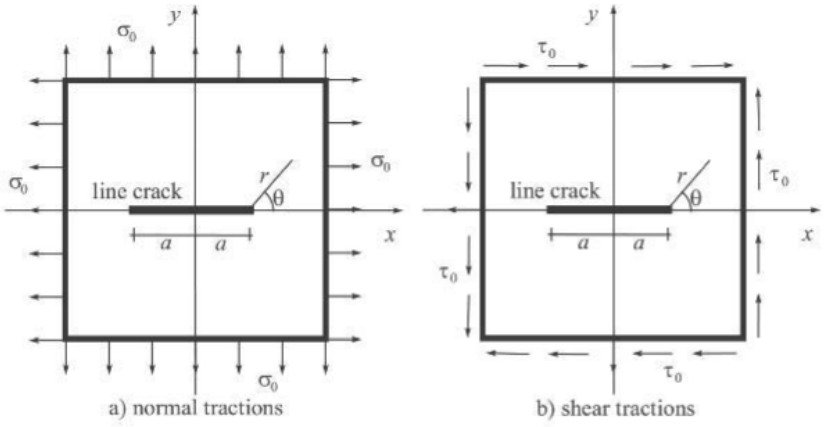

Figure 4: Typical REV considered in Griffith Theory [194].

Noting $\mathcal{E}$ the total energy stored in the REV, W_{ext} the work input from external mechanical forces, and Q the heat input, the conservation of the total energy of the system writes

$$\begin{aligned} \dot{W}_{ext} + \dot{Q} &= \dot{\mathcal{E}} \\ \dot{W}_{ext} + \dot{Q} &= \dot{K} + \dot{U} + \dot{U}_\Gamma \end{aligned} \tag{1}$$

in which K is the kinetic energy, and U, U_Γ is the internal energy stored in the bulk material, and is the internal surface energy of the cracked material. The work of external forces applied to the system is transformed into kinetic energy, potential energy, Π, elastic

deformation energy, U^e

$$\dot{W}_{ext} = \dot{K} - \dot{\Pi} + \dot{U}^e \qquad \Rightarrow -\dot{\Pi} + \dot{Q} = \dot{U}^p + \dot{U}_\Gamma \tag{2}$$

in which U^p is the internal plastic deformation energy. For an adiabatic transformation, $\dot{Q} = 0$, so

$$-\frac{\partial \Pi}{\partial a} = \frac{\partial U^p}{\partial a} + \frac{\partial U_\Gamma}{\partial a} \tag{3}$$

where a is the half length of the crack. The equation above indicates that the decrease rate of potential energy is equal to the rate of energy dissipated by plastic deformation and crack growth. For a purely brittle material, there is no plastic deformation and therefore, no dissipated plastic energy,

$$-\frac{\partial \Pi}{\partial a} = \frac{\partial U_\Gamma}{\partial a} = 2\gamma_s \tag{4}$$

in which γ_s is the surface energy at one of the two faces of the crack. Griffith crack growth energy (G) is defined as

$$G = -\frac{\partial \Pi}{\partial a} = 2\gamma_s \tag{5}$$

For a flat crack of length $2a$ subjected to a unilateral tensile stress $\sigma(x)$ at the lips and to σ_0 in the far field,

$$G = -\frac{\partial \Pi}{\partial a} = \frac{\pi a \sigma^2}{E} \tag{6}$$

where E is the Young's modulus. The critical stress that defines the threshold for crack propagation in mode I (tension normal to the crack planes) is

$$\sigma_{cr} = \sqrt{\frac{2\gamma_s E}{\pi a}} \tag{7}$$

The corresponding stress intensity factor is (see the details in the following paragraphs)

$$K^I_{cr} = \sigma_{cr}\sqrt{\pi a} \tag{8}$$

According to Griffith theory, the crack extends if the energy release rate ($-G$) exceeds the surface energy of the two crack faces:

$$-G = \frac{\partial \Pi}{\partial a} \geq 2\gamma_s \tag{9}$$

Equation 4 shows that when the crack propagates, the energy of the system reaches an extremum. Crack propagation is said to be stable if this extremum is a minimum

$$\frac{\partial^2(\Pi + U_\Gamma)}{\partial a^2} \begin{cases} < 0 & \text{unstable crack propagation} \\ = 0 & \text{stable crack propagation} \\ > 0 & \text{neutral equilibrium} \end{cases} \tag{10}$$

2.2.1.2 Stress Intensity Factors

Elastic stress fields around a crack tip are symmetrically distributed, and the local stress quantity is controlled by stress intensity factors (noted K), which are proportional to $\sigma\sqrt{\pi r}$. In a general form,

$$\sigma_{ij} = \frac{1}{\sqrt{r}}\left[K^{(I)} f_{ij}^{(I)}(\theta) + K^{(II)} f_{ij}^{(II)}(\theta) + K^{(III)} f_{ij}^{(III)}(\theta)\right] + \text{higher order terms} \tag{11}$$

in which functions f_{ij} depend on the orientation of the position vector of the point considered for the calculation of microscopic stress. Referring to the coordinate system in Figure 4, the stress intensity factors for fracture modes I, II and III are defined as

$$\begin{aligned} K^{(I)} &= lim_{r\to 0,\,\theta\to 0}\, \sigma_{yy}\sqrt{2\pi r} \\ K^{(II)} &= lim_{r\to 0,\,\theta\to 0}\, \sigma_{xy}\sqrt{2\pi r} \\ K^{(III)} &= lim_{r\to 0,\,\theta\to 0}\, \sigma_{yz}\sqrt{2\pi r} \end{aligned} \tag{12}$$

Stress intensity factors were computed to determine stress concentrations around flaws in infinite media subjected to "far field boundary conditions". Fracture mechanics states that unstable fracture propagation occurs when one of the stress intensity factors, K^k , or a combination of them (for mixed mode propagation), reaches a critical value, K^{kc} . This critical value, K^{kc} , is called fracture toughness and represents the potential ability of a material to withstand a given stress field at the tip of a crack and to resist progressive tensile crack extension. When several fracture mechanisms occur simultaneously, the general form of the failure criterion writes

$$f\left(K^{(I)}, K^{(Ic)}, K^{(II)}, K^{(IIc)}, K^{(III)}, K^{(IIIc)}\right) = 0 \tag{13}$$

In 2-D problem, mixed mode crack propagation problems only deal with the combination of mode I and mode II fractures. In general, only the mode I fracture toughness $K^{(Ic)}$ is experimentally measured, and

$$f\left(K^{(I)}, K^{(Ic)}, K^{(II)}\right) = 0 \tag{14}$$

The crack propagation criterion f can be derived theoretically, from optimization procedures (maximum circumferential stress, minimum strain energy density, maximum energy release rate), or empirically, from experiments. Griffith model describes the failure of a solid material satisfying a critical energy criterion rather than a maximum-stress-based failure control, which avoids the dependency of the criterion on the flaw size.

2.2.1.3 J Integral

In the absence of body force applied to the REV, in the absence of traction applied to the crack faces, and for a crack oriented parallel to the x-axis, the 2D J-integral is defined as

$$J = \oint_{\Gamma} \left(W_s \, \mathrm{d}y - \mathbf{t} \cdot \frac{\partial \mathbf{u}}{\partial x} \, \mathrm{d}\Gamma \right) \tag{15}$$

in which Γ is a closed contour containing two segments of crack faces and two portions in the solid REV, as illustrated in Figure 5. $\mathbf{u}$ is the displacement vector measured on surface Γ, and $\mathbf{t}$ is the traction vector that applies on Γ. W_s is the strain energy of the REV, defined as

$$W_s = \int_0^{\varepsilon} \boldsymbol{\sigma} : \mathrm{d}\boldsymbol{\varepsilon} \tag{16}$$

The total potential energy of a two-dimensional domain including a traction free crack that is surrounded by a contour curve Γ under quasi-static conditions and in the absence of body forces can be defined as

$$\Pi = \int_V W_s \, \mathrm{d}V - \oint_{\Gamma} \mathbf{t} \cdot \mathbf{u} \, \mathrm{d}\Gamma \tag{17}$$

For a virtual crack extension $\mathrm{d}a$,

$$-\frac{\mathrm{d}\Pi}{\mathrm{d}a} = -\int_V \frac{\mathrm{d}W_s}{\mathrm{d}a} \, \mathrm{d}V + \oint_{\Gamma} \frac{\mathrm{d}\mathbf{t}}{\mathrm{d}a} \cdot \mathbf{u} \, \mathrm{d}\Gamma + \oint_{\Gamma} \mathbf{t} \cdot \frac{\mathrm{d}\mathbf{u}}{\mathrm{d}a} \, \mathrm{d}\Gamma \tag{18}$$

After applying the divergence theorem,

$$-\frac{\mathrm{d}\Pi}{\mathrm{d}a} = \oint_{\Gamma}\left(W_s\,\mathrm{d}y - \mathbf{t}\cdot\frac{\mathrm{d}\mathbf{u}}{\mathrm{d}x}\,\mathrm{d}\Gamma\right) \tag{19}$$

As a result,

$$J = -\frac{\mathrm{d}\Pi}{\mathrm{d}a} = G \tag{20}$$

The J integral is equal to the rate of change of the potential energy, for an elastic nonlinear solid during a unit crack extension [194, 226]. Let us consider the rate of change of the potential energy for the portion of the crack on boundaries Γ_2 and Γ_4 in Figure 5, and a contour Γ_1 and Γ_3 in the unfractured domain. We have $dy = 0$ and $\boldsymbol{t} = \mathbf{0}$ on Γ_2 and on Γ_4, therefore,

$$J = J_{\Gamma_1} + J_{\Gamma_2} + J_{\Gamma_3} + J_{\Gamma_4} = J_{\Gamma_1} + J_{\Gamma_3} \tag{21}$$

In a state of equilibrium,

$$0 = -\frac{\mathrm{d}\Pi}{\mathrm{d}\Pi} = J = J_{\Gamma_1} + J_{\Gamma_3} \tag{22}$$

as a result, the value of J is independent of the path taken to define the contour in the unfractured domain. This is a "a path independent contour integral". The J-integral can be conveniently computed at integration points. As a result, Griffith crack propagation criterion can be easily implemented in Finite Element codes. In the Equivalent Domain Integral (EDI) Method,

$$J = \int_{A^*}\left(\sigma_{ij}\frac{\partial u_j}{\partial x_1} - W_s\delta_{1i}\right)\frac{\partial q}{\partial x_i}\mathrm{d}A \tag{23}$$

in which "$\Gamma_2 = \Gamma_4 = 0$", i.e. the J-integral is evaluated for a change in rate of potential energy at the crack tip. As a result the contour J-integral is replaced by an equivalent area integral, in which q is an arbitrary smoothing function which is equal to unity on Γ_3 and zero on Γ_1.

2.2.2 Classical Models of Fracturing under Pressurization

2.2.2.1 Theoretical Models

By contrast with stress analyses, fracture mechanics can be used to model the initiation and propagation of cracks with or without pre-existing discontinuities. Fracture toughness

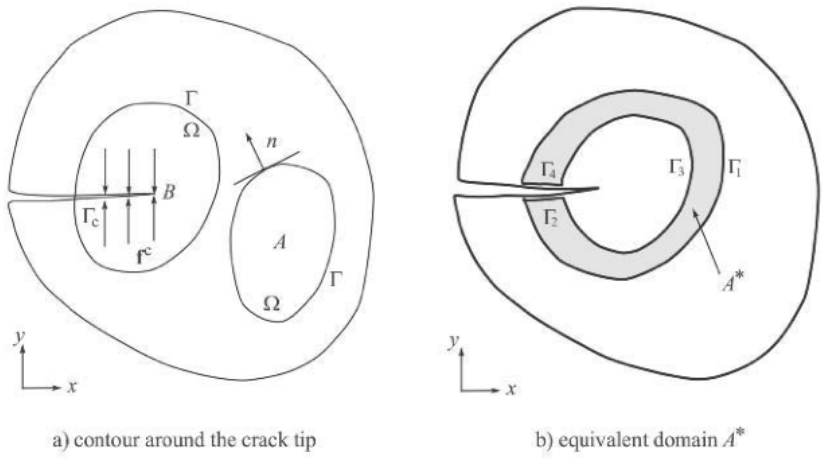

Figure 5: Geometry of the problem used to define the J-Integral [194].

is the parameter that controls crack propagation. Approaches based on Fracture Mechanics not only account for the stress distribution around a borehole, but also for the borehole geometry and the size of the cracks [4, 228]. Fracture Mechanics initiation and propagation criteria are based on the theory of elasticity.

When cracks exist prior to fluid injection, the injected fluid can pressurize crack surfaces. A concentration of stress on crack surfaces indicates that the fractures will propagate from pre-existing cracks rather than initiate at other locations around the borehole [282]. Abou-Sayed et al. [4] proposed a Fracture Mechanics model in which a borehole embedded an infinite medium is subjected to a biaxial stress. It is assumed that two radial cracks, symmetrically opposite, develop with an arbitrary angle with respect to the maximum principal stress. Internal pore pressure acts not only on the borehole but also on the crack surfaces. The location and direction of the cracks is postulated, and the predictions of stress are based on the same principles as in classical stress analyses. Rummel and Winter [228] also suggested a model with two symmetrical radial cracks, but contrary to Abou-Sayed et al's model, cracks are assumed to be aligned along the direction of the maximum principal stress. Moreover, Rummel and Winter take different stress intensity factors into account, in order to study the contribution from the fluid pressure on the borehole, the pressure distribution on crack surfaces, and the variation of pressurization under different confining stress states. The total stress intensity factor is computed as the sum of the stress

intensity factors associated to each type of stress gradient imposed in the problem. Zoback and Pollard [304] expressed stress intensity factors to study two cases of hydraulic fracture propagation: a two-dimensional pressurized blade shaped fracture under (1) concentrated loading and (2) under uniformly distributed pressure. Sih and Liebowitz [246] developed a model to predict mode I fracture propagation for penny shaped cracks under constant pressure loading. Abe et al. [2] modeled the growth of vertical penny-shaped fractures due to the continuous injection of fluid from a small borehole at the center of the crack.

The propagation of pressurized fracture was studied extensively with linear elastic models. For instance, a model of radial propagation of penny-shaped fractures (Figure 6) under constant fluid pressure was proposed by Sneddon [250]. The problem of a flat elliptical crack under constant loading was studied by Green and Sneddon [112]. Perkins and Kern [216] developed the "PK" model, based on Sneddon's plane strain crack solution [251]. Later, Nordgren [205] considered the fluid loss and adapted the PK model into the "PKN" model, which is applicable to long fractures of limited height, with an elliptical vertical cross-section (Figure 7). Knristianovic and Zheltov [147] and Geersma and de Klerk [101] developed the "KGD" model, in which the width of the fractures is independent of their height. The KGD model is used for short fractures where plane strain assumptions can be applied to the horizontal crack plane (Figure 8).

None of the models mentioned above is applicable to layered reservoirs. "P3D" models were developed in the 1980s to study multiple layers (Figure 9(b)). The domain of the material is sub-divided into a series of "PKN-like" cells or half lumped ellipses. Hydraulic fracturing is modeled on separate sub-domains (considered to be homogeneous). Resulting models range in two categories: cell-based models, and lumped models [182]. Planar 3D ("PL3D") models were formulated after the P3D model, and describe the fracture footprint and the coupled fluid flow equation by a 2D mesh of cells, typically a moving triangular mesh (Figure 10(a)), or a fixed rectangular mesh (Figure 10(b)), oriented in a (vertical) plane [7]. 3D elasticity equations are used to describe the fracture width as a function of fluid pressure. PL3D is more accurate than P3D, but requires more CPU.

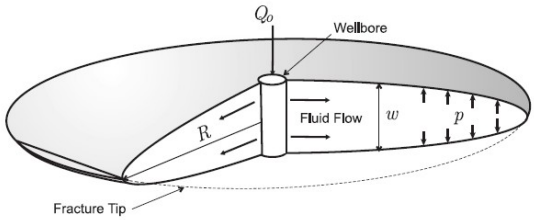

Figure 6: Model of radial propagation of penny-shaped fractures [7].

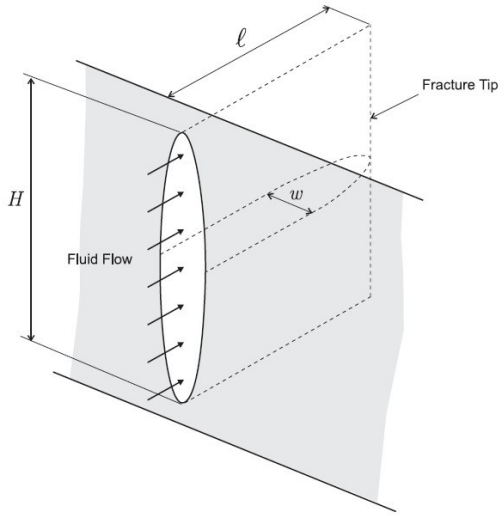

Figure 7: "PKN" fracture geometry [7].

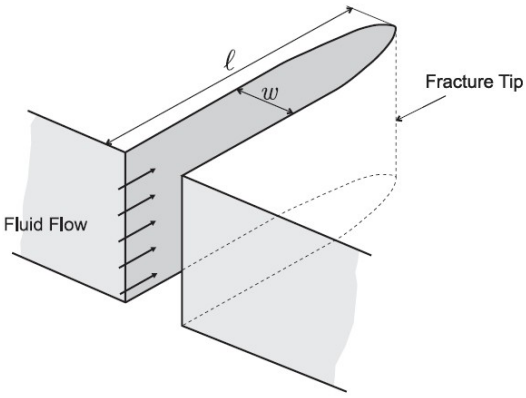

Figure 8: "KGD" fracture geometry.

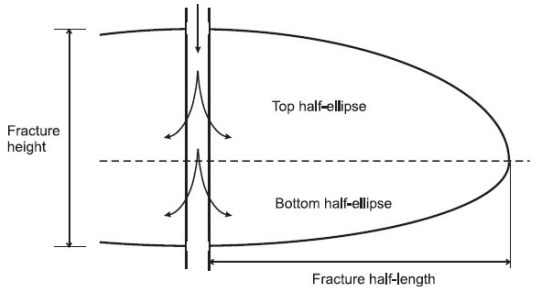

(a) Fracture geometry based on pseudo 3D lumped elliptical model.

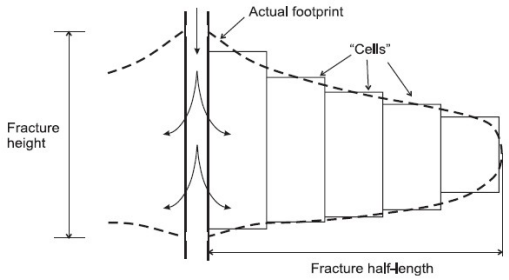

(b) Cell-based pseudo-3D fracture geometry.

Figure 9: Pseudo 3D model with lumped elliptical geometry and cell-based geometry [7].

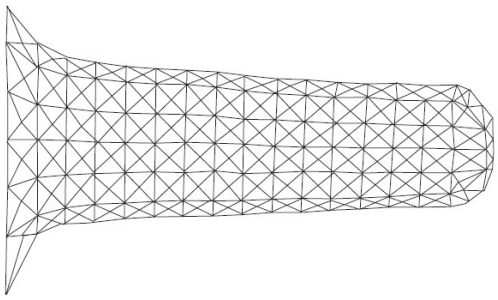

(a) Planar 3D fracture geometry based on moving mesh system of triangular elements.

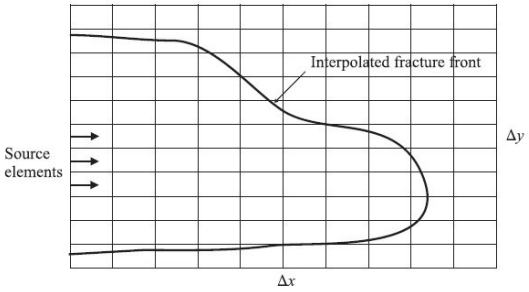

(b) Planar 3D fracture geometry based on regular (fix) system of quadrangular elements.

Figure 10: Planar 3D fracture geometry based on moving mesh system of triangular elements and ased on regular (fix) system of quadrangular elements.[7]

2.2.2.2 *Experimental Studies*

In addition to the pressurization tests mentioned above, experiments on hydraulic fracturing aim to study:

- ***The influence of the type of fluid injected***: Ishida et al. [136] found that viscous oil tends to generate thick and planar cracks with few branches, while water tends to generate thin and wavelike cracks with many secondary branches. The fluid loss equation (below) indicates that high viscosity fracturing fluid results in low fluid-loss velocity,

$$v_l = \frac{K_l}{\sqrt{t-\tau}} \tag{24}$$

  where v_l is the fluid-loss velocity normal to the fracturing faces, K_l is the overall fluid-loss coefficient, t is the current time, and τ is the time when filtration starts. Fluids mixed with particles were also studied in Civil Engineering: Germanovich and Murdoch [108] proposed a technique of injection with sediment-laden slurry in order to raise the level of the ground and prevent flood.

- ***Mixed crack propagation modes (tensile versus shear cracking)***: The results of Acoustic Emission (AE) show that shear-type mechanisms are dominant during water injection and sleeve pressurization, whereas tensile-type mechanisms were dominant during oil injection [136].

- ***The relationship between microseismic events and crack density***: Zoback et al. [275, 71, 305] used microseismic monitoring in order to evaluate the evolution of the size and orientation of fractures. They found that the triggering of seismic slip on faults that are well-oriented could potentially lead to unstable crack propagation. On faults that are not so well-oriented however, the triggered slip proved to be slow.

2.2.3 Analytical Prediction of Fracture Propagation upon Pressurization

2.2.3.1 *Theoretical Studies*

The propagation of a penny-shaped fracture driven by an incompressible Newtonian fluid flow is either due to a migration of the fracture tip (toughness-dominated regime), or to

the propagation of a fluid front (viscosity-dominated regime). Savitski and Detournay [231] developed an analytical method to predict the evolution of the aperture ($w(r,t)$), radius ($R(t)$) and pressure ($p(r,t)$) of a fracture caused by the injection of a viscous fluid at the center of a wellbore. Fracture aperture and pressure are determined by solving a system of four equations:

- The momentum balance equations;
- A non-local integral relation stemming from the theory of elasticity:

$$w = \frac{8R}{\pi E'} \int_{r/R}^{1} \frac{\xi}{\sqrt{\xi^2 - (r/R)^2}} \int_0^1 \frac{xp(x\xi R, t)}{\sqrt{1-x^2}} \, \mathrm{d}x \, \mathrm{d}\xi \tag{25}$$

  where r is the radial coordinate, t is time, R is the fracture radius, and E' is the plane strain modulus: $E' = E/(1-\nu^2)$.

- The equation expressing the conservation of fluid mass;
- Poiseuille flow equation.

The combination of the mass conservation equation and Poiseuille law provides Reynolds equation, which is the equation founding the theory of lubrication (i.e. the theory of flow in spaces that have one dimension much smaller than the others):

$$\frac{\partial w}{\partial t} = \frac{1}{12\mu} \frac{1}{r} \frac{\partial}{\partial r} \left(r w^3 \frac{\partial p}{\partial r} \right) \tag{26}$$

in which μ is the viscosity of the fluid. The fracture propagation problem can be scaled by using the non-dimensional toughness $\mathscr{K}$ (defined from the elasticity PDEs) or the non-dimensional viscosity $\mathscr{M}$ (defined from the lubrication equation). The linear-elastic fracture toughness of a material is determined from the Stress Intensity Factor (SIF, $K_{i,\, i=1\ldots3}$) at which a thin crack in the material begins to grow. The problem is solved for dimensionless crack opening Ω, net pressure Π, and fracture radius γ

$$w(r,t) = \varepsilon(t) L(t) \Omega(\rho, \mathscr{P}(t)) \tag{27}$$

$$p(r,t) = \varepsilon(t) E' \Pi(\rho, \mathscr{P}(t)) \tag{28}$$

$$R(t) = L(t) \gamma(\mathscr{P}(t)) \tag{29}$$

where $\rho = r/R\,(0 \leqslant \rho \leqslant 1)$ is the the dimensionless radial coordinate, $\varepsilon(t)$ is a small number, $L(t)$ is a length scale of the same order of magnitude as $R(t)$, and $\mathscr{P}(t)$ is a dimensionless evolution parameter. Based on a dimensionless analysis, two equations are used to identify ε and L. The first is global mass conservation:

$$\varepsilon L^3 = Q_0 t \tag{30}$$

where Q_0 is the rate of injection, assumed to be constant. The second equation depends on the non-dimensional parameter used to scale the solution. For a formulation depending on the non-dimensional viscosity defined in the lubrication theory,

$$\frac{\mu'}{\varepsilon^3 E' t} = 1 \tag{31}$$

From equation (30) and (31), the small parameter ε_m and the lengthscale L_m can be obtained

$$\varepsilon_m = \left(\frac{\mu'}{E' t}\right)^{1/3},\ L_m = \left(\frac{E' Q_0^3 t^4}{\mu'}\right)^{1/9} \tag{32}$$

and the dimensionless toughness $\mathscr{K}$ can be deduced

$$\mathscr{K} = K' \left(\frac{t^2}{\mu'^5 Q_0^3 E'^{13}}\right)^{1/18} \tag{33}$$

For a formulation depending on the non-dimensional toughness defined in fracture mechanics,

$$\frac{K'}{\varepsilon E' L^{1/2}} = 1 \tag{34}$$

The dimensionless parameters ε_k and L_k are determined from equation (30) and (34)

$$\varepsilon_k = \left(\frac{K'^6}{E'^5 Q_0 t}\right)^{1/5},\ L_k = \left(\frac{Q_0 E'^2 t^2}{K'}\right)^{1/9} \tag{35}$$

where

$$\mu' = 12\mu,\ K' = 4\left(\frac{2}{\pi}\right)^{1/2} K_{\mathrm{Ic}} \tag{36}$$

Therefore, the dimensionless viscosity $\mathscr{M}$ is defined as

$$\mathscr{M} = \mu' \left(\frac{Q_0^3 E'^1 3}{K'^{18} t^2}\right)^{1/5} \tag{37}$$

From the above calculations, the dimensionless viscosity $\mathscr{M}$ (in toughness dominated propagation) and toughness $\mathscr{K}$ (in viscosity dominated propagation) can be related

$$\mathscr{M} = \mathscr{K}^{-18/5} \tag{38}$$

Asymptotic solutions for zero and large toughness can be determined. In the large toughness regime for instance, the solution $\mathscr{F}_k(\Omega_k, \Pi_k, \gamma_k)$ is replaced by a Taylor series:

$$\mathscr{F}_k(\mathscr{M}) = \mathscr{F}_{k0} + \mathscr{M}\mathscr{F}_{k1} + \bigcirc(\mathscr{M}^2) \tag{39}$$

The reference regimes of fracture propagation are: (1) viscosity-dominated regime, when $\mathscr{K} < \mathscr{K}_{m0}$; (2) mixed-regime, when $\mathscr{K}_{m0} < \mathscr{K} < \mathscr{K}_{k0}$; and (3) toughness-dominated regime, when $\mathscr{K} > \mathscr{K}_{k0}$. $\mathscr{K}_{m0}$ is the dimensionless toughness parameter under the condition of zero-toughness, while $\mathscr{K}_{k0}$ is the dimensionless toughness under the condition of zero-viscosity. The mixed regime is found to occur for a very small range of values: $1 < \mathscr{K} < 3.5$. Physically, as soon as the fluid reaches the tip of the crack (i.e. when there is a negligible lag between fracture tip and fluid front), fracture first propagates in the elastic medium (in the toughness regime), and then grows according to the lubrication theory (in the viscosity regime) [231, 47]. Toughness and viscosity regimes alternate.

2.2.3.2 Application to the Modeling of Fracturing in Laboratory Tests

An experimental technique was introduced by Wu et al. [284] in order to control a circular, planar fracture. The fracture is initiated by thermal stress, which controls crack orientation. In the case of heating, a fracture is generated perpendicular to the cylindric sample axis, while in the case of cooling, the fracture is oriented parallel to the sample axis. The volume of the the pressurized fracture is

$$V(a) = \frac{16(1-\nu^2)}{3E} p a^3 G(a/R) \tag{40}$$

where E is Young's modulus, ν is Poisson's ratio, and the function G(a/R) can be replaced by F(a/R), where

$$F(a/R) = \frac{1 - 0.5(a/R) + 0.148(a/R)^3}{\sqrt{1 - a/R}} \tag{41}$$

in which a is the fracture radius, R is the radius of the cylinder. The fracture size (radius) is controlled by varying the volume $V(a)$ injected into the sample. The effective pressure in the fracture p can be expressed as

$$p(a) = \frac{\sqrt{\pi} K_{Ic}}{2\sqrt{R} F(a/R)} \sqrt{\frac{R}{a}} \tag{42}$$

where K_{Ic} is the mode I fracture toughness. The mode I stress intensity factor K_I is computed

$$K_I = \frac{2}{\pi} p \sqrt{\pi a} F(a/R) \tag{43}$$

The volume of fluid injected in the fracture and in the tubing (V_0) is obtained by considering the initial and final fracture sizes

$$V_0 = CR^3 \left[\left(\frac{a_2}{R}\right)^{5/2} - \left(\frac{a_1}{R}\right)^{5/2} \right] \left[\frac{\sqrt{R/a_1}}{F(a_1/R)} - \frac{\sqrt{R/a_2}}{F(a_2/R)} \right]^{-1} \tag{44}$$

with the constant,

$$C = \frac{16 K_f (1 - \nu^2)}{3E} \tag{45}$$

where K_f is the bulk modulus of the injection liquid, a_1 and a_2 are the initial and final fracture radii.

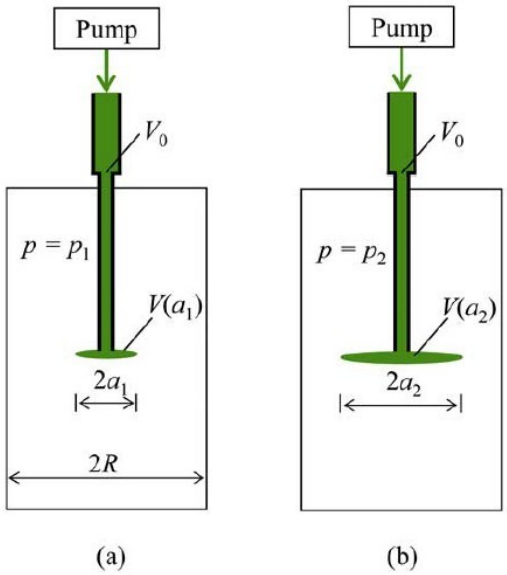

Figure 11: (a) Initial and (b) final states of fracture propagation [284].

2.3 Damage Models

2.3.1 Principles of Continuum Damage Mechanics (CDM)

Fracture Mechanics models allow predicting the state of stress around crack tips, and the propagation of the crack. Formulation get very complex as several cracks propagate simultaneously. Continuum Damage Mechanics (CDM) avoids modeling each crack individually. Damage effects are analyzed from the average stress at the REV scale, and evolution laws are derived from the two first laws of thermodynamics. The first contribution to CDM is the work done by Kachanov [142], who introduced a continuity parameter to study the time to rupture during creep processes. Rabotnov continued Kachanov's research and defined a damage variable to compute effective stresses [221]. CDM initially aimed to predict deformation and stiffness in solids subject to cracking. With the work done by Lemaître, Chaboche, Hult and others, the framework of CDM was extended to various materials including porous media [164, 54, 132]. Stresses and strains in damaged materials were computed according to various principles, including the Strain Equivalence Hypothesis, the Strain Energy Equivalence Hypothesis and the Power Equivalence Hypothesis [6, 5].

Geomaterials have a heterogeneous porous structure needing rigorous characterization by *ad hoc* parameters, in order to determine the "reference state", i.e. the mechanical state in which the material is considered undamaged. Porous networks are generally complex, especially in micro-porous rock such as coal and shale, which comprise flaws ranging from the nano-scale to the millimeter scale [171]. Extending the framework of CDM to geomechanics thus raises many theoretical issues associated to the multiple scales of observation that need to be considered. Micro-mechanics allows predicting the initiation and propagation of individual defects. Sophisticated homogenization schemes were proposed in order to upscale material properties at the scale of a REV of rock [214, 3], including the effects of rock saturation [155] and the non-local influence of damage [220]. Assumptions have to be made on the shape of the cracks. Models were often restricted to the growth of cracks having the same shape, orientation and growth rate. In theory, micro-mechanical models could predict the evolution of as many kinds of defects and defect orientations as needed, as long as evolution laws can be provided. The CDM thermodynamic framework is well-suited

for numerical implementation in Finite Element Methods (FEM) because discontinuities are modeled as energy losses at the REV scale.

The fabric (or "morphology") of the intact medium has a strong impact on damage evolution in heterogeneous media such as concrete and rock, and even in composites. Voronoi cell FEMs were used to predict the influence of microstructure on crack propagation [168] in a medium containing stress-induced heterogeneities. Extended Finite Element Methods (X-FEM) were used to predict fracture propagation in homogeneous and layered media including composites with delamination [199]. However, modeling the damaged zone ahead of the fracture tip, as would be of interest for rock subject to hydraulic fracturing or shear faulting for instance, still raises many issues related to the difficult modeling of the transition between damaged continuum and discontinuous medium [189]. Several numerical methods were proposed, either by means of a multi-scale framework [151, 235], or by means of an averaged damage quantity defined at the scale of a REV [259, 274]. The former methods do not allow tracking a damage variable explicitly, while in the latter, the link between length scales involved in stress intensity factors is not justified.

2.3.2 Thermodynamic framework

CDM models are based on a thermodynamic framework similar to plasticity, in which stress-strain and other conjugation relationships are derived from energy potentials. This subsection recalls the thermodynamic principles used in CDM [66, 67]. We define Eulerian variables, such as Eulerian porosity n, as variables that are measured in reference to the current state of the Representative Elementary Volume. We define Lagrangian variables, such as Lagrangian porosity Φ, as variables that are measured in reference to the initial state of the Representative Elementary Volume. The thermodynamic conjugation relationships are recalled for both configurations. The DSID model is formulated in a Lagrangian configuration.

2.3.2.1 First law of thermodynamics

The first law expresses the conservation of energy. The change of a total energy $\mathcal{E}$ of a system is equal to the sum of the work rate $\dot{W}_{ext}$ of the external forces acting on the system, and

of the rate $\dot{Q}$ of external heat supply,

$$\frac{\mathrm{d}\mathcal{E}}{\mathrm{d}t} = \dot{W}_{ext} + \dot{Q} \tag{46}$$

Total energy $\mathcal{E}$ of a system equals to the amount of the kinetic energy K and its internal energy U; thus, the change of total energy also can be decomposed into two parts,

$$\frac{\mathrm{d}\mathcal{E}}{\mathrm{d}t} = \frac{\mathrm{d}K}{\mathrm{d}t} + \frac{\mathrm{d}U}{\mathrm{d}t} \tag{47}$$

In porous media, the kinetic energy contains skeleton kinetic energy and fluid kinetic energy,

$$\begin{aligned} &\frac{\mathrm{d}K}{\mathrm{d}t} = \frac{\mathrm{d}^s K_s}{\mathrm{d}t} + \frac{\mathrm{d}^f K_f}{\mathrm{d}t} \\ =&\frac{\mathrm{d}^s}{\mathrm{d}t}\int_{V_t} \frac{1}{2}\rho_s(1-n)(\mathbf{v}^s)^2 \mathrm{d}V_t + \frac{\mathrm{d}^f}{\mathrm{d}t}\int_{V_t} \frac{1}{2}\rho_f n(\mathbf{v}^f)^2 \mathrm{d}V_t \end{aligned} \tag{48}$$

in which the particle derivative $\mathrm{d}^\pi K_\pi/\mathrm{d}t$ is defined as

$$\frac{\mathrm{d}^\pi K_\pi}{\mathrm{d}t} = \frac{\partial K_\pi}{\partial t} + (\nabla_x K_\pi)\cdot \mathbf{V}^\pi, \qquad \pi = f,\, s \tag{49}$$

where n is the Eulerian porosity; $\mathrm{d}V_t$ is the total volume of system under current configuration; ρ_s and ρ_f are the mesoscopic matrix and fluid densities. Let e_s be the specific internal energy of skeleton per mass unit, and e_f be the specific internal energy of fluid per mass unit. The derivative of internal energy U can be calculated as follow

$$\frac{\mathrm{d}U}{\mathrm{d}t} = \frac{\mathrm{d}^s}{\mathrm{d}t}\int_{V_t} \rho_s(1-n)e_s \,\mathrm{d}V_t + \frac{\mathrm{d}^f}{\mathrm{d}t}\int_{V_t} \rho_f n e_f \,\mathrm{d}V_t \tag{50}$$

Introducing the overall density of internal energy per unit of volume, e, which is defined as

$$e = \rho_s(1-n)e_s + \rho_f n e_f \tag{51}$$

The derivative of internal energy can be described as

$$\frac{\mathrm{d}U}{\mathrm{d}t} = \frac{\mathrm{d}^\pi}{\mathrm{d}t}\int_{V_t} e \,\mathrm{d}V_t \tag{52}$$

$$
\begin{aligned}
\frac{\mathrm{d}U}{\mathrm{d}t} &= \int_{V_t}\left(\frac{\mathrm{d}^s(\rho_s(1-n)e_s)}{\mathrm{d}t} + \rho_s(1-n)e_s\nabla_x\cdot\mathbf{v}^s\right)\mathrm{d}V_t \\
&\quad + \int_{V_t}\left(\frac{\mathrm{d}^s(\rho_f n e_f)}{\mathrm{d}t} + \rho_f n e_f\nabla_x\cdot\mathbf{v}^f\right)\mathrm{d}V_t \\
&= \int_{V_t}\left(\frac{\mathrm{d}^s(e-\rho_f n e_f)}{\mathrm{d}t} + (e-\rho_f n e_f)\nabla_x\cdot\mathbf{v}^s + \frac{\mathrm{d}^s(\rho_f n e_f)}{\mathrm{d}t} + \rho_f n e_f\nabla_x\cdot\mathbf{v}^f\right)\mathrm{d}V_t \\
&= \int_{V_t}\left(\frac{\mathrm{d}^s e}{\mathrm{d}t} + e\nabla_x\cdot\mathbf{v}^s - \frac{\mathrm{d}^s(\rho_f n e_f)}{\mathrm{d}t} + \frac{\mathrm{d}^f(\rho_f n e_f)}{\mathrm{d}t} + \rho_f n e_f\nabla_x\cdot(\mathbf{v}^f-\mathbf{v}^s)\right)\mathrm{d}V_t \\
&= \int_{V_t}\left(\frac{\mathrm{d}^s e}{\mathrm{d}t} + e\nabla_x\cdot\mathbf{v}^s + \rho_f n e_f\nabla_x\cdot(\mathbf{v}^f-\mathbf{v}^s)\right)\mathrm{d}V_t \\
&\quad + \int_{V_t}\left[\left(\frac{\partial(\rho_f n e_f)}{\partial t} + (\nabla_x(\rho_f n e_f))\cdot\mathbf{v}^f\right) - \left(\frac{\partial(\rho_f n e_f)}{\partial t} + (\nabla_x(\rho_f n e_f))\cdot\mathbf{v}^s\right)\right]\mathrm{d}V_t \\
&= \int_{V_t}\left(\frac{\mathrm{d}^s e}{\mathrm{d}t} + e\nabla_x\cdot\mathbf{v}^s + \nabla_x\cdot(e_f\mathbf{w})\right)\mathrm{d}V_t
\end{aligned}
\tag{53}
$$

where $\mathbf{w} = \rho_f n(\mathbf{v}^f - \mathbf{v}^s)$. The work rate of the external body and surface forces $\dot{W}_{ext}$ is calculated

$$
\dot{W}_{ext} = \int_{V_t}\left(\rho_s\,(1-n)\,\mathbf{f}\cdot\mathbf{v}^s + \rho_f n\mathbf{f}\cdot\mathbf{v}^f\right)\mathrm{d}V_t + \int_{\partial V_t}(\mathbf{T}^s\cdot\mathbf{v}^s + \mathbf{T}^f\cdot\mathbf{v}^f)\mathrm{d}a \tag{54}
$$

where $\mathbf{f}$ is a body force density per mass unit; $\mathbf{T}$ is a surface force density; $\mathbf{v}^s$ and $\mathbf{v}^f$ are the velocities of matrix and fluid. The strain work rate associated with skeleton particles and fluid particles:

$$
\begin{aligned}
\dot{W}_d = &\int_{V_t}\left(\rho_s(1-n)\mathbf{f}\cdot\mathbf{v}^s + \rho_f n\mathbf{f}\cdot\mathbf{v}^f\right)\mathrm{d}V_t + \int_{\partial V_t}(\mathbf{T}^s\cdot\mathbf{v}^s + \mathbf{T}^f\cdot\mathbf{v}^f)\,\mathrm{d}a \\
&- \int_{V_t}\left(\rho_s(1-n)\boldsymbol{\gamma}^s\cdot\mathbf{v}^s + \rho_f n\boldsymbol{\gamma}^f\cdot\mathbf{v}^f\right)\mathrm{d}V_t
\end{aligned}
\tag{55}
$$

where $\boldsymbol{\gamma}^\pi$ is the acceleration of particle π, which is the particle derivative of velocity $\mathbf{v}^\pi(\mathbf{x},t)$

$$
\boldsymbol{\gamma}^\pi = \frac{\mathrm{d}^\pi\mathbf{v}^\pi}{\mathrm{d}t} = \frac{\partial\mathbf{v}^\pi}{\partial t} + (\nabla_x\mathbf{v}^\pi)\cdot\mathbf{v}^\pi \tag{56}
$$

Therefore, the work rate of the external body and surface forces $\dot{W}_{ext}$ can be rewritten in the form

$$
\dot{W}_{ext} = \dot{W}_d + \frac{\mathrm{d}K}{\mathrm{d}t} \tag{57}
$$

Combining the equation 46, 47 and 57, the first law of thermodynamics can be represented in another form

$$
\frac{\mathrm{d}U}{\mathrm{d}t} = \dot{W}_d + \dot{Q} \tag{58}
$$

Equation 58 expresses that in any infinitely slow transport system, the change of the internal energy of the system is the sum of the mechanical work performed by the external forces on the system and the external heat supply. Assuming a partial volumetric stress tensor $\boldsymbol{\sigma}^s$ related to the skeleton and a partial volumetric stress tensor $\boldsymbol{\sigma}^f$ related to the fluid, the momentum balance gives the relations

$$\mathbf{T}^s = (1-n)\boldsymbol{\sigma}^s \cdot \mathbf{n}, \quad \mathbf{T}^f = n\,\boldsymbol{\sigma}^f \cdot \mathbf{n} \tag{59}$$

Moreover, partial stresses $\boldsymbol{\sigma}^s$ and $\boldsymbol{\sigma}^f$ should satisfy the local equations of motion:

$$\nabla_x \cdot [(1-n)\boldsymbol{\sigma}^s] + \rho_s(1-n)(\mathbf{f} - \boldsymbol{\gamma}^s) + \mathbf{f}_{int}^{\rightarrow s} = 0 \tag{60}$$

$$\nabla_x \cdot (n\boldsymbol{\sigma}^f) + \rho_f n(\mathbf{f} - \boldsymbol{\gamma}^f) + \mathbf{f}_{int}^{\rightarrow f} = 0 \tag{61}$$

where the volume force $\mathbf{f}_{int}^{\rightarrow \pi}$ accounts for the macroscopic interaction force exerted by the other continuum. Obviously, $\mathbf{f}_{int}^{\rightarrow s}$ and $\mathbf{f}_{int}^{\rightarrow f}$ are one pair of action-reaction forces, so

$$\mathbf{f}_{int}^{\rightarrow s} + \mathbf{f}_{int}^{\rightarrow f} = 0 \tag{62}$$

In addition,

$$\mathbf{T} = \mathbf{T}^s + \mathbf{T}^f \tag{63}$$

$$\boldsymbol{\sigma} = (1-n)\boldsymbol{\sigma}^s + n\boldsymbol{\sigma}^f \tag{64}$$

In the mesoscopic scale, the fluid stress can be written as a spherical tensor

$$\boldsymbol{\sigma}^f = -p\mathbf{I} \tag{65}$$

As this result, the equation 61 can be rewritten in the form

$$-\nabla_x(np) + \rho_f n(\mathbf{f} - \boldsymbol{\gamma}^f) + \mathbf{f}_{int}^{\rightarrow f} = 0 \tag{66}$$

The divergence theorem and the symmetry of the Cauchy stress tensor result in

$$\begin{aligned} \int_{\partial V_t} \mathbf{T}^s \cdot \mathbf{v}^s \mathrm{d}a &= \int_{\partial V_t} ((1-n)\boldsymbol{\sigma}^s \cdot \mathbf{n}) \cdot \mathbf{v}^s \mathrm{d}a \\ &= \int_{V_t} \left[(1-n)\boldsymbol{\sigma}^s : \mathbf{d}^s + \mathbf{v}^s \cdot (\nabla_x \cdot ((1-n)\boldsymbol{\sigma}^s))\right] \mathrm{d}V_t \end{aligned} \tag{67}$$

$$\int_{\partial V_t} \mathbf{T}^f \cdot \mathbf{v}^f \mathrm{d}a = \int_{\partial V_t} \left(n\boldsymbol{\sigma}^f \cdot \mathbf{n}\right) \cdot \mathbf{v}^f \mathrm{d}a = \int_{V_t} \left[n\boldsymbol{\sigma}^f : \mathbf{d}^f + \mathbf{v}^f \cdot (\nabla_x \cdot (n\boldsymbol{\sigma}^f))\right] \mathrm{d}V_t \tag{68}$$

where $\mathbf{n}$ is the outward unit vector normal to the surface $\mathrm{d}a$, and

$$\mathbf{d}^{\pi} = \frac{1}{2}\left(\nabla_x \mathbf{v}^{\pi} + (\nabla_x \mathbf{v}^{\pi})^T\right) \tag{69}$$

Accordingly, taking equations 59-69 into equation 55, the equation 55 can expressed as

$$\dot{W}_d = \int_{V_t} \left(\boldsymbol{\sigma} : \mathbf{d}^s - \nabla_x \cdot \left(\frac{p}{\rho_f}\mathbf{w}\right) + \left(\mathbf{f} - \gamma^f\right) \cdot \mathbf{w}\right) \mathrm{d}V_t \tag{70}$$

The external heat supply is due to the external heat conduction and external volume heat sources. Therefore, the heat rate $\dot{Q}$ is written in the form

$$\dot{Q} = \int_{\partial V_t} Q_c(\mathbf{x}, \mathbf{n}, t)\, \mathrm{d}a + \int_{V_t} q_s(\mathbf{x}, t)\, \mathrm{d}V_t \tag{71}$$

where Q_c is a surface rate density of heat supply by conduction, and q_s is as volume rate density of the heat provided by external heat sources. The tetrahedron lemma applied to Q_c implies that it has the form of an influx per surface unit

$$Q_c = -\mathbf{q} \cdot \mathbf{n} \tag{72}$$

where $\mathbf{q}$ is the heat flow vector. Introducing the fluid-specific enthalpy h_f

$$h_f = e_f + \frac{p}{\rho_f} \tag{73}$$

After computations, the Eulerian formulation for the first law is obtained as

$$\frac{\mathrm{d}^s e}{\mathrm{d}t} + e\nabla_x \cdot \mathbf{v}^s = \boldsymbol{\sigma} : \mathbf{d}^s - \nabla_x \cdot (h_f \mathbf{w} + \mathbf{q}) + (\mathbf{f} - \gamma^f) \cdot \mathbf{w} + q_s \tag{74}$$

Lagrangian quantities are introduced in order to study the evolution of thermodynamic variables relative to the initial configuration. Using the Lagrangian density of internal energy U and the Lagrangian heat flow vector $\mathbf{Q}$ corresponding to the initial volume $\mathrm{d}V_0$

$$U\, \mathrm{d}V_0 = e\, \mathrm{d}V_t, \quad \mathbf{Q} \cdot \mathbf{N}\, \mathrm{d}A = \mathbf{q} \cdot \mathbf{n}\, \mathrm{d}a \tag{75}$$

with

$$\boldsymbol{\sigma} : \mathbf{d}^s\, \mathrm{d}V_t = \boldsymbol{\pi} : \frac{\mathrm{d}\boldsymbol{\Delta}}{\mathrm{d}t}\, \mathrm{d}V_0 \tag{76}$$

$$\mathbf{w} \cdot \mathbf{n}\, \mathrm{d}a = \mathbf{M} \cdot \mathbf{N}\, \mathrm{d}A \tag{77}$$

$$q_s\, \mathrm{d}V_t = Q_s\, \mathrm{d}V_0 \tag{78}$$

where $\boldsymbol{\pi}$ is the second Piola-Kirchhoff stress tensor, and $\boldsymbol{\Delta}$ is the Lagrangian strain tensor

$$\boldsymbol{\pi} = J\mathbf{F}^{-1} \cdot \boldsymbol{\sigma} \cdot \mathbf{F}^{-T} \tag{79}$$

$$\boldsymbol{\Delta} = \frac{1}{2}(\mathbf{F}^T \cdot \mathbf{F} - \mathbf{I}) \tag{80}$$

In equation 79, $J = \det\mathbf{F}$ is the Jacobian of the deformation. From the equations above, the Lagrangian energy equation can be expressed as

$$\frac{\mathrm{d}U}{\mathrm{d}t} = \boldsymbol{\pi} : \frac{\mathrm{d}\boldsymbol{\Delta}}{\mathrm{d}t} - \nabla_X \cdot (h_f\mathbf{M} + \mathbf{Q}) + (\mathbf{f} - \boldsymbol{\gamma}^f) \cdot \mathbf{F} \cdot \mathbf{M} + Q_s \tag{81}$$

2.3.2.2 Second law of thermodynamics

The second law of thermodynamics expresses the loss of efficient mechanical work upon irreversible processes, which translates into an increase of entropy (noted $d\mathbb{S}$). During irreversible thermodynamic processes, energy is dissipated in the form of heat (elastic entropy rate), and in the form of irreversible microstructure changes (inelastic entropy rate, due to plasticity or damage for instance). The total entropy rate (elastic and inelastic) exceeds the production of heat

$$\frac{\mathrm{d}\mathbb{S}}{\mathrm{d}t} \geqslant \frac{\dot{Q}}{T} \tag{82}$$

$$\mathbb{S} = \int_{V_t} s \,\mathrm{d}V_t \tag{83}$$

where s sands for the overall Eulerian density of entropy per unit of volume $\mathrm{d}V_t$

$$s \,\mathrm{d}V_t = (\rho_s(1-n)s_s + \rho_f n s_f)\,\mathrm{d}V_t \tag{84}$$

Combining Equations 83 and 72 with Equation 82,

$$\frac{\mathrm{d}^s}{\mathrm{d}t}\int_{V_t} \rho_s(1-n)s_s \,\mathrm{d}V_t + \frac{\mathrm{d}^f}{\mathrm{d}t}\int_{V_t} \rho_f n s_f \,\mathrm{d}V_t \geqslant \int_{\partial V_t} -\frac{\mathbf{q}\cdot\mathbf{n}}{T}\,\mathrm{d}a + \int_{V_t}\frac{q_s}{T}\,\mathrm{d}V_t \tag{85}$$

The left side of Equation 85 is expanded, in thee same way as in Equation 52

$$\frac{\mathrm{d}}{\mathrm{d}t}\int_{V_t} s \,\mathrm{d}V_t = \int_{V_t}\left(\frac{\mathrm{d}^s s}{\mathrm{d}t} + s\nabla_x \cdot \mathbf{v}^s + \nabla_x \cdot (s_f \mathbf{w})\right)\mathrm{d}V_t \tag{86}$$

The Eulerian expression of the second law is

$$\frac{\mathrm{d}^s s}{\mathrm{d}t} + s\nabla_x \cdot \mathbf{v}^s + \nabla_x \cdot (s_f \mathbf{w}) \geqslant \frac{q_s}{T} - \nabla_x \cdot \frac{\mathbf{q}}{T} \tag{87}$$

Noting S the overall Lagrangian density

$$S\,\mathrm{d}V_0 = (\rho_s(1-n)s_s + \rho_f n s_f)\mathrm{d}V_t \tag{88}$$

In a Lagrangian configuration, the second law writes

$$\frac{\mathrm{d}S}{\mathrm{d}t} + \nabla_x \cdot (s_f \mathbf{M}) \geqslant \frac{Q_s}{T} - \nabla_x \cdot \frac{\mathbf{Q}}{T} \tag{89}$$

2.3.2.3 The Inequality of Clausius-Duhem and the Thermodynamic Relationships

Eulerian approach

The first law of thermodynamics (Equation 74) is rewritten as

$$\nabla_x \cdot \mathbf{q} - q_s = \boldsymbol{\sigma} : \mathbf{d}^s - \nabla_x \cdot (h_f \mathbf{w}) + (\mathbf{f} - \gamma^f) \cdot \mathbf{w} - \frac{\mathrm{d}^s e}{\mathrm{d}t} - e \nabla_x \cdot \mathbf{v}^s \tag{90}$$

Multiplying the equation 87 by T,

$$T\frac{\mathrm{d}^s s}{\mathrm{d}t} + Ts\nabla_x \cdot \mathbf{v}^s + T\,\nabla_x \cdot (s_f \mathbf{w}) \geqslant q_s - T\,\nabla_x \cdot \frac{\mathbf{q}}{T} = q_s + \frac{\mathbf{q}}{T}\nabla_x T - \nabla_x \cdot \mathbf{q} \tag{91}$$

Combining the above equation with Equation 90,

$$T\frac{\mathrm{d}^s s}{\mathrm{d}t} + (Ts - e)\nabla_x \cdot \mathbf{v}^s + T\,\nabla_x \cdot (s_f \mathbf{w}) - \frac{\mathbf{q}}{T}\nabla_x T + \boldsymbol{\sigma} : \mathbf{d}^s - \nabla_x \cdot (h_f \mathbf{w}) + (\mathbf{f} - \gamma^f) \cdot \mathbf{w} - \frac{\mathrm{d}^s e}{\mathrm{d}t} \geqslant 0 \tag{92}$$

Introducing the fluid-specific Helmholtz free energy ψ_f and the fluid-specific free enthalpy g_f

$$\psi_f = e_f - T s_f \tag{93}$$

$$g_f = \psi_f + \frac{p}{\rho_f} = h_f - T s_f \tag{94}$$

Defining $h_f = g_f + T s_f$,

$$T\,\frac{\mathrm{d}^s s}{\mathrm{d}t} + (Ts - e)\nabla_x \cdot \mathbf{v}^s - \frac{\mathbf{q}}{T}\nabla_x T + \boldsymbol{\sigma} : \mathbf{d}^s - \nabla_x \cdot (g_f \mathbf{w}) - (s_f \mathbf{w}) \cdot \nabla_x T + (\mathbf{f} - \gamma^f) \cdot \mathbf{w} - \frac{\mathrm{d}^s e}{\mathrm{d}t} \geqslant 0 \tag{95}$$

Let ψ denote the overall Eulerian density of Helmholtz free energy

$$\psi = e - Ts \tag{96}$$

The internal energy density e in equation 92 can be represented by the overall Eulerian density ψ, temperature T and the overall entropy s

$$\frac{\mathrm{d}^s e}{\mathrm{d}t} = \frac{\mathrm{d}^s \psi}{\mathrm{d}t} + s\frac{\mathrm{d}T}{\mathrm{d}t} + T\frac{\mathrm{d}^s s}{\mathrm{d}t} \tag{97}$$

Combining Equations 97 and 92,

$$-s\frac{\mathrm{d}T}{\mathrm{d}t}-\psi\nabla_x\cdot\mathbf{v}^s-\frac{\mathbf{q}}{T}\nabla_x T+\boldsymbol{\sigma}:\mathbf{d}^s-\nabla_x\cdot(g_f\mathbf{w})-(s_f\mathbf{w})\cdot\nabla_x T+(\mathbf{f}-\boldsymbol{\gamma}^f)\cdot\mathbf{w}-\frac{\mathrm{d}^s\psi}{\mathrm{d}t}\geqslant 0 \quad (98)$$

and

$$\nabla_x\cdot(g_f\mathbf{w})=\mathbf{w}\cdot\nabla_x g_f+g_f\nabla_x\cdot\mathbf{w} \quad (99)$$

$$\boldsymbol{\sigma}:\mathbf{d}^s-g_f\nabla_x\cdot\mathbf{w}-s\frac{\mathrm{d}T}{\mathrm{d}t}-\frac{\mathrm{d}^s\psi}{\mathrm{d}t}-\psi\nabla_x\cdot\mathbf{v}^s-[\nabla_x g_f+s_f\nabla_x T-(\mathbf{f}-\boldsymbol{\gamma}^f)]\cdot\mathbf{w}-\frac{\mathbf{q}}{T}\cdot\nabla_x T\geqslant 0 \quad (100)$$

Lagrangian approach

Introducing the overall Lagrangian density of Helmholtz free energy Ψ

$$\Psi=U-TS \quad (101)$$

$$\Psi\,\mathrm{d}V_0=\psi\,\mathrm{d}V_t \quad (102)$$

The inequality of Clausius-Duhem for the Lagrangian configuration is obtained in a similar way as with the Eulerian configuration

$$\boldsymbol{\pi}:\frac{\mathrm{d}\boldsymbol{\Delta}}{\mathrm{d}t}-g_f\nabla_X\cdot\mathbf{M}-S\frac{\mathrm{d}T}{\mathrm{d}t}-\frac{\mathrm{d}\Psi}{\mathrm{d}t}-[\nabla_X g_f+s_f\nabla_X T-(\mathbf{f}-\boldsymbol{\gamma}^f)\cdot\mathbf{F}]\cdot\mathbf{M}-\frac{\mathbf{Q}}{T}\cdot\nabla_X T\geqslant 0 \quad (103)$$

2.3.2.4 The Dissipation Potential

The left side of inequality (103) is the overall dissipation Φ, which can be divided into three distinct sources of dissipation

$$\Phi=\Phi_s+\Phi_f+\Phi_{th}\geqslant 0 \quad (104)$$

In the Eulerian approach,

$$\phi_s=\boldsymbol{\sigma}:\mathbf{d}^s-g_f\nabla_x\cdot\mathbf{w}-s\,\frac{\mathrm{d}T}{\mathrm{d}t}-\frac{\mathrm{d}^s\psi}{\mathrm{d}t}-\psi\nabla_x\cdot\mathbf{v}^s \quad (105)$$

$$\phi_f=-[\nabla_x g_f+s_f\nabla_x T-(\mathbf{f}-\boldsymbol{\gamma}^f)]\cdot\mathbf{w} \quad (106)$$

$$\phi_{th}=-\frac{\mathbf{q}}{T}\cdot\nabla_x T \quad (107)$$

In the Lagrangian approach,

$$\Phi_s=\boldsymbol{\pi}:\frac{\mathrm{d}\boldsymbol{\Delta}}{\mathrm{d}t}-g_f\nabla_X\cdot\mathbf{M}-S\,\frac{\mathrm{d}T}{\mathrm{d}t}-\frac{\mathrm{d}^s\Psi}{\mathrm{d}t} \quad (108)$$

$$\Phi_f=-[\nabla_X g_f+s_f\nabla_X T-(\mathbf{f}-\boldsymbol{\gamma}^f)]\cdot\mathbf{M} \quad (109)$$

$$\Phi_{th}=-\frac{\mathbf{Q}}{T}\cdot\nabla_X T \quad (110)$$

Skeleton dissipation

The first source of dissipation Φ_s relates to the solid skeleton. Using the mass balance equation for fluid continuity:

$$\frac{\mathrm{d}^s m_f}{\mathrm{d}t} + \nabla_X \cdot \mathbf{M} = 0 \tag{111}$$

where m_f is the Lagrangian fluid mass content. The dissipation of skeleton can be rewritten as

$$\Phi_s = \boldsymbol{\pi} : \frac{\mathrm{d}\boldsymbol{\Delta}}{\mathrm{d}t} + g_f \frac{\mathrm{d}^s m_f}{\mathrm{d}t} - S\,\frac{\mathrm{d}T}{\mathrm{d}t} - \frac{\mathrm{d}^s \Psi}{\mathrm{d}t} \tag{112}$$

The Lagrangian densities of free energy (Ψ_s) and entropy (S_s) per unit of initial volume $\mathrm{d}V_0$ are expressed as

$$\Psi_s = \Psi - m_f \psi_f; \quad S_s = S - m_f s_f \tag{113}$$

Combining Equation 94, the relation $m_f = \rho_f \phi$, and the energy balance equation $\mathrm{d}e_f = -p\mathrm{d}(\frac{1}{\rho_f}) + T\mathrm{d}s_f$, the dissipation Φ_s can be expressed as

$$\Phi_s = \boldsymbol{\pi} : \frac{\mathrm{d}\boldsymbol{\Delta}}{\mathrm{d}t} + p\frac{\mathrm{d}^s \phi}{\mathrm{d}t} - S_s \frac{\mathrm{d}T}{\mathrm{d}t} - \frac{\mathrm{d}^s \Psi_s}{\mathrm{d}t} \tag{114}$$

Fluid dissipation

The second source of dissipation, Φ_f, relates to the fluid mass transport. This term accounts for the dissipation due to the relative motion of the fluid in the solid skeleton. Using Equation 94, the relation $m_f = \rho_f \phi$, and the energy balance equation, the fluid dissipation is obtained, in the form

$$\Phi_f = [-\nabla_X p + (\mathbf{f} - \boldsymbol{\gamma}^{\mathbf{f}}) \cdot \mathbf{F} \cdot \mathbf{M}] \tag{115}$$

Thermal dissipation

The third source of dissipation, Φ_{th}, is associated with heat transfer

$$\Phi_{th} = -\frac{\mathbf{Q}}{T} \cdot \nabla_X T \tag{116}$$

2.3.3 Constitutive equations of the skeleton

In a Lagrangian configuration, the constitutive models of non-isothermal porous media account for Δ_{ij} (Lagrangian deformation), ϕ (Lagrangian porosity) and T (temperature)

as the state variables related to the matrix. Based on the postulate of local state, the free energy of the skeleton can be generally expressed in the form

$$\Psi_s = \Psi_s(\Delta_{ij}, \phi, T; \chi_J) \tag{117}$$

The variables Δ_{ij}, ϕ and T are subset of external state variables while variables χ_J are subset of internal variables. Introducing equation 117 in equation 114,

$$\left(\pi_{ij} - \frac{\partial \Psi_s}{\partial \Delta_{ij}}\right) \frac{\mathrm{d}\Delta_{ij}}{\mathrm{d}t} + \left(p - \frac{\partial \Psi_s}{\partial \phi}\right) \frac{\mathrm{d}\phi}{\mathrm{d}t} - \left(S_s + \frac{\partial \Psi_s}{\partial T}\right) \frac{\mathrm{d}T}{\mathrm{d}t} - \frac{\partial \Psi_s}{\partial \boldsymbol{\chi}} \frac{\mathrm{d}\boldsymbol{\chi}}{\mathrm{d}t} \geqslant 0 \tag{118}$$

Since the variables can vary irrespective of the others and the inequality should always hold. If the internal variables do not vary, it can be concluded that

$$\pi_{ij} = \frac{\partial \Psi_s}{\partial \Delta_{ij}}; \quad p = \frac{\partial \Psi_s}{\partial \phi}; \quad S_s = -\frac{\partial \Psi_s}{\partial T} \tag{119}$$

Equation 119 associate the state variables Δ_{ij}, ϕ and T to their conjugate thermodynamic state variables π_{ij}, p and $-S_s$. This work focuses on the modeling of damage in the brittle deformation regime of rock materials, which occurs before the ductile deformation regime. We adopt the assumption of small deformation. Under this condition of infinitesimal transformation, the Lagrangian deformation can be linearized into Green-Lagrange deformation ε_{ij}, and Piola-Kirchoff stress tensor can be approximated at the first order by Cauchy stress σ_{ij}. Therefore, the conjugation relationship between stress and strain can be rewritten as

$$\sigma_{ij} = \frac{\partial \Psi_s}{\partial \varepsilon_{ij}} \tag{120}$$

2.3.4 Challenges of Continuum Damage Mechanics in Rocks

2.3.4.1 Damage Mechanics for Geomaterials

In geomaterials such as rock and concrete, compression strength typically differs by one order of magnitude from tensile strength. Although damage under isotropic compression was observed in hardened cement paste [109], "compression damage" in geomaterials is in general associated to cracking under a differential stress. Let us consider a brittle material sample subjected to a triaxial compression stress (Fig. 12). If the sample is homogeneous and if there is no friction at the top and bottom boundaries, the sample undergoes lateral

expansion (Fig. 12(a)). If boundaries are frictional and the sample is homogeneous, shear cracks will form (Fig. 12(b)). The granular fabric of rock and concrete tends to drive cracks around the stiffest crystals or aggregates, which results in "splitting effects" in tension and "crossing effects" in compression [209] (Fig. 13(b)-13(a)). In CDM, crossing effects in geomaterials are most often modeled as tension damage: a crack parallel to the axis, driven by axial compression, is considered to have the same mechanical effects as a crack parallel to the axis, driven by lateral tension.

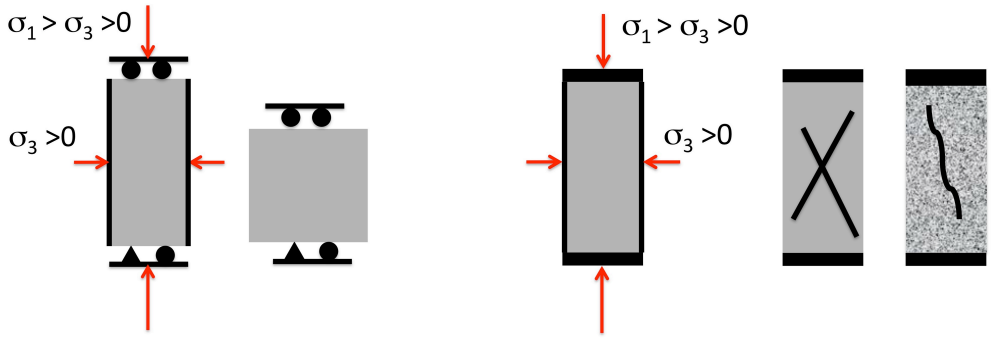

(a) Non Frictional Boundaries (b) Frictional Boundaries

Figure 12: Expected Crack Path During a Triaxial Compression Test (soil mechanics convention, compression counted positive): (a) non frictional boundaries ; (b) frictional boundaries for a homogeneous material (left) and a granular material (right)

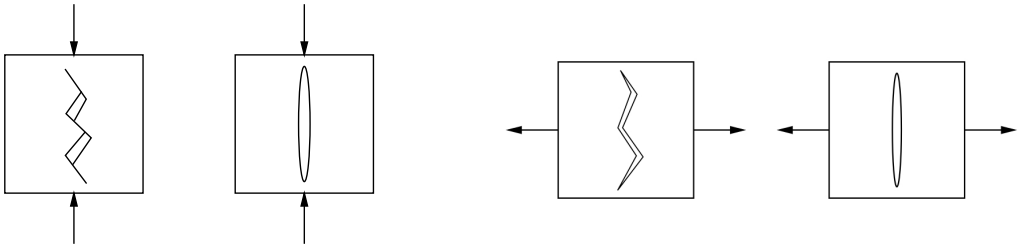

(a) Crossing Effects (b) Splitting Effects

Figure 13: Schematic representation of crossing (a) and splitting (b) mechanisms.

2.3.4.2 Tension and Compression Damage with Scalar Variables

CDM initially aimed to model brittle behavior observed in metals [153, 163]. In early damage models proposed for concrete [187, 188], two damage scalar variables were introduced in order to distinguish stiffness degradation rates in tension and compression. Following the

same idea, Frémond [90] split the damaged elastic deformation energy into potentials associated to tension and compression. Damage evolution laws are made dependent on negative and positive strains, for compression and tension, respectively. The formulation allows modeling unilateral effects of crack closure on stiffness, i.e. the recovery of compression strength without recovery of tension strength when cracks close. Note that damage models resorting to two different scalar variables are weakly anisotropic models: the determination of the principal directions of the strain (or stress) tensor is necessary to evaluate the energy dissipated in tension and in compression. However the scalar form adopted for the damage variables does not allow predicting damage-induced anisotropy: anisotropy of strain (or stress) controls damage rates, but stiffness anisotropy does not depend on damage.

In Lubliner's concrete damage model [175], the damage variable is defined as the ratio of dissipated plastic energy for both tensile and compressive cases. Based on this framework, [161] coupled damage and plasticity by using different hardening variables for different stress states. Damage models that are not coupled to plasticity require the definition of damage potentials. [5] used two separate potentials for two different damage variables (damage due to tensile stress, damage due to compressive stress). In Frémond's model [90], the variables that are work-conjugate to damage variables (called "affinities" or "energy release rates") are discontinuous functions of strain: $\partial \Psi_s / \partial \beta_c$ depends on $\boldsymbol{\varepsilon}^-$, and $\partial \Psi_s / \partial \beta_t$ depends on $\boldsymbol{\varepsilon}^+$. This implies that the rate of damage depends on a non-differentiable field function, which needs special conditional computation in a numerical code. In Θ-Stock Finite Element code for instance [98], the damage model assumes an associate flow rule for damage (noted $\boldsymbol{\Omega}$), in which the damage criterion ($f_d(\mathbf{Y}^+, \boldsymbol{\Omega})$) is a homogeneous function of degree one in $\mathbf{Y}^+$, and in which the positive part of the energy release rate, $\mathbf{Y}^+$, is proportional to positive deformation: $\mathbf{Y}^+ = g\boldsymbol{\varepsilon}^+$. The computation of the increment of damage at iteration i of load step k ($\mathrm{d}\boldsymbol{\Omega}_{(k,i)}$) requires dynamic storage of $\mathbf{Y}^+$ at iterations i and $i-1$

$$\mathrm{d}\boldsymbol{\Omega} = \dot{\lambda}_d \frac{\partial f_d(\mathbf{Y}^+, \boldsymbol{\Omega})}{\partial \mathbf{Y}^+} \quad \text{parallel to} \quad \mathrm{d}\mathbf{Y}^+$$

$$[\mathrm{d}\mathbf{Y}^+]_{(k,i)} = g\,[\mathrm{d}\boldsymbol{\varepsilon}^+]_{(k,i)} = g\left([\boldsymbol{\varepsilon}^+]_{(k,i)} - [\boldsymbol{\varepsilon}^+]_{(k,i-1)}\right) = g\left([\mathbf{Y}^+]_{(k,i)} - [\mathbf{Y}^+]_{(k,i-1)}\right) \tag{121}$$

in which $\dot{\lambda}_d$ is the damage multiplier. In [90], it is assumed that damage in compression actually produces tension damage - but that the reverse is not true. The elastic domain is defined as

$$(\beta_t, \beta_c) \in C = \{(x, y), x \in [0, 1]; y \in [0, 1], x \leq y\} \tag{122}$$

The rate of damage (computed from the normality rule) is not unique at singularity points, which raises important numerical issues.

Another modeling challenge is material softening after the failure peak, which is known to induce localization effects. In quasi-static problems, the ellipticity of the governing equations is lost, while dynamic hyperbolic equations become elliptic [158]. Energy dissipated by opening new crack surfaces tends to zero, non-elastic deformation localizes at a few integration points, and Finite Element solutions are mesh-dependent. In order to account for the influence of damage defined at $\mathbf{x}$ at location $\mathbf{x} + \mathrm{d}\mathbf{x}$, an internal length parameter needs to be introduced in the formulation. Regularization techniques include (i) microstructure-enriched models [193, 104, 105, 137], (ii) integral and differential non-local formulations [27, 28, 140], (iii) viscoplastic models [31]. In [90], a gradient-enhanced damage model is proposed, in which damage gradients ($\nabla\beta_c$, $\nabla\beta_t$) are part of the internal variables.

2.3.4.3 Splitting and Crossing Effects with One Tensor Variable

Anisotropic damage models derive naturally from damage models formulated with a compression damage scalar and a tension damage scalar. In geomechanics, the anisotropic damage variable is usually a second-order tensor which can be viewed as Kachanov's crack density tensor [142]

$$\mathbf{\Omega} = \sum_{k=1}^{N} d_k \, \mathbf{n}_k \otimes \mathbf{n}_k \tag{123}$$

in which the REV is assumed to contain N cracks characterized by a normal direction $\mathbf{n}_k$ and a volumetric fraction d_k, or as Oda's fabric tensor [206]

$$\mathbf{F} = \frac{1}{V_{REV}} \int_0^{\infty} \int_{\Omega} E\,(r, \mathbf{n}) \, \mathrm{d}\mathbf{n} \, \mathrm{d}r \tag{124}$$

in which $E\,(r, \mathbf{n})$ is the mathematical expectancy of a crack of radius r and normal direction $\mathbf{n}$ in the REV V_{REV}. In [5] and [63] for instance, a second-order damage tensor is introduced

in the free energy potential, which is expressed in terms of elastic strains. In [196], the same approach is adopted with a different free energy expressed in terms of elastic strain and modified strains. However elastic strains cannot be controlled in an experiment, or imposed as a boundary condition in a numerical code. To overcome this limitation, rock skeleton free energy was expressed in terms of total strains [115, 125]. Other authors [55, 212] employed a similar strategy, with the additional use of a parameter accounting for non-orthotropic damage. Anisotropic damage models based on a stress-dependent free energy potential were proposed in [242, 238, 298, 120].

The main limitations of anisotropic damage models used in geomechanics are:

(1) *The difficult expression of a flow rule for anisotropic damage.* As illustrated in Fig. 13(a)-13(b), damage is modeled as tensile cracks, even under (differential) compression stress. Consequently, the damage criterion is generally not expressed in terms of the energy release rate (noted $\mathbf{Y}$) thermodynamically conjugate to damage, but rather in terms of a projection of this energy release rate in the space of positive deformation or positive stress (noted $\mathbf{Y}^+$). As a result, damage evolution law is generally not a true associate flow rule. The damage function is usually expressed in the following form

$$f_d(\mathbf{Y}^+, \mathbf{\Omega}) = \sqrt{\frac{1}{2}\mathbf{Y}^+ : \mathbf{Y}^+} - C_0 - C_1 \mathrm{Tr}\,(\mathbf{\Omega}) \tag{125}$$

in which C_0 is the initial damage threshold and C_1 is a material parameter controlling the rate of damage according to the accumulated damage. Based on the flow rule expressed in Eq. 121, Eq. 125 gives a smooth "damage surface" in the space of $\mathbf{Y}^+$ components (octant of a sphere), but a non-smooth surface in the space of $\mathbf{Y}$ (with edges). In general, models that split tensile and compressive strains ([196]) or stresses ([5, 63, 120]), exhibit a non-smooth damage surface (in general, several branches with sharp connections).

(2) *The difficult account for possible damage rotation.* Shear induced by crack opening and closure affect material stiffness and make it difficult to ensure thermodynamic consistency [54]. Shear rotates the principal bases of stress and strain, which would require updating the principal base of damage at each iteration. To simplify, anisotropic CDM models generally assume that the principal directions of damage correspond to the principal directions of

stress or strain. The anisotropic models proposed by Pellet are orthotropic [212, 213]. This allows studying planar and cylindrical transverse isotropic configurations - usually, with no rotation of damage directions.

2.3.4.4 Shear Damage Models

Mixed mode crack propagation is a long-standing problem of fatigue modeling in metals [135]. In rock, the transition from tensile failure (mode I) to shear failure (mode II) is generally modeled by combining Griffith criterion or the modified Griffith criterion (depending on the Unconfined Compressive Strength (UCS)) with Mohr-Coulomb failure criterion [114, 110]. Most models accounting for "shear damage" depend on deviatoric stress - not on shear stress - which actually represents differential stress. In general, two damage potentials governing two different damage variables are introduced: one potential controls isotropic damage under the influence of mean stress, and the other controls "shear damage " under the influence of deviatoric stress. Of particular interest is the series of models proposed for salt rock [56]. Because deformation induced by dislocation creep is isochoric, crack damage in salt has often been associated to inelastic dilatant deformation. Damage grows in stress states above the "dilatancy boundary", whereas below this boundary, inelastic contractant strains compensate damage deformation [128, 177]. Within the dilatancy boundary, damage cannot grow nor decrease [133].

Microscopic mechanisms explaining crack initiation under compression were studied in [22]. Locally, axial and radial stresses initiate wing cracks at the tips of inclined flaws (wedge opening), whereas stress concentrations around holes initiate tensile cracks. Both types of cracks can be predicted by expressing Stress Intensity Factors. A damage model considering the influence of pure shear stress was proposed in [89, 236]: the damage variable is used to account for the reduction of shear modulus in laminated composite materials. Other models were proposed to predict shear failure in pure ductile materials - for instance, the modified Gurson model, which is based on micro mechanics. The micro-mechanical model presented in [272] accounts for: (1) the growth of existing voids due to plastic incompressibility, (2) void nucleation, and (3) void softening during shear mechanisms. However, the effect of

damage on elastic properties is not captured.

2.4 Summary

This chapter reviewed damage and fracture mechanics models in rocks. Strategies to simulate crack propagation at the micro-, meso-, and macro-scale were investigated. In particular, fundamental equations of Linear Elastic Fracture Mechanics (LEFM) based on Griffith theory, stress intensity factors, and the J integral were summarized. Previous fracture models based on LEFM were used to analyze the stress state around boreholes and crack tips, but neglected the presence of micro-scale discontinuities in the process zone. Another limitation of LEFM is the dependence of analytical solutions to a pre-determined fracture geometrical shape. An alternative theoretical framework, based on Continuum Damage Mechanics (CDM), was presented: thermodynamic principles were summarized, and the method to obtain a closed formulation was explained. Challenges to derive thermodynamically consistent CDM models to predict rock isotropic and anisotropic damage were discussed, which highlighted the need for a new anisotropic damage model for rocks that have different strength properties in tension and compression.

CHAPTER III

THEORETICAL MODELING OF ANISOTROPIC DAMAGE INDUCED BY DIFFERENTIAL STRESS

Capturing the difference of resistance of geomaterials in tension and compression is still an open issue in CDM, mainly because the representation of microscopic cracks at the REV scale relies on equivalent mesoscopic cracks that open in pure tension ("splitting effects", Fig. 13(b)) and in compression under differential stress conditions ("crossing effects", Fig. 13(a)). The Differential Stress Induced Damage (DSID) model presented in the following aims to overcome this limitation. Rock/fluid interactions are not accounted for: the model is purely mechanical. The DSID model is constructed so as to ensure thermodynamic consistency requirements and maintain the physical meaning of the anisotropic damage and deformation variables introduced in the formulation.

3.1 Basic Theoretical Elements of the DSID Model

3.1.1 Representative Elementary Volume

In Continuum Mechanics, the Representative Elementary Volume (REV) is the critical material element size, below which a physical property is non-uniform, and above which this physical property can be considered uniform. The concept of any specific property REV is illustrated in Figure 3. The REV size can be defined as a multiple of the typical size of rock discontinuities (typically, the REV should be at least two orders of magnitude larger than rock internal length), or as the minimum size required to ensure the statistical homogeneity of a field variable or field property. A geometrical definition of the REV (in reference to the size of discontinuities) is provided in Figure 14.

If the size of the rock sample is small enough, it can be considered as a homogeneous intact sample. In Finite Elements, the behavior of rock at that scale can be captured by the constitute equations of a pure mineral. A larger sample will contain one or multiple fractures, which can be modeled with Linear Elastic Fracture Mechanics (LEFM) or Discrete

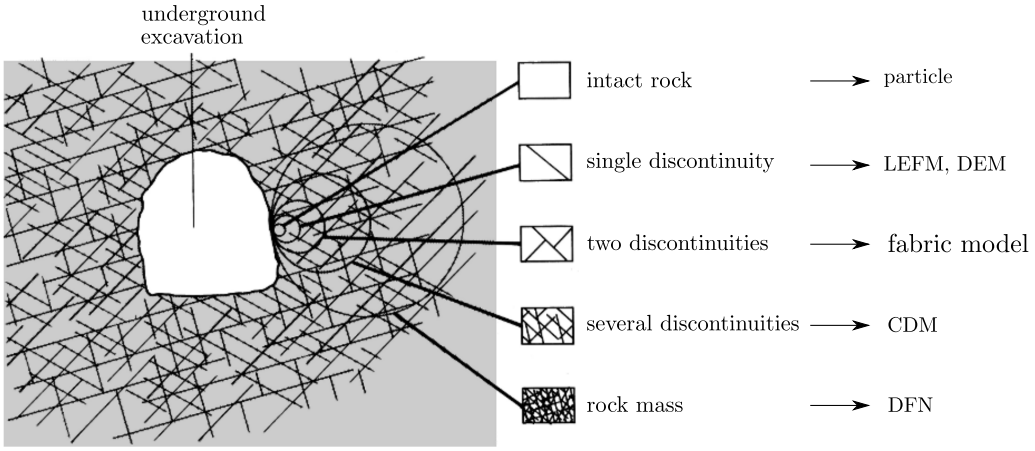

Figure 14: Idealized illustration of the transition from intact rock to a heavily jointed rock mass with increasing sample size. Taken from [44].

Element Methods (DEM). If the REV domain expands, the number of cracks increases. Modeling frameworks based on fabric variables, such as Continuum Damage Mechanics (CDM), are appropriate at that scale. At a larger scale, especially in cases where cracks connect and interact, it is Discrete Fracture Network (DFN) models are more suitable.

Statistical definitions of the REV lead to different material element sizes depending on the field variable or physical property observed. For instance, the REV size necessary to ensure the statistical homogeneity of stress is often different from that for stiffness. A complete discussion about the definition of the REV in CDM, illustrated in Figure 15, is provided in [156].

3.1.2 Damage Variable Employed in the DSID Model

In isotropic damage models, damage is a scalar, usually defined as the fraction of the effective (undamaged) surface across a material section by the total area of the material section considered. The computation of A'/A requires determining the area of cracks intercepted across the material section. Alternatively, damage can be defined as the ratio of the damaged material's Young's modulus by the undamaged Young's modulus. Both the undamaged and damaged Young's moduli are determined by computing the slope of the stress-strain curve during uniaxial or triaxial unloading. It is impossible to define anisotropic damage from effective surface ratios similar to A'/A, because in one cross section, porosity induced by

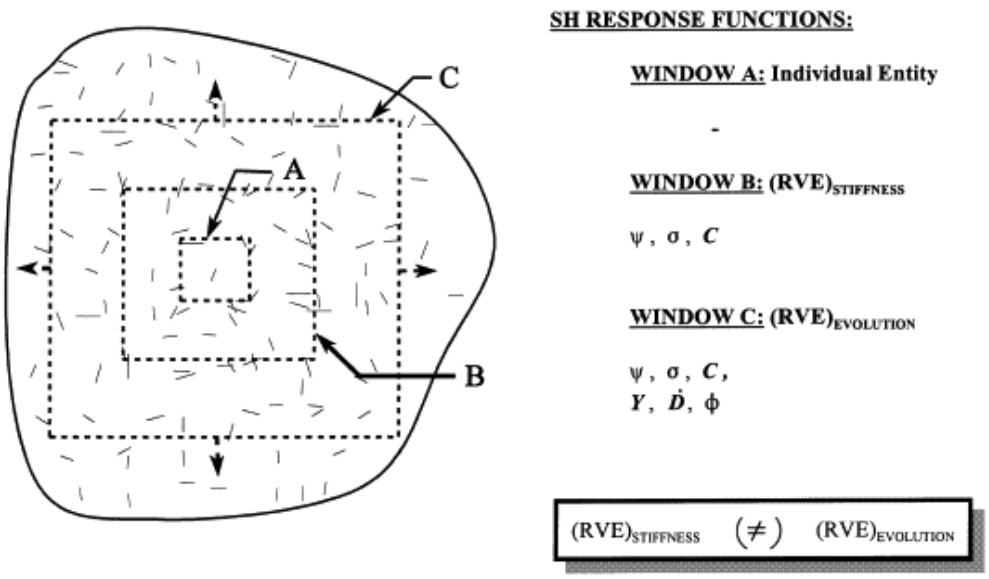

Figure 15: The size of the REV depends on the physical property observed: the REV size necessary to ensure the statistical homogeneity of stiffness is often different from that necessary to ensure the statistical homogeneity of stress. Taken from [156].

crack propagation evolves with stresses in the plane and out of the plane of the section considered; therefore, the link between loading stress and microstructure changes is not straightforward. Oda's fabric tensor is often used to account for the density, size and orientation of cracks [206]

$$\mathbf{F} = \frac{1}{V_{REV}} \int_0^\infty \int_\Omega E(r, \mathbf{n}) \, \mathrm{d}\mathbf{n} \, \mathrm{d}r \tag{126}$$

where $E(r, \mathbf{n})$ is the mathematical expectancy of a crack of radius r and normal direction $\mathbf{n}$ in the REV V_{REV}). Oda's fabric tensor is similar to the second-order crack density tensor defined by Kachanov [143], as illustrated in Figure 16. This tensor provides the average size of penny-shaped cracks, and, for each representative crack size, the average orientation of the vector normal to the crack planes. Other tensorial definitions are possible, for instance, a second-order damage tensor can be defined in terms of elastic strains and introduced in the free energy [5, 63].

Damage is always measured in reference to an initial state or in reference to an ultimate state. Therefore, damage is relative: it is either a measure of the loss of stiffness or strength compared to a reference undamaged state, or a measure of the percentage of

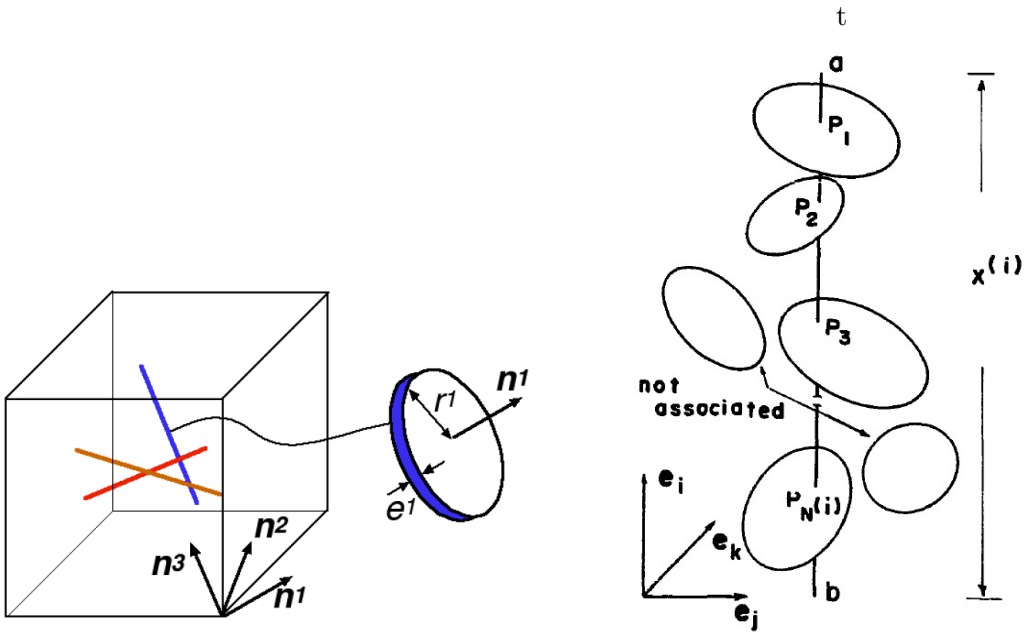

(a) Micro-represent of the crack in 3D [19]

(b) An e_i-scanning line and its associated cracks [206].

Figure 16: Representation of Oda's fabric tensor

damage compared to the maximum damage that is expected to occur before the complete failure of the material. Failure occurs when cracks coalesce into a discrete fracture that ultimately splits the Representative Elementary Volume considered into several pieces. At failure, the behavior of the material can no longer be captured with Continuum Damage Mechanics: a discrete model based fracture mechanics is needed. In the Differential Stress Induced Damage (DSID) model presented in the following, damage is a purely mathematical second-order tensor, used as a dissipation variable in the expression of the free energy. It is not a fabric tensor; therefore, it cannot be used directly to interpret microstructure changes during damage propagation.

3.1.3 Thermodynamic Framework of the DSID Model

The constitutive equations of the DSID model are derived from energy potentials, under the assumption of small deformation, in an Eulerian configuration. In this context, the stress variable is Cauchy stress tensor $\boldsymbol{\sigma}$, and the deformation variable is the Green-Lagrange deformation tensor, $\boldsymbol{\varepsilon}$. The main reason supporting the hypothesis of small deformation

is that host rocks studied in the context of oil and gas extraction and geological storage exhibit:

- Either a quasi-brittle behavior that leads to failure at rather small deformation (e.g., granite, sandstone, limestone),
- Or a brittle deformation regime prior to the ductile deformation regime that ultimately leads to failure (e.g. clay rock, shale).

As an example, a typical stress-stain path of rock under triaxial compression test is shown in Figure 17. It can be divided into three main regimes. First, rock exhibits a brittle behavior: zone I describes early strain hardening; elastic moduli measured upon unloading are lower than the ones of the pristine rock, due to microcrack generation. The elastic response of shale is expected to be a small portion of the curve represented in zone I. In zone II, shale exhibits a ductile behavior: plastic deformation accumulates upon triaxial loading. Irreversible strains are more important than during the brittle deformation regime in zone I. Zone III is the post-peak domain, which starts at the failure point. After failure, the sample fails and stress drops to zero. In zone III, microcracks intersect and coalesce to form a macroscopic fracture, therefore the strength of the rock decreases rapidly. The present work focuses on zone I, i.e. the brittle deformation regime. Classical linear elastic models cannot capture this early strain hardening phenomenon. Non-linear elastic models could capture strain hardening, but not the decrease of elastic moduli resulting from crack propagation. The DSID model allows predicting the anisotropy of deformation and stiffness induced by crack propagation, and the associated energy dissipation.

A hyperelastic framework is adopted, in which stress derives from the elastic deformation energy [129]. The thermodynamic conjugation relationships write

$$\boldsymbol{\sigma} = \frac{\partial \Psi_s}{\partial \boldsymbol{\varepsilon}^E} = \mathbb{C}_{\mathbb{e}}(\boldsymbol{\Omega}) : \boldsymbol{\varepsilon}^E \tag{127}$$

$$\mathbf{Y_d} = -\frac{\partial \Psi_s}{\partial \boldsymbol{\Omega}} \tag{128}$$

where Ψ_s is the Helmoltz free energy of solid matrix; $\mathbb{C}_{\mathbb{e}}$ is the damaged elastic stiffness tensor ,which depends on the current damage variable $\boldsymbol{\Omega}$; $\mathbf{Y_d}$ is the damage driving force;

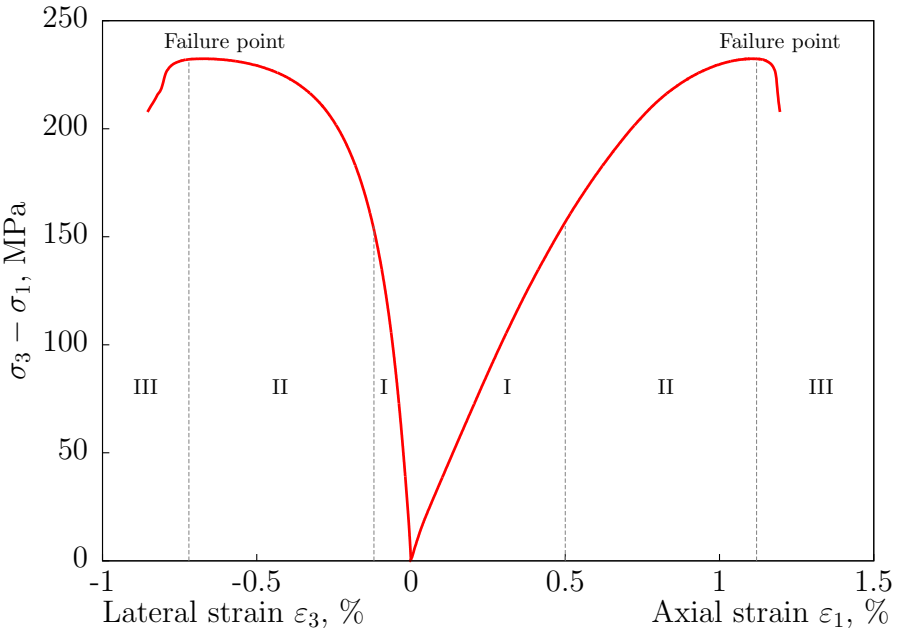

Figure 17: Typical stress-strain curve of shale under triaxial compression: (I) Brittle deformation regime. (II) Ductile deformation regime. (III) Post-peak behavior (after failure). Modified from [110, 144].

$\boldsymbol{\varepsilon}^E$ is the total elastic deformation. Classical CDM models usually assume that the free energy of the skeleton is elastic [163]

$$\Psi_s = W_e = \frac{1}{2}\boldsymbol{\varepsilon}^E : \mathbb{C}_e(\boldsymbol{\Omega}) : \boldsymbol{\varepsilon}^E \tag{129}$$

It is proposed instead to account for irreversible remaining crack openings induced by damage. The total deformation tensor is split as follows

$$\boldsymbol{\varepsilon} = \boldsymbol{\varepsilon}^{el} + \boldsymbol{\varepsilon}^{ed} + \boldsymbol{\varepsilon}^{id} = \boldsymbol{\varepsilon}^E + \boldsymbol{\varepsilon}^{id} \tag{130}$$

in which $\boldsymbol{\varepsilon}^{el}$ is the purely elastic deformation, $\boldsymbol{\varepsilon}^{ed}$ is the elastic damage-induced deformation due to the degradation of mechanical stiffness, and $\boldsymbol{\varepsilon}^{id}$ is the irreversible deformation tensor. A residual stress $\boldsymbol{\sigma}_R$ is introduced into the model in order to predict the corresponding irreversible damage deformation $\boldsymbol{\varepsilon}^{id}$ (see Figure 18). In order to include the irreversible term due to damage, an additional potential Ψ_d is added in the expression of the total free energy of solid skeleton

$$\Psi_s = W_e + \Psi_d = \Psi_e + \Psi_d \tag{131}$$

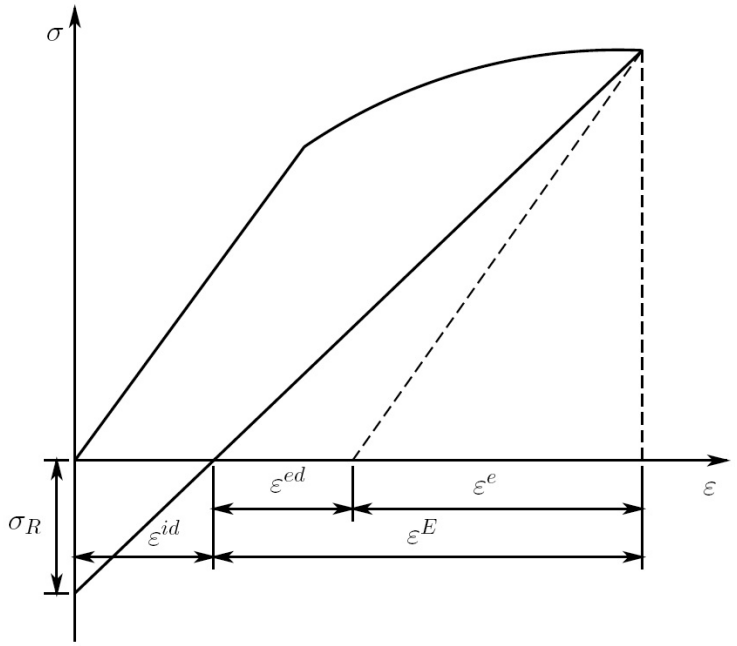

Figure 18: Stress-strain response resulting from damage generation [19, 261]

As explained in [129, 64], two functionals are needed to close the model formulation: Helmholtz free energy and a dissipation potential, allowing to derive the evolution laws of the internal variables. The latter one is equal to the yield (or damage) function if the flow rule is associated. In the following, we are proposing a new damage model to capture the effects of anisotropic mode I crack propagation on deformation and stiffness. The damage flow rule is non associate, while irreversible deformation is derived from the damage criterion. Three functionals are thus introduced in the model (Helmholtz free energy, the damage criterion, and the dissipation potential). In the most general case, the Helmoltz free energy depends on state and internal variables (noted $\boldsymbol{E}$ and $\boldsymbol{\chi}$ respectively). In our particular problem, state variables are restricted to elastic deformation ($\boldsymbol{\varepsilon^E}$). Internal variables include the damage tensor ($\boldsymbol{\Omega}$) and possibly, hardening variables (noted $\boldsymbol{\alpha}$ and r for kinetic and isotropic hardening, respectively)

$$\Psi_s(\boldsymbol{E}, \boldsymbol{\chi}) = \Psi_s(\boldsymbol{\varepsilon}^E, \boldsymbol{\Omega}, \boldsymbol{\alpha}, r) \tag{132}$$

The damage criterion can be defined as $f_d(\mathbf{Y}, \mathbf{X}, R)$, in which $\mathbf{Y}$, $\mathbf{X}$ and R are thermodynamic forces conjugate to the damage variable $\boldsymbol{\Omega}$, the kinetic hardening variable $\boldsymbol{\alpha}$, and

the isotropic hardening variable r [6, 81]

$$f_d = \sqrt{(\mathbf{Y}-\mathbf{X}):(\mathbf{Y}-\mathbf{X})} - (R_0 + R) \leq 0 \tag{133}$$

$$\boldsymbol{\sigma} = \frac{\partial \Psi_s}{\partial \boldsymbol{\varepsilon}^E} \tag{134}$$

$$\mathbf{Y} = -\frac{\partial \Psi_s}{\partial \boldsymbol{\Omega}} \tag{135}$$

$$\mathbf{X} = -\frac{\partial \Psi_s}{\partial \boldsymbol{\alpha}} \tag{136}$$

$$R = -\frac{\partial \Psi_s}{\partial r} \tag{137}$$

The Inequality of Clausius-Duhem is derived from the combination of the two first laws of thermodynamics

$$\Phi_s = \boldsymbol{\sigma} : \dot{\boldsymbol{\varepsilon}} - \dot{\Psi}_s \geq 0 \tag{138}$$

The free energy rate writes

$$\dot{\Psi}_s = \frac{\partial \Psi_s}{\partial \boldsymbol{\varepsilon}^E} : \dot{\boldsymbol{\varepsilon}}^E + \frac{\partial \Psi_s}{\partial \boldsymbol{\alpha}} : \dot{\boldsymbol{\alpha}} + \frac{\partial \Psi_s}{\partial \boldsymbol{\Omega}} : \dot{\boldsymbol{\Omega}} + \frac{\partial \Psi_s}{\partial r}\dot{r} \tag{139}$$

The dissipation potential of the solid skeleton should satisfy the Clausius-Duhem Inequality

$$\Phi_s = \boldsymbol{\sigma} : \dot{\boldsymbol{\varepsilon}}^{id} + \mathbf{Y} : \dot{\boldsymbol{\Omega}} + \mathbf{X} : \dot{\boldsymbol{\alpha}} + R\dot{r} \geq 0 \tag{140}$$

For a non-associated flow rule, a new dissipation potential function $g_d(\boldsymbol{\sigma}, \mathbf{Y}, \mathbf{X}, R) = 0$ is needed in order to predict damage propagation. Damage is produced so as to maximize the energy dissipated during damage propagation. Damage evolution can be predicted by maximizing the dissipation function Φ_s under the constrain $g = 0$, which is also called Kuhn-Tucker condition. The optimization problem is solved by introduction the Lagrange Multiplier $\dot{\lambda}_d$

$$\mathcal{F}(\boldsymbol{\sigma}, \mathbf{Y}, \mathbf{X}, R, \dot{\lambda}_d) = \Phi_s - \dot{\lambda}_d\, g_d(\boldsymbol{\sigma}, \mathbf{Y}, \mathbf{X}, R) \tag{141}$$

The necessary conditions for this optimization problem are

$$\frac{\partial \mathcal{F}}{\partial \boldsymbol{\sigma}} = \frac{\partial \Phi_s}{\partial \boldsymbol{\sigma}} - \dot{\lambda}_d \frac{\partial g_d}{\partial \boldsymbol{\sigma}} = 0, \qquad \frac{\partial \mathcal{F}}{\partial \mathbf{Y}} = \frac{\partial \Phi_s}{\partial \mathbf{Y}} - \dot{\lambda}_d \frac{\partial g_d}{\partial \mathbf{Y}} = 0 \tag{142}$$

$$\frac{\partial \mathcal{F}}{\partial \mathbf{X}} = \frac{\partial \Phi_s}{\partial \mathbf{X}} - \dot{\lambda}_d \frac{\partial g_d}{\partial \mathbf{X}} = 0, \qquad \frac{\partial \mathcal{F}}{\partial R} = \frac{\partial \Phi_s}{\partial R} - \dot{\lambda}_d \frac{\partial g_d}{\partial R} = 0 \tag{143}$$

$$\frac{\partial \mathcal{F}}{\partial \dot{\lambda}_d} = g = 0 \tag{144}$$

which results into

$$\dot{\boldsymbol{\varepsilon}}^{id} = \dot{\lambda}_d \frac{\partial g_d}{\partial \boldsymbol{\sigma}}, \dot{\boldsymbol{\Omega}} = \dot{\lambda}_d \frac{\partial g_d}{\partial \mathbf{Y}} \tag{145}$$

$$\dot{\boldsymbol{\alpha}} = \dot{\lambda}_d \frac{\partial g_d}{\partial \mathbf{X}}, \dot{r} = \dot{\lambda}_d \frac{\partial g_d}{\partial R} \tag{146}$$

It is assumed that damage and irreversible strains are governed by rate-independent evolution laws. In the absence of hardening (or if hardening can be controlled with internal variables), the reduced inequality of dissipation (see equation 140) writes

$$\Phi_s = \boldsymbol{\sigma} : \dot{\boldsymbol{\varepsilon}}^{id} + \mathbf{Y} : \dot{\boldsymbol{\Omega}} \geq 0 \tag{147}$$

To satisfy inequality 147, it is sufficient to ensure

$$\begin{aligned} \boldsymbol{\sigma} : \dot{\boldsymbol{\varepsilon}}^{id} &\geq 0 \\ \mathbf{Y} : \dot{\boldsymbol{\Omega}} &\geq 0 \end{aligned} \tag{148}$$

3.2 Constitutive equations of the DSID Model

3.2.1 Postulate 1: Expression of the Free Energy

Most anisotropic damage models for geomaterials postulate a skeleton free energy expressed in terms of deformation. As a result, the energy release rate $\mathbf{Y}$ conjugate to damage (also called damage driving force) is also a function of deformation. In order to predict the propagation of mesoscopic cracks due to "splitting effects" (Fig. 13(b)) and the propagation of mesoscopic cracks due to "crossing effects" (Fig. 13(a)), it is necessary to make the damage criterion depend on a tensile damage driving force (Eq. 125 for instance). The damage rate is thus defined as

$$\dot{\boldsymbol{\Omega}} = \dot{\lambda}_d \frac{\partial g_d}{\partial \mathbf{Y}^+} \neq \dot{\lambda}_d \frac{\partial g_d}{\partial \mathbf{Y}} \tag{149}$$

which poses two main problems:

1. The damage flow rule does not fit into the standard thermodynamic framework, in which the rate of an internal variable is proportional to the derivative of a potential by its conjugate driving force.

2. The damage flow rule expressed in Eq. 149 depends on the derivatives of absolute values, which brings some numerical issues (see Eq. 121 for instance).

In order to better account for states of tensile deformation under differential stress, the free energy potential is expressed in terms of stress (Gibbs free energy, G_s). To stay within the framework of linear elasticity in the absence of damage, the expression of the free energy should have at most quadratic terms in $\boldsymbol{\sigma}$ [115, 242]. In addition, it is assumed that G_s is linear in $\boldsymbol{\Omega}$, according to the expression proposed by [242]. The following constitutive assumption is made:

$$\begin{aligned} G_s\left(\boldsymbol{\sigma},\boldsymbol{\Omega}\right) = \frac{1}{2}\boldsymbol{\sigma} : \mathbb{S}_0 : \boldsymbol{\sigma} + a_1 \mathrm{Tr}\boldsymbol{\Omega}\left(\mathrm{Tr}\boldsymbol{\sigma}\right)^2 + a_2 \mathrm{Tr}(\boldsymbol{\sigma}\cdot\boldsymbol{\sigma}\cdot\boldsymbol{\Omega}) \\ + a_3 \mathrm{Tr}\boldsymbol{\sigma}\,\mathrm{Tr}(\boldsymbol{\Omega}\cdot\boldsymbol{\sigma}) + a_4 \mathrm{Tr}\boldsymbol{\Omega}\,\mathrm{Tr}(\boldsymbol{\sigma}\cdot\boldsymbol{\sigma}) \end{aligned} \tag{150}$$

in which $\mathbb{S}_0$ is the compliance of the intact material, in the absence of damage. Note that this expression of G_s can actually be obtained from the expression of Ψ_s chosen by [115] through a Legendre transform

$$\Psi_s\left(\boldsymbol{\varepsilon}^E,\boldsymbol{\Omega}\right) + G_s\left(\boldsymbol{\sigma},\boldsymbol{\Omega}\right) = \boldsymbol{\sigma} : \boldsymbol{\varepsilon}^E \tag{151}$$

The material parameters a_i require numerical calibration [242]; an example is presented in the following sections. According to Eq. 150, the stress-strain relationship writes

$$\begin{aligned} \boldsymbol{\varepsilon}^E = \boldsymbol{\varepsilon} - \boldsymbol{\varepsilon}^{id}(\boldsymbol{\Omega}) = \frac{\partial G_s}{\partial \boldsymbol{\sigma}} = \frac{1+\nu_0}{E_0}\boldsymbol{\sigma} - \frac{\nu_0}{E_0}(\mathrm{Tr}\boldsymbol{\sigma})\,\boldsymbol{\delta} + 2a_1(\mathrm{Tr}\boldsymbol{\Omega}\,\mathrm{Tr}\boldsymbol{\sigma})\,\boldsymbol{\delta} \\ + a_2(\boldsymbol{\sigma}\cdot\boldsymbol{\Omega} + \boldsymbol{\Omega}\cdot\boldsymbol{\sigma}) + a_3[\,\mathrm{Tr}(\boldsymbol{\sigma}\cdot\boldsymbol{\Omega})\,\boldsymbol{\delta} + (\mathrm{Tr}\boldsymbol{\sigma})\,\boldsymbol{\Omega}\,] + 2a_4(\mathrm{Tr}\boldsymbol{\Omega})\,\boldsymbol{\sigma} \end{aligned} \tag{152}$$

where $\boldsymbol{\delta}$ is the second-order identity tensor, and E_0 and ν_0 are Young's modulus and Poisson's ratio of the intact (i.e., undamaged) material. Similarly the damage driving force writes

$$\mathbf{Y} = -\frac{\partial \Psi_s}{\partial \boldsymbol{\Omega}} = \frac{\partial G_s}{\partial \boldsymbol{\Omega}} = a_1(\mathrm{Tr}\boldsymbol{\sigma})^2\,\boldsymbol{\delta} + a_2\boldsymbol{\sigma}\cdot\boldsymbol{\sigma} + a_3\mathrm{Tr}(\boldsymbol{\sigma})\boldsymbol{\sigma} + a_4\mathrm{Tr}(\boldsymbol{\sigma}\cdot\boldsymbol{\sigma})\boldsymbol{\delta} \tag{153}$$

3.2.2 Postulate 2: Damage Function

3.2.2.1 Original Drucker-Prager Yield Surface

Drucker-Prager model is a plasticity model capturing "crossing effects" under differential stress and accounting for the difference of material behavior when the material is in net tension or in net compression. Drucker-Prager yield function writes

$$f(\boldsymbol{\sigma}) = \sqrt{J_2} - \alpha I_1 - k \tag{154}$$

in which I_1 and J_2 are the first and second stress invariants, respectively. Material parameters are given as

$$\alpha = \frac{2\sin\phi}{\sqrt{3}(3-\sin\phi)}, \quad k = \frac{6c\cos\phi}{\sqrt{3}(3-\sin\phi)} \tag{155}$$

where ϕ is the angle of internal friction, and c is cohesion. Figure 19(a) shows the yield surface in 3-D space with $\phi = 20°$, $c = 2\,kPa$. Note that in this figure, the soil mechanics sign convention is adopted, i.e. compression is counted positive, and tension is counted negative. A natural choice would be to use the first and second invariants of the damage driving force $\mathbf{Y}$ instead of I_1 and J_2 in Eq. 154, in order to obtain the damage criterion. The damage surface in $\mathbf{Y}$ space would be the same as the yield surface plotted in stress space for plasticity. But Fig. 19(b) shows that if the free energy is expressed as stated in Eq. 150, the damage surface in stress space would have symmetries resulting in similar damage thresholds in tension and in compression. This is not satisfactory for geomaterials. To overcome this problem, one possibility is to change the expression of the free energy in order to avoid having a damage driving force depend only on quadratic stress terms (Eq. 153). However, it is not desirable, because the polynomial expression of G_s in (Eq. 150) is in part dictated by elasticity requirements (for the terms in $\boldsymbol{\sigma}$), and in part verified by experiments (for the terms in $\boldsymbol{\Omega}$). It is proposed instead to adapt the expression of the damage function to distinguish compression and tension strengths.

3.2.2.2 Modified Damage Surface

The modified expression of the damage function is written in the following form

$$f_d = \sqrt{J^*} - \alpha I^* - k \tag{156}$$

J^* and I^* are defined as

$$J^* = \frac{1}{2}(\mathbb{P}_1 : \mathbf{Y} - \frac{1}{3}I^*\boldsymbol{\delta}) : (\mathbb{P}_1 : \mathbf{Y} - \frac{1}{3}I^*\boldsymbol{\delta}), \quad I^* = (\mathbb{P}_1 : \mathbf{Y}) : \boldsymbol{\delta} \tag{157}$$

in which $\mathbb{P}_1$ is a fourth-order projection tensor defined as

$$\mathbb{P}_1(\boldsymbol{\sigma}) = \sum_{p=1}^{3} \left[H(\sigma^{(p)}) - H(-\sigma^{(p)})\right] \mathbf{n}^{(p)} \otimes \mathbf{n}^{(p)} \otimes \mathbf{n}^{(p)} \otimes \mathbf{n}^{(p)} \tag{158}$$

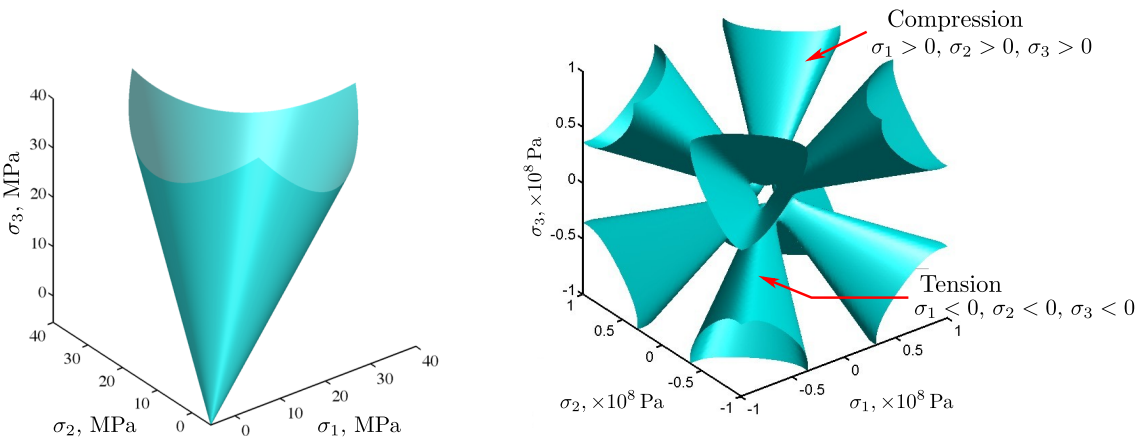

(a) Drucker-Prager Yield Surface.

(b) Drucker-Prager Model in Damage Mechanics.

Figure 19: For the chosen expression of free energy G_s, replacing stress by damage driving force in Drucker-Prager 's yield function does not define a satisfactory damage surface: damage thresholds are the same in tension and in compression.

in which $H(\cdot)$ is the Heaviside distribution function, $\sigma^{(p)}$ is the p^{th} eigenstress value, and $\mathbf{n}^{(p)}$ is the vector aligned with the p^{th} principal direction of stress. α is a material parameter accounting for the aperture of the cone in the $\mathbb{P}_1 : \mathbf{Y}$ space. The threshold k in Eq. 156 is defined as a linear function of damage (similar to Eq. 125), suitable for rock [125, 242, 238]

$$k = C_0 + C_1 \mathrm{Tr}\,(\mathbf{\Omega}) \tag{159}$$

Note that in the preceding equations, the soil mechanics sign convention is adopted (compression positive, tension negative). The projection tensor $\mathbb{P}_1$ ensures that the occurrence of damage be controlled by the action of the damage driving force in the stress principal directions, and that in each stress principal direction, the eigenvalues of the "physical damage driving force tensor" $(\mathbb{P}_1 : \mathbf{Y})$ be of the same sign as the stress eigenvalues. In $\mathbb{P}_1 : \mathbf{Y}$ space, the damage surface is a cone - similar to Drucker-Prager yield surface. The plots of the damage surface (Fig. 20(a)-20(b)), show that the damage surface is locally convex but globally non convex. Note that surface convexity is a sufficient but not necessary condition to satisfy the positivity of the dissipation potential [73]: the thermodynamic framework is indeed consistent as long as the damage rate is non-negative. In fact the sign of energy dissipation is only load path dependent, i.e. it should only be *locally* positive. If the surface is locally non-convex, the load path may cross the damage surface, and the

predicted state of stress may fall outside the damage surface. Numerical solutions were proposed in [52, 211].

In elasto-plasticity, an associate flow rule based on Drucker-Prager yield function allows accounting for plastic dilatant volumetric strains due to mean stress. The term αI_1 in Eq. 154 is used to account for dilatant effects. The computation of the damage rates obtained from an associate flow rule (with the damage function defined in Eq. 156) is detailed in Appendix A. It can be shown that the term αI^* may cause the damage rate to be negative. For instance, Fig. 21 shows that some components of the rate of a dissipation variable computed from an associate flow rule can be negative, depending on the location of the state of stress on the yield surface. To ensure the positivity of dissipation, it is proposed resort to a non-associate flow rule, i.e. to introduce a damage potential $g_d \neq f_d$ in the formulation.

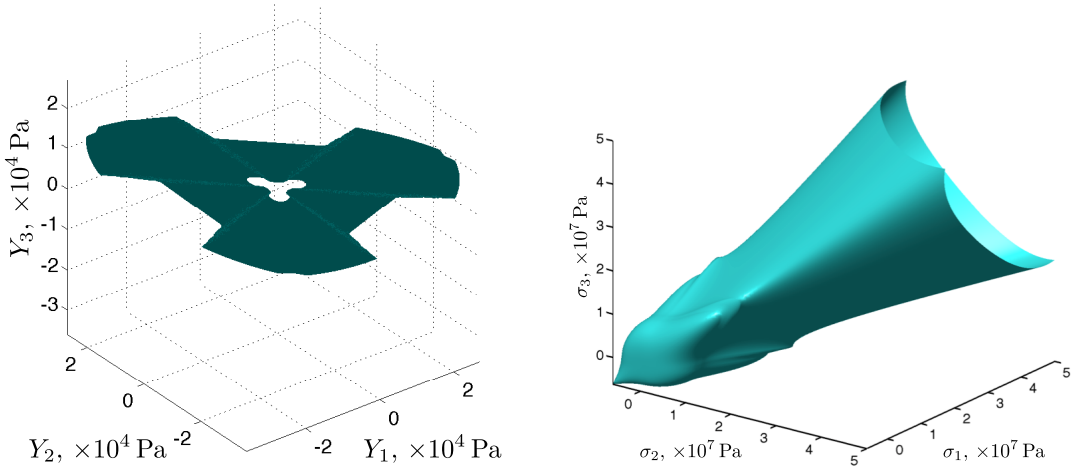

(a) Damage surface in $\mathbf{Y}$ space.

(b) Damage surface in $\boldsymbol{\sigma}$ space.

Figure 20: Representation of damage surface in 3-D spaces.

3.2.3 Postulate 3: Expression of the Damage Potential

It is proposed to define the damage potential as a homogeneous function of degree one in $\mathbf{Y}$ [234, 64]

$$g_d = \sqrt{\frac{1}{2}(\mathbb{P}_2 : \mathbf{Y}) : (\mathbb{P}_2 : \mathbf{Y})} - C_2 \tag{160}$$

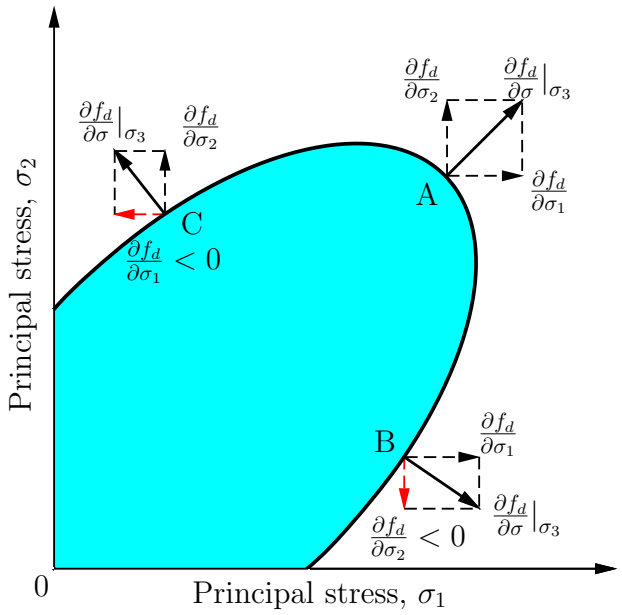

Figure 21: With an associate flow rule, some components of the rate of damage are negative.

The projection tensor $\mathbb{P}_2$ is introduced to represent both "crossing" and "splitting" effects (Fig. 13(a)-13(b))

$$\mathbb{P}_2 = \sum_{p=1}^{3} H\left[\max_{q=1}^{3}(\sigma^{(q)}) - \sigma^{(p)}\right] \mathbf{n}^{(p)} \otimes \mathbf{n}^{(p)} \otimes \mathbf{n}^{(p)} \otimes \mathbf{n}^{(p)} \tag{161}$$

Due to the definition of the projection tensor $\mathbb{P}_2$, the surface of the dissipation potential in the space of the components of $\mathbf{Y}$ exhibits three "branches", corresponding to the three possible directions of maximum eigenstress (these three "branches" are plotted with three different colors in Fig. 22). When the maximum eigenstress changes from one direction to another, the state of stress represented by the thermodynamic damage driving force jumps from one "branch" (or subsurface) to another. For the special case when two eigenstresses are equal, the plot of the damage potential exhibits a discontinuity, and the state of stress is characterized by a plane or a line. That could pose numerical problems if there was no unique way to compute the derivative of the damage potential. As a result, the model is thermodynamically consistent and the incremental equations can be implemented in a numerical code. Computations of damage for basic loading paths show that with the dissipation potential defined in Eq. 160, it is possible to calibrate the material parameters a_i in order to ensure the positivity of the components of $\frac{\partial g_d}{\partial \mathbf{Y}}$. All the verifications are reported

in Appendix B. The positivity of $\frac{\partial g_d}{\partial \mathbf{Y}}$ ensures the positivity of the damage rate, and therefore, the thermodynamic consistency of the model. Note that in the space of the "physical damage driving force" $\mathbb{P}_2 : \mathbf{Y}$, the surface of the damage potential is an octant of a sphere (Fig. 23(a)). Fig. 23(b) shows the shape of the damage potential in the space of stress: the three "branches" have the shape of cones. The three planes departing from the cone intersections illustrate the states of stress for which two maximum eigenstresses have the same value.

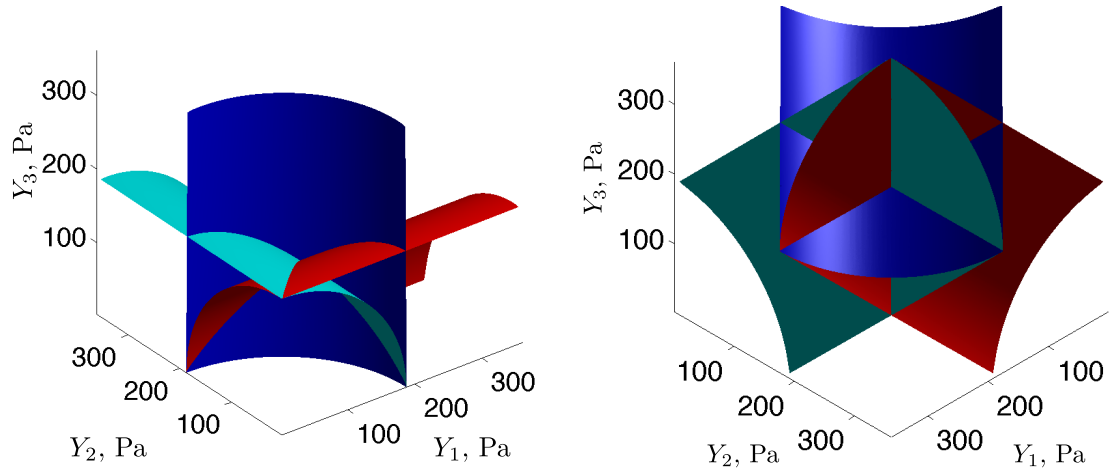

Figure 22: Damage potential in $\mathbf{Y}$ space. For a given state of stress, the elastic domain is delimited by one of the three colored surfaces (the red (respectively blue and turquoise) surface corresponds to a stress state in which $\sigma^{(1)}$ (respectively $\sigma^{(2)}$ and $\sigma^{(3)}$) is maximum. The figure on the right shows the convex elastic domain common to all possible states of stress.

3.2.4 Postulate 4: Irreversible Deformation Flow Rule

As explained above (Eq. 148), a sufficient condition to ensure the positivity of dissipation is to ensure that both $\mathbf{Y} : \dot{\mathbf{\Omega}} \geq 0$ and $\boldsymbol{\sigma} : \dot{\boldsymbol{\varepsilon}}^{id} \geq 0$. According to the computations presented in Appendix C, the condition $\mathbf{Y} : \dot{\mathbf{\Omega}} \geq 0$ is ensured by calibrating the material parameters (a_i) in such a way that the damage rate remains positive for the states of stress expected in geomechanical problems (mainly: triaxial and uniaxial compression, and uniaxial tension). A logical choice for the flow rule of irreversible deformation would be to use a non-associate

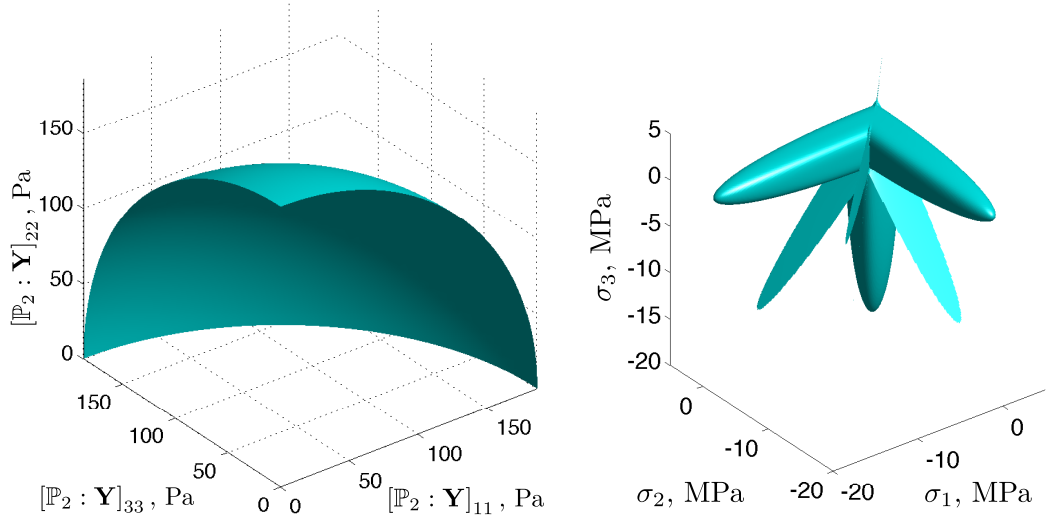

(a) Damage potential in $\mathbb{P}_2 : \mathbf{Y}$ space

(b) Damage potential in $\boldsymbol{\sigma}$ space.

Figure 23: Representation of damage potential in 3-D spaces.

flow rule deriving from the same potential as damage, which would would write

$$\dot{\boldsymbol{\varepsilon}}^{id} = \dot{\lambda}_d \frac{\partial g_d}{\partial \boldsymbol{\sigma}} = \dot{\lambda}_d \frac{\partial g_d}{\partial \mathbf{Y}} : \frac{\partial \mathbf{Y}}{\partial \boldsymbol{\sigma}} = \dot{\boldsymbol{\Omega}} : \frac{\partial \mathbf{Y}}{\partial \boldsymbol{\sigma}} \tag{162}$$

The flow of irreversible deformation should be normal to the surface of the plot shown in Fig. 23(b). A quick glance at the plot shows that the principal directions of the irreversible strain rate are equal to the stress principal directions, and that in each principal direction, the rate of irreversible strains has the same sign as the stress rate. However, it is assumed (from Postulate 3) that damage propagates in planes normal to the major principal stress direction, i.e. that cracks opening due to a compression in direction 1 should induce dilatant irreversible deformation in directions 2 and 3. As a result, we cannot reasonably assume that the rate of irreversible deformation remains parallel and of the same sign as the rate of stress. Instead of deriving the rate of irreversible deformation from the potential (Eq. 160), the evolution law of irreversible deformation is derived from an associate flow rule

$$\dot{\boldsymbol{\varepsilon}}^{id} = \dot{\lambda}_d \frac{\partial f_d}{\partial \boldsymbol{\sigma}} = \dot{\lambda}_d \frac{\partial f_d}{\partial \mathbf{Y}} : \frac{\partial \mathbf{Y}}{\partial \boldsymbol{\sigma}} \tag{163}$$

with

$$\frac{\partial f_d}{\partial \boldsymbol{\Omega}} = -C_1\boldsymbol{\delta}; \quad \frac{\partial g}{\partial \mathbf{Y}} = \frac{(\mathbb{P}_2{:}\mathbf{Y}){:}\mathbb{P}_2}{\sqrt{2(\mathbb{P}_2{:}\mathbf{Y}){:}(\mathbb{P}_2{:}\mathbf{Y})}}$$

$$\frac{\partial f_d}{\partial \mathbf{Y}} = \frac{\left[\mathbb{P}_1{:}\mathbf{Y}-\frac{1}{3}(\boldsymbol{\delta}{:}\mathbb{P}_1{:}\mathbf{Y})\boldsymbol{\delta}\right]{:}\left[\mathbb{P}_1-\frac{1}{3}\boldsymbol{\delta}\otimes(\boldsymbol{\delta}{:}\mathbb{P}_1)\right]}{\sqrt{2\left[\mathbb{P}_1{:}\mathbf{Y}-\frac{1}{3}(\boldsymbol{\delta}{:}\mathbb{P}_1{:}\mathbf{Y})\boldsymbol{\delta}\right]\left[\mathbb{P}_1{:}\mathbf{Y}-\frac{1}{3}(\boldsymbol{\delta}{:}\mathbb{P}_1{:}\mathbf{Y})\boldsymbol{\delta}\right]}} - \alpha\boldsymbol{\delta} : \mathbb{P}_1 \tag{164}$$

3.3 Mechanical and Energetic Analysis of the DSID Model

3.3.1 Microscopic and Macroscopic Damage Rotation

3.3.1.1 Micro-mechanisms Driving Damage Rotation

Macroscopic stress depends on the orientation of the material element (REV) considered (Figure 24). According to the constitutive equations of the DSID model, damage only depends on stress principal directions, therefore the state of damage does not depend on the orientation of the stress element. For instance, Figure 25 shows that the orientation of the macroscopic crack represented by the damage tensor is 45^o from the horizontal, shall shear or deviatoric stress be considered at the macroscopic level. If the same stress were applied locally, at the crack faces, shear and deviatoric stresses would produce different crack orientations: a horizontal or vertical shear micro-crack, or a diagonal tensile micro-crack. It was shown that dislocations generated at the tips of microscopic shear cracks result in a pair of tensile cracks [57, 261]. Macroscopic shear damage in the DSID model represents the linkage between microscopic tensile cracks by shear wing cracks [36], known as crossing effects (Figure 26).

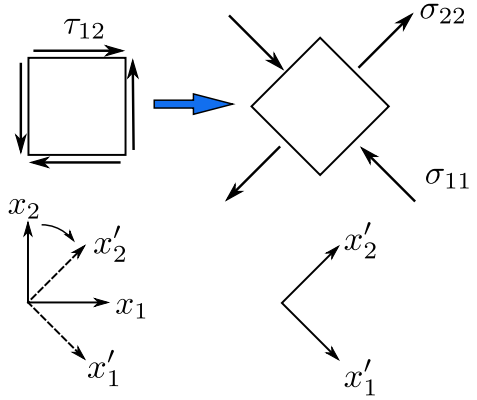

Figure 24: State of stress represented in material elements of different orientations.

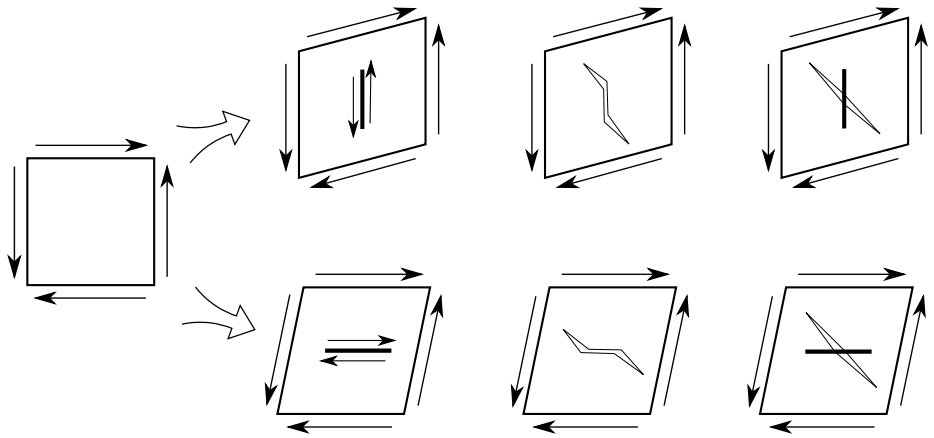

Figure 25: Macroscopic crack propagation driven by macroscopic shear stress, as a result of the linkage of microscopic tensile dislocations and microscopic shear wing cracks.

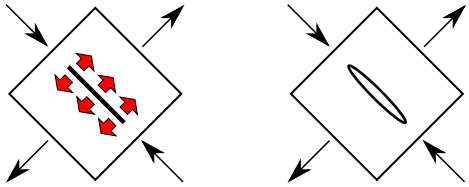

Figure 26: Macroscopic crack propagation driven by macroscopic differential stress, as a result of the propagation of microscopic tensile cracks.

3.3.1.2 Effects of Macroscopic Stress Paths on Damage Rotation

In the DSID model, the same state of damage can correspond to macroscopic crack propagation driven by shear stress or by differential stress, depending on the orientation of the stress element considered. However, a rotation of the state of stress changes the state of damage. Furthermore, the sequence of the loading affects the total amount of damage generated in the stress element. This is due to the non-linear stress-strain response expected in the presence of damage. Table 1 shows an example, in which damage was computed for a pure shear loading followed by a differential stress (triaxial compression), and for the same differential stress followed by shear stress.

Table 1: Damage evolution under different stress paths

Test	Stress paths		Accumulated damage	
	Stress 1	Stress 2	Damage 1	Damage 2
	$\Delta\sigma^{(1)}$, MPa	$\Delta\sigma^{(2)}$, MPa	$\Omega_{11}, \times 10^{-4}$	$\Omega_{22}, \times 10^{-4}$
Path 1:	$\begin{bmatrix} 0 & 60 & 0 \\ 60 & 0 & 0 \\ 0 & 0 & 0 \end{bmatrix}$	$\begin{bmatrix} 100 & 0 & 0 \\ 0 & 10 & 0 \\ 0 & 0 & 10 \end{bmatrix}$	$\begin{bmatrix} 75 & -75 & 0 \\ -75 & 75 & 0 \\ 0 & 0 & 1.90 \end{bmatrix}$	$\begin{bmatrix} 163 & -227 & 0 \\ -227 & 338 & 0 \\ 0 & 0 & 65 \end{bmatrix}$
Path 2:	$\begin{bmatrix} 100 & 0 & 0 \\ 0 & 10 & 0 \\ 0 & 0 & 10 \end{bmatrix}$	$\begin{bmatrix} 0 & 60 & 0 \\ 60 & 0 & 0 \\ 0 & 0 & 0 \end{bmatrix}$	$\begin{bmatrix} 0 & 0 & 0 \\ 0 & 35 & 0 \\ 0 & 0 & 35 \end{bmatrix}$	$\begin{bmatrix} 35 & -86 & 0 \\ -86 & 265 & 0 \\ 0 & 0 & 267 \end{bmatrix}$

Stress paths can be tracked by using Mohr's circles. The corresponding path of damage accumulation can be plotted in a similar plane, showing the admissible states of macroscopic shear damage for given states of normal damage. Figures 27 and 28 illustrate the stress and damage paths for the two examples in Table 1 (for clarity, Mohr's circles were plotted in a 2D $x_1 - x_2$ plane): the final state of stress is the same in the two cases, while the cumulated damage differs.

Pure shear stress (step 1 in stress path 1, Figure 27(a)), produces shear and normal damage of the same magnitude ($\Omega_{11} = \Omega_{22} = |\Omega_{12}|$), as illustrated in Figure 27(b)). A triaxial compression (step 1 in stress path 2, Figure 28(a)) induces damage Ω_{22} only (cracks normal to the direction of the major principal stress). The differential stress that builds up

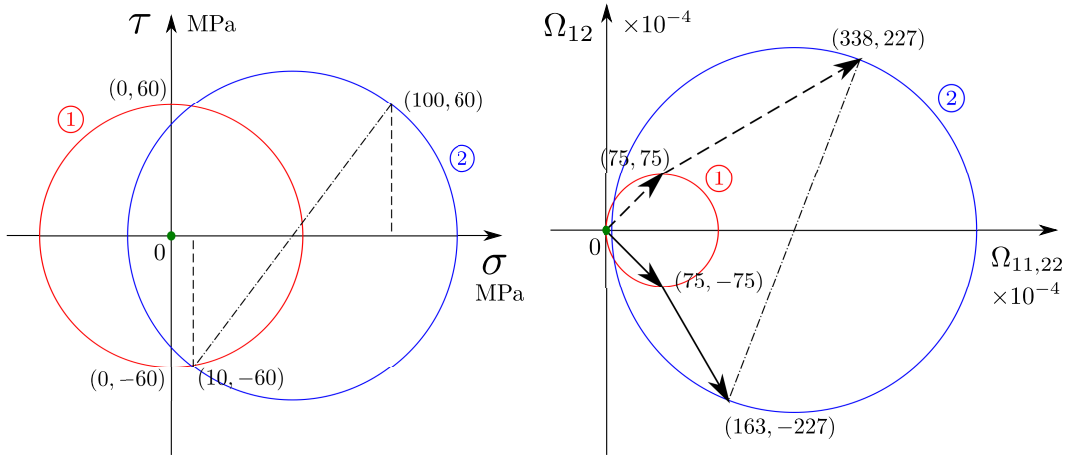

(a) Stress path (b) Damage evolution

Figure 27: Stress path 1: pure shear stress followed by triaxial compression. Paths of stress loading and resulting damage accumulation illustrated with Mohr's circles (dashed lines: paths of damage Ω_{22} and Ω_{21} for surfaces perpendicular to the x_2 axis; solid lines: paths of damage Ω_{11} and Ω_{12} for surfaces perpendicular to x_1 axis).

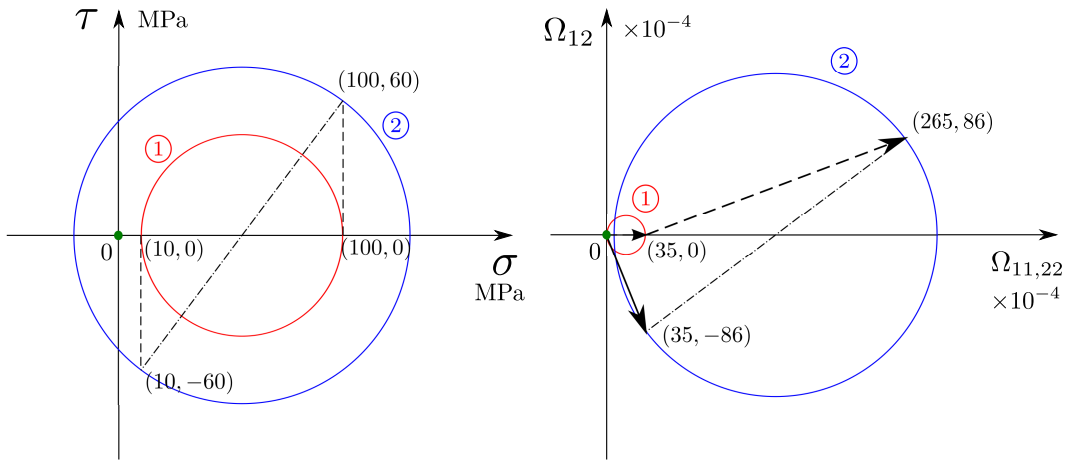

(a) Stress path (b) Damage evolution

Figure 28: Stress path 2: triaxial compression loading followed by pure shear stress. Paths of stress loading and resulting damage accumulation illustrated with Mohr's circles (dashed lines: paths of damage Ω_{22} and Ω_{21} for surfaces perpendicular to the x_2 axis; solid lines: paths of damage Ω_{11} and Ω_{12} for surfaces perpendicular to x_1 axis).

during the first loading step is higher for stress path 1 (pure shear applied first) than stress path 2 (triaxial compression applied first). As a result, higher damage is produced at the end of the first loading step of path 1. The additional differential stress imposed during step 2 is smaller in path 1 than in path 2. Consequently, damage in the second step of stress path 1 does not increase significantly, and does not change orientation markedly. The opposite phenomenon is observed for stress path 2: the shear stress applied during step 2 significantly increases the cumulated damage and significantly rotates the principal directions of damage. In stress path 1, shear damage can be represented by an equivalent mesocrack (defined at REV scale), inclined by angle of 45^o to the horizontal. During triaxial compression, the mesocrack propagates and also rotates counter-clockwise (Figure29(a)). Similarly, in stress path 2, damage induced by stress difference is a horizontal mesocrack. During the shearing phase, the macro-crack grows and rotates clockwise (Figure29(b)).

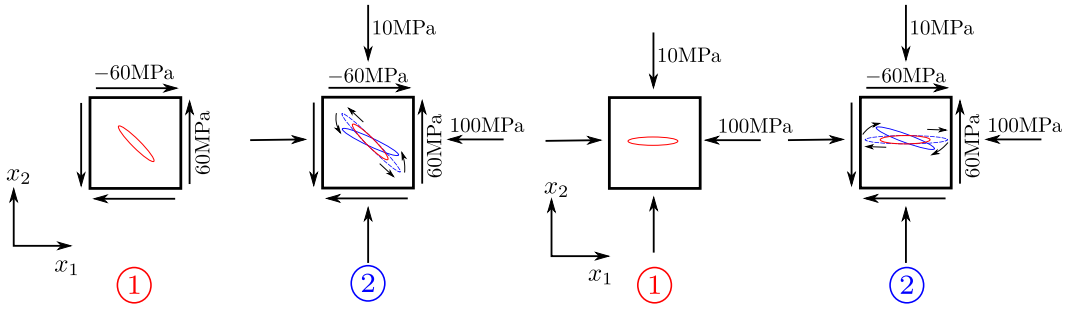

(a) Stress Path 1: pure shear, triaxial compression

(b) Stress Path 2: triaxial compression, pure shear

Figure 29: Schematic representation of crack propagation captured by the DSID model at the REV scale.

3.3.2 Forms of Energy Dissipation in the DSID model

Let us recall that the Inequality of Clausius-Duhem, derived from the combination of the two first laws of thermodynamics, writes

$$\Phi_s = \boldsymbol{\sigma} : \dot{\boldsymbol{\varepsilon}} - \dot{\Psi}_s \geq 0 \tag{165}$$

in which the free energy rate is

$$\dot{\Psi}_s = \frac{\partial \Psi_s}{\partial \boldsymbol{\varepsilon}^E} : \dot{\boldsymbol{\varepsilon}}^E + \frac{\partial \Psi_s}{\partial \boldsymbol{\Omega}} : \dot{\boldsymbol{\Omega}} \tag{166}$$

The dissipation potential of the solid skeleton should satisfy the Clausius-Duhem Inequality

$$\Phi_s = \boldsymbol{\sigma} : \dot{\boldsymbol{\varepsilon}}^{id} + \mathbf{Y} : \dot{\boldsymbol{\Omega}} \geq 0 \tag{167}$$

where Φ_s is the dissipated energy during each load increment. The elastic deformation energy stored in the solid body is $\frac{1}{2}\boldsymbol{\sigma} : \boldsymbol{\varepsilon}^E$. The work by the external force is $\boldsymbol{\sigma} : \dot{\boldsymbol{\varepsilon}}$ for each loading step, so the cumulated work is $\int \boldsymbol{\sigma} : \dot{\boldsymbol{\varepsilon}}\, \mathrm{d}t$. The dissipated energy is the difference between the external work and the recoverable strain energy

$$\int \Phi_d \, \mathrm{d}t = \int \boldsymbol{\sigma} : \dot{\boldsymbol{\varepsilon}} \, \mathrm{d}t - \frac{1}{2}\boldsymbol{\sigma} : \boldsymbol{\varepsilon}^E \geq 0 \tag{168}$$

The mechanical energy loss, $\int \dot{\Phi}_d \, \mathrm{d}t$, is represented by the area shaded in pink color in Figure 30: it should be always non-negative. The recoverable elastic strain energy is the area of the triangle shaded in light green in Figure 30.

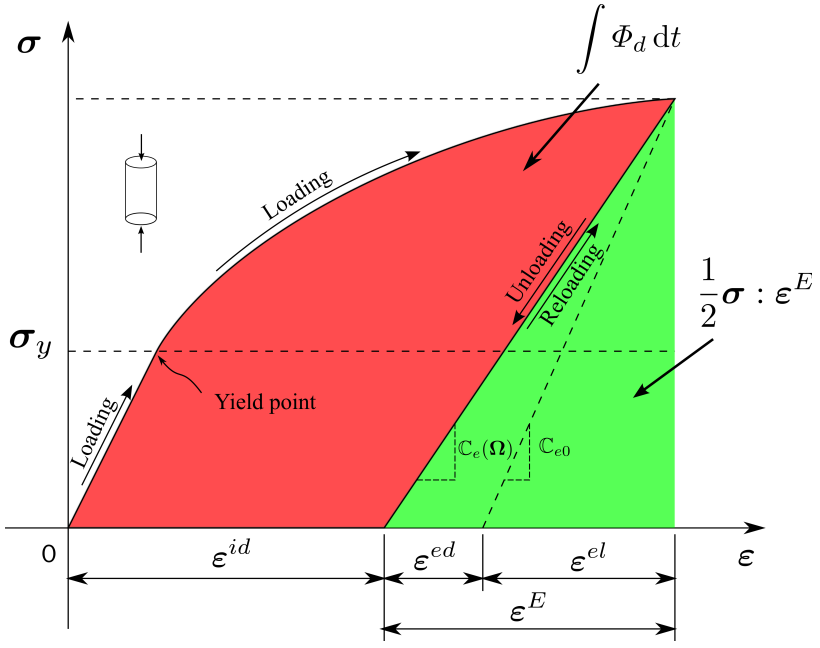

Figure 30: Evolution of the REV internal energy during one loading increment: recoverable elastic deformation is shown in green, dissipated energy is shown in red.

The propagation of damage affects the evolution of the REV energy in two ways: (1) crack debonding and opening without residual deformation, and (2) crack opening producing inelastic deformation. Both forms of dissipation can be characterized by the mechanical behavior of the damaged material. Crack debonding decreases the stiffness of material,

which decreases the capacity of that material to store deformation energy. Crack opening produces elastic and non-elastic non-linear strains. The energy dissipated by crack debonding and opening without residual deformation is actually the deformation energy related to $\boldsymbol{\varepsilon}^{ed}$. In the absence of energy transfer (thermal transport or radiation for instance), the total energy should be conserved: the work supplied to the REV by external loading is split into three parts, as shown in Figure 31. The energy conservation is expressed as

$$\int \boldsymbol{\sigma} : \dot{\boldsymbol{\varepsilon}} \, \mathrm{d}t = \int \boldsymbol{\sigma} : \dot{\boldsymbol{\varepsilon}}^{el} \, \mathrm{d}t + \int \boldsymbol{\sigma} : \dot{\boldsymbol{\varepsilon}}^{ed} \, \mathrm{d}t + \int \boldsymbol{\sigma} : \dot{\boldsymbol{\varepsilon}}^{id} \, \mathrm{d}t \tag{169}$$

The deformation energy due to the irreversible deformation component $\boldsymbol{\varepsilon}^{id}$ is fully dissipated, and corresponds to the energy necessary to displace crack faces irreversibly. The deformation energy due to the deformation component $\boldsymbol{\varepsilon}^{ed}$ is only partially dissipated: the deformation energy necessary to open cracks to the amount of $\frac{1}{2}\boldsymbol{\sigma} : \dot{\boldsymbol{\varepsilon}}^{ed}$ is recoverable. The other part of the deformation energy associated to $\boldsymbol{\varepsilon}^{ed}$ is related to crack debonding and equals $\int \mathbf{Y} : \dot{\boldsymbol{\Omega}} \, \mathrm{d}t$

$$\int \boldsymbol{\sigma} : \dot{\boldsymbol{\varepsilon}}^{ed} \, \mathrm{d}t = \frac{1}{2}\boldsymbol{\sigma} : \boldsymbol{\varepsilon}^{ed} + \int \mathbf{Y} : \dot{\boldsymbol{\Omega}} \, \mathrm{d}t \tag{170}$$

The distinction between these two energy contributions is illustrated in Figure 32. The energy balance can be rewritten as

$$\int \boldsymbol{\sigma} : \dot{\boldsymbol{\varepsilon}} \, \mathrm{d}t - \frac{1}{2}\boldsymbol{\sigma} : \boldsymbol{\varepsilon}^{E} = \int \dot{\Phi}_d \, \mathrm{d}t = \int \boldsymbol{\sigma} : \dot{\boldsymbol{\varepsilon}}^{id} \, \mathrm{d}t + \int \mathbf{Y} : \dot{\boldsymbol{\Omega}} \, \mathrm{d}t \geq 0 \tag{171}$$

Note that in the Finite Element Method, the energy balance is obtained by summing all increments of stress and strain

$$\sum \boldsymbol{\sigma}_{\theta n} : \dot{\boldsymbol{\varepsilon}}_n - \frac{1}{2}\boldsymbol{\sigma}_n : \boldsymbol{\varepsilon}_n^{E} = \sum \boldsymbol{\sigma}_{\theta n} : \dot{\boldsymbol{\varepsilon}}_n^{id} + \sum \mathbf{Y}_{\theta n} : \dot{\boldsymbol{\Omega}}_n \tag{172}$$

in which $\boldsymbol{\sigma}_{\theta n}$ and $\mathbf{Y}_{\theta n}$ are the resultant stress and damage force at the current increment, computed as

$$\boldsymbol{\sigma}_{\theta n} = (1-\theta)\boldsymbol{\sigma}_{n-1} + \theta \, \boldsymbol{\sigma}_n \tag{173}$$

$$\mathbf{Y}_{\theta n} = (1-\theta)\mathbf{Y}_{n-1} + \theta \, \mathbf{Y}_n \tag{174}$$

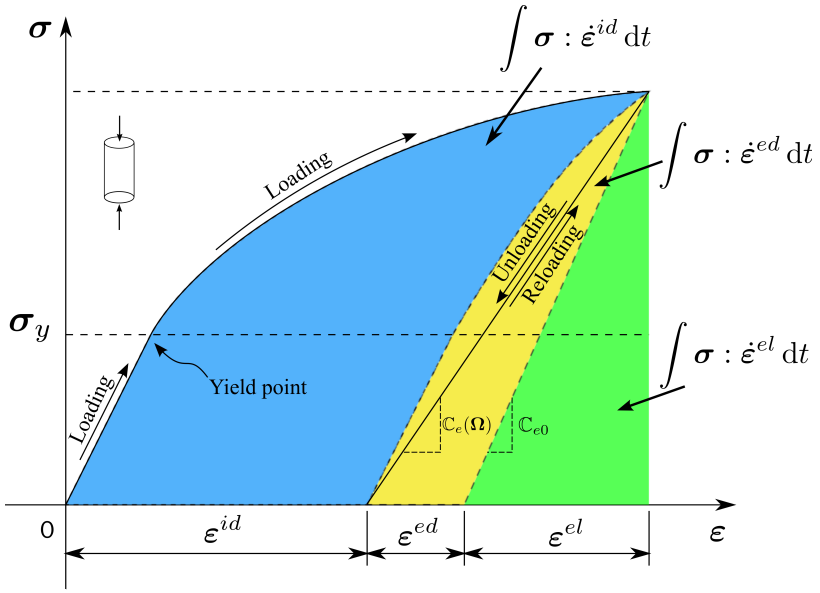

Figure 31: Decomposition of the REV energy during one loading increment: the zone shaded in green represents purely elastic deformation energy; the zone in yellow represents the energy spent due to crack debonding and elastic opening; the blue zone represents the energy dissipated by non-elastic crack opening.

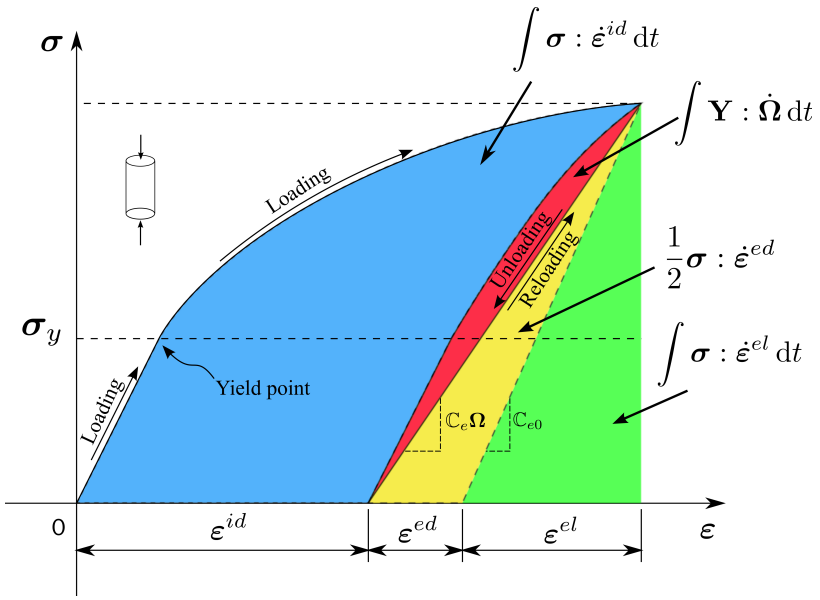

Figure 32: Decomposition of the REV energy during one loading increment: the zone shaded in green represents purely elastic deformation energy; the zone in red represents the energy spent due to crack debonding (resulting in material softening); the zone in yellow corresponds to subsequent elastic opening of the cracks; the blue zone represents the energy dissipated by non-elastic crack opening.

θ is the approximation factor. In Equation 172 above, the total elastic strain is obtained as

$$\boldsymbol{\varepsilon}_n^E = \boldsymbol{\varepsilon}_{n-1}^E + \dot{\boldsymbol{\varepsilon}}_n^E = \boldsymbol{\varepsilon}_{n-1}^E + \dot{\boldsymbol{\varepsilon}}_n - \dot{\boldsymbol{\varepsilon}}_n^{id} \tag{175}$$

3.4 Calibration of the DSID parameters

3.4.1 Review of Model Calibration Strategies

3.4.1.1 Experimental evidence of rock anisotropic behavior

Rocks develop an anisotropic behavior upon crack propagation, and can also exhibit intrinsic anisotropy due to their formation. For instance, sedimentary rocks are structured in layers by the process of deposition. At the microscopic scale, anisotropy is manifested by the sliding of clay sheets and the twilling in a few large calcite grains - two phenomena which are related to the distribution of voids in the clay matrix. At the scale of the laboratory sample (REV), anisotropy can be seen during a hydrostatic compression loading (e.g., claystone [61]): the response of the material to the applied loading exhibits different deformation in the axial and radial directions. In order to capture the resulting intrinsic anisotropy of rock mechanical behavior, loading tests have to be performed in directions parallel and perpendicular to the bedding planes. Figure 33 shows examples of typical stress-strain curves obtained during triaxial compression tests, for various confining pressures. The plots (reported from [40]) highlight the non-linear response of claystone under deviatoric stress loading. It is worth noticing that non-linearities occur early during the loading path, which implies that when damage occurs, micro-cracks start propagating at low stress and low deformation.

3.4.1.2 Review of calibration methods used in Damage Rock Mechanics

In most anisotropic damage models proposed for geomaterials, the free energy of the solid skeleton is expressed in terms of deformation [115, 116, 5, 63, 196, 125, 55, 212]. As a result, the energy release rate $\mathbf{Y}$ (also called damage driving force) that is work-conjugate to damage is also a function of deformation. In most rock mechanics problems of interest in engineering however, the REV is subject to known conditions of stress - not deformation. That is one of the reasons why the free energy potential used in the DSID model was expressed in terms of stress (Gibbs free energy, G_s). Damage models proposed for rock that are based on expressions of the free energy similar to the one adopted in the DSID

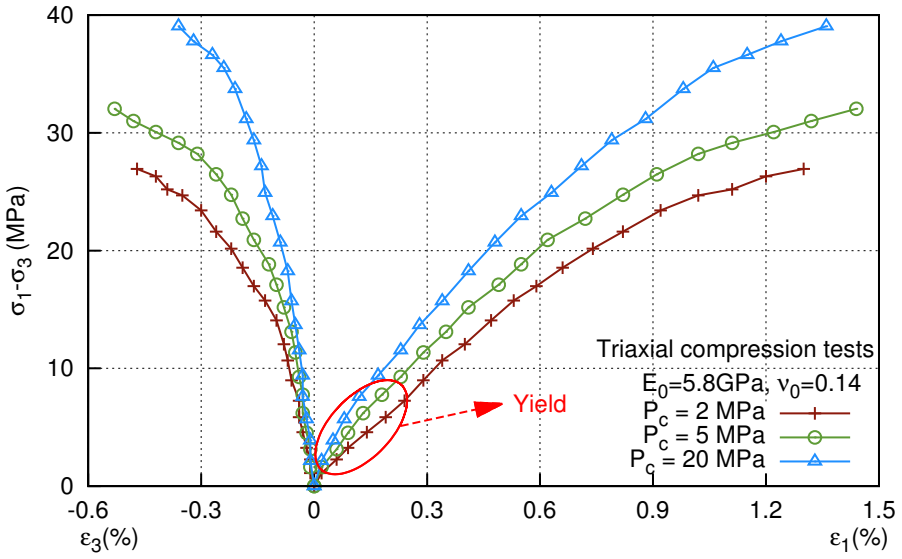

Figure 33: Typical stress-strain curves of claystone during triaxial compression tests (re-plotted, after [40]): effect of the confining pressure (p_c) on the initiation of damage and on damage-induced anisotropy.

model have a damage criterion and dissipation flow rules different from the ones used in the DSID model: the definition of the damage driving force is unique to the DSID model, which requires appropriate calibration. Parameters a_1, a_2, a_3, a_4, C_0 and C_1 were calibrated by Halm and Dragon [116] and by Shao et al. [242]. However, none of the two papers contains calibrated values for the entire set of parameters (a_1, a_2, a_3, a_4, C_0, C_1). One may argue that the set of values for a_1, a_2, a_3, a_4 found in [242] may be combined with the set of values for C_0 and C_1 found in [116], since the two papers deal with the same rock material. However, the two studies are based on different experimental data, so the set of model parameters could be inconsistent, or contain redundant parameters.

Calibration methods are rarely proposed in damage rock mechanics: only Halm and Dragon [116] and Hayakawa and Murakami [120] provided mathematical measurement strategies for calibration, which were later followed by other authors [239, 172]. Halm and Dragon's method is based on an iterative process, which reduces its applicability to models that have a limited number of parameters. Hayakawa and Murakami proposed different strategies for different experimental tests. In both Halm and Dragon's and Hayakawa and Murakami's techniques, parameters are all determined from one type of experiment,

which implies that the calibrated parameters may provide erroneous predictions for stress paths other than the ones tested. Therefore, calibration methods employed so far are not sufficient to determine the DSID parameters: a more comprehensive analysis is needed, based on datasets obtained for different types of experiments (i.e., stress paths), with a sufficient number of experiments for each stress path.

In rock mechanics, experimental tests are mainly the triaxial compression test, the uniaxial compression test, the uniaxial tension test and the Brazilian test. In the DSID model, the damage driving force and damage variable cannot be measured directly: they are back-calculated from constitutive parameters and other variables. Components of the damage tensor have to be derived first, which then allows determining the DSID model parameters. Constitutive parameters of the DSID model include the Young's modulus (E_0) and the Poisson's ratio (ν_0) of the pristine (undamaged) rock, the four constitutive damage parameters (a_1, a_2, a_3 and a_4) involved in the expression of the free energy, the initial damage threshold C_0, the damage hardening parameter C_1, and a damage parameter α, related to rock dilatancy angle [129, 295].

3.4.2 Proposed Calibration Approach

The calibration of the DSID parameters is performed in two steps:

1. The iterative calibration method suggested by Halm and Dragon [116] is used in order to bound the range of values of the damage model parameters.

2. A probabilistic method is then used in order to optimize the choice of the damage parameters within the range of values determined in the first step.

3.4.2.1 Step 1: range of values of the damage parameters

Since the damage criterion defined in the DSID model differentiates compression and tension, it is necessary to calibrate the model against experimental stress-strain curves obtained under both compression and tension tests. In the following, equations are derived in order to apply Halm and Dragon's calibration method with a set of triaxial/uniaxial compression tests and uniaxial tension tests. For each experimental data set used for calibration, it

is necessary to have at least one loading step that exhibits a reduction of stiffness, and one unloading step at the end of which the sample is free of stress (i.e. the load is fully relaxed). The very beginning of the tests is used to calculate the linear elastic moduli of the rock in the initial state (undamaged rock if the initial state is chosen as the reference state): the initial Poisson's ratio (ν_0) and the initial Young's modulus (E_0). The damaged Poisson's ratio (i.e. ν_{13}) and Young's modulus (E_1) are calculated from the slope of the unloading curve in the stress-strain diagram, as illustrated in Figure 34. The initiation of damage starts from point A, which indicates the initial damage threshold C_0 in the damage criterion:

$$J^*(\boldsymbol{\sigma}_A) - \alpha I^*(\boldsymbol{\sigma}_A) - C_0 = 0 \tag{176}$$

Point B of in the damaged state gives a second equation related to the damage criterion

$$J^*(\boldsymbol{\sigma}_B) - \alpha I^*(\boldsymbol{\sigma}_B) - C_0 - 2C_1 D_B = 0 \tag{177}$$

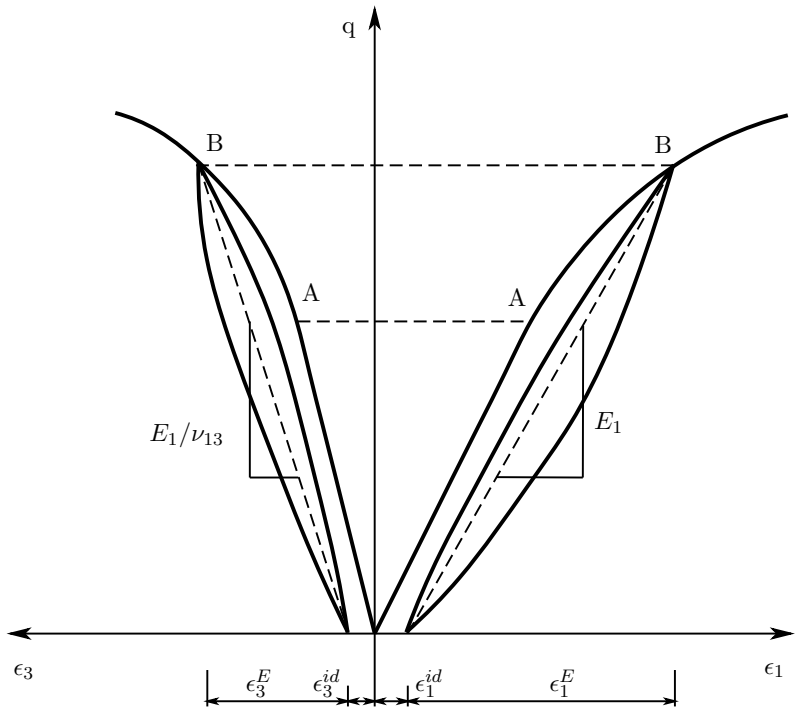

Figure 34: Halm and Dragon's Calibration Procedure - Example of Triaxial Compression [116]

Triaxial and Uniaxial Compression Tests. We assume that damage only propagates in tensile directions during the triaxial compression tests used for calibration. For a compression in direction 1, we have: $\Omega_{11} = 0$. This assumption is in agreement with the expected damage trends as predicted by the DSID model (which is an orthotropic damage model). Moreover, since we are focusing on axis-symmetric tests, we have: $\Omega_{22} = \Omega_{33}$. During the unloading stage, $\sigma_{11} = q$, and $\sigma_{22} = \sigma_{33} = 0$. Equations necessary to determine the damaged elastic moduli can be found by using the stress-strain relationships established in the preceding section

$$E_1 = \frac{1}{\frac{1}{E_0} + 4a_1\Omega_{33} + 4a_4\Omega_{33}} \tag{178}$$

$$\frac{E_1}{\nu_{13}} = \frac{1}{\frac{\nu_0}{E_0} - 4a_1\Omega_{33} - a_3\Omega_{33}} \tag{179}$$

The damage criterion at point A (Eq. 176) and point B (Eq. 177) provide two independent equations in addition to equations 178 and 179 above.

Uniaxial Tension Test. For the uniaxial compression test, we also assume that the damage only propagates in the tensile directions, so that $\Omega_{22} = \Omega_{33} = 0$ for a tension in direction 1, and

$$E_1 = \frac{1}{\frac{1}{E_0} + 2(a_1 + a_2 + a_3 + a_4)\Omega_{11}} \tag{180}$$

$$\frac{E_1}{\nu_{13}} = \frac{1}{\frac{\nu_0}{E_0} - 2a_1\Omega_{11} - a_3\Omega_{11}} \tag{181}$$

Using the damage criterion at two different points (Eq. 176 and 177) provides two independent equations in addition to equations 180 and 181 above.

Therefore, based on the analysis above, we have 4 equations for the uniaxial compression test and 4 equations for the uniaxial tension test. In total, 7 damage parameters need to be calibrated (a_1, a_2, a_3, a_4, C_0, C_1, α), and two damage values are unknown (Ω_{33} for the uniaxial compression test and Ω_{11} for the uniaxial tension test), therefore we have 8 independent equations for 9 unknowns. The value of either Ω_{33} or Ω_{11} is initialized and an iterative computation process is used in order to calibrate the entire set of unknowns. In order to do so, the flow rule (Eq. 163) is calculated for each test, and the difference between

the stress-strain curve in the model prediction (obtained from the calibration algorithm) and the experimental data is utilized as a convergence criterion.

3.4.2.2 Step 2: probabilistic calibration within the reduced range of values

Definition of the Known Variables and Unknown Parameters. stress-strain curves obtained from experiments are compared to predictions made with the DSID model, for known damage states. For one component of the total strain, the probabilistic model can be written as

$$\varepsilon^{(i)}(\mathbf{x}, \mathbf{B}) = \gamma(\mathbf{x}, \boldsymbol{\beta}) + s\xi \tag{182}$$

where $\varepsilon^{(i)}$ is the predicted total cumulated strain at increment (i). Selected explanatory functions γ provide a way to relate the total strains' component $\varepsilon^{(i)}$ to loading measures and rock properties. $\mathbf{x}$ is a vector of basic variables, assumed to be known or measurable, such as the stress tensor and the elastic material parameters. $\mathbf{B}$ is the vector of unknown model parameters, s is the standard deviation of the model error, and ξ is a normal random variable with zero mean and unit variance. $\boldsymbol{\beta}$ is the vector of unknown model parameters that can be optimized.

In the proposed probabilistic model, two assumptions are made: (1) the *homoskedasticity assumption* (i.e., s is assumed to be a constant independent of $\mathbf{x}$), and (2) the *normality assumption* (i.e., ξ is assumed to have a normal distribution). Usually, both assumptions can be satisfied by performing transformations to stabilize the variance of the quantities of interest [41]. In this work, a natural logarithmic transformation of total strain is adopted, and after transformation, the model writes

$$\ln\left\{\varepsilon^{(i)}(\mathbf{x}, \mathbf{B})\right\} = \ln\{\gamma(\mathbf{x}, \boldsymbol{\beta})\} + s\xi \tag{183}$$

Note that the model error is written in the logarithm of predicted strain in equation 183), which is the sum of the logarithm of this function and the logarithm of a function of error.

Application of the Maximum Likelihood Method. The purpose of the probabilistic calibration is to optimize the estimation of the vector of unknown model parameters

$\mathbf{B} = (\boldsymbol{\beta}, s)$. One of the best methods to obtain a point estimator of a parameter is the method of Maximum Likelihood [195, 102, 42], in which the estimation of $\mathbf{B}$ is based on an unbiased estimator $\hat{\mathbf{B}}$ that maximizes the likelihood function. Data points (noted $\varepsilon_{\text{exp}}^{(i)}$ to refer to experimental data) used as reference observation data are points of stress-strain curves collected from the literature (Tab. 2). The vector of unknown model parameters is estimated ($\mathring{\mathbf{B}} = \{\mathring{a}_1, \mathring{a}_2, \mathring{a}_3, \mathring{a}_4, \mathring{C}_0, \mathring{C}_1, \mathring{\alpha}, \mathring{s}\}$), which allows computing the total strain $\mathring{\varepsilon}^{(i)}$ using Eq. 182: this provides a strain prediction with a certain error. Then the natural logarithmic transformation explained above is performed.

The model error ξ is assumed to have a normal distribution. Therefore, using the well known Gaussian distribution, the probability distribution corresponding to $\mathring{\mathbf{B}}$ is written as

$$P(\mathring{\mathbf{B}}) = \frac{1}{\mathring{s}\sqrt{2\pi}} e^{-\left(\varepsilon_{\text{exp}}^{(i)} - \mathring{\varepsilon}^{(i)}\right)^2 / \left(2\mathring{s}^2\right)} \tag{184}$$

The likelihood function for a set of n independent experimental observations is written as

$$L(\mathring{\mathbf{B}}) = \prod_{j=1}^{n} \frac{1}{\mathring{s}\sqrt{2\pi}} e^{-\left(\varepsilon_{\text{exp}_j}^{(i)} - \mathring{\varepsilon}_j^{(i)}\right)^2 / \left(2\mathring{s}^2\right)} \tag{185}$$

The value of the likelihood function is obtained for the assumed set of values $\mathring{\text{B}}$ taken by the unknown model parameters. The set of parameters that maximizes the likelihood function is retained to estimate the vector of unknown model parameters B. Other statistical properties, such as the standard deviation and the correlation coefficient matrix, can also be determined.

3.4.3 Probabilistic Optimization of the DSID Model for Claystone under Deviatoric Stress Loading

The probabilistic calibration of the DSID model needs to be based on a sufficient and consistent set of experimental data (i.e. on a large enough number of experiments performed on the same type of rock). In the following, it is proposed to focus on the calibration of the damage parameters of the DSID model (a_1, a_2, a_3, a_4, C_0, C_1, α) for claystone, based on given stress-strain curves obtained during triaxial compression and proportional tests reported in [61, 254, 40]. The probabilistic calibration is therefore based on the same material and on similar deviatoric stress paths. Table 2 explains the experimental data

used in this study. Note that the calibration procedure is expected to be applicable for other types of rocks and for other stress paths.

Table 2: Experimental results used as reference datasets in the probabilistic calibration.

References	Elastic parameters		
	Number of tests	E_0	ν_0
Chiarelli *et al.*, 2003 [61]	12	7.6GPa	0.14
Bourgeois *et al.*, 2002 [40]	3	5.8GPa	0.14
Souley *et al.*, 2011 [254]	1	4GPa	0.3

3.4.3.1 Probabilistic Calibration of the DSID Model: All Damage Parameters Included

In the following analysis, the vector of unknown parameters is initialized with damage parameters found in the literature for granite: a_1, a_2, a_3 and a_4 are taken from the work by Shao et al. [242] for Lac du Bonnet granite; C_0 and C_1 are taken from the work of Halm and Dragon [116] for Vienne granite. The optimization method employed here assumes that the unknown parameters can take any value, and the final result is independent of the values of the parameters taken in the initialization phase. However, a proper initialization helps to converge faster to the optimized results. The initial set of values for the components of the vector of unknown parameters $\boldsymbol{\beta}$ is presented in Table 3.

Table 3: Initial set of damage parameters for probabilistic calibration (from [116, 242]).

a_1 Pa^{-1}	a_2 Pa^{-1}	a_3 Pa^{-1}	a_4 Pa^{-1}	C_0 Pa	C_1 Pa	α -
1.26×10^{-13}	3.94×10^{-11}	-1.26×10^{-12}	2.51×10^{-13}	1.10×10^{5}	2.20×10^{6}	0.231

From the high departure from the 1:1 line in Figure 35a., it can be seen that the stress-strain curves predicted with the derived equations and the set of parameters tabulated in Table 3 do not match the experimental stress-strain curves used as reference data (Table 2). Moreover, the standard deviation of the model increases for the larger values of strain. Using a natural logarithmic transformation (Eq. 183) allows stabilizing the standard deviation, but does not improve the performance of the model (Figure 35b.). Therefore, a rigorous calibration is needed to determine the set of unknown damage parameters $\boldsymbol{\beta} = \{a_1, a_2, a_3, a_4, C_0, C_1, \alpha\}$.

For high levels of damage, important irreversible deformation is expected: this behavior trend is herein referred to as "ductile deformation regime". To simplify the optimization process, the value of C_0 was fixed to a low value ($C_0 = 1.1 \times 10^5$ Pa, as reported in Table 3), which made it possible to predict damage even at low deformation and stay in the brittle deformation regime - the focus of this study. Table 4 summarizes the values of the remaining constitutive damage parameters $\{a_1, a_2, a_3, a_4, C_1, \alpha\}$, optimized by the maximum likelihood method. A comparison between results obtained using these values against experimental data is presented in Fig. 35b. and Fig. 35c. in normal and logarithmic scales, respectively. As it can be seen in these figures, predictions are noticeably improved after optimization, and the standard deviation in logarithmic scale remains constant for different values of strain. The standard deviation for the model is equal to 0.29. The standard deviation s for the model after logarithmic transformation is approximately equal to the Coefficient Of Variation (C.O.V in Table 4) of the model before logarithmic transformation [95]. The Coefficient Of Variation (C.O.V in Table 4), defined as

$$C.O.V = SD/\mu \tag{186}$$

provides an indication on model uncertainty associated to a specific constitutive parameter. The C.O.V. is representative of the non-linearities of the DSID model, of the uncertainties involved in the prediction of the mechanical behavior of rock (which are natural materials), and of the measurement errors.

Table 4: Damage parameters calibrated with the maximum likelihood method, with $C_0 = 1.1 \times 10^5$ Pa.

param.	μ	scale	SD	C.O.V
a_1 (Pa^{-1})	21.92	10^{-13}	1.28	0.06
a_2 (Pa^{-1})	704.94	10^{-11}	28.58	0.04
a_3 (Pa^{-1})	-98.88	10^{-12}	5.15	0.05
a_4 (Pa^{-1})	11.10	10^{-13}	1.04	0.09
C_1 (Pa)	64.35	10^6	4.02	0.06
α (-)	3.31	0.1	0.09	0.03
s	0.2875	1	-	-

μ: mean value. SD: standard deviation. C.O.V.: coefficient Of Variation.

3.4.3.2 Probabilistic Optimization of the DSID Model: Removing Parameters

It is interesting to know whether the DSID model could be simplified for cases where damage is expected to occur due to deviatoric stress. In the following, it is proposed to assess the performance of the DSID model for the prediction of compression-induced damage, with a reduced number of constitutive parameters. Because the damage function is necessary to predict the occurrence of damage itself, related parameters C_0, C_1 and α are maintained in the model formulation. Probabilistic optimization is focused on parameters a_1, a_2, a_3 and a_4, involved in the expression of the free energy of the damaged rock. The objective of the following probabilistic optimization is to justify the form of the polynomial used in the free energy of damaged claystone from a mathematical stand point, for differential stress loading.

Interestingly, the model standard deviation does not change after removal of the a_4 parameter: this means that for the stress path and material under study, a_4 does not contribute significantly to stress-strain prediction, and that a_4 (and its associated explanatory function) can be safely removed from the model formulation. The comparison between model predictions (without a_4) and experimental observations (Fig. 35e. and Fig. 35f.) confirm that model performance is not sensitive to a_4. By following the same procedure, parameters a_1 and a_3 are successively removed from the model formulation. Final probabilistic results are presented in Table 5. Comparisons between the predictions with a reduced number of model parameters and experimental observations show that neither a_1 (Fig. 35g. and Fig. 35h.) or a_3 (Fig. 36c. and Fig. 36d.) significantly affects the performance of the DSID model. Moreover, predictions obtained with a_2 only (Fig. 36c. and Fig. 36d.) are not significantly different from the ones obtained with the four constitutive parameters (Fig. 35c. and Fig. 35d). The performance of the model was assessed for other choices of single-parameter based formulations (i.e. a_1, a_3 or a_4 only): results confirm that a_2 is the only constitutive parameter needed to predict differential stress-induced damage in Eastern France claystone (Fig. 36).

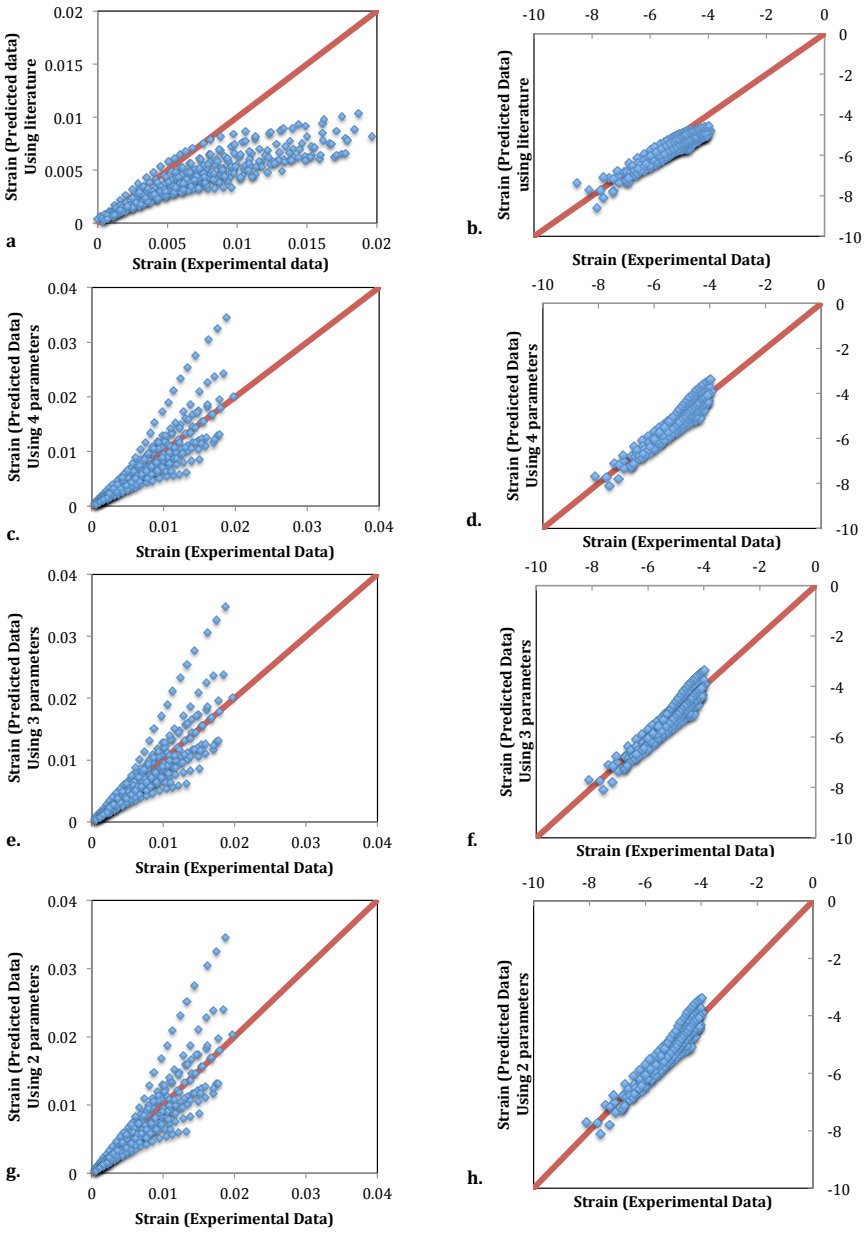

Figure 35: Comparison of the deformation predicted with the DSID model with deformation points taken from experimental stress-strain curves reported in Table 2. Plots on the left (resp. on the right) display the results before (resp. after) performing the logarithmic transformation of strain. (a)&(b): Before model calibration, using model parameters obtained by curve-fitting in [116, 242]. (c)&(d): After calibration based on the Maximum Likelihood Method. (e)&(f): After calibration, without a_4. (g)&(h): After calibration, without a_4 and a_1.

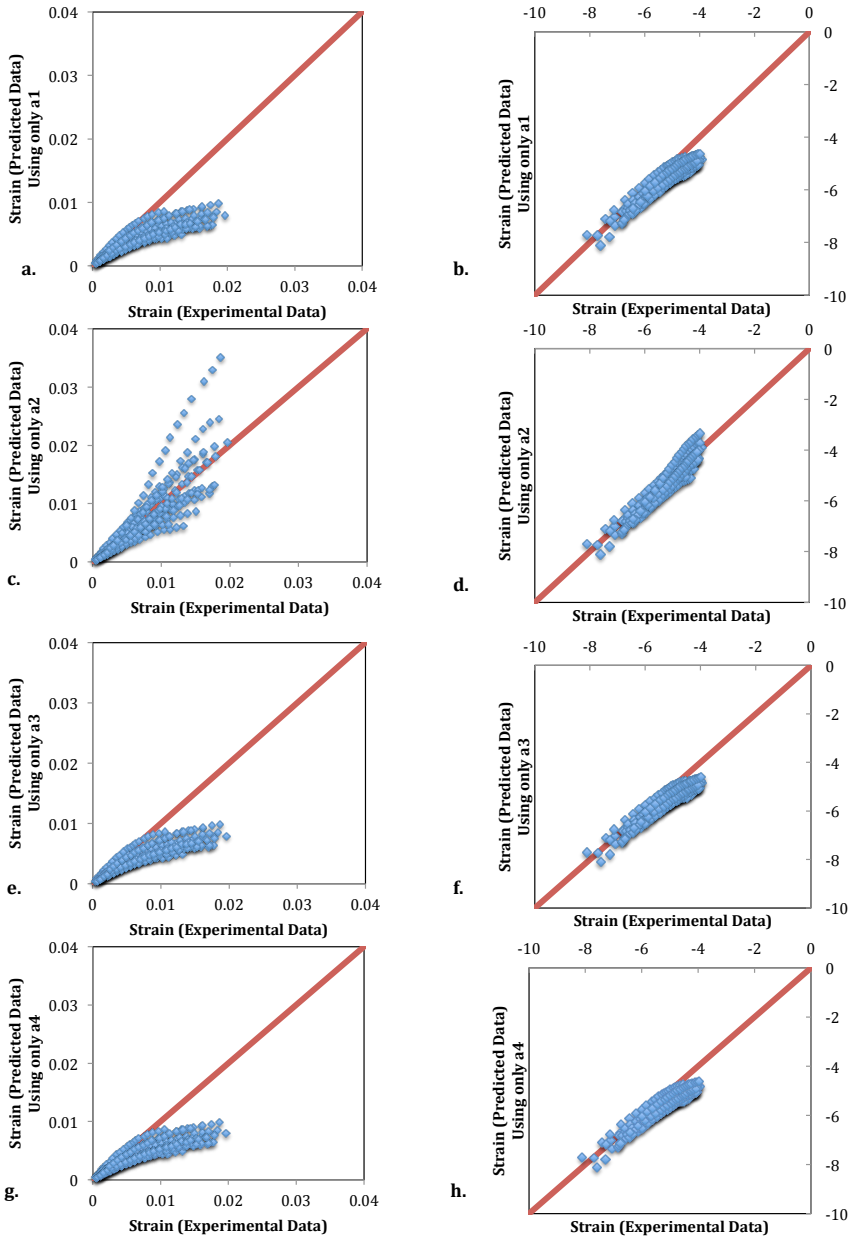

Figure 36: Performance of the DSID model to predict experimental stress-strain curves reported in Table 2, when only one constitutive model parameter is used in the formulation. Plots on the left (resp. on the right) display the results before (resp. after) performing the logarithmic transformation of strain. (a)&(b): Only a_1. (c)&(d): Only a_2. (e)&(f): Only a_3. (g)&(h): Only a_4.

Table 5: Damage parameters calibrated with the maximum likelihood method, with $C_0 = 1.1 \times 10^5$ Pa, after removing a_4, a_1 and a_3.

param.	μ	scale	SD	C.O.V
a_2 (Pa^{-1})	704.94	10^{-11}	35.80	0.05
C_1 (Pa)	64.34	10^6	6.30	0.10
α (-)	3.29	0.1	0.26	0.08
s	0.2862	1	-	-

μ: mean value. SD: standard deviation. C.O.V.: coefficient Of Variation.

3.4.3.3 Probabilistic Optimization of the DSID Model: Combining Parameters

The correlation coefficient matrix for the remaining variables is shown in Table 6. If the absolute value of the correlation coefficient between two variables (β_i and β_j) is close to one, the two variables have high correlation and may be combined using the following equation obtained from statistical relations [95, 255]

$$\hat{\beta}_i = \mu_{\beta_i} + \rho_{\beta_i\beta_j} \frac{SD_{\beta_i}}{SD_{\beta_j}} \left(\beta_j - \mu_{\beta_j}\right) \tag{187}$$

where μ_{β_i} (resp. μ_{β_j}) is the mean value of β_i (resp. β_j); $\rho_{\beta_i\beta_j}$ is the correlation coefficient between β_i and β_j; SD_{β_i} (resp. SD_{β_j}) is the standard deviation of β_i (resp. β_j); and $\hat{\beta}_i$ is the new estimate for β_i. According to Table 6, the correlation coefficient between all variables is almost one. This means these variables are highly correlated with each other, which allows using Eq. 187 to combine parameters and reduce the number of independent model parameters in the formulation of the DSID model.

Table 6: Correlation coefficient matrix for the DSID model parameters, using only a_2.

param.	a_2 (Pa^{-1})	C_1 (Pa)	α (-)
a_2 (Pa^{-1})	1	1	0.99
C_1 (Pa)	1	1	0.99
α (-)	0.99	0.99	1

By substituting the values from Table 6 into Eq. 187, the new estimates of C_1 and α can be written as functions of a_2

$$\hat{C}_1 = 64.34 \times 10^6 + \frac{6.30 \times 10^6}{35.80 \times 10^{-11}} \left(a_2 - 704.94 \times 10^{-11}\right) \tag{188}$$

$$\hat{\alpha} = 3.29 \times 10^{-1} + \frac{0.26 \times 10^{-1}}{35.80 \times 10^{-11}} \left(a_2 - 704.94 \times 10^{-11}\right) \tag{189}$$

According to the preceding probabilistic optimization, the free energy of damaged claystone can be written as

$$G_s(\boldsymbol{\sigma}, \boldsymbol{\Omega}) = \frac{1}{2}\boldsymbol{\sigma} : \mathbb{S}_0 : \boldsymbol{\sigma} + a_2 \,\mathrm{Tr}(\boldsymbol{\sigma} \cdot \boldsymbol{\sigma} \cdot \boldsymbol{\Omega}) \tag{190}$$

The damage function writes

$$f_d = \sqrt{J^*} - \hat{\alpha} I^* - C_0 - \hat{C}_1 \mathrm{Tr}\boldsymbol{\Omega} \tag{191}$$

in which C_1 and α are functions of a_2. Optimized values of a_2, C_1 and α, obtained by using the combinations above in the explanatory functions used in the maximum likelihood method, are provided in Table 7.

Table 7: Optimized DSID parameters, calibrated with the maximum likelihood method, using a_2 as the sole constitutive parameter.

param.	Suggested Value	SD
a_2 (Pa^{-1})	704.94×10^{-11}	35.80×10^{-11}
$\hat{C}_1$ (Pa)	$64.34 \times 10^6 + 1.76 \times 10^{17}\left(a_2 - 704.94 \times 10^{-11}\right)$	6.30×10^6
$\hat{\alpha}$ (-)	$3.29 \times 10^{-1} + 7.26 \times 10^9\left(a_2 - 704.94 \times 10^{-11}\right)$	0.026×10^{-1}
s	0.2862	-

SD: standard deviation

3.4.3.4 Discussion

Physical Interpretation of the Model Optimization The main finding of the preceding probabilistic analysis is that only two damage parameters are needed to predict damaged stress-strain curves of claystone subjected to deviatoric stress loading: C_0 and a_2. It may be concluded that the only constitutive parameter needed to predict differential stress-induced damage in claystone is a_2, the coefficient multiplying the monomial $\mathrm{Tr}(\boldsymbol{\sigma} \cdot \boldsymbol{\sigma} \cdot \boldsymbol{\Omega})$ in the expression of the damaged free energy. The optimized formulation of the DSID model obtained after applying the maximum likelihood method is therefore much simpler than the one dictated by elasticity and thermodynamic principles, in section 3.2. The most general formulation of the DSID model needs however to be used as is, when no information is available on the type of rock material tested or stress path expected.

As a result, it is expected that explanatory functions depending on stress, differences of principal stresses in particular, should be the most affected by the stress path. Table 8

summarizes the relation of each a_i parameter to the free energy G_s, the total elastic deformation $\boldsymbol{\varepsilon}^E$ and the damage driving force $\mathbf{Y}$. In the expression of the free energy, every a_i multiplies a trace of stress, damage or products of stress and damage. Therefore it is impossible to conclude on the relative importance of the constitutive parameters for the prediction of anisotropic damage induced by stress difference.

In the expression of total elastic strain, a_1 and a_3 multiply traces. Although the term in a_3 allows quantifying the deviation of stress from the principal directions of damage (i.e. from the "past" principal directions of stress), the relation to the anisotropic stress path is expected to be better captured by the terms in a_2 and a_4, which indeed contain a non-volumetric term of stress. In the expression of the damage driving force, only a_2 and a_3 multiply a non-volumetric stress. Hence, a_2 influences stress-induced damage and the subsequent anisotropy of both the elastic deformation and the damage driving force. Conceptually, it could be expected that a_2 would play the most important role in the damage model for the tests.

However, the order of magnitude of constitutive parameters is also critical in the analysis. From Table 8,

$$|a_4| < |a_1| < |a_3| < |a_2| \tag{192}$$

where a_2 is two orders of magnitude larger than a_3, which is one order of magnitude larger than a_1 and a_4, a_1 being slightly larger than a_4. From this analysis, it can be recommended to simplify the DSID model by removing a_4 first, then a_1, and finally a_3. a_2 turns out to be again the most significant parameter in the model. All of these analyses concur with the conclusions raised in the probabilistic optimization of the damage model.

Table 8: Relative influence of the a_i parameters in the formulation of the DSID model.

a_i	μ	Scale	Terms in G_s	Terms in $\boldsymbol{\varepsilon}^E$	Terms in $\mathbf{Y}$	Reduction
a_1	21.92	10^{-13}	$\mathrm{Tr}\boldsymbol{\Omega}(\mathrm{Tr}\boldsymbol{\sigma})^2$	$(\mathrm{Tr}\boldsymbol{\Omega}\,\mathrm{Tr}\boldsymbol{\sigma})\boldsymbol{\delta}$	$(\mathrm{Tr}\boldsymbol{\sigma})^2\boldsymbol{\delta}$	2
a_2	704.94	10^{-11}	$\mathrm{Tr}(\boldsymbol{\sigma}\cdot\boldsymbol{\sigma}\cdot\boldsymbol{\Omega})$	$(\sigma\cdot\boldsymbol{\Omega}+\boldsymbol{\Omega}\cdot\boldsymbol{\sigma})$	$\boldsymbol{\sigma}\cdot\boldsymbol{\sigma}$	-
a_3	-98.88	10^{-12}	$\mathrm{Tr}\boldsymbol{\sigma}\,\mathrm{Tr}(\boldsymbol{\Omega}\cdot\boldsymbol{\sigma})$	$\mathrm{Tr}(\boldsymbol{\sigma}\cdot\boldsymbol{\Omega})\boldsymbol{\delta}+(\mathrm{Tr}\boldsymbol{\sigma}\boldsymbol{\Omega})$	$\mathrm{Tr}(\boldsymbol{\sigma})\boldsymbol{\sigma}$	3
a_4	11.10	10^{-13}	$\mathrm{Tr}\boldsymbol{\Omega}\,\mathrm{Tr}(\boldsymbol{\sigma}\cdot\boldsymbol{\sigma})$	$(\mathrm{Tr}\boldsymbol{\Omega})\boldsymbol{\sigma}$	$\mathrm{Tr}(\boldsymbol{\sigma}\cdot\boldsymbol{\sigma})\boldsymbol{\delta}$	1

The "reduction" column indicates in which order the model parameters should be removed, according to their relative importance in the DSID model formulation.

Probabilistic Assessment of the Optimized DSID Model The probabilistic calibration presented above is based on the optimization of the estimation of axial strain only. In order to properly assess the model performance, both axial (ε_{11}) and lateral (ε_{33}) strains predicted by the calibrated and optimized DSID model were compared to experimental stress-strain curves, in Fig. 37. It appears that after simplification and calibration, the DSID model does not perform equally well for all the tests used as reference data (Fig. 37(c), 37(d)). The main reason for these differences is that the model was optimized on the basis of the entire experimental dataset, and the plots in Fig. 37 only show the results for one test at a time, which may deviate from the average response measured from all the reference tests.

Experimentally, it is observed that claystones generally do not dilate significantly upon deviatoric loading: the volumetric deformation is compressive. However, the important increase of radial strains at higher deviatoric stress results in less compressive volumetric strains. In proportional tests, experimental measures indicate that lateral strains are almost zero, especially at low stress. Some of the predicted stress-strain curves underestimate radial strains, which tend to decrease upon deviatoric compression. Based on the simulation results obtained, it is noted that DSID predictions generally underestimate lateral strains for the higher deviatoric stress levels: the model does not capture the degradation of compressive volumetric strains. Moreover, it can be concluded that stress paths chosen for model calibration affects the values of the calibrated parameters.

3.4.4 Simplified Calibration Method of the DSID model for Shale Brittle Deformation Regime

Shale is a sedimentary rock characterized by discontinuities along thin laminae or parallel layering or bedding (Figure 38(a)). Shales are naturally anisotropic, which make them difficult to test: usually, samples (called "plugs") are cored parallel and perpendicular to the bedding planes, in order to determine shale properties in the principal fabric directions of the rock. Experimental data used for the calibration of the DSID model were obtained with shale samples that were assumed homogeneous (Figure 38(b)).

Triaxial compression tests conducted in *ConocoPhillips* rock mechanics laboratory were

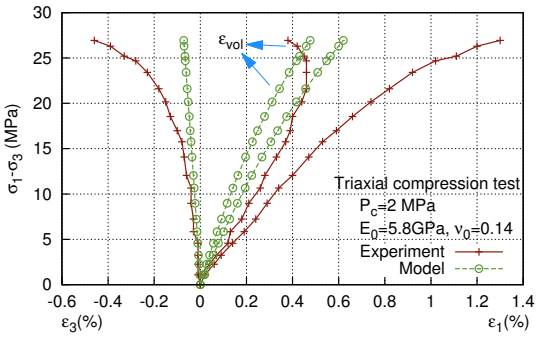

(a) Test 1 (Experimental data from [40])

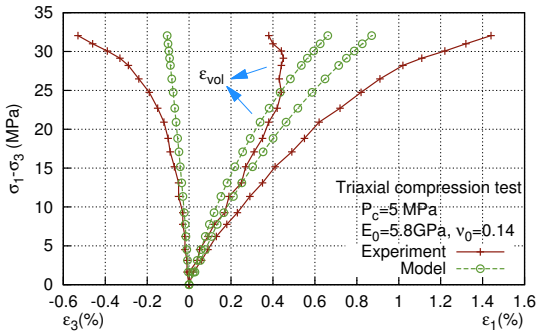

(b) Test 2 (Experimental data from [40])

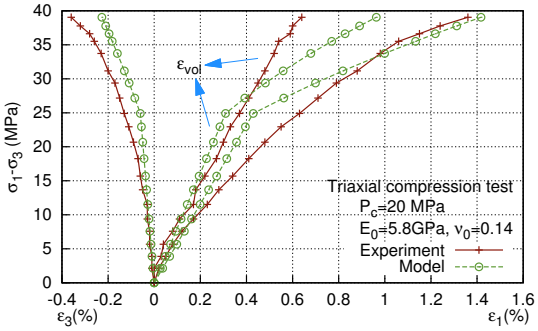

(c) Test 3 (Experimental data from [40])

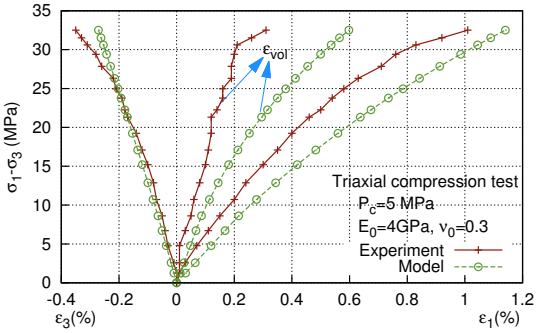

(d) Test 4 (Experimental data from [254])

Figure 37: Comparison between model predictions and experimental data, after model optimization: stress-strain plots for tests performed on claystone.

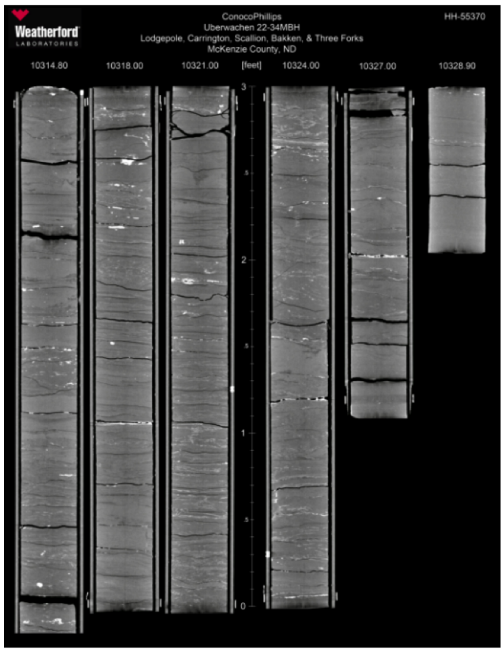

(a) CT scan photo of shale cores with 4 inch in diameter.

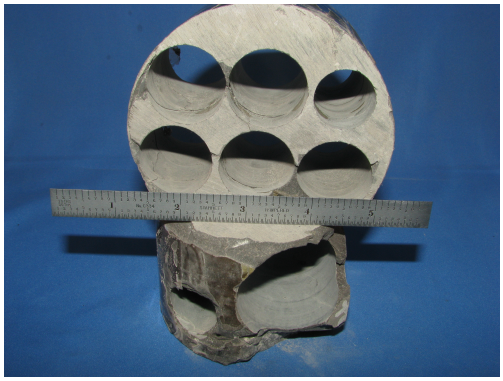

(b) Preparation of shale plugs

Figure 38: Photos of shale cores and shale plugs *(courtesy of ConocoPhillips, Houston, TX)*.

used to determine the DSID model parameters. The calibration was done iteratively, with an algorithm similar to the one used in the probabilistic calibration method presented above (published in [25]). By contrast with the Maximum Likelihood Method presented above, the optimization problem was solved by minimizing the squared residuals of the distance, r_i, between experimental data, y_i, and numerical predictions, $f(\mathbf{x}, \mathbf{B})$

$$S = \sum_{i=1}^{n} r_i^2, \qquad r_i = y_i - f(\mathbf{x}, \mathbf{B}) \tag{193}$$

where $\mathbf{x}$ is the vector of known input variables and $\mathbf{B}$ is the vector of parameters that need to be calibrated. A dedicated MATLAB code was written to perform the calibration automatically. The algorithm is initialized with the mean, minimum and maximum values of the model parameters. Using these parameters, a triaxial compression test was simulated at the material point using the DISD model. The gradient method was employed to minimize the difference between numerical and experimental stress-strain curves, and find the optimal set of parameters. The algorithm starts with the initialized vector $\mathbf{B}_0$, and iteratively finds the sequence $\mathbf{B}_1$, $\mathbf{B}_2$, $\ldots \mathbf{B}_{n+1}$ by solving

$$\mathbf{B}_{n+1} = \mathbf{B}_n - \gamma_n \nabla f(\mathbf{B}_n) \tag{194}$$

in which the value of the step size γ_n is allowed to change at each iteration.

The stress-strain curve used for model calibration was obtained for a sample first subjected to a 4,000 psi (27.6 MPa) isotropic compressive stress, and then subjected to an axial strain (which causes some deviatoric stress in the sample). Figure 39 shows the experimental stress-strain curve (in blue) and the numerical stress-strain curve obtained after model calibration (in red). Lateral deformation predicted with the DSID model matches the experimental results. However the DSID model seems to under-estimate axial deformation. Variations of the DSID model parameters were imposed around the optimum: predicted stress-strain curves lie within a domain (shaded in grey in Figure 39 which is obtained by modifying the damage threshold and damage hardening variables.) that contains the experimental stress-strain plot. An optimum set of DSID parameters for Bakken Shale from North Dakota is given in Table 9.

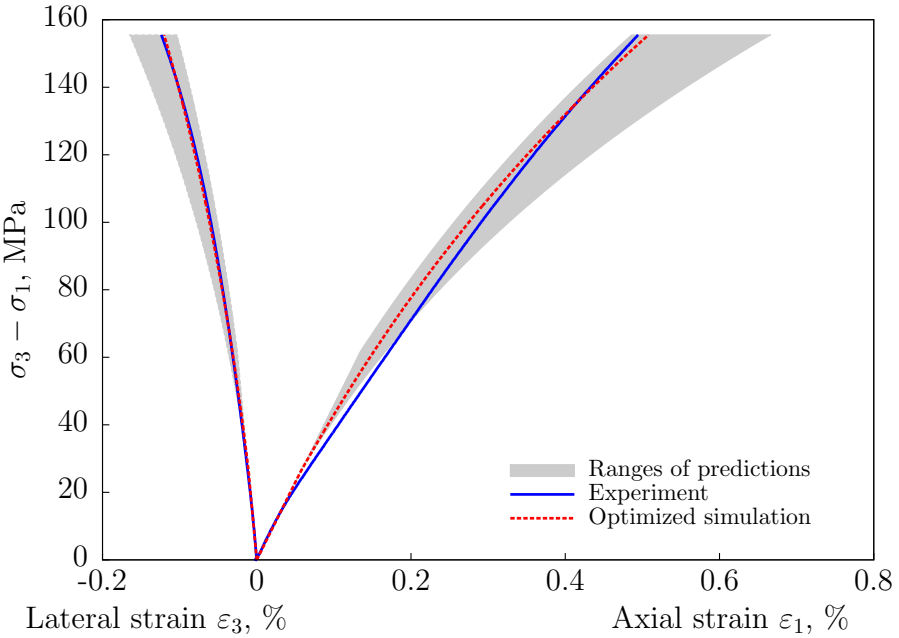

Figure 39: Calibration of the DSID model parameters against experimental stress-strain curves obtained during triaxial compression tests performed on North Dakota Bakken shale *(data: courtesy of Conocophillips)*.

Table 9: Optimal DSID parameters for shale (calibration based on the Least Square Method).

Free energy				Damage function		
a_1 $(\text{GPa})^{-1}$	a_2 $(\text{GPa})^{-1}$	a_3 $(\text{GPa})^{-1}$	a_4 $(\text{GPa})^{-1}$	C_0 MPa	C_1 MPa	α (-) -
7.35×10^{-4}	0.121	-3.15×10^{-2}	2.39×10^{-3}	0.01	1.18	0.399

3.5 Summary

3.5.1 Theoretical Continuum Damage Mechanics model

In this chapter, an approach based on Continuum Damage Mechanics (CDM) was adopted, in order to improve the prediction of rock stiffness in the damaged zone surrounding fractures. In the proposed model, called the Differential Stress Induced Damage (DSID) model, emphasis is put on the dependence of anisotropic crack propagation to differential stress, which is accounted for in the expression of the free energy of the rock solid skeleton. The DSID model allows predicting anisotropic damage and damage rotation, and distinguishes compression strength and tension strength. Contrary to existing damage models proposed for geomaterials, flow rules are derived with the energy release rate (work-conjugate to damage), which is thermodynamically consistent. The damage criterion is adapted from Drucker-Prager yield function: the criterion is expressed in terms of damage energy release rate, and a projector is used in order to distinguish between tension and compression damage thresholds. The positivity of dissipation is ensured by computing the damage rate by a non-associate flow rule. Non-elastic deformation due to damage is computed by an associate flow rule, in order to maintain the physical meaning of the model predictions. The use of a damage non-elastic deformation avoids coupling damage potentials to additional plasticity potentials. This economical formulation depends on 7 constitutive parameters only.

3.5.2 Calibration and sensitivity analysis

Laboratory tests were simulated with the DSID model at the integration point, which allowed calibrating material parameters against experimental stress-strain curves. Experimental data published on Eastern France claystone was used to analyze the performance of the DSID model with the maximum likelihood method. It was found that, for claystone subjected to triaxial stress states: (1) only one damage parameter ("a_2") is needed in the expression of the free energy to predict stress-strain curves; (2) a_2 controls the deviation of the current principal directions of stress to the principal directions of damage (which are co-axial with the cumulated deviatoric stress), which means "a_2" is dominant in the the rock behavior due to differential stress under triaxial compression; (3) model parameters

involved in the damage criterion cannot be removed from the simulation, but can be related to a_2. Therefore, the DSID model can be simplified when used for claystone under triaxial compression tests and proportional tests: the model can be formulated with only one unknown a_2, which can be viewed as the only parameter needed to model differential-stress induced damage in Eastern France claystone. The DSID model calibrated with the maximum Likelihood Method tends to underestimate lateral deformation. In order to overcome this limitation, the gradient method was employed in order to determine the optimal damage parameters for Bakken shale samples provided by *ConocoPhillips*. Calibration was performed to reproduce shale brittle deformation regime only. Results show a good match between experimental and numerical results, for both axial and lateral strain evolution.

CHAPTER IV

FINITE ELEMENT IMPLEMENTATION OF THE DSID MODEL

4.1 Short Review on the Finite Element Method (FEM)

4.1.1 Discretization in Standard FEM

In the Finite Element Method, degrees of freedom are approximated with interpolation functions. Consider an element of solid matrix of rock with 3 degrees of freedom for displacements $\mathbf{u}$. For an element with an interpolation order n for displacements

$$\begin{cases} u_x(x,y,z) = \sum_{j=1}^{n} u_x^{(j)} \psi_j^{(x)}(x,y,z) \\ u_y(x,y,z) = \sum_{j=1}^{n} u_y^{(j)} \psi_j^{(y)}(x,y,z) \\ u_z(x,y,z) = \sum_{j=1}^{n} u_z^{(j)} \psi_j^{(z)}(x,y,z) \end{cases} \tag{195}$$

in which ψ_j is the j^{th} interpolation function. The equation of equilibrium writes

$$\mathbf{K}\boldsymbol{\delta} = \mathbf{F} + \mathbf{Q} \tag{196}$$

in which $\boldsymbol{\delta}$ is the unknown vector of degrees of freedom (containing nodal displacements). $\mathbf{F}$ and $\mathbf{Q}$ are the vectors of (known) bulk and surface forces applied to the domain considered. The general form of the elementary stiffness matrix $\mathbf{K}$ is

$$\mathbf{K} = \int_{V_e} (\boldsymbol{\Psi})^T \cdot (\mathbf{D})^T \cdot \mathbf{C} \cdot \mathbf{D} \cdot \boldsymbol{\Psi} \, \mathrm{d}V \tag{197}$$

with

$$\mathbf{Q} = \int_{\mathrm{L}_e} (\boldsymbol{\Psi})^T \cdot \dot{\mathbf{t}} \, \mathrm{d}s = \left\{ \begin{array}{cccc} T_x & T_y & T_z & q_f \end{array} \right\}^T \tag{198}$$

$$\mathbf{F} = \int_{V_e} (\boldsymbol{\Psi})^T \cdot \dot{\mathbf{f}} \, \mathrm{d}V = \left\{ \begin{array}{cccc} F_x & F_y & F_z & Q \end{array} \right\}^T \tag{199}$$

$$\boldsymbol{\delta} = \left\{ \begin{array}{c} \mathbf{u}^T \end{array} \right\}^T \tag{200}$$

where $\mathbf{\Psi}$ is the interpolation function matrix

$$\mathbf{\Psi} = \begin{bmatrix} \psi_1 & 0 & 0 & \psi_2 & 0 & 0 & \psi_3 & 0 & 0 & \psi_4 & 0 & 0 \\ 0 & \psi_1 & 0 & 0 & \psi_2 & 0 & 0 & \psi_3 & 0 & 0 & \psi_4 & 0 \\ 0 & 0 & \psi_1 & 0 & 0 & \psi_2 & 0 & 0 & \psi_3 & 0 & 0 & \psi_4 \end{bmatrix} \tag{201}$$

$\mathbf{C}$ is elasticity tensor, $\mathbf{D}$ is the derivative operator.

$$\mathbf{D} = \begin{bmatrix} \frac{\partial}{\partial x} & 0 & 0 & \frac{\partial}{\partial y} & 0 & \frac{\partial}{\partial z} \\ 0 & \frac{\partial}{\partial y} & 0 & \frac{\partial}{\partial x} & \frac{\partial}{\partial z} & 0 \\ 0 & 0 & \frac{\partial}{\partial z} & 0 & \frac{\partial}{\partial y} & \frac{\partial}{\partial x} \end{bmatrix}^T \tag{202}$$

Fracturing induces discontinuity in the medium to be modeled. The Finite Element Method is a continuum-based approach, which can thus evaluate fracture evolution only indirectly. The FEM is suitable for Continuum Damage Mechanics, where the intent is not to represent the geometry of the cracks, but rather to model the effects of cracking on poroelastic and flow properties. Dissipation variables (such as damage and inelastic strains) are computed in the same way as state variables, most of the times by post-processing the updated primary variables [19]. In Linear Elastic Fracture Mechanics (LEFM), the most common approach is energetic and consists in computing energy release rates (such as Griffith crack growth energy). Energy release rates can be computed at integration points after solving for the field variables (such as stress and strain). Griffith crack growth energy can also be computed by means of contour integrals (see Eq. 20). The contour integral J is path independent but in most approaches, it is necessary to define the path through nodes. Remeshing is often required to catch the crack tip in the contour during crack propagation [194].

4.1.2 Modified Newton-Raphson Method

The DSID model presented in the previous section was implemented in a Finite Element algorithm based on the modified Newton-Raphson Method (Figure 40). It allows solving non linear algebra equations without calculating the derivative of the stiffness matrix at each iteration: instead, the initial stiffness matrix is used. Therefore, calculations with the

modified Newton-Raphson are faster than in the original method, although convergence is slower. Forces are applied in small load increments

$$F_N = \sum_{k=1}^{N} \Delta F_k \tag{203}$$

$$Q_N = \sum_{j=k}^{N} \Delta Q_k \tag{204}$$

Defining $\delta_{k,i+1}$ as the displacement for $i+1$th iteration at the kth load increment,

$$(\mathrm{d}\boldsymbol{\delta})_{k,i+1} = [\mathbf{K}_0]^{-1}\, \mathbf{r}_{k,i} \tag{205}$$

in which $\mathbf{K}_0$ is the initial stiffness matrix, and $\mathbf{r}_{k,i}$ is the residual vector at the ith iteration

$$\mathbf{r}_{k,i} = \mathbf{r}_{k,i-1} - [\mathbf{K}(\boldsymbol{\delta}_{k,i-1})]\, (\mathrm{d}\boldsymbol{\delta})_{k,i} \tag{206}$$

with

$$\mathbf{r}_{k,0} = \Delta\mathbf{F}_k + \Delta\mathbf{Q}_k \tag{207}$$

The vector of degrees of freedom is updated at each iteration, according to

$$\boldsymbol{\delta}_{k,i+1} = \boldsymbol{\delta}_{k,i} + (\mathrm{d}\boldsymbol{\delta})_{k,i+1} \tag{208}$$

A tolerance value, ε , is set to check the convergence. The criteria can be expressed as

$$\|\mathbf{r}_{k,i}\| \leq \varepsilon \tag{209}$$

When the criteria is reached, the iterative process is aborted and the vector of degrees of freedom is assigned the value $\boldsymbol{\delta}_{k,i}$, which is an approximate solution, $\boldsymbol{\delta}_k$, at the loading increment k. Then, the initial displacement at the next loading increment is $\boldsymbol{\delta}_{k+1,0} = \boldsymbol{\delta}_k$.

4.2 Finite Element Algorithm at the Material Point Level

The computational methods presented below explain the algorithm written at the material point level in order to predict damage, stress, strain and stiffness under controlled conditions of stress or strains.

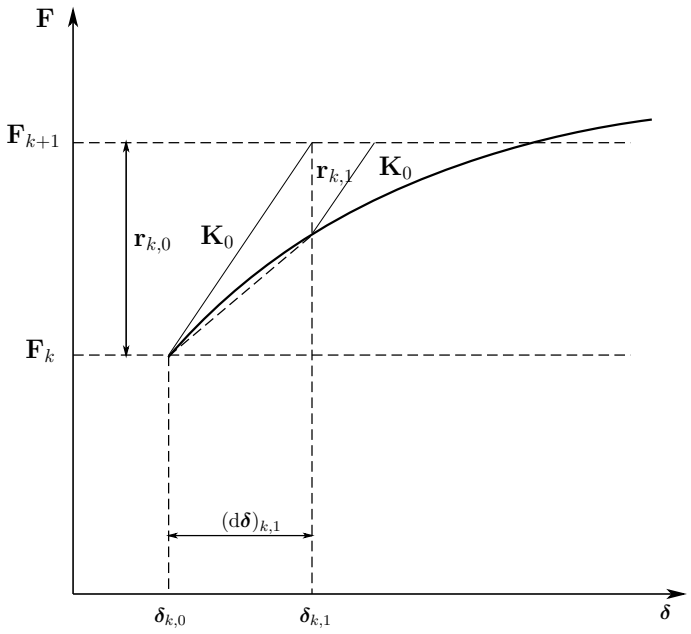

Figure 40: Modified Newton-Raphson Method.

4.2.1 Principle of the Finite Element implementation in ABAQUS UMAT

UMAT is the name given to subroutines written by ABAQUS users to use their own constitutive models. The input parameters will be given either by ABAQUS/CAE or by input files. The DSID UMAT subroutines were written in Fortran, like the other subroutines in ABAQUS. At the beginning of each UMAT subroutine, ABAQUS initializes strain, stress and other user-defined state variables calculated from the values stored at the previous iteration step $(i-1)$. Then, the strain increment $\Delta\varepsilon_{k,i}$ for the current iteration step i is computed by the ABAQUS solver and is given to UMAT as initial input. In a UMAT subroutine, the developer needs to provide the formulas to calculate the stress and other state variables for the current step, i. The general flow chart for the DSID model is illustrated in Figure 41, and the main computational steps are detailed below.

1. Initialization

   In the UMAT subroutine, ABAQUS gives the converged strain increment $\Delta\boldsymbol{\varepsilon}_{k+1} = \Delta\boldsymbol{\varepsilon}_{t+\Delta t}$ of the current iteration for the load step applied during Δt. The previous stress $\boldsymbol{\sigma}_k = \boldsymbol{\sigma}_t$, previous strain $\boldsymbol{\varepsilon}_k = \boldsymbol{\varepsilon}_t$ and the damage variable $\boldsymbol{\Omega}_k = \boldsymbol{\Omega}_t$ are already stored in the ABAQUS solver at this stage.

2. Conversion of the stored variables

   Material parameters are provided as an input by the user and are stored in the vector "PROPS(NPROPS)". Because ABAQUS stores the damage variable and other useful strain components in the "STATEV(NSTATV)" vector, the first step in the algorithm is to select the value of the variable that needs to be updated at the right location in STATEV vector. Then the selected components of STATEV are converted into tensors for each mechanical variable (damage tensor, deformation tensor).

3. Trial computations in the elastic domain

   The stress increment is updated, first assuming that the material is in the elastic domain: this allows computing the trial stress. The damaged elastic modulus is calculated with the value of damage from the previous increment

$$\Delta\boldsymbol{\sigma}_{k,i}^{tr} = \Delta\boldsymbol{\sigma}_{k,i}^{E} = \mathbb{C}_{\mathrm{e}}(\boldsymbol{\Omega}_{k,i-1}) : \Delta\boldsymbol{\varepsilon}_{k,i} \tag{210}$$

$$\boldsymbol{\sigma}_{k,i}^{tr} = \boldsymbol{\sigma}_{k,i-1} + \Delta\boldsymbol{\sigma}_{k,i}^{tr} \tag{211}$$

4. Damage test

   The damage driving force depends on the stress state

$$\mathbf{Y}_{k,i}^{tr} = \mathbf{Y}(\boldsymbol{\sigma}_{k,i}^{tr}) = a_1(\mathrm{Tr}\boldsymbol{\sigma}_{k,i}^{tr})\mathbf{I} + a_2\boldsymbol{\sigma}_{k,i}^{tr}\cdot\boldsymbol{\sigma}_{k,i}^{tr} + a_3\mathrm{Tr}(\boldsymbol{\sigma}_{k,i}^{tr})\boldsymbol{\sigma}_{k,i}^{tr} + a_4\mathrm{Tr}(\boldsymbol{\sigma}_{k,i}^{tr})\mathbf{I} \tag{212}$$

   The damage function is updated with the damage driving force, and the condition of damage propagation is checked

$$f_d^{tr}(\mathbf{Y}_{k,i}^{tr}, \boldsymbol{\Omega}_{k,i-1}) \tag{213}$$

   If $f_d < 0$, the material is still elastic, and the cumulated stress can be computed by adding the trial stress increment to the previous cumulated stress. If $f_d \geq 0$, damage propagates, and the increment of stress needs to be computed iteratively.

5. Iterative computation of stress (in the damaged domain)

Strain controlled test

In general, the damage criterion is a non-linear function of the Lagrangian multiplier. The new stress state should be updated with the current damage variable and the current strain

$$\begin{aligned}\boldsymbol{\sigma}_{k,i} &= \mathbb{C}_{e}(\boldsymbol{\Omega}_{k,i})(\boldsymbol{\varepsilon}_{k,i} - \boldsymbol{\varepsilon}^{id}_{k,i}) \\ &= \mathbb{C}_{e}(\boldsymbol{\Omega}_{k,i})(\boldsymbol{\varepsilon}_{k,i-1} + \Delta\boldsymbol{\varepsilon}_{k,i} - \boldsymbol{\varepsilon}^{id}_{k,i-1} - \Delta\boldsymbol{\varepsilon}^{id}_{k,i})\end{aligned} \tag{214}$$

The current damage is updated as

$$\begin{aligned}\boldsymbol{\Omega}_{k,i} &= \boldsymbol{\Omega}_{k,i-1} + \Delta\boldsymbol{\Omega}_{k,i} \\ &= \boldsymbol{\Omega}_{k,i-1} + \dot{\lambda}_{dk,i}\frac{\partial g_d}{\partial \mathbf{Y}}\Big|_{k,i-1} \\ &= \boldsymbol{\Omega}(\boldsymbol{\Omega}_{k,i-1}, \dot{\lambda}_{dk,i}, \mathbf{Y}_{k,i-1}) \\ &= \boldsymbol{\Omega}(\boldsymbol{\Omega}_{k,i-1}, \dot{\lambda}_{dk,i}, \mathbf{Y}(\boldsymbol{\sigma}_{k,i-1})) \\ &= \boldsymbol{\Omega}(\boldsymbol{\Omega}_{k,i-1}, \dot{\lambda}_{dk,i}, \boldsymbol{\sigma}_{k,i-1})\end{aligned} \tag{215}$$

The damaged stiffness at the current state of damage is obtained by a Taylor series expansion at the preceding state of damage

$$\begin{aligned}\mathbb{C}_{e}(\boldsymbol{\Omega}_{k,i}) &= \mathbb{C}_{e}(\boldsymbol{\Omega}_{k,i-1}) + \frac{\partial \mathbb{C}_{e}}{\partial \boldsymbol{\Omega}}\Big|_{k,i-1} : \Delta\boldsymbol{\Omega}_{k,i} \\ &= \mathbb{C}_{e}(\boldsymbol{\Omega}_{k,i-1}) + \frac{\partial \mathbb{C}_{e}}{\partial \boldsymbol{\Omega}}\Big|_{k,i-1} : \dot{\lambda}_{dk,i}\frac{\partial g_d}{\partial \mathbf{Y}}\Big|_{k,i-1}\end{aligned} \tag{216}$$

The associated flow rule gives the relation between irreversible strain and the Lagrangian multiplier

$$\Delta\boldsymbol{\varepsilon}^{id}_{k,i} = \dot{\lambda}_{dk,i}\frac{\partial f_d}{\partial \sigma}\Big|_{k,i-1} \tag{217}$$

The stress can then be related to the Lagrangian multiplier

$$\begin{aligned}
\boldsymbol{\sigma}_{k,i} &= \left[\mathbb{C}_{\mathbb{e}}(\boldsymbol{\Omega}_{k,i-1}) + \frac{\partial \mathbb{C}_{\mathbb{e}}}{\partial \boldsymbol{\Omega}}\Big|_{k,i-1} : \dot{\lambda}_{dk,i} \frac{\partial g_d}{\partial \mathbf{Y}}\Big|_{k,i-1}\right] : \left(\boldsymbol{\varepsilon}_{k,i-1} + \Delta\boldsymbol{\varepsilon}_{k,i} - \boldsymbol{\varepsilon}^{id}_{k,i-1} - \Delta\boldsymbol{\varepsilon}^{id}_{k,i}\right) \\
&= \mathbb{C}_{\mathbb{e}}(\boldsymbol{\Omega}_{k,i-1}) : \left(\boldsymbol{\varepsilon}_{k,i-1} - \boldsymbol{\varepsilon}^{id}_{k,i-1} + \Delta\boldsymbol{\varepsilon}_{k,i}\right) - \mathbb{C}_{\mathbb{e}}(\boldsymbol{\Omega}_{k,i-1}) : \Delta\boldsymbol{\varepsilon}^{id}_{k,i} \\
&\quad + \left[\dot{\lambda}_{dk,i} \frac{\partial \mathbb{C}_{\mathbb{e}}}{\partial \boldsymbol{\Omega}}\Big|_{k,i-1} : \frac{\partial g_d}{\partial \mathbf{Y}}\Big|_{k,i-1}\right] : \left(\boldsymbol{\varepsilon}_{k,i-1} + \Delta\boldsymbol{\varepsilon}_{k,i} - \boldsymbol{\varepsilon}^{id}_{k,i-1} - \Delta\boldsymbol{\varepsilon}^{id}_{k,i}\right) \\
&= \boldsymbol{\sigma}^{tr}_{k,i} - \dot{\lambda}_{dk,i} \mathbb{C}_{\mathbb{e}}(\boldsymbol{\Omega}_{k,i-1}) : \frac{\partial f_d}{\partial \boldsymbol{\sigma}}\Big|_{k,i-1} \\
&\quad + \dot{\lambda}_{dk,i} \left(\frac{\partial \mathbb{C}_{\mathbb{e}}}{\partial \boldsymbol{\Omega}} : \frac{\partial g_d}{\partial \boldsymbol{\sigma}}\right)\Big|_{k,i-1} : \left(\boldsymbol{\varepsilon}_{k,i-1} + \Delta\boldsymbol{\varepsilon}_{k,i} - \boldsymbol{\varepsilon}^{id}_{k,i-1} - \dot{\lambda}_{dk,i} \frac{\partial f_d}{\partial \boldsymbol{\sigma}}\Big|_{k,i-1}\right) \\
&= \boldsymbol{\sigma}^{tr}_{k,i} - \dot{\lambda}^{2}_{dk,i} \left(\frac{\partial \mathbb{C}_{\mathbb{e}}}{\partial \boldsymbol{\Omega}} : \frac{\partial g_d}{\partial \boldsymbol{\sigma}} : \frac{\partial f_d}{\partial \boldsymbol{\sigma}}\right)\Big|_{k,i-1} \\
&\quad - \dot{\lambda}_{dk,i} \left[\left(\mathbb{C}_{\mathbb{e}}(\boldsymbol{\Omega}) : \frac{\partial f_d}{\partial \boldsymbol{\sigma}}\right)\Big|_{k,i-1} - \left(\frac{\partial \mathbb{C}_{\mathbb{e}}}{\partial \boldsymbol{\Omega}} : \frac{\partial g_d}{\partial \boldsymbol{\sigma}}\right)\Big|_{k,i-1} : \left(\boldsymbol{\varepsilon}_{k,i-1} + \Delta\boldsymbol{\varepsilon}_{k,i} - \boldsymbol{\varepsilon}^{id}_{k,i-1}\right)\right]
\end{aligned} \tag{218}$$

From the equations above, the current stress is a non-linear function of the Lagrangian multiplier λ, and a non-linear function of the damage-driving force $\mathbf{Y}$ (equation 212). As the result, $\mathbf{Y}$ is a non-linear function of λ, and the damage function is also a non-linear function of λ

$$\begin{aligned}
f_{dk,i} &= f_d(\mathbf{Y}_{k,i}, \boldsymbol{\Omega}_{k,i}) \\
&= f_d(\mathbf{Y}(\boldsymbol{\sigma}_{k,i}), \boldsymbol{\Omega}_{k,i}) \\
&= f_d(\boldsymbol{\sigma}_{k,i}, \boldsymbol{\Omega}_{k,i}) \\
&= f_d\left(\boldsymbol{\sigma}(\boldsymbol{\sigma}_{k,i-1}, \Delta\boldsymbol{\varepsilon}_{k,i}, \boldsymbol{\Omega}_{k,i-1}, \dot{\lambda}_{dk,i}), \boldsymbol{\Omega}(\boldsymbol{\Omega}_{k,i-1}, \dot{\lambda}_{dk,i}, \boldsymbol{\sigma}_{k,i-1})\right) \\
&= f_d(\boldsymbol{\sigma}_{k,i-1}, \Delta\boldsymbol{\varepsilon}_{k,i}, \boldsymbol{\Omega}_{k,i-1}, \dot{\lambda}_{dk,i})
\end{aligned} \tag{219}$$

Stress controlled Test

In a stress-controlled test, the stress-strain relationship is given in terms of the current compliance tensor, which is the inverse of the stiffness tensor

$$\begin{aligned}
\boldsymbol{\varepsilon}_{k,i} =& \boldsymbol{\varepsilon}^{E}_{k,i} + \boldsymbol{\varepsilon}^{id}_{k,i} = \mathbb{S}(\boldsymbol{\Omega}_{k,i})\boldsymbol{\sigma}_{k,i} + \boldsymbol{\varepsilon}^{id}_{k,i} \\
&= \mathbb{S}(\boldsymbol{\Omega}_{k,i})\left[\boldsymbol{\sigma}_{k,i-1} + \Delta\boldsymbol{\sigma}_{k,i}\right] + \boldsymbol{\varepsilon}^{id}_{k,i}
\end{aligned} \tag{220}$$

The current damage is updated as

$$\begin{aligned}\boldsymbol{\Omega}_{k,i} &= \boldsymbol{\Omega}_{k,i-1} + \Delta\boldsymbol{\Omega}_{k,i} \\ &= \boldsymbol{\Omega}_{k,i-1} + \dot{\lambda}_{dk,i}\frac{\partial g_d}{\partial \mathbf{Y}}\Big|_{k,i-1} \\ &= \boldsymbol{\Omega}(\boldsymbol{\Omega}_{k,i-1}, \dot{\lambda}_{dk,i}, \boldsymbol{\sigma}_{k,i-1})\end{aligned} \tag{221}$$

The damaged compliance tensor at the current state of damage is obtained by a Taylor series expansion at the preceding state of damage

$$\begin{aligned}\mathbb{S}(\boldsymbol{\Omega}_{k,i}) &= \mathbb{S}(\boldsymbol{\Omega}_{k,i-1}) + \frac{\partial \mathbb{S}}{\partial \boldsymbol{\Omega}}\Big|_{k,i-1} : \Delta\boldsymbol{\Omega}_{k,i} \\ &= \mathbb{S}(\boldsymbol{\Omega}_{k,i-1}) + \frac{\partial \mathbb{S}}{\partial \boldsymbol{\Omega}}\Big|_{k,i-1} : \dot{\lambda}_{dk,i}\frac{\partial g_d}{\partial \mathbf{Y}}\Big|_{k,i-1}\end{aligned} \tag{222}$$

The irreversible strain is given as

$$\Delta\boldsymbol{\varepsilon}^{id}_{k,i} = \dot{\lambda}_{dk,i}\frac{\partial f_d}{\partial \sigma}\Big|_{k,i-1} \tag{223}$$

The total strain can then be updated as follows

$$\begin{aligned}\boldsymbol{\varepsilon}_{k,i} &= \mathbb{S}(\boldsymbol{\Omega}_{k,i})\left[\boldsymbol{\sigma}_{k,i-1} + \Delta\boldsymbol{\sigma}_{k,i}\right] + \boldsymbol{\varepsilon}^{id}_{k,i} \\ &= \left[\mathbb{S}(\boldsymbol{\Omega}_{k,i-1}) + \frac{\partial \mathbb{S}}{\partial \boldsymbol{\Omega}}\Big|_{k,i-1} : \dot{\lambda}_{dk,i}\frac{\partial g_d}{\partial \mathbf{Y}}\Big|_{k,i-1}\right]\left[\boldsymbol{\sigma}_{k,i-1} + \Delta\boldsymbol{\sigma}_{k,i}\right] + \dot{\lambda}_{dk,i}\frac{\partial f_d}{\partial \sigma}\Big|_{k,i-1}\end{aligned} \tag{224}$$

From the equations above, the damage function is still a non-linear function of $\dot{\lambda}_{dk,i}$

$$\begin{aligned}f_{dk,i} &= f_d(\mathbf{Y}_{k,i}, \boldsymbol{\Omega}_{k,i}) \\ &= f_d(\boldsymbol{\sigma}_{k,i-1}, \Delta\boldsymbol{\sigma}_{k,i}, \boldsymbol{\Omega}_{k,i-1}, \dot{\lambda}_{dk,i})\end{aligned} \tag{225}$$

The above function 225 is non-linear, and must be solved by a numerical procedure. The secant method iteration is used here

$$\begin{aligned}\dot{\lambda}_{dk,i,j} &= \dot{\lambda}_{dk,i,j-1} - \frac{f_d(\dot{\lambda}_{dk,i,j-1})}{\frac{\Delta f_{dk,i,j-1}}{\Delta \dot{\lambda}_{dk,i,j-1}}} \\ &= \dot{\lambda}_{dk,i,j-1} - \frac{f_d(\dot{\lambda}_{dk,i,j-1})}{\frac{f_d(\dot{\lambda}_{dk,i,j-1}) - f_d(\dot{\lambda}_{dk,i,j-2})}{\dot{\lambda}_{dk,i,j-1} - \dot{\lambda}_{dk,i,j-2}}} \\ &= \dot{\lambda}_{dk,i,j-1} - f_d(\dot{\lambda}_{dk,i,j-1})\frac{\dot{\lambda}_{dk,i,j-1} - \dot{\lambda}_{dk,i,j-2}}{f_d(\dot{\lambda}_{dk,i,j-1}) - f_d(\dot{\lambda}_{dk,i,j-2})} \\ &= \dot{\lambda}_{dk,i,j-1} - f_{dk,i,j-1}\frac{\dot{\lambda}_{dk,i,j-1} - \dot{\lambda}_{dk,i,j-2}}{f_{dk,i,j-1} - f_{dk,i,j-2}}\end{aligned} \tag{226}$$

The equation $f_d(\dot{\lambda}_{dk,i}) = 0$ is solved for $\dot{\lambda}_{dk,i}$. The numerical solution is said to be convergent if $|f_d(\dot{\lambda}_{dk,i,j})| < Tol$ (for a certain tolerance Tol). When the convergence criterion is reached, the current Lagrangian multiplier $\dot{\lambda}_{dk,i}$ is updated so as to ensure that the current stress is on the damage surface ($f_{dk,i} = 0$).

6. State Variables Update

   The current stress and the current damage variable are updated from equations 218 and 215

$$\boldsymbol{\sigma}_{k,i} = \boldsymbol{\sigma}^{tr}_{k,i} - \dot{\lambda}^{\,2}_{dk,i} \left(\frac{\partial \mathbb{C}_{\mathrm{e}}}{\partial \boldsymbol{\Omega}} : \frac{\partial g_d}{\partial \boldsymbol{\sigma}} : \frac{\partial f_d}{\partial \boldsymbol{\sigma}} \right) \Big|_{k,i-1} \tag{227}$$
$$-\dot{\lambda}_{dk,i} \left[\left(\mathbb{C}_{\mathrm{e}}(\boldsymbol{\Omega}) : \frac{\partial f_d}{\partial \boldsymbol{\sigma}} \right) \Big|_{k,i-1} + \left(\frac{\partial \mathbb{C}_{\mathrm{e}}}{\partial \boldsymbol{\Omega}} : \frac{\partial g_d}{\partial \boldsymbol{\sigma}} \right) \Big|_{k,i-1} : \left(\boldsymbol{\varepsilon}_{k,i-1} + \Delta \boldsymbol{\varepsilon}_{k,i} - \boldsymbol{\varepsilon}^{id}_{k,i-1} \right) \right]$$

$$\boldsymbol{\Omega}_{k,i} = \boldsymbol{\Omega}_{k,i-1} + \dot{\lambda}_{dk,i} \frac{\partial g_d}{\partial \mathbf{Y}} \Big|_{k,i-1} \tag{228}$$

   If using stress controlling, the total strain can then be updated following Eq. 224.

   The corresponding damage driving force is updated based on the current stress

$$\mathbf{Y}_{k,i} = \mathbf{Y}(\boldsymbol{\sigma}_{k,i}) = a_1(\mathrm{Tr}\boldsymbol{\sigma}_{k,i})\mathbf{I} + a_2\boldsymbol{\sigma}_{k,i} \cdot \boldsymbol{\sigma}_{k,i} + a_3\mathrm{Tr}(\boldsymbol{\sigma}_{k,i})\boldsymbol{\sigma}_{k,i} + a_4\mathrm{Tr}(\boldsymbol{\sigma}_{k,i})\mathbf{I} \tag{229}$$

7. Storage of updated variables

   Updated variables are stored in the ABAQUS solver in the form of vectors (instead of tensors), so that they can be used in the post-processing stage for each load increment.

8. Update of the Jacobian matrix

   The Jacobian matrix DDSDDE used in UMAT subroutine provides an approximate stiffness matrix in the algorithm: the elastic stiffness $\mathbb{C}_0$ is used in the Modified Newton-Raphson Method - with a constant stiffness matrix in the entire resolution algorithm. In order to accelerate the convergence, the damaged stiffness $\mathbb{C}_{\mathrm{e}}(\boldsymbol{\Omega})$ is used: it is updated at each increment.

Table 10 lists the algorithms used in different models, such as elasto-plasticity models in classical FEM algorithms, the THHMD model implemented in Θ-Stock Finite Element program [16], and the DSID model in ABAQUS.

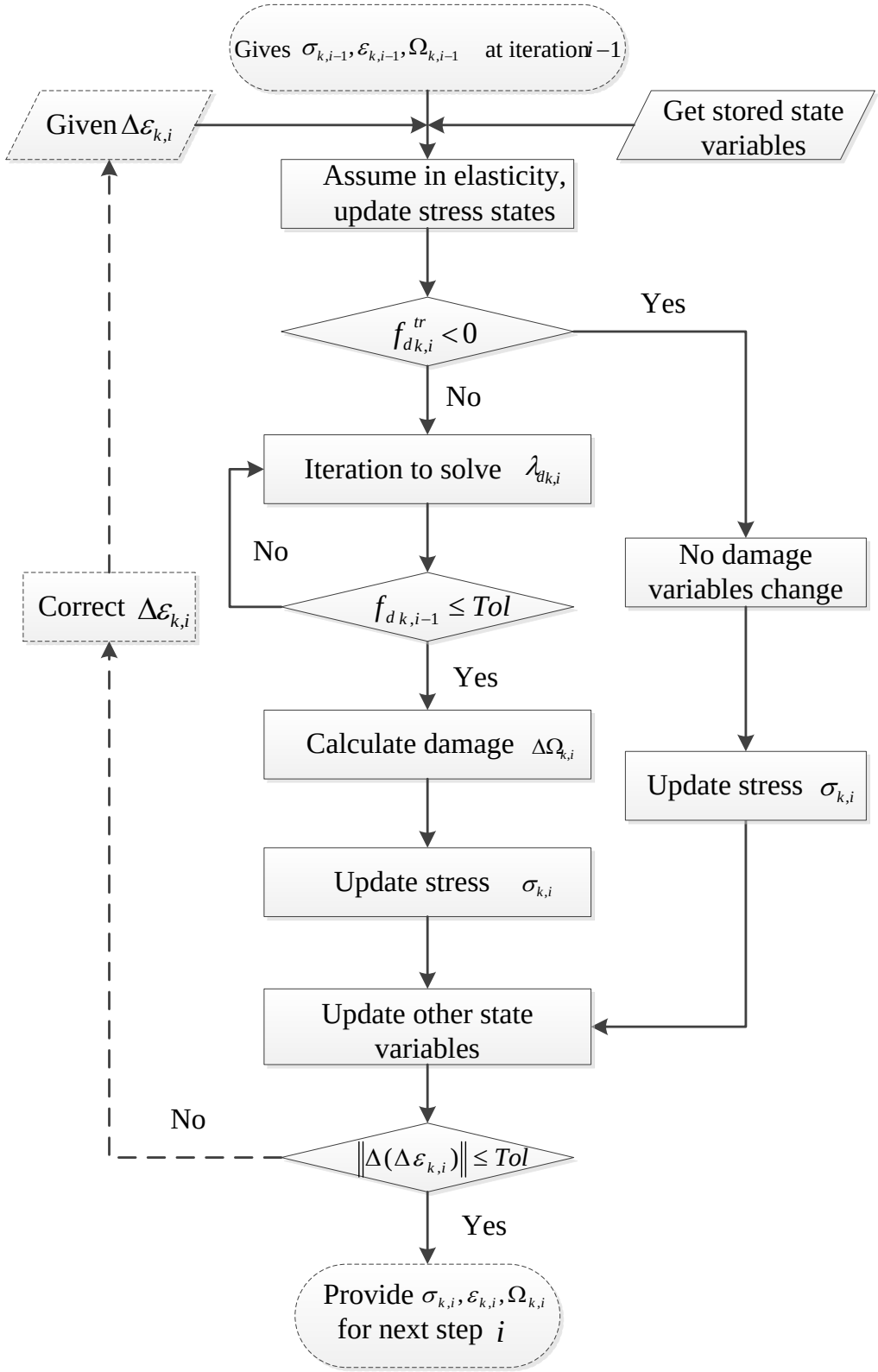

Figure 41: Computational method of the UMAT subroutine implemented in ABAQUS for the DSID model. Solid lines represent computational steps controlled by the programs written in UMAT for this research project. Dashed lines represent computational steps controlled by built-in subroutines of ABAQUS.

Table 10: Algorithms

Steps	Elasto-plasticity	THHMD	DSID
1. "Trial stress"	$\sigma_{k,i}^{tr} = \sigma_{k,i-1} + \Delta\sigma_{k,i}^{tr}$	$\mathbf{Y}_{d1\,k,i}^{+\,tr} = \mathbf{Y}_{d1\,k,i-1}^{+} + \Delta\mathbf{Y}_{d1\,k,i}^{+\,e}$	$\boldsymbol{\sigma}_{k,i}^{tr} = \boldsymbol{\sigma}_{k,i-1} + \Delta\sigma_{k,i}$ $\mathbf{Y}_{k,i}^{tr} = \mathbf{Y}(\boldsymbol{\sigma}_{k,i}^{tr}) = a_1(\mathrm{Tr}\boldsymbol{\sigma}_{k,i}^{tr})\mathbf{I} + a_2\boldsymbol{\sigma}_{k,i}^{tr}\cdot\boldsymbol{\sigma}_{k,i}^{tr}$ $+a_3\mathrm{Tr}(\boldsymbol{\sigma}_{k,i}^{tr})\boldsymbol{\sigma}_{k,i}^{tr} + a_4\mathrm{Tr}(\boldsymbol{\sigma}_{k,i}^{tr})\mathbf{I}$
2. Yield condition	$f_{p\,k,i}^{\;tr} = f_p(\sigma_{k,i}^{tr}, \varepsilon_{k,i-1}^{p})$	$f_{d\,k,i}^{\;tr} = f_d(\mathbf{Y}_{d1\,k,i}^{+\,tr}, \boldsymbol{\Omega}_{k,i-1})$	$f_{d\,k,i}^{\;tr} = f_d(\mathbf{Y}_{k,i}^{tr}, \boldsymbol{\Omega}_{k,i-1})$
3. "Stresses"	$\sigma_{k,i} = \sigma_{k,i-1} + r_{p\,k,i}\mathrm{d}\sigma_{k,i} + \mathrm{d}\sigma_{k,i}^{p}$	$\mathbf{Y}_{d1\,k,i}^{+} = \mathbf{Y}_{d1\,k,i-1}^{+} + r_{d\,k,i}\mathrm{d}\mathbf{Y}_{d1\,k,i}^{+\,tr} + \mathrm{d}\mathbf{Y}_{d1\,k,i}^{+\,d}$ $r_{d\,k,i}^{(1)} = -\frac{f_{d\,k,i-1}}{f_{d\,k,i}^{\;tr} - f_{d\,k,i-1}}$ $r_{d\,k,i}^{(2)} = r_{d\,k,i}^{(1)} - \frac{\partial f_{d\,k,i}^{(2)}}{\partial \mathbf{Y}_{d1}^{+}} \cdot \mathrm{d}\mathbf{Y}_{d1\,k,i}^{+\,e}$	$f_{d\,k,i} = f_d(\mathbf{Y}_{k,i}, \boldsymbol{\Omega}_{k,i})$ $= f_d(\boldsymbol{\sigma}_{k,i-1}, \boldsymbol{\Omega}_{k,i-1}, \dot{\lambda}_{d\,k,i})$
4. Iteration	Goal: $f_{p\,k,i} < Tol$ $\dot{\lambda}_{d\,k,i,j} = \dot{\lambda}_{d\,k,i,j-1} - \frac{f_p}{\frac{\partial f_p}{\partial \dot{\lambda}}}\vert_{\dot{\lambda}_{d\,k,i,j-1}}$	$\Delta(\mathrm{d}\mathbf{Y}_{d1\,k,i}^{+\,d}) = \boldsymbol{\Omega}_{YY\,k,i}^{-1} : \Psi_{d\,k,i,j-1}$ $\Psi_{d\,k,i,j} = \Psi_{d\,k,i,j} - \Delta(\mathrm{d}\mathbf{Y}_{d1}^{+\,d})_{k,i,j}$ $\mathrm{d}\mathbf{Y}_{d1\,k,i,j}^{+\,d} = \mathrm{d}\mathbf{Y}_{d1\,k,i,j-1}^{+\,d} - \Delta(\mathrm{d}\mathbf{Y}_{d1}^{+\,d})_{k,i,j}$	Goal: $f_{d\,k,i} < Tol$ $\dot{\lambda}_{d\,k,i,j} =$ $\dot{\lambda}_{d\,k,i,j-1} - f_{d\,k,i,j-1}\frac{\dot{\lambda}_{d\,k,i,j} - \dot{\lambda}_{d\,k,i,j-1}}{f_{d\,k,i,j} - f_{d\,k,i,j-1}}$
5. Correction	$\sigma_{k,i} = \sigma_{k,i}^{tr} - \mathrm{d}\sigma_{k,i}^{c}$ $\mathrm{d}\sigma_{k,i}^{c} = \dot{\lambda}_{d\,k,i}\boldsymbol{\Omega}_e\frac{\partial g_d}{\partial \sigma}$	$\mathbf{Y}_{d1\,k,i}^{+} = \mathbf{Y}_{d1\,k,i-1}^{+} + \mathrm{d}\mathbf{Y}_{d1\,k,i}^{+\,c}$ $\mathrm{d}\mathbf{Y}_{d1\,k,i}^{+\,c} = -\frac{\partial f_{d\,k,i}^{(3)}}{\partial \mathbf{Y}_{d1}^{+}} \frac{f_{d\,k,i}^{(3)}}{(\frac{\partial f_{d\,k,i}^{(3)}}{\partial \mathbf{Y}_{d1}^{+}})\cdot(\frac{\partial f_{d\,k,i}^{(3)}}{\partial \mathbf{Y}_{d1}^{+}})}$	$\boldsymbol{\sigma}_{k,i} = \boldsymbol{\sigma}(\dot{\lambda}_{d\,k,i}, \boldsymbol{\sigma}_{k,i-1}, \boldsymbol{\Omega}_{k,i})$ $= \boldsymbol{\sigma}_{k,i}^{tr} - \Delta\boldsymbol{\sigma}_{k,i}^{c}$ $\Delta\sigma_{k,i}^{c} = \dot{\lambda}_{d\,k,i}\boldsymbol{\Omega}_e(\boldsymbol{\Omega}_{k,i-1})\frac{\partial g_d}{\partial \sigma}$

4.3 Summary

The DSID model was implemented in *ABAQUS* Finite Element software. The main algorithm to solve the set of governing equations was presented in this chapter. The main difference between the return-mapping algorithm employed for the DSID model and that of classical plasticity models is that the damage multiplier is coupled to two dissipation variables: damage and irreversible deformation. Computing the damage multiplier requires solving a non-linear incremental equation. The resolution algorithm is based on the modified Newton-Raphson Method, in which the stiffness matrix is updated at each iteration to accelerate convergence.

CHAPTER V

SIMULATIONS

5.1 Simulation of Laboratory Tests at the Material Point

Simulations were first performed with a MATLAB program computing stress and damage at the material point. The purpose of the following simulations is to illustrate the ability of the proposed model to capture essential features of damaged rock behavior. The loading paths simulated are described below. Note that in the following sketches, the soil mechanics sign convention is adopted (i.e. tension counted negative, compression counted positive). The values of material parameters (in Tab. 11) are taken from the work of Shao et al. [238], who calibrated their model for granite rock. The damage model proposed herein is different, so the simulation results are not expected to be the same as in [238]: results presented in this subsection are used as a parametric study.

Table 11: Parameters used in the simulations with the proposed damage model.

E_0	ν_0	a_1	a_2	a_3	a_4	α	C_0	C_1
		$\times 10^{-4}$	$\times 10^{-4}$	$\times 10^{-4}$	$\times 10^{-4}$			
GPa	-	GPa^{-1}	GPa^{-1}	GPa^{-1}	GPa^{-1}	-	MPa	MPa
68	0.21	1.2565	393.71	-12.565	2.513	0.2309	0.001	0.55

5.1.1 Uniaxial Tension

The uniaxial tension test starts with a uniaxial tensile strain imposed on top and bottom of the element (Fig. 42(a)). Then the strain is released to simulate unloading (Fig. 42(b)). According to the assumptions made in the proposed model, horizontal cracks will open due to tensile strain (Fig. 42(a)). Then during the unloading process, the crack is expected to close – but not completely, since irreversible damage-induced deformation is expected. At the end of the test, the top and bottom surfaces will indeed be free of stress but with residual strain due to crack opening (Fig. 42(b)).

In the simulated uniaxial tension test, a strain is applied by increments in direction 1

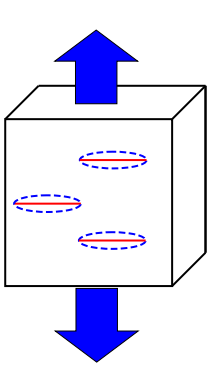

(a) Axial tension loading (O→B)

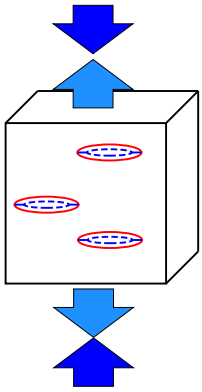

(b) Axial unloading (B→C)

Figure 42: Stress path simulated in MATLAB for the uniaxial tension test

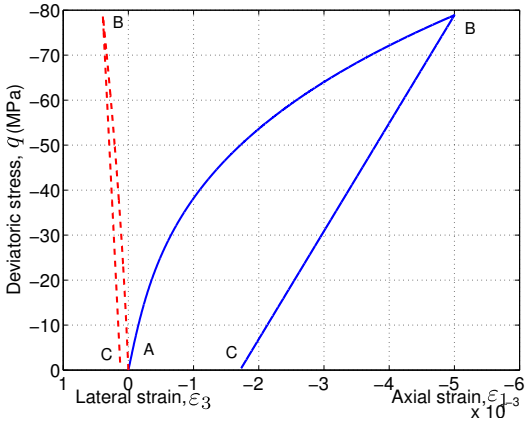

(a) Deviatoric stress versus axial strains.

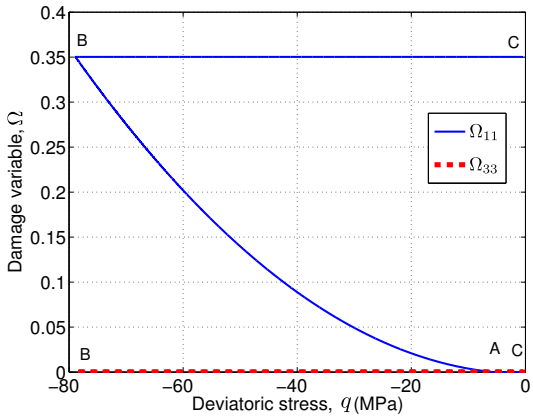

(b) Evolution of Damage with Deviatoric Stress.

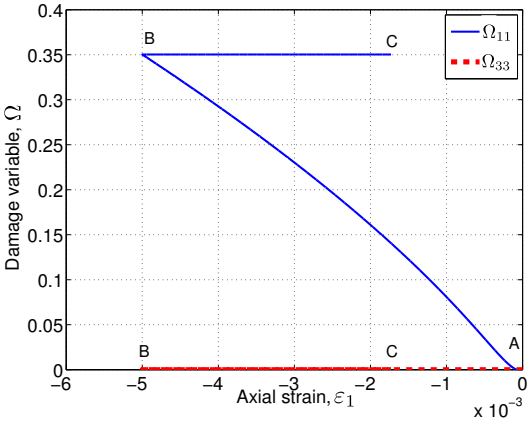

(c) Damage evolution with axial strain ε_1.

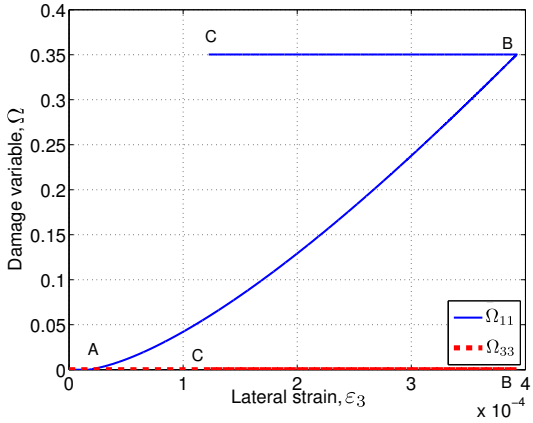

(d) Damage evolution with lateral strain ε_3.

Figure 43: Simulations results of Uniaxial Tension Test.

(negative with the soil mechanics sign convention, up to $\varepsilon_1 = -0.5\%$). It is expected to get damage only in planes perpendicular to direction 1 ($\Omega_{11} > 0$), while irreversible strains should be tension deformation in direction 1 ($\varepsilon_1^{ir} < 0$) and compression deformation in directions 2 and 3 ($\varepsilon_2^{ir} = \varepsilon_3^{ir} > 0$). Fig. 43(a)-43(d) illustrate the results obtained: OA is the tension path in the elastic domain, and AB is the non-elastic tension phase (cracks propagate). The unloading phase BC, when ε_1 is relaxed, is also simulated. The model predicts that the damaged stiffness of the material will be less than the original stiffness (Fig. 43(a)), which proves that damage occurred (Fig. 43(b)). It can also be noticed that relaxing deformation is not sufficient to release the tension stress originated by the strain imposed to the sample during the test. The residual tension stress observed after unloading proves that some irreversible deformation developed during the test: tensile deformation in direction 1, and compression deformation in direction 3. The maximum tension stress during the test is -78.9 MPa, which corresponds to the maximum strain imposed in direction 1 (-0.5%). For this state of stress, lateral deformation (in directions 2 and 3) amounts to 0.04%. Fig. 43(c) & 43(d) show the relation between damage and deformation. As the strain in direction 1 is increased, cracks in planes perpendicular to direction 1 propagate: correspondingly, damage accumulates in direction 1 (up to $\Omega_{11} = 35\%$). Then Ω_1 remains constant during the unloading phase. In addition, no lateral damage occurs during the test: $\Omega_{22} = \Omega_{33} = 0$.

5.1.2 Triaxial Compression

Under triaxial compression, damage propagates due to differential stress. If there were some friction between the sample and the loading frame, damage would initiate in the form of shear cracks. In this material point simulation however, boundary effects are not represented, and it is assumed that damage in compression initiates in the form of mode I Griffith cracks (parallel to the loading axis): this is what is modeled as "crossing effects" in the DSID model. The loading phases in the triaxial compression simulation are: (1) isotropic compression (confining phase), (2) strain-controlled axial compression at constant confining pressure, (3) unloading. The main steps are illustrated in Fig. 44.

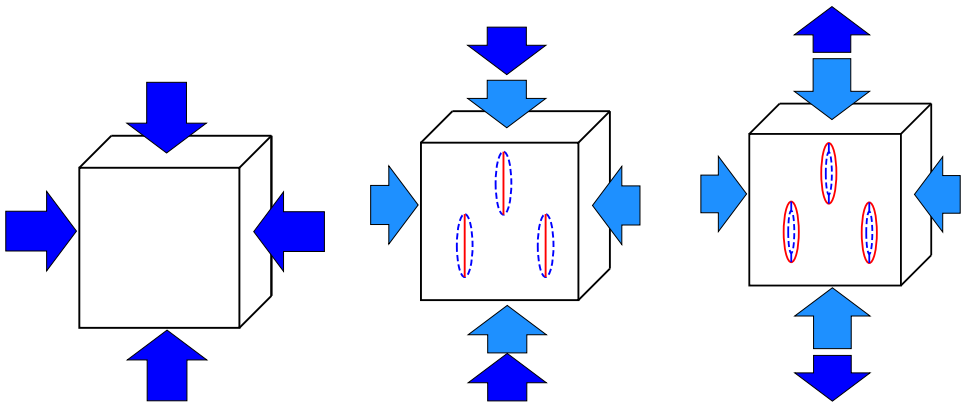

(a) Isotropic compression (O→A) (b) Axial loading (A→C) (c) Axial unloading (C→D)

Figure 44: Stress path simulated for the triaxial compression test.

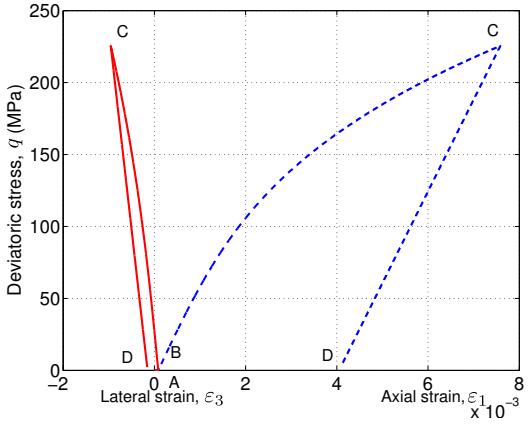

(a) Deviatoric stress versus axial strains.

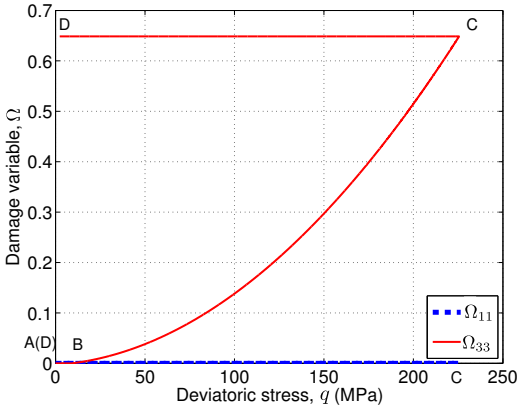

(b) Evolution of Damage with Deviatoric Stress.

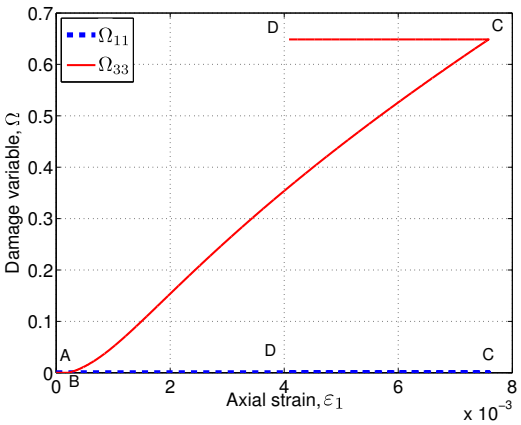

(c) Damage evolution with axial strain ε_1.

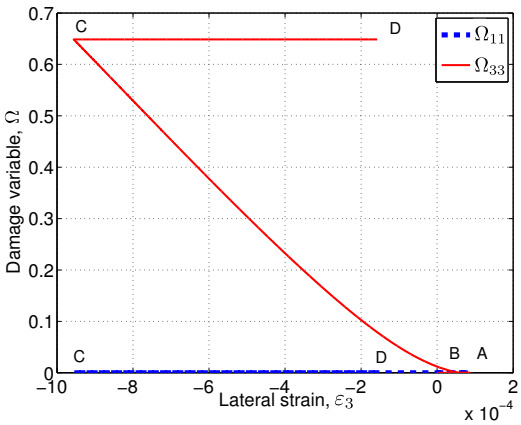

(d) Damage evolution with lateral strain ε_3.

Figure 45: Simulations results of Triaxial Compression Test.

Results obtained for the triaxial compression test are shown in Fig. 45(a)-45(d). The first loading stage (OA) consists in imposing an isotropic confining pressure of 10MPa. In a second stage, strain in direction 1 is increased by increments (positive with the soil mechanics sign convention, up to 0.75%), while stress in directions 2 and 3 is maintained constant ($\dot{\sigma}_2 = \dot{\sigma}_3 = 0$). The increase of strain in direction 1 will thus cause an increase of deviatoric stress $\dot{\sigma}_1 - \dot{\sigma}_3 \neq 0$: AB represents the elastic loading path, while BC is the non-elastic loading path (when cracks propagate). The unloading phase (CD), when ε_1 is relaxed, is also simulated. It is expected to get damage only in planes perpendicular to directions 2 and 3 ($\Omega_{22} = \Omega_{33} > 0$), while irreversible strains should be compression deformation in direction 1 ($\varepsilon_1^{ir} > 0$) and tension deformation in directions 2 and 3 ($\varepsilon_2^{ir} = \varepsilon_3^{ir} < 0$).

The model predicts that the damaged stiffness of the material will be less than the original stiffness (Fig. 45(a)), which proves that damage occurred (Fig. 45(b)). It can also be noticed that relaxing deformation is not sufficient to release the compression stress originated by the strain imposed to the sample during the test. Despite the important compression strain imposed in direction 1 (0.75%) the irreversible deformation that develops during the triaxial compression test is much less than the irreversible deformation predicted for the uniaxial compression test. It may be due to an inappropriate calibration of the model parameters. The maximum deviatoric stress during the test is 235 MPa (i.e. a total compression of 245MPa in direction 1). This corresponds to the maximum strain imposed in direction 1 (0.75%). Fig. 45(c) & 45(d) show the relation between damage and deformation. As the strain in direction 1 is increased, cracks in planes perpendicular to directions 2 and 3 propagate: correspondingly, damage accumulates in directions 2 and 3 (up to $\Omega_{22} = \Omega_{33} = 65\%$). Then $\Omega_{22} = \Omega_{33}$ remains constant during the isotropic compression and unloading phases (horizontal lines on the plots). In fact damage is generated when the lateral surface of the sample is subjected to compression stress, but lateral strains change from compression deformation (OA) to tension deformation (AC) (Fig. 45(a)). No damage occurs in the vertical direction during the test.

5.1.3 Effects of the Confining Pressure

Confinement delays the occurrence of damage. Fig. 46 shows that during a strain-controlled triaxial compression test, the damage threshold is reached for a higher deviatoric stress when the confining stress increases. For lower confining stress, damage occurs at a smaller deviatoric stress, the cumulated damage is less, and the lateral residual strain is higher . The simulation results obtained with the parameters suggested by Shao [238] show that the proposed model captures qualitatively the most important features of damaged rock behavior under differential stress. The values of parameters a_1, a_2, a_3 and a_4 may be adjusted to brittle or ductile responses. A parametric study on a_1 is shown in Fig. 47 for the triaxial compression test under 10 MPa of confining stress (with the values of a_2, a_3 and a_4 reported in Tab. 11). Decreasing the value of parameter a_1 tends to increase lateral expansion due to residual crack openings, which could be appropriate for a more ductile rock.

5.2 Finite Element simulation of laboratory tests

A UMAT subroutine was written in order to use the DSID model in ABAQUS Finite Element software. Triaxial compression tests were simulated at the scale of the whole core and at the scale of a standard plug sample, in two stages: first, an isotropic confining stress of 4,000 psi was applied on the top, bottom and lateral boundaries of the domain; second, the top and bottom boundaries were subjected to an axial displacement of equal magnitude (given in the following sections), under constant lateral confining stress. The simulations presented below aim to study the effects of sample size, intrinsic anisotropy and initial delamination planes on the overall mechanical response of shale under states of differential stress. All the simulations were conducted with the optimum set of parameters reported in Table 9, with hexahedral linear elements (each element had 8 integration points). Both the rock specimen and the metal platens at the top and bottom of the sample were modeled with the FEM. At the interface between the rock sample and the metal platens, normal and tangential displacements were constrained by a normal non-penetration condition and a friction law (Figure 48). Before the critical shear stress limit line is reached, the surfaces

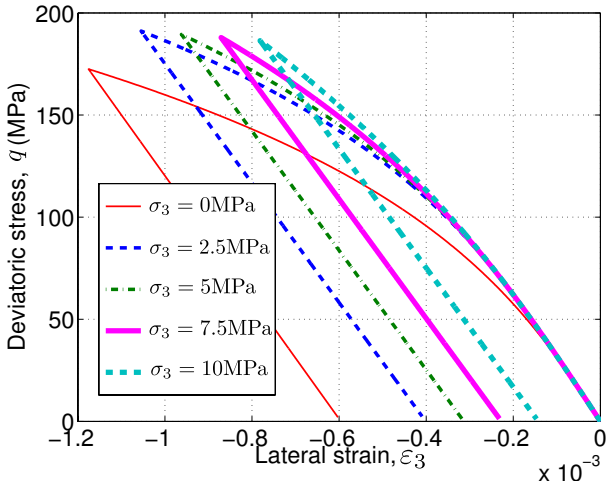

(a) Deviatoric stress versus lateral strain ε_3 (set to 0 after applying the confining stress).

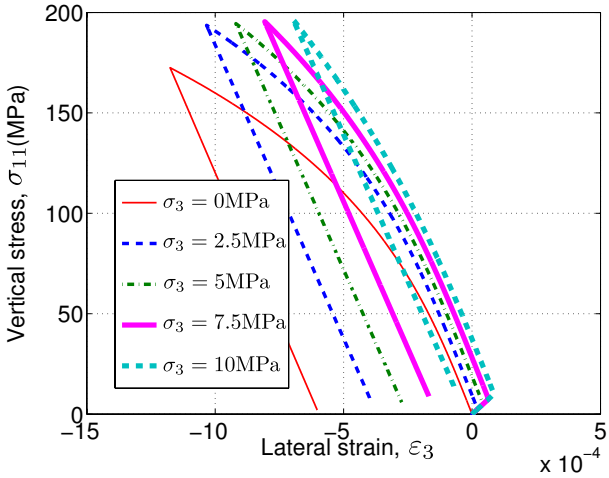

(b) Vertical stress versus lateral strain ε_3.

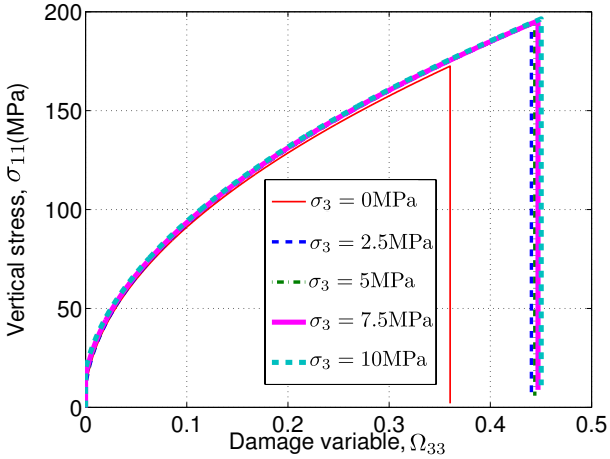

(c) Vertical stress versus damage variable Ω_{33}.

Figure 46: Triaxial compression Tests with different confining stresses.

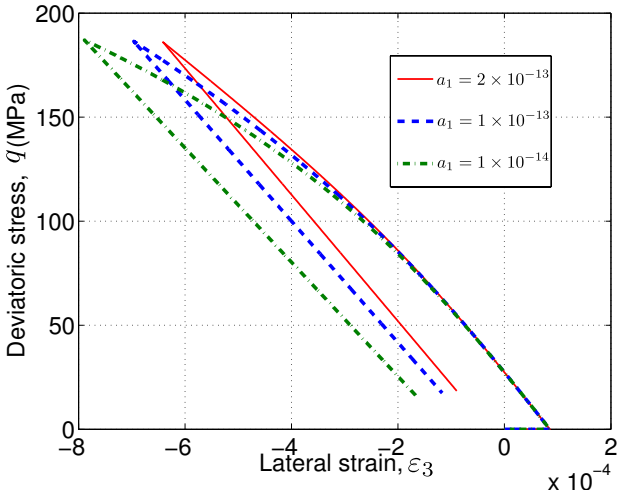

(a) Deviatoric stress versus lateral strain ε_3.

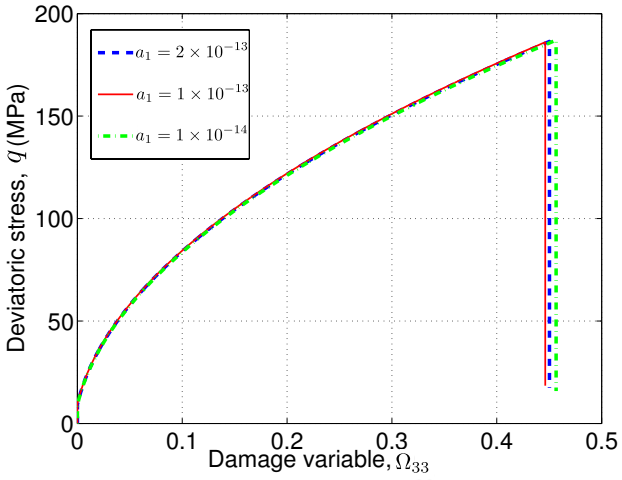

(b) Deviatoric stress versus damage variable Ω_{33}.

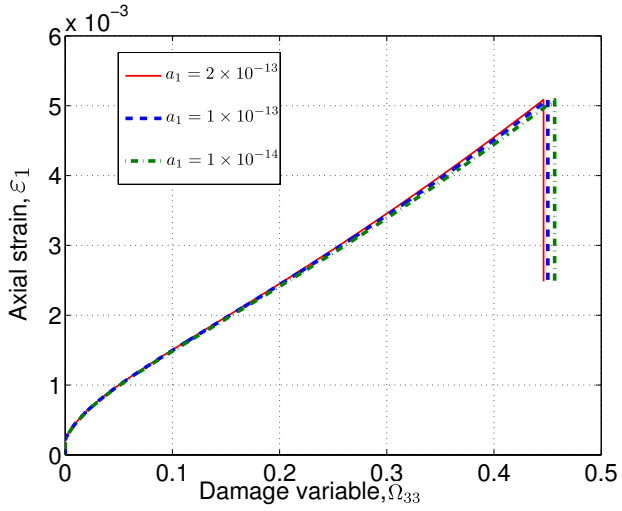

(c) Damage evolution with axial strains ε_1.

Figure 47: Triaxial compression Tests with different values of a_1.

are fully bonded. If the equivalent shear stress exceeds the critical line, the surfaces start to slide. The equivalent shear stress is computed as

$$\overline{\tau} = \sqrt{\sum_{i=1}^{n} \tau_i^2} \tag{230}$$

For the rock/metal contact, a friction coefficient $\mu = 0.8$ was adopted.

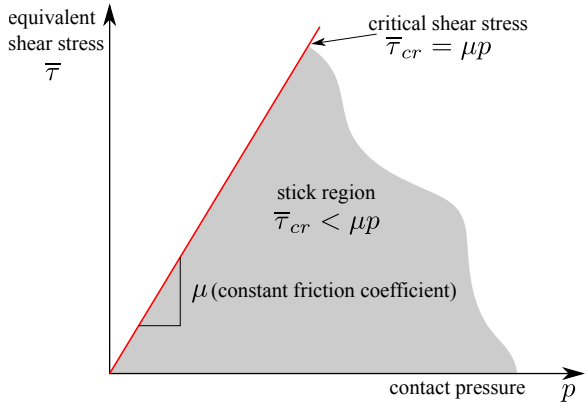

Figure 48: Friction law governing the sliding mechanism between surfaces in contact. Modified from [1].

5.2.1 Effect of sample size on stress concentrations and damage localization

Cylindric samples of two different sizes (Figure 49), placed between two metal platens, were considered to simulate a triaxial compression test conducted under 4,000 psi confining stress:

- The standard size recommended by the American Society for Testing and Materials (ASTM) for plug tests: 1 inch (25.4 mm) in diameter and 2 inch (50.8 mm) in height;
- A portion of whole core: 4 inch in diameter and 6 inch in height.

In order to focus the comparison on sample size effects, both the plug test and the core test were simulated with Finite Elements of the same size: $2.5 \times 2.5 \times 2.5$ mm. 2,200 elements were used to model the plug, and 93,208 elements were used to model the whole core.

Figures 50-52 show the vertical stress σ_{11} concentration and horizontal damage (representing vertical micro-cracks) at the edges of the contact surfaces between the platens and

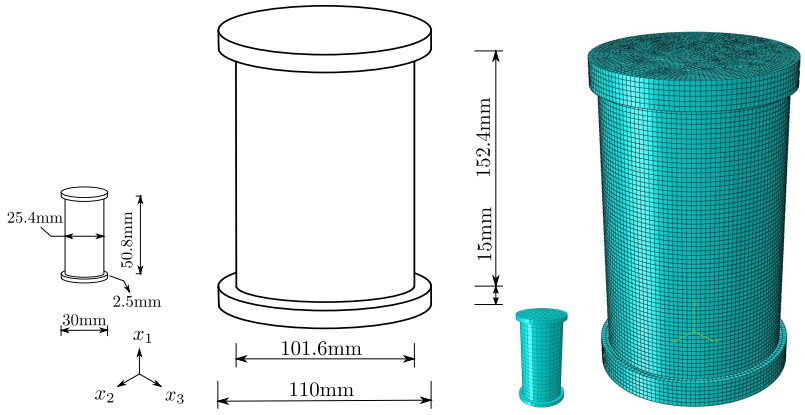

Figure 49: Sizes of the sample modeled with the FEM: the left sketch represents the standard plug test, in which the sample is assumed to be 25.4×50.8 mm (1×2 inch); the right sketch represents a portion of a whole core, with dimensions 101.6×152.4 mm (4×6 inch). The figure on the right shows the mesh adopted in the simulations.

the rock specimen. Stress decreases gradually from the edges to the center of the contact surface. Boundary effects decrease from the platens to the center of the sample (Figures 50-51), whereas damage (Figure 52) concentrates in the corners of the sample. For the two sample sizes tested, the vertical stress distribution is not uniform. Stress in elements located in the middle of the sample is not equal to the stress applied at the boundary. Stress components in the other directions (not shown here) also exhibits a heterogeneous (i.e., non uniform) and anisotropic (i.e. directionally variant) distribution in the sample.

In order to assess the boundary effects noted above, the stress-strain curve computed in a central element of the mesh was compared to the stress-strain curve obtained numerically with the MATLAB code written to simulate one-element tests. The one-element test corresponds to ideal conditions - with no edge effects. Figure 53 shows the axial loading phase of the triaxial compression test, for the one-element simulation and for the two Finite Element models described in Figure 49. Note that for consistency, the strains at the end of the confining stage were subtracted from the cumulated strains, which explains why the plots start at zero strains in Figure 53. As expected, simulation results obtained with the FEM show some deviation from the ideal stress-strain curve predicted in the one-element simulation. Despite stress heterogeneity in the sample due to edge effects (<10% variability in the plug test; <5% for the core size in axial strain, and >10% for the core size in lateral strain)

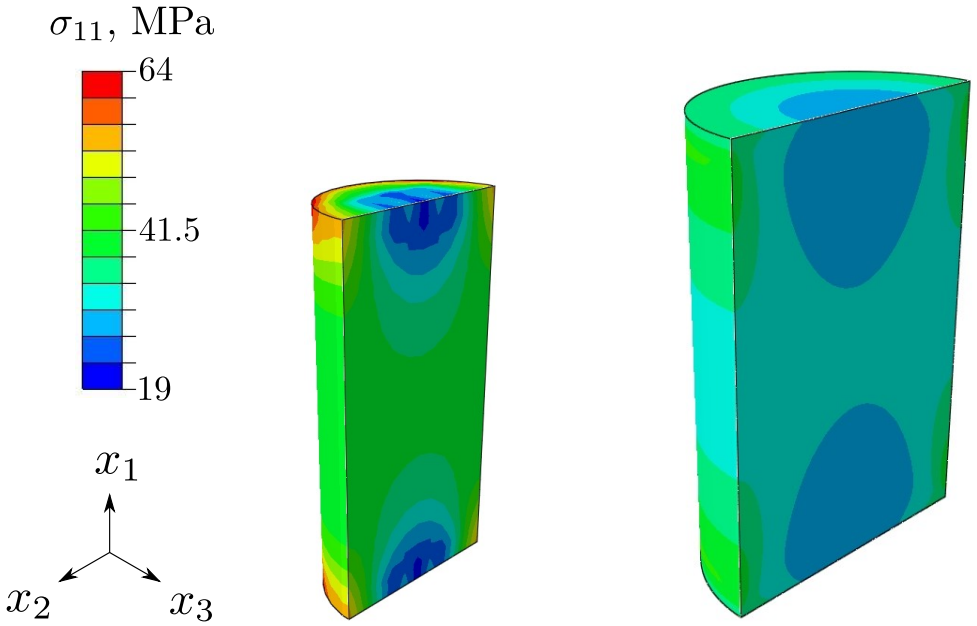

(a) Standard plug test (b) Core sample

Figure 50: Vertical stress distribution in the plug and in the whole core sample after the confining phase (4,000 psi).

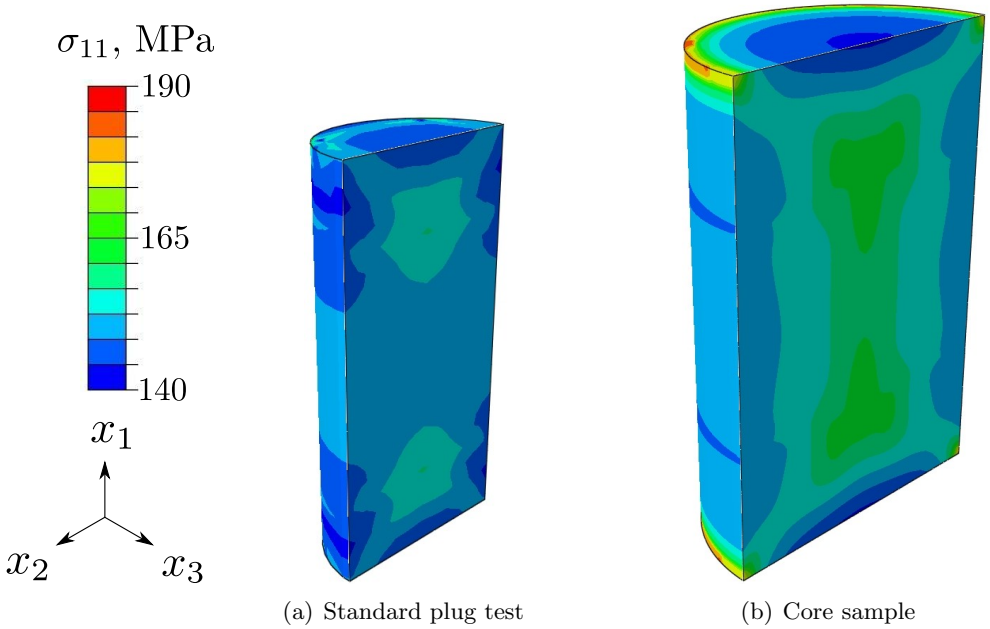

(a) Standard plug test (b) Core sample

Figure 51: Vertical stress distribution in the plug and in the whole core sample after the axial loading phase (confining stress of 4,000 psi).

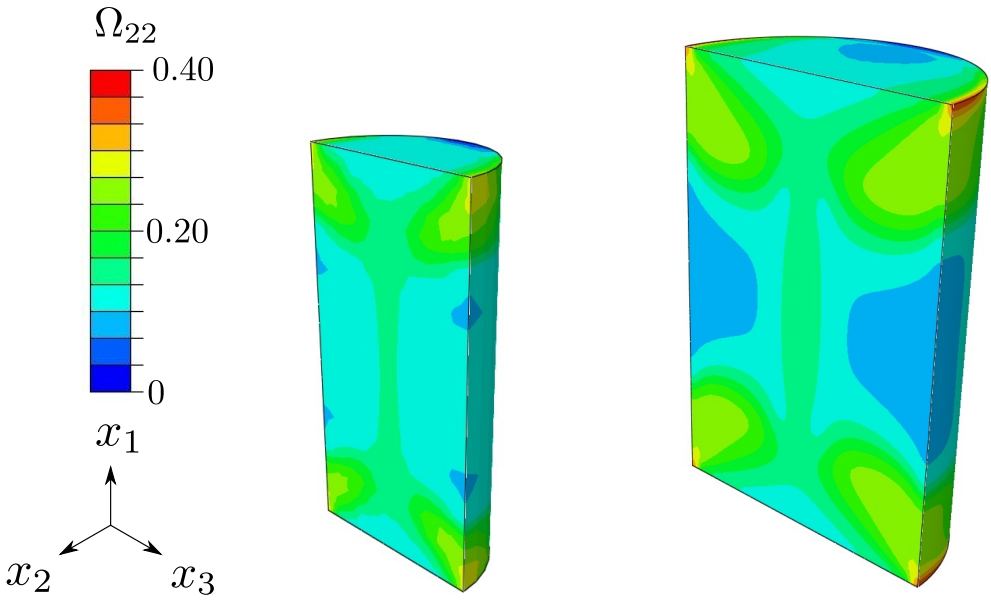

(a) Standard plug test (b) Core sample

Figure 52: Horizontal damage distribution (i.e. distribution of vertical cracks) in the plug and in the whole core sample, after the axial loading phase (confining stress of 4,000 psi).

stress-strain curves obtained in individual Finite Elements are similar to the ones obtained at the material point with MATLAB. Higher heterogeneity and stress concentration was noted in the whole core sample, because simulations involved the same element size but a larger domain than in the plug test. Consequently, higher departure from the reference one-element test is noted in the results obtained for the whole core sample test than for the plug test, especially for the radial strains. The pattern of stress observed within the whole core sample is a main departure from uniformity assumption required for property calibrations, and should be considered when calibrating to lab and field tests. Overall, edge effects do not appear to significantly affect the overall constitutive response of elements in the model, and the finite element simulations are considered acceptable at both scales. These findings suggest that for the quasi-linear elastic deformation stage (zone I, Figure 17), the single-element calibrated material model is suitably scalable to larger geometric configurations in order to predict stress concentrations and damage localization.

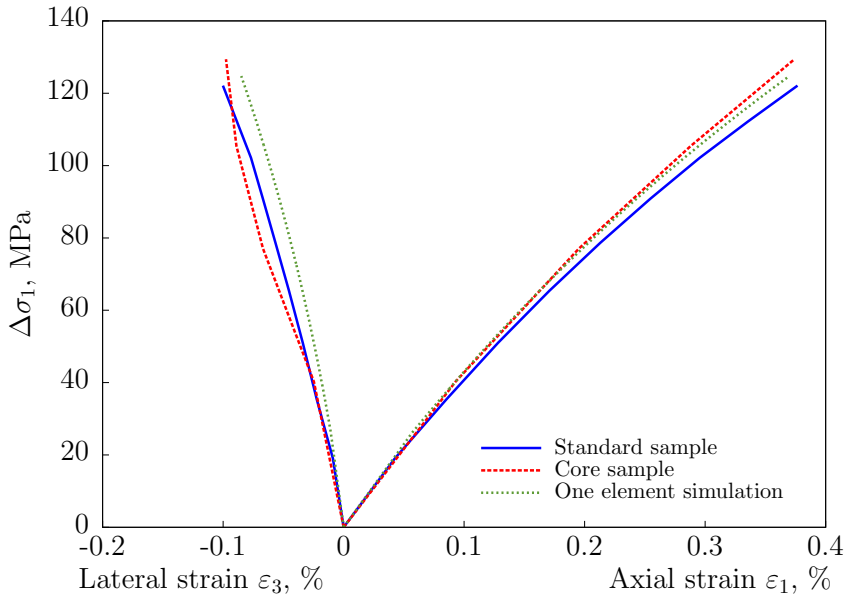

Figure 53: Stress-strain curve obtained numerically with MATLAB (for the ideal one-element test with no edge effects) and with ABAQUS (for a central element of the mesh), for a triaxial compression test performed under 4,000 psi confining pressure.

5.2.2 Effect of initial anisotropy on stress-induced anisotropy

Due to sedimentary deposition, shale is naturally anisotropic. The DSID model can be used to account for initial anisotropy (existing prior to loading), and for stress-induced anisotropy (due to damage propagation in the three directions of space). Note that in the following, $\Omega = 0$ refers to intact rock and $\Omega = 1$ refers to a state of pervasive microcracking. The current version of the DSID model is limited to pervasive microcracking with no crack coalescence (zone I in Figure 17); therefore, the DSID model cannot be used to predict full weakening (zero strength). The triaxial compression test described above was simulated for a plug 1 inch in diameter, and 2 inches in height, for the following initial damage conditions:

- No initial damage: the sample is initially homogeneous and isotropic ($\Omega_{11} = \Omega_{22} = \Omega_{33} = 0$), where direction 1 is vertical and directions 2 and 3 are in the horizontal plane;
- Initial damage in the lateral directions ($\Omega_{11} = 0$, $\Omega_{22} = \Omega_{33} = 0.1$), this condition represents natural microcracking damage (vertical cracks), due to tectonic loading, or

uplift for instance;

- Initial damage in the vertical direction ($\Omega_{11} = 0.1$, $\Omega_{22} = \Omega_{33} = 0$), this condition represents bedding delamination planes (horizontal cracks).

In the second loading phase, a vertical strain of 0.8% was applied. The ratio between the vertical elastic modulus and horizontal elastic modulus is used as an anisotropy index

$$\alpha = \frac{E_1}{E_3} \tag{231}$$

Figure 54 illustrates the evolution of stiffness anisotropy for an element with no initial damage, i.e., initially isotropic. Isotropic materials have an elastic anisotropy index of $\alpha = 1$ at the beginning of the axial loading stage. Damage propagates as differential stress increases, which results in a decrease of the elastic moduli. However, vertical microcracks are more prone to open during the axial loading, so that the horizontal Young's moduli E_2 and E_3 decrease faster than the vertical modulus E_1.

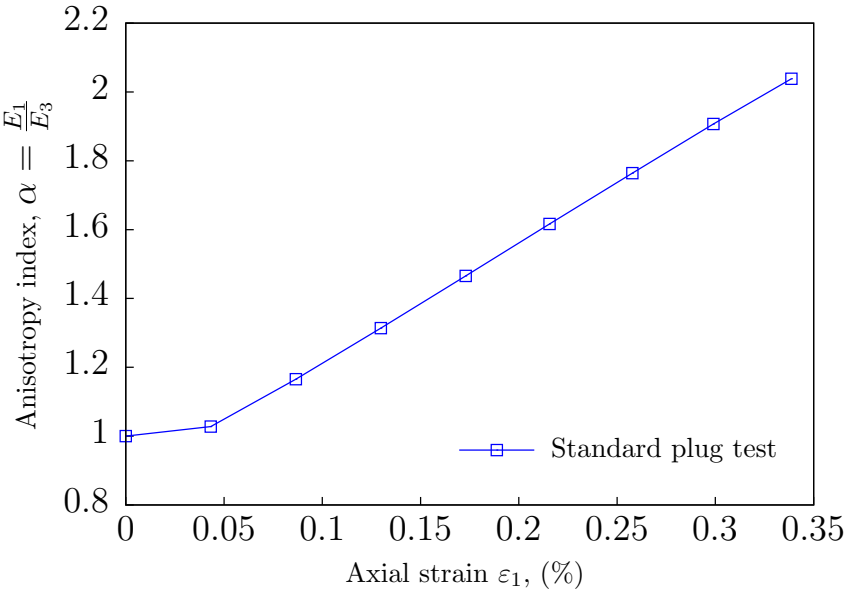

Figure 54: Evolution of the elastic anisotropy index in the standard plug test, for an initially undamaged sample.

Figure 55 shows the changes of Young's modulus observed during the tests, normalized by the initial undamaged modulus. Note that the modulus plotted was the one calculated

in a central element of the mesh, in which the axial strain is not equal to the loading strain. This explains why the final axial strain is not the same for the samples tested. This difference does not change the conclusions drawn from the results concerning the evolution of mechanical anisotropy. During the initial confinement loading stage, damage weakening occurs. The pre-damaged samples (red and green lines, Figure 55) experience less stiffness reduction than the samples without pre-damage (blue lines, Figure 55)). In other words, the existence of pre-existing micro-cracks in the sample makes the material more compliant, and it also tends to reduce stress amplification inhibiting subsequent micro-cracking.

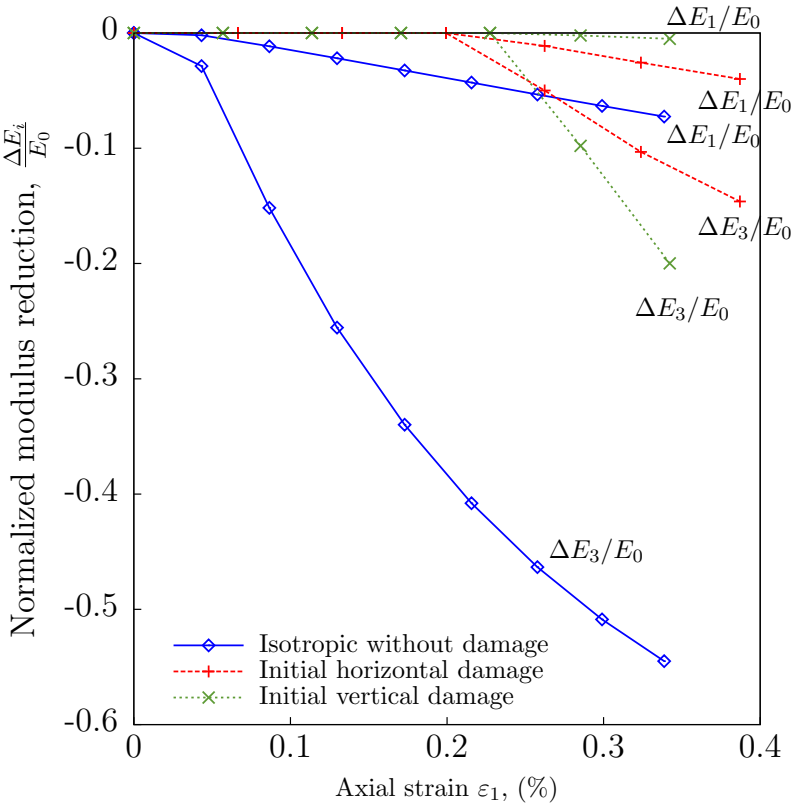

Figure 55: Evolution of the normalized elastic moduli change with loading in the standard plug test

Figure 56 shows the evolution of horizontal damage (vertical micro-cracks) at the end of the triaxial compression test. In accordance with the boundary conditions, the space distribution of damage is symmetric. The final amount of horizontal damage in the sample with initial vertical cracks is similar to that in the initially undamaged sample, which means that

less damage is accumulated during the test simulated with the initially damaged sample, and that stress in the sample with initial damage remains in the elastic domain for a higher axial displacement load than in the initially undamaged sample. Once vertical cracks have formed in the initially damaged sample, damage evolves in a similar way as in the sample that already contained vertical cracks. The sample with initial vertical damage (horizontal micro-cracks) is more compliant in the vertical direction (i.e., the Young's modulus E_1 is initially smaller than in the other samples). Loading is controlled in displacement. Therefore, the sample with initial vertical damage develops less internal stress than in the other samples, and remains in elasticity for a higher axial displacement load. As a result, the horizontal damage cumulated in the sample with initial vertical damage is almost zero except at the edges. Overall, the intensity of deformation throughout the sample follows a similar distribution in the three samples. The space distribution of horizontal damage in Figure 56 explains the space distribution of horizontal deformation in Figure 57: a higher increment of horizontal damage calculated during the test leads to higher horizontal irreversible deformation, and therefore, higher horizontal total deformation. It follows that horizontal deformation in the sample with no initial damage is higher that in the sample with initial horizontal damage, which is itself higher than that in the sample with initial vertical damage.

In a core that contains vertical cracks, the plug modeled here with initial vertical cracks can represent a sample cored in the axial direction of the core, and the plug containing initial horizontal cracks can represent a sample cored in the transversal direction of that core. Therefore, the numerical results above indicate that plugs extracted from the same core in two orthogonal directions can exhibit very different stress-strain responses: a high compression strength is expected for the plug cored in the transversal direction, whereas a low compression strength is expected for the plug cored along the axis of the core. The DSID model can be used to characterize intrinsic mechanical anisotropy from induced damage anisotropy. A sample containing one family of vertical cracks subject to vertical compression can be seen as the equivalent of a sample containing a family of horizontal cracks subject to lateral compression. Therefore, experiments on samples with different states of initial

damage can be done to test three-dimensional states of stress with triaxial compression cells, and modeling initial damage allows predicting the behavior of anisotropic rock under different states of differential stress.

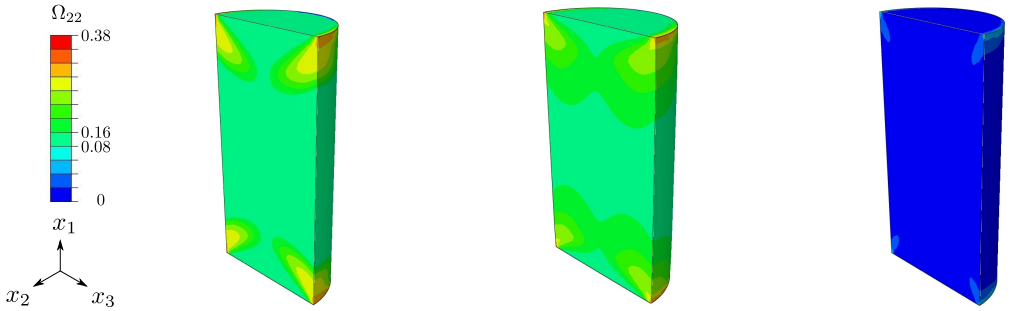

(a) No initial damage (b) Initial horizontal damage (vertical cracks) (c) Initial vertical damage (horizontal cracks)

Figure 56: Horizontal damage distribution (i.e., vertical micro-cracks) after the axial loading phase.

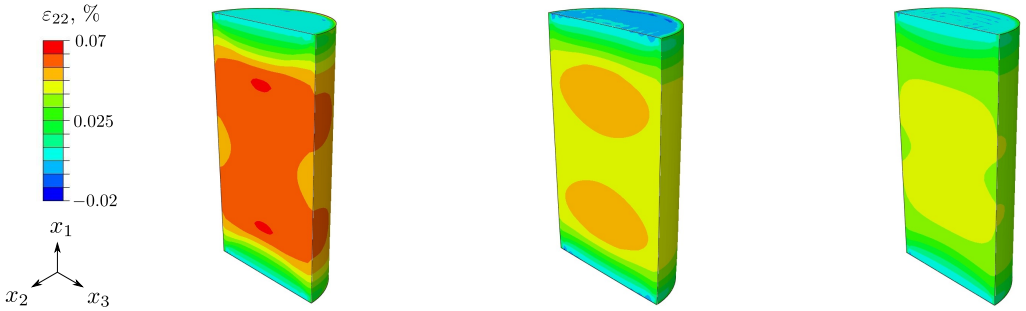

(a) No initial damage (b) Initial horizontal damage (vertical cracks) (c) Initial vertical damage (horizontal cracks)

Figure 57: Horizontal strain distribution after the axial loading phase in the plug test.

5.2.3 Influence of delamination planes on damage propagation

The influence of a horizontal bedding delamination plane on damage propagation within a whole core sample (4 inches in diameter, 6 inches in height) was studied with two different numerical models (Figure 58):

- A discrete fracture model: at mid-height of the sample, a discontinuity was introduced. The top and bottom parts of the sample were debonded. At the interface, a non-penetration condition was adopted in the normal direction, and a friction law (Figure 48) was used in the tangential directions, with a friction coefficient of 0.8 (note that

in real geological conditions, this coefficient varies largely with the type of fracture surface and gouge material in the fracture).

- A smeared damaged zone: a 5 mm thick layer of initially damaged Finite Elements ($\Omega_{11} = 0.2$) is introduced in the middle of the shale sample.

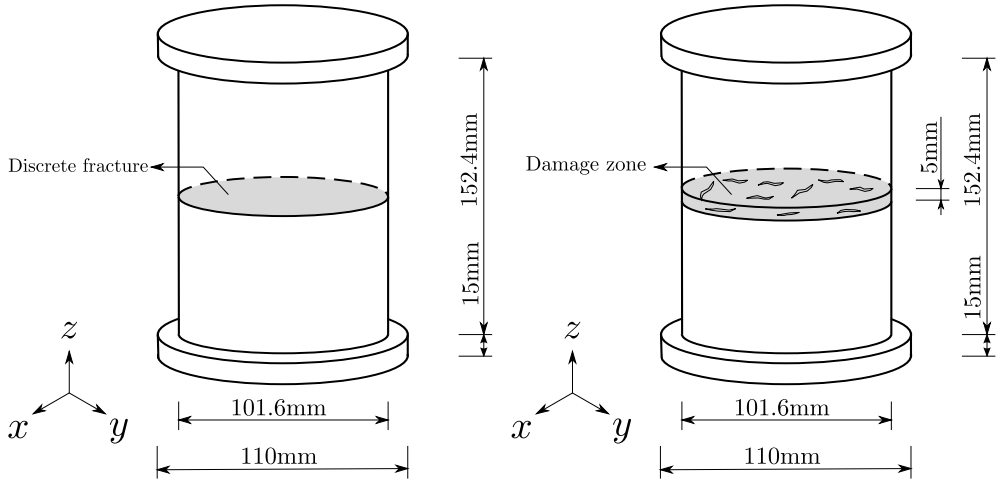

(a) Simulation domain with an embed discrete crack.

(b) Simulation domain with a smeared damage zone.

Figure 58: Sample with a horizontal bedding delamination plane, modelied with: (a) an embedded discrete crack; and (b) an equivalent smeared damage zone.

During the axial compression phase, a vertical strain of 1% was imposed under a constant confining stress of 4,000 psi. As noted previously, stress concentrations occur near the contact surfaces between the steel platens and the rock sample, due to friction. In the discrete fracture model, sliding can occur once friction at the interface between the top and bottom parts of the sample exceeds its frictional strength. Compared to a linear elastic model (Figure 59(a)), contact properties introduced in the discrete crack model (Figure 59(b)) constrain the material at the crack surfaces, which results in slightly higher stress. Overall results in the homogeneous sample (Figure 59(a)) are similar to those in the sample containing a horizontal discrete fracture (Figure 59(b)), because the fracture is closed during the axial compression phase. By contrast, the behavior of a plug containing a uniform distribution of initial horizontal micro-cracks (Figure 57(c)) differs from that of a plug that is initially undamaged (Figure 57(a)), because the DSID model assumes that closed horizontal-microcracks affect stiffness in the same way as open horizontal micro-cracks. In order to

account for the increase of compression strength during crack closure, a unilateral condition would have to be added in the DSID model [55]. In the test with a smeared damaged zone (Figure 59(c), the stiffness tensor decreases only in the zone that contains micro-cracks, due to damage propagation. As expected, internal stress developed in the sample is lower than in the linear elastic test. The main difference with the discrete fracture case is the presence of stress concentrations near the damaged zone. The delamination results indicate that the DSID model can be used to approximate discrete features. However, the triaxial stress-strain calibration approach is based on capturing the effect of crack generating processes. If the model is used for discrete crack-closing processes, then stiffness evolution should instead be calibrated to experiments on fracture closing and asperity weakening (e.g., considering Hertzian contact theory).

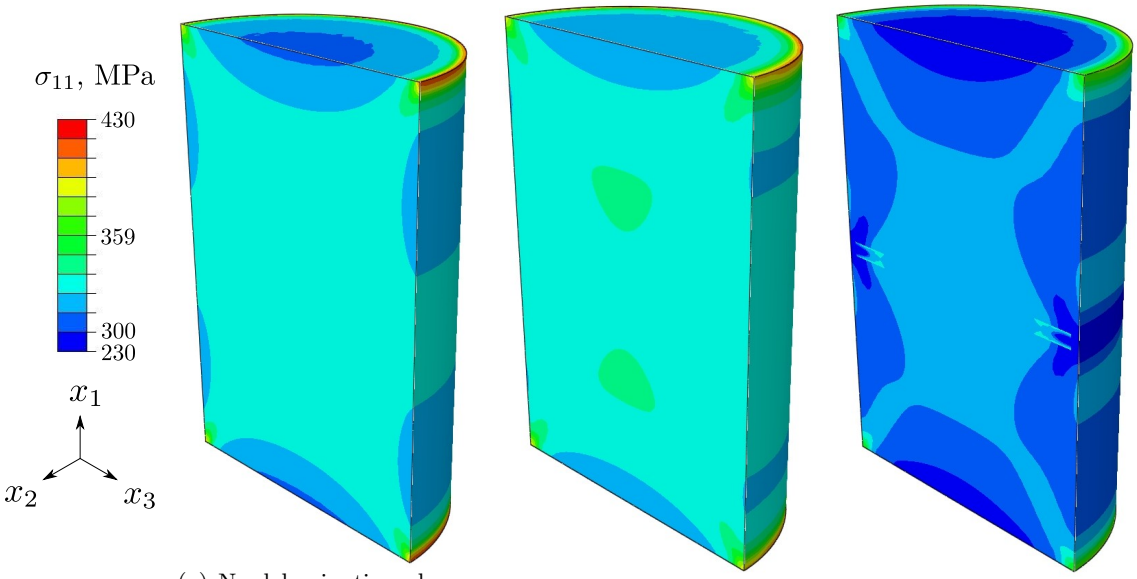

(a) No delamination plane (b) Discrete fracture (c) Smeared damage zone

Figure 59: Comparison of the vertical stress distribution in the core sample with a linear elastic model, with a discrete fracture and with a smeared damage zone.

The evolution of the energy dissipation provides a way to analyze the physical processes, such as crack opening and crack debonding, which dominate damage propagation before failure. Figures 60 and 61 show the energy dissipated in the smeared damaged zone due to the accumulation of irreversible deformation (induced by crack opening: W_{irr}) and due to

crack debonding (W_d)

$$W_{irr} = \int \boldsymbol{\sigma} : \dot{\boldsymbol{\varepsilon}}^{id} \, \mathrm{d}t \tag{232}$$

$$W_d = \int \mathbf{Y} : \dot{\boldsymbol{\Omega}} \, \mathrm{d}t \tag{233}$$

Energy dissipation starts at the external boundary of the sample and propagates towards the center. Finite Elements close to the boundary experience less confinement than the elements in the center, which results in higher deformation close to the lateral boundary. The space distribution of the energy dissipated by crack debonding is similar to that of the energy dissipated by irreversible deformation.

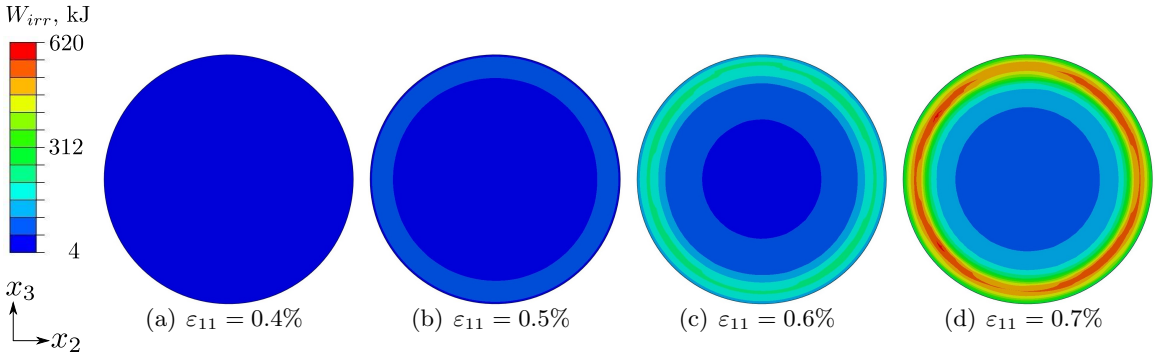

Figure 60: Energy dissipated in the smeared damage zone due to crack opening (accumulation of irreversible strain $\boldsymbol{\varepsilon}^{id}$).

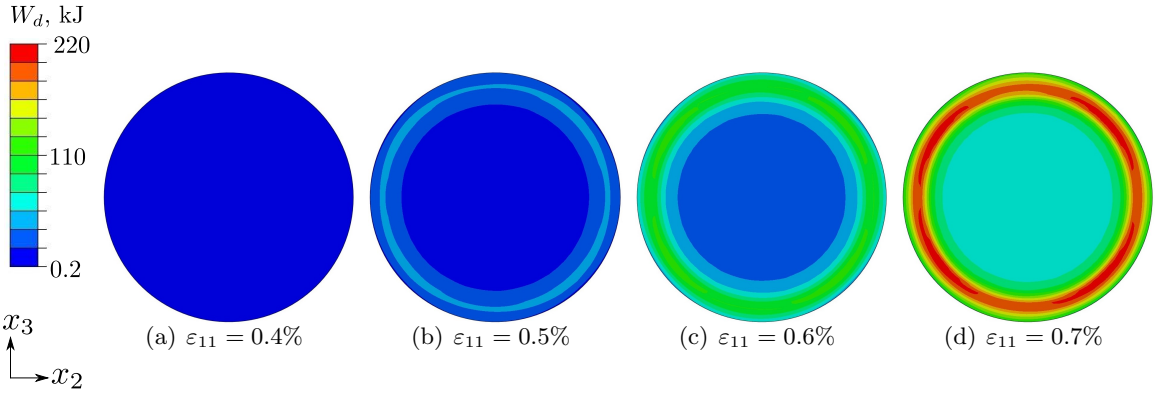

Figure 61: Energy dissipated in the smeared damaged zone due to crack debonding (accumulation of damage $\boldsymbol{\Omega}$).

5.3 Reservoir Geomechanics Applications

5.3.1 Damaged Zone around a Circular Cavity: Stress Relaxation and Pressurization

A Finite Element analysis is conducted in order to characterize the development of shear damage around a circular cavity subjected to pressurization or depressurization (i.e. excavation). Simulations are performed in three dimensions. The domain adopted for this study is a hexahedron bearing a cylindrical hole, as shown in Figure 62. The ratio width/length is chosen so as to be close to a state of plane strain in the central cross-sections of the domain. In the initial state, the same confining stress is applied normal to the external boundaries and normal to the cavity walls. In the loading phase, the confining stress is maintained in the far field (on the external boundaries), and a variation of pressure is applied at the cavity wall. The geometric shape of the domain used for this Finite Element analysis allows imposing an anisotropic state of stress around the circular cavity, which enables the study of shear damage. Table 12 summarizes the simulations performed in this analysis. Constitutive parameters used in the DSID model are listed in Table 13. Former studies [116, 242] indicates that this set of parameters is suitable for granite.

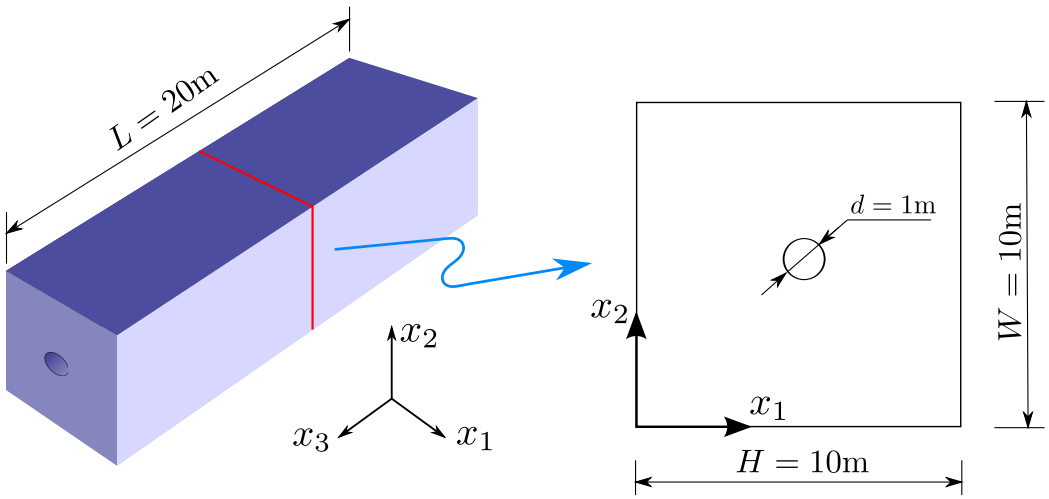

Figure 62: Domain of study in the Finite Element Analysis: simulations are performed in three dimensions, and analyses are restricted to a central cross-section of the domain (right), which can be considered in a state of plane strain

Table 12: Simulation plan for the study of stress relaxation and pressurization under uniform far field stress.

Test	Stress configuration		Loading path
	Confining stress σ_0(MPa)	Internal pressure $\Delta\sigma_p$(MPa)	
Stress relaxation	20	-20	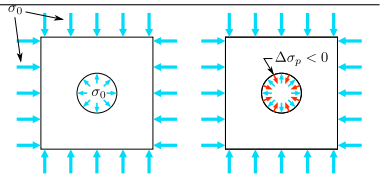
	40	-40	
	60	-60	
	80	-80	
	100	-100	
Pressurization	10	20-100	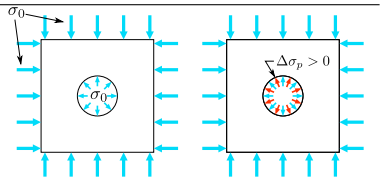
	20	20-100	
	30	20-100	
	40	20-100	
	50	20-100	

Table 13: Damage parameters for granite [116, 242].

Free energy				Damage function		
a_1 GPa^{-1}	a_2 GPa^{-1}	a_3 GPa^{-1}	a_4 GPa^{-1}	C_0 MPa	C_1 MPa	α (-) -
1.26×10^{-4}	3.94×10^{-2}	-1.26×10^{-3}	2.51×10^{-4}	0.11	2.2	0.231

5.3.1.1 Anisotropy of Stress and Damage Induced by Stress Relaxation

The stress relaxation of the cylindrical cavity is simulated by releasing the initial confining stress at the wall. According to the theory of elasticity [138], the distribution of stress around a circular hole of radius R embedded in an infinite medium subjected to a uniform state of stress in the far field is given by

$$\sigma_{\theta\theta} = \sigma_0 \left[1 + \left(\frac{R}{r}\right)^2\right] \tag{234}$$

$$\sigma_{rr} = \sigma_0 \left[1 - \left(\frac{R}{r}\right)^2\right] \tag{235}$$

Figure 63 shows the radial distribution of stress along a vertical line across the section, for several hypothetical initial confining pressures (σ_0). The stress predicted numerically matches the elastic solution for $\sigma_0 = 20$ MPa and $\sigma_0 = 40$ MPa. The plots in Figure 64 confirm that no damage occurs for these two confining pressures. For an initial confining pressure over 60MPa, the damage criterion is reached, and the rock becomes softer (due to the reduction of stiffness). Close to the cavity, rock elements experience higher strains and lower internal stress than in the elastic case. The net stress in the rock mass is compressive, therefore macro-cracks propagate due to crossing effects, and the intensity of damage (perpendicular to the radial direction, Ω_{rr}) increases with the confining stress, which is equal to the opposite of the stress difference applied at the wall during the simulation of the stress relaxation. Orthoradial damage ($\Omega_{\theta\theta}$) remains negligible.

As an example, Figures 65 and 66 show the state of stress and damage after stress relaxation in the entire section of the domain, for a rock mass initially subjected to a confining pressure of 100 MPa. The colored stress maps confirm the absence of shear stress at the top of the wall, and also show that shear stresses concentrate in narrow zones oriented by an angle of 45^o to the horizontal and vertical directions. Stresses follow a symmetric distribution around the cavity, consistent with the shape of the external boundaries where the far field confining pressure is applied. The distribution of horizontal and vertical macro-cracks (Figures 64(a) and 64(b)) illustrates the crossing effects induced by stress differences at the top, bottom, left, and right sides of the cavity. The symmetry of the damage

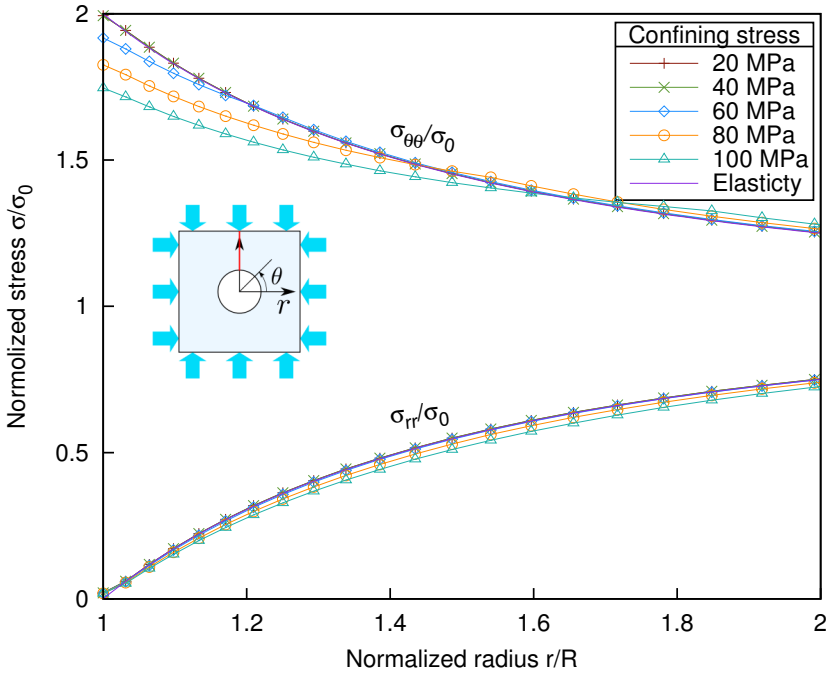

Figure 63: Radial distribution of stress (normalized by the initial confining stress), after stress relaxation ($r = 0.5 \sim 1$ m; $\theta = \frac{\pi}{2}$; $R = 0.5$ m is the radius of the cavity). Comparison of the numerical predictions (with the DSID model) with the analytical solution (in elasticity).

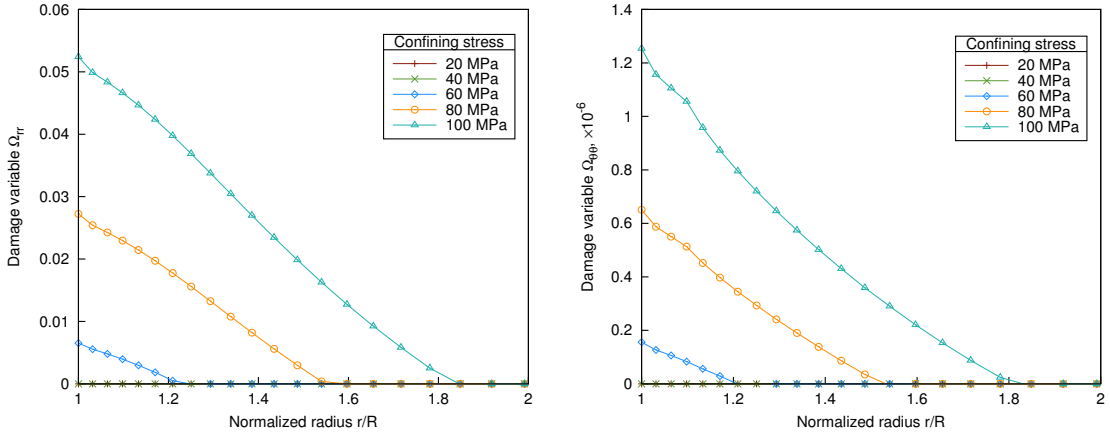

(a) Macro-cracks perpendicular to the radial direction (Ω_{rr})

(b) Macro-cracks parallel to the radial direction ($\Omega_{\theta\theta}$)

Figure 64: Radial distribution of damage after stress relaxation ($r = 0.5 \sim 1$ m; $\theta = \frac{\pi}{2}$; $R = 0.5$ m is the radius of the cavity).

distribution around the cavity explains the symmetry noted in the distribution of shear stress (Figures 65(c)). Note that by definition, damage eigenvalues cannot be negative, but components of the damage tensor off the diagonal can be negative, as this is the case here for shear damage. It is worth noticing that in spite of the isotropic initial state of stress and in spite of the isotropic stress difference applied at the wall, the order of magnitude of shear damage is the same as tension damage (a few percents).

5.3.1.2 Anisotropy of Stress and Damage Induced by Pressurization

In the following simulations, the cylindrical cavity is subjected to a pressure increase at the wall. According to the theory of elasticity [138], the distribution of stress around a circular hole of radius R embedded in an infinite medium subjected to a uniform internal pressure σ_p and an isotropic far field stress σ_0, the state of stress at an arbitrary point of the domain is given by

$$\sigma_{\theta\theta} = \sigma_0 \left[1 + \left(\frac{R}{r}\right)^2\right] - \left(\frac{R}{r}\right)^2 \sigma_p \tag{236}$$

$$\sigma_{rr} = \sigma_0 \left[1 - \left(\frac{R}{r}\right)^2\right] + \left(\frac{R}{r}\right)^2 \sigma_p \tag{237}$$

Figure 67 shows the radial distribution of stress along a vertical line across the section, for an initial confining pressure (σ_0) of 10 MPa. The internal pressure at the wall is increased by increments, and stress is computed for pressure differences ($\Delta\sigma_p$) ranging from 20 MPa to 100 MPa. The stress distribution predicted with the DSID model matches the elastic solution for pressure differences up to 50 MPa. Above this value, the stress magnitude at the wall decreases due to material softening. It is worth noticing that the impact of damage on the distribution of radial stress is negligible. This can be explained by the state of damage developed at the vicinity of the cavity (Figure 68): radial damage is negligible compared to orthoradial damage. These results reveal the presence of macro-cracks that propagate by crossing effects, and indicate that stress elements at the top of the cavity are almost in a state of pure compression in the radial direction and in a state of pure tension in the orthoradial direction.

For illustrative purposes, Figures 69 and 70 show the state of stress and damage in the

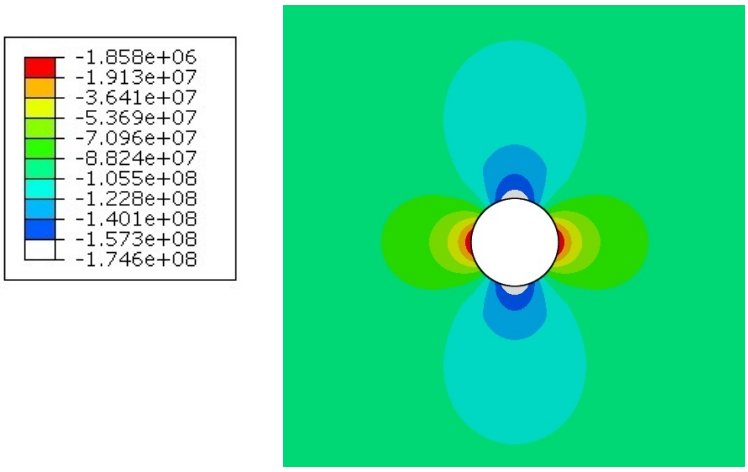

(a) Horizontal stress (σ_{11}, Pa)

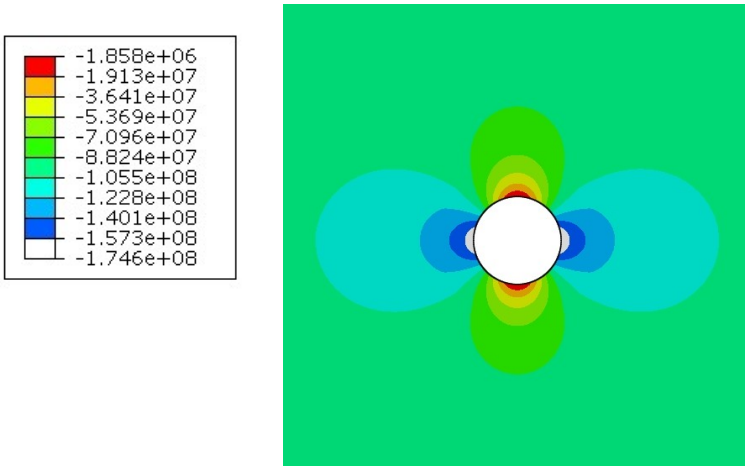

(b) Vertical stress (σ_{22}, Pa)

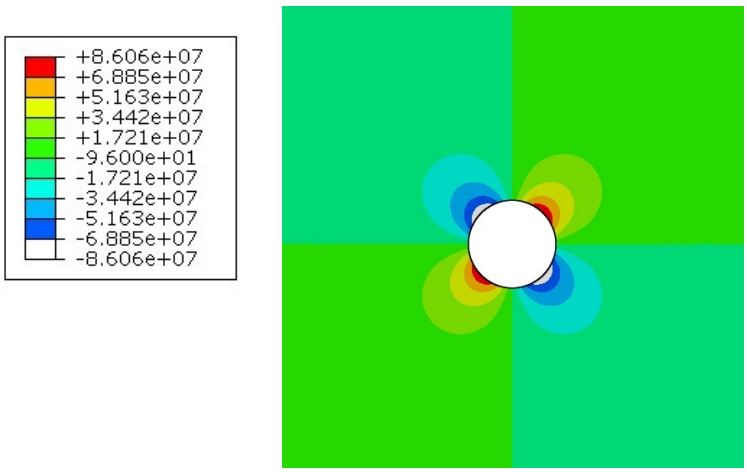

(c) Shear stress (σ_{12}, Pa)

Figure 65: Stress distribution after stress relaxation in a rock mass subjected to a confining pressure of $\sigma_0 = 100$ MPa in the far field. Note: in the FEM program, compression was counted negative and tension was counted positive.

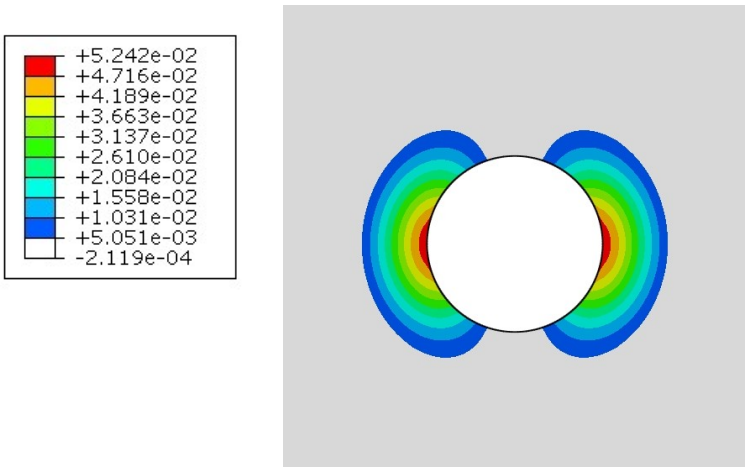

(a) Vertical macrocracks (Ω_{11})

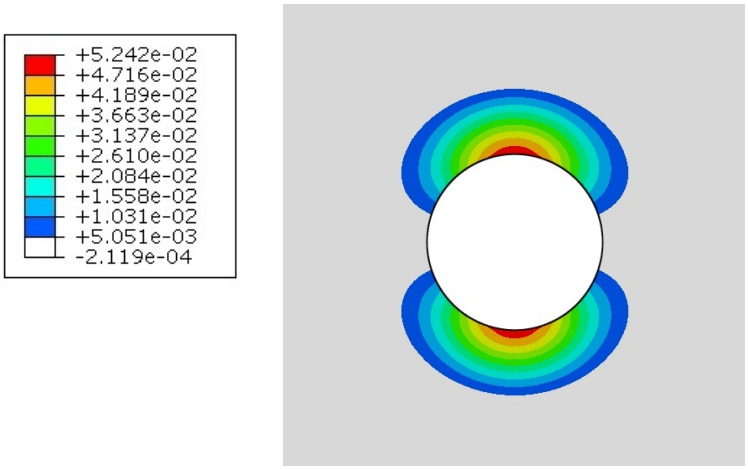

(b) Horizontal macro-cracks (Ω_{22})

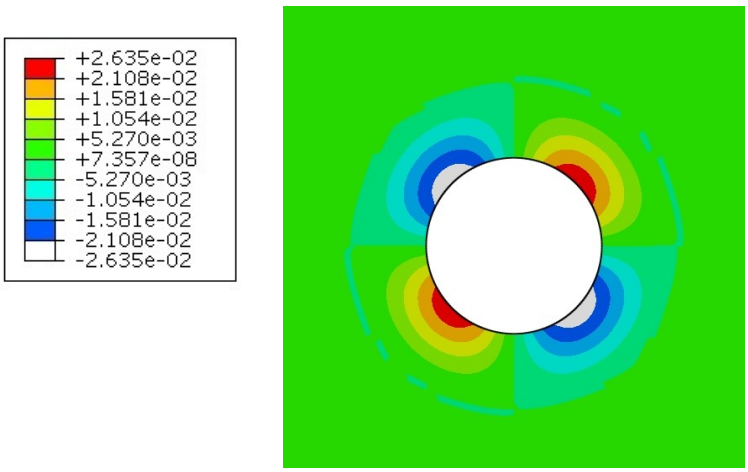

(c) Shear damage (Ω_{12})

Figure 66: Damage distribution after stress relaxation in a rock mass subjected to a confining pressure of $\sigma_0 = 100$ MPa in the far field. Note that by definition, damage eigenvalues cannot be negative, but components of the damage tensor off the diagonal can be negative.

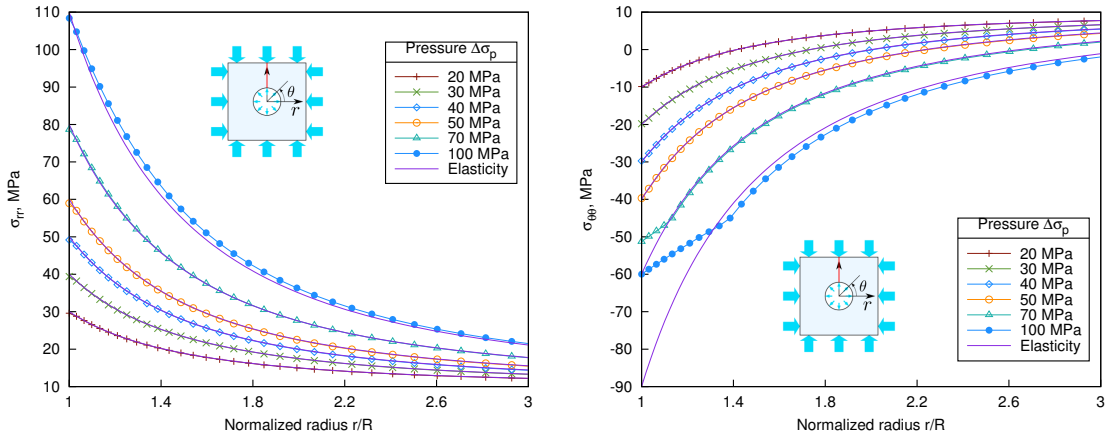

(a) Radial stess (σ_{rr})

(b) Hoop stress ($\sigma_{\theta\theta}$)

Figure 67: Radial distribution of stress, after pressurization under a confining pressure of $\sigma_0 = 10$ MPa ($r = 0.5 \sim 1$ m, $\theta = \frac{\pi}{2}$, $R = 0.5$ m is the radius of the cavity). Comparison of the numerical predictions (with the DSID model) with the analytical solution (in elasticity).

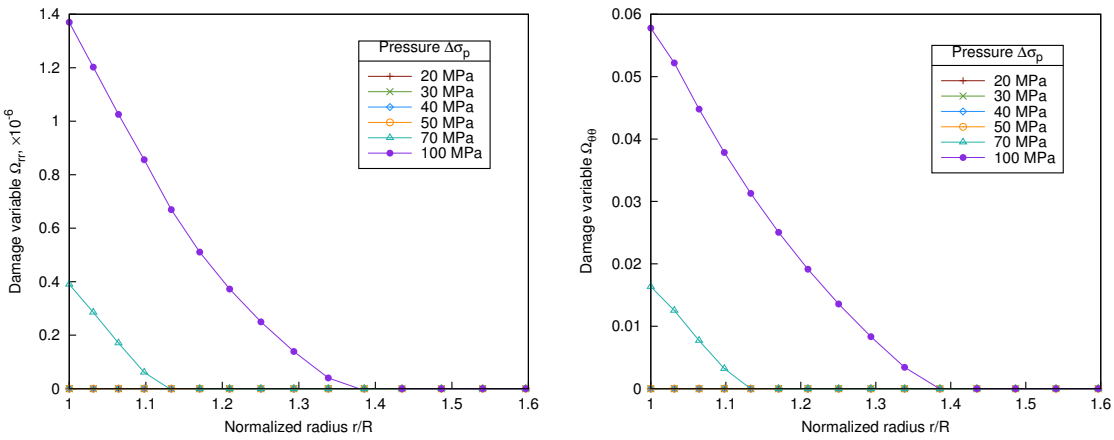

(a) Macro-cracks perpendicular to the radial direction (Ω_{rr})

(b) Macro-cracks parallel to the radial direction ($\Omega_{\theta\theta}$)

Figure 68: Radial distribution of damage after pressurization under a confining pressure of $\sigma_0 = 10$MPa ($r = 0.5 \sim 1$m, $\theta = \frac{\pi}{2}$, $R = 0.5$ m is the radius of the cavity).

entire section of the domain, after a pressurization of 100 MPa under a confining stress of 10 MPa. Similar conclusions as for the stress relaxation case can be drawn, mainly:

(i) Shear stresses concentrate in narrow zones oriented by an angle of 45^o to the horizontal and vertical directions.

(ii) Tension and compression stresses follow a symmetric distribution around the cavity, consistent with the shape of the external boundaries.

(iii) Horizontal and vertical macro-cracks (Figures 70(a) and 70(b)) propagate due to crossing effects. At the top and bottom of the cavity, higher compression in the vertical direction produces vertical cracks. On the left and right sides of the cavity, higher compression in the horizontal direction produces horizontal cracks.

(iv) The symmetry noted in the distribution of shear damage (Figures 70(c)) follows the symmetry of shear stress (with possible negative values of the components of the damage tensor off the diagonal). In spite of the isotropic initial state of stress and in spite of the isotropic stress difference applied at the wall, the order of magnitude of shear damage is the same as tension damage (a few percents).

5.3.1.3 Simulation of Anisotropic Damage Paths around Circular Cavities

A parametric study on far field stress anisotropy and on the loading sequence is conducted, in order to identify the stress conditions in which the principal directions of damage are expected to rotate. Tables 14 and 15 summarize the simulation plan for the stress relaxation and pressurization of the cylindrical cavity shown in Figure 62.

Competing Crossing Effects. A pressurization of 50 MPa is simulated for various additional vertical loadings, under a far-field confining stress $\sigma_0 = 50$ MPa. The final state of stress is achieved after three loading phases (Table 14): (1) Isotropic confinement at the external boundary and at the cavity wall (σ_0); (2) Increase of vertical far-field stress (additional $\Delta\sigma_{22}$); (3) Pressure increase at the cavity wall (pressurization). With the lower additional vertical load, damage corresponding to the vertical and horizontal crack planes

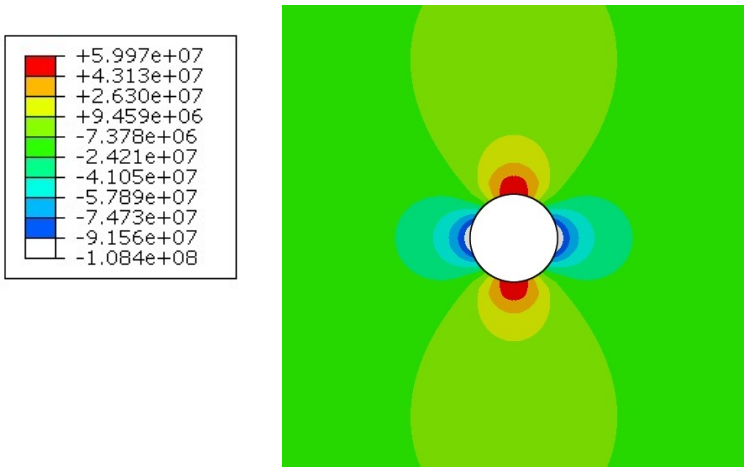

(a) Horizontal stress (σ_{11}, Pa)

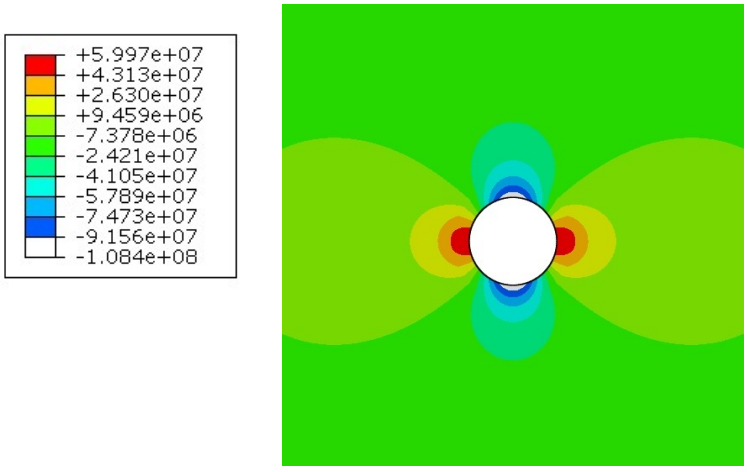

(b) Vertical stress (σ_{22}, Pa)

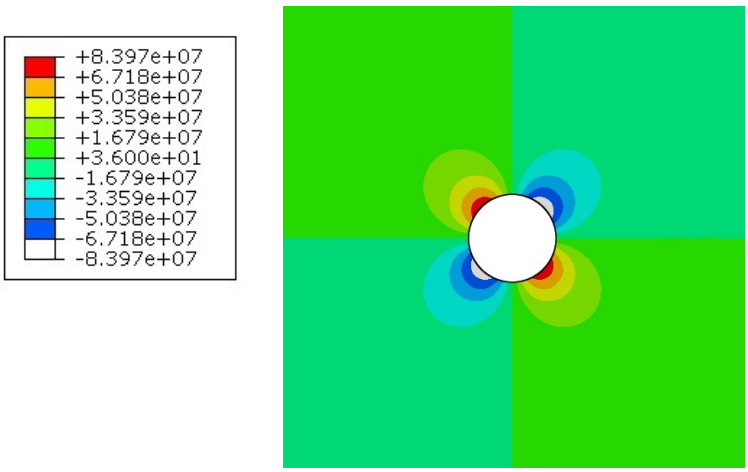

(c) Shear stress (σ_{12}, Pa)

Figure 69: Stress distribution after a pressurization of $\Delta\sigma_p = 100$ MPa in a rock mass subjected to a confining pressure of $\sigma_0 = 10$ MPa in the far field. Note: in the FEM program, compression was counted negative and tension was counted positive.

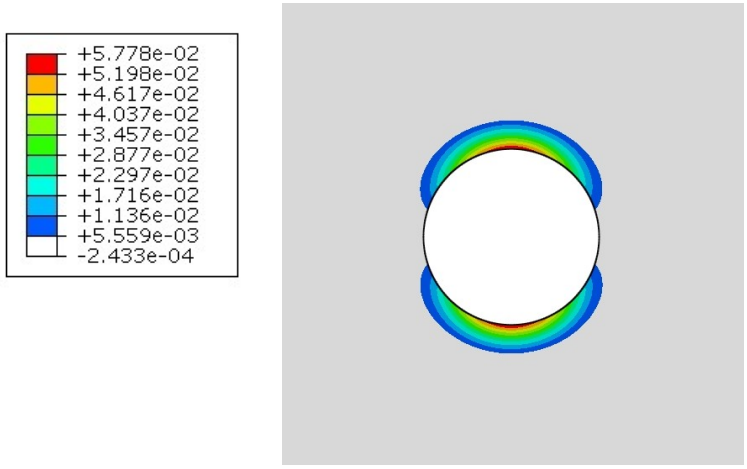

(a) Vertical macro-cracks (Ω_{11})

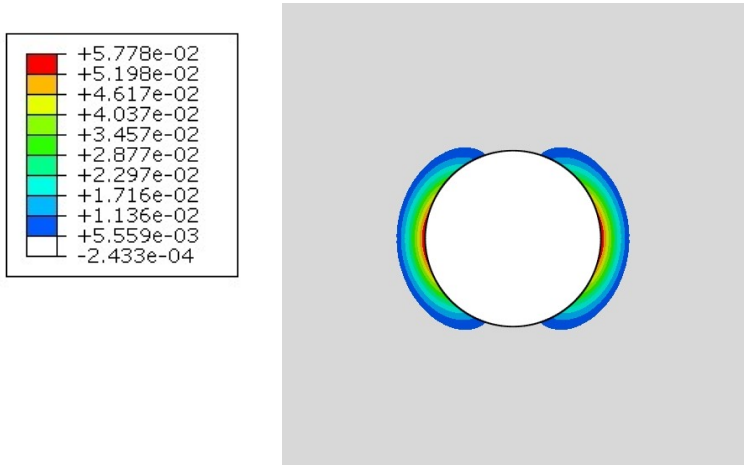

(b) Horizontal macro-cracks (Ω_{22})

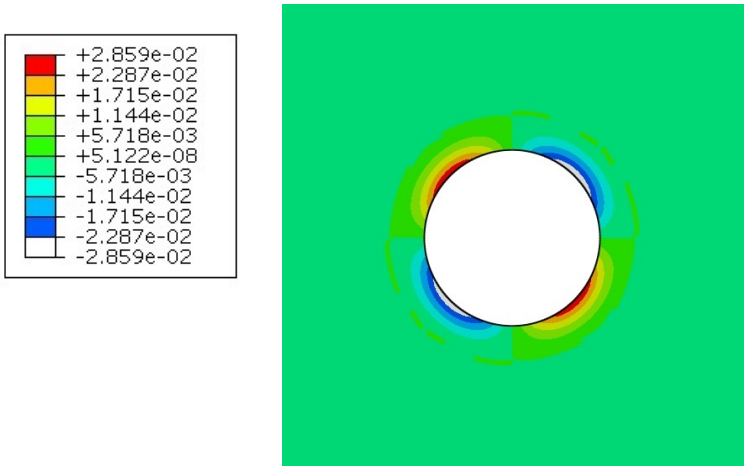

(c) Shear damage (Ω_{12})

Figure 70: Damage distribution after a pressurization of $\Delta\sigma_p = 100$ MPa in a rock mass subjected to a confining pressure of $\sigma_0 = 10$ MPa in the far field. Note that by definition, damage eigenvalues cannot be negative, but components of the damage tensor off the diagonal can be negative.

Table 14: Simulation plan for the study of pressurization under anisotropic far field stress.

Test	Stress configuration			Loading path
	Confining stress σ_0(MPa)	Internal pressure $\Delta\sigma_p$(MPa)	Additional load $\Delta\sigma_1$(MPa)	
	50	50	20	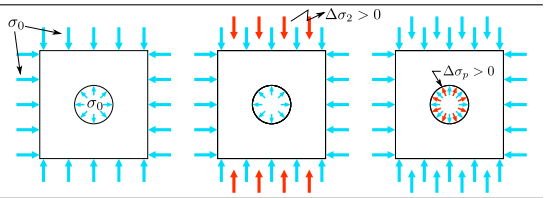
	50	50	30	
	50	50	40	
	50	50	50	

Table 15: Simulation plan for the study of stress relaxation under anisotropic far field stress.

Test	Stress configuration			Loading path
	Confining stress σ_0(MPa)	Internal pressure $\Delta\sigma_p$(MPa)	Additional load $\Delta\sigma_1$(MPa)	
Sequence 1	10	-10	20-50	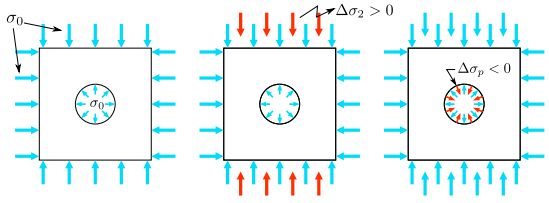
	20	-20	20-50	
	30	-30	20-50	
	40	-40	20-50	
	50	-50	20-50	
Sequence 2	10	-10	20-50	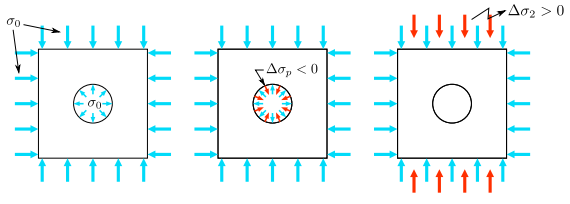
	20	-20	20-50	
	30	-30	20-50	
	40	-40	20-50	
	50	-50	20-50	

(Ω_{11} and Ω_{22}) only occur at the top and bottom of the hole (Fig.71(a) and 71(c)). A higher additional vertical load increases the potential that crack open vertically (Ω_{11}), due to crossing effects. Figure 71(b) shows that damage Ω_{11} spreads horizontally at the top and bottom of the cavity, and that damage Ω_{22} develops along inclined planes. The presence of an additional vertical load redistributes the zones of maximum differential stress $\sigma_{11} - \sigma_{22}$, which results in different damage localization zones around the cavity. At a given point at the cavity wall, the rotation of the principal directions of damage is governed by the competition between the crossing effects due to pressurization and the crossing effects due to the squeezing vertical load. A comparison between Figures 70 and 71 illustrates this phenomenon.

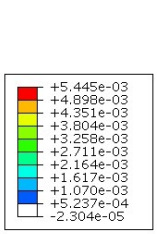

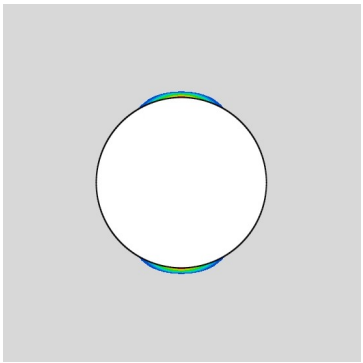

(a) Vertical macro-cracks (Ω_{11}, $\Delta\sigma_{22} = 20$ MPa)

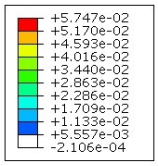

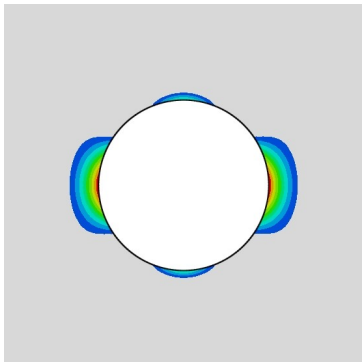

(b) Vertical macro-cracks (Ω_{11}, $\Delta\sigma_{22} = 50$ MPa)

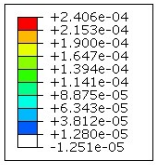

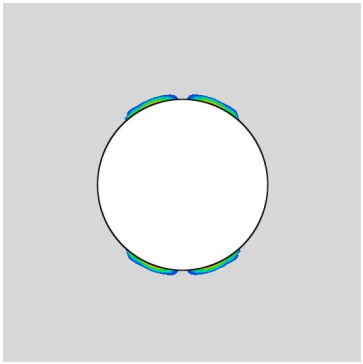

(c) Horizontal macro-cracks (Ω_{22}, $\Delta\sigma_{22} = 20$ MPa)

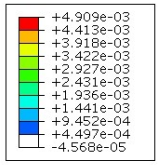

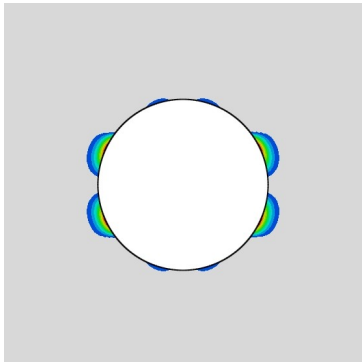

(d) Horizontal macro-cracks (Ω_{22}, $\Delta\sigma_{22} = 50$ MPa)

Figure 71: Damage distribution after application of an additional vertical load $\Delta\sigma_{22}$ followed by a pressurization, under a confining pressure of $\sigma_0 = 50$ MPa.

Damage Rotation Induced by Additional Vertical Stress. stress relaxation is simulated for various additional loadings. The final distributions of stress and damage are shown in Figures 72 and 73 respectively, for $\sigma_0 = \Delta\sigma_{22}$ =50 MPa. Note that the net stress difference applied during the stress relaxation is the difference between the final stress displayed in the figures and the stress computed at the end of the confining and extra loading phases. From the state of stress at the wall of the cavity, one would expect vertical tensile macro-cracks on left and right sides of the cavity (Figure 72(a)), and horizontal tensile macro-cracks at the top and bottom of the cavity (Figures 72(b)). Vertical cracks in Figure 73(a) follow the expected cracks distribution, but not horizontal cracks in Figure 73(b). It is worth noticing that for the same initial wall pressure σ_0, an stress relaxation without extra load indeed results in horizontal cracks at the top and bottom of the cavity (Figure 66(b)). The presence of an extra load redistributes the relative intensity of the damage components around the cavity, which results in a rotation of the principal directions of damage. This conclusion is confirmed by the distribution of shear stresses and shear damage in Figure 72(c) and Figure 73(c). Damage assessment can therefore be used a posteriori to evaluate the additional vertical load applied on the top of a tunnel. In addition, it is noted that for the same external confining stress, the damage criterion is reached under lower vertical load during an stress relaxation than during a pressurization.

Figures 74 and 75 show the evolution of the proportions between damage components generated by stress relaxation, for four values of extra vertical pressure, under a far-field confining pressure of 50 MPa. Distributions along a radial axis oriented by 22.5° to the horizontal and by 45° to the horizontal have been plotted. The main observations are the following:

(i) As expected, damage intensity decreases as the distance to the cavity increases.

(ii) Shear damage is not negligible compared to horizontal and vertical damage.

(iii) The proportion between damage components is not maintained when the extra load is increased, which indicates that the principal directions of damage rotate upon application of an additional vertical pressure.

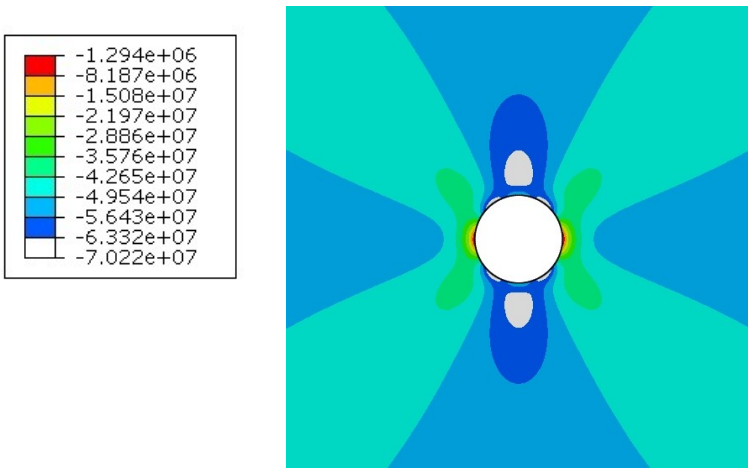

(a) Horizontal stress (σ_{11}, Pa)

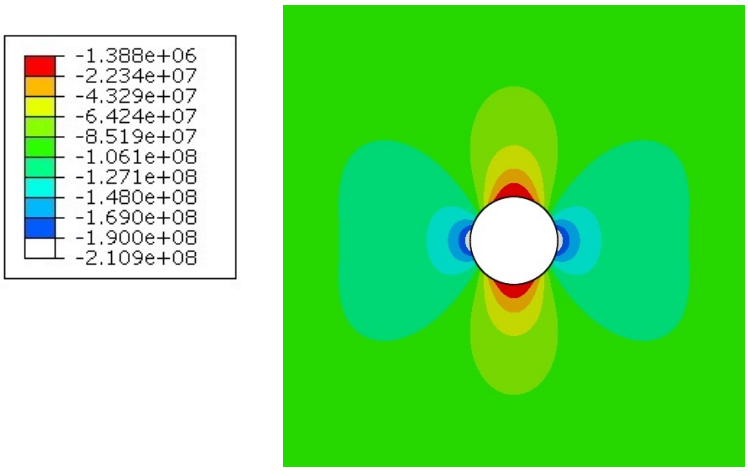

(b) Vertical stress (σ_{22}, Pa)

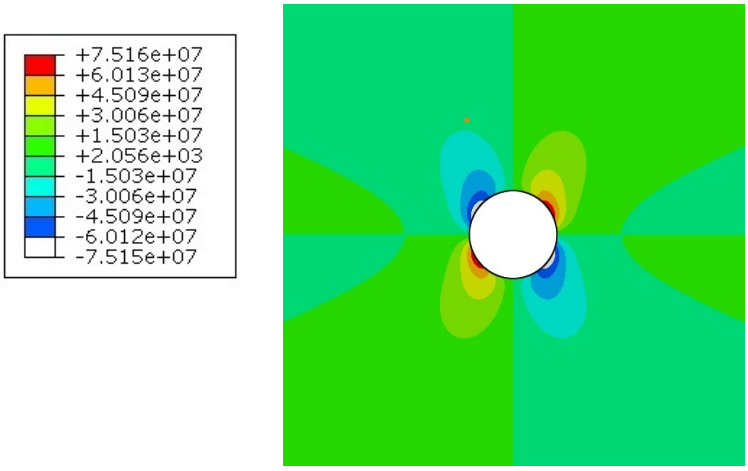

(c) Shear stress (σ_{12}, Pa)

Figure 72: Stress distribution after application of an extra vertical load $\Delta\sigma_{22} = 50$ MPa followed by an stress relaxation, under a confining pressure of $\sigma_0 = 50$ MPa (Sequence 1). Note: in the FEM program, compression was counted negative and tension was counted positive.

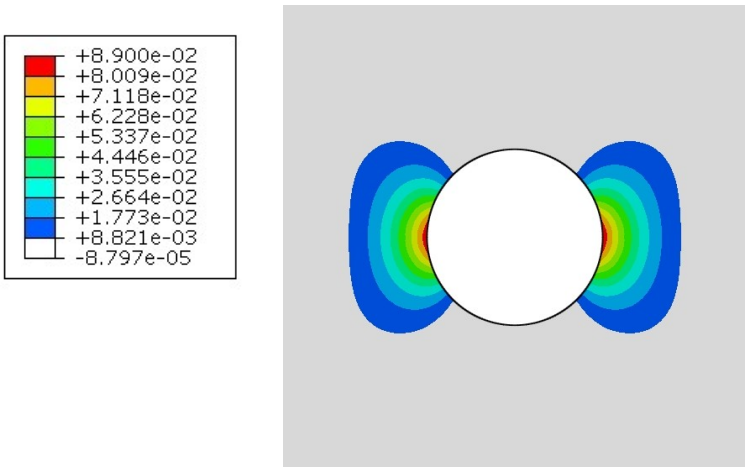

(a) Vertical macro-cracks (Ω_{11})

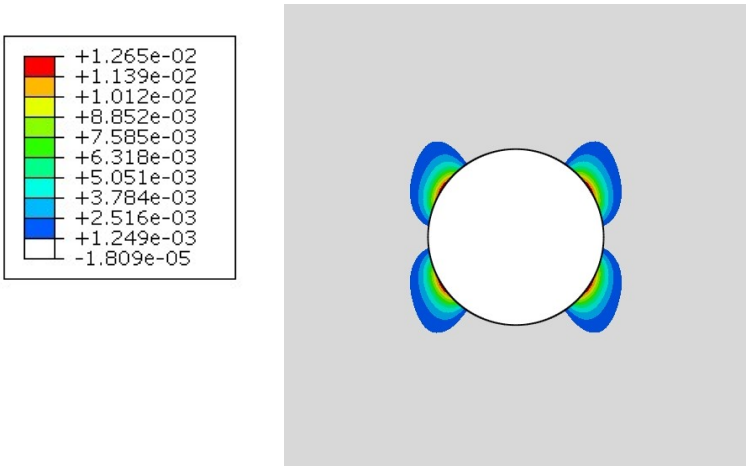

(b) Horizontal macro-cracks (Ω_{22})

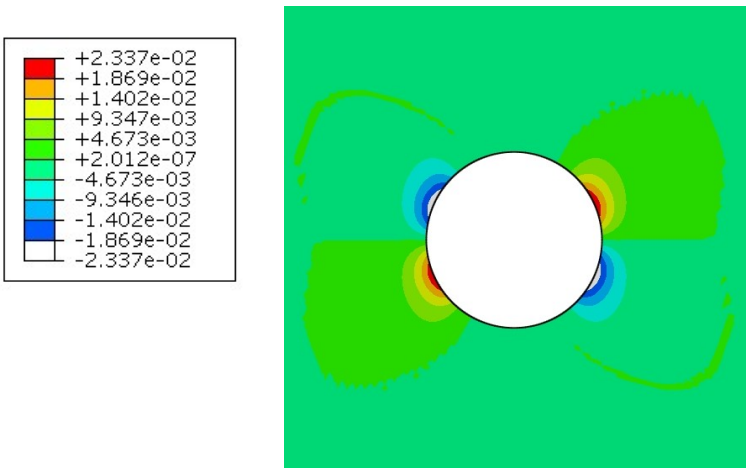

(c) Shear damage (Ω_{12})

Figure 73: Damage distribution after application of an additional vertical load $\Delta\sigma_{22} = 50$ MPa followed by an stress relaxation, under a confining pressure of $\sigma_0 = 50$ MPa (Sequence 1).

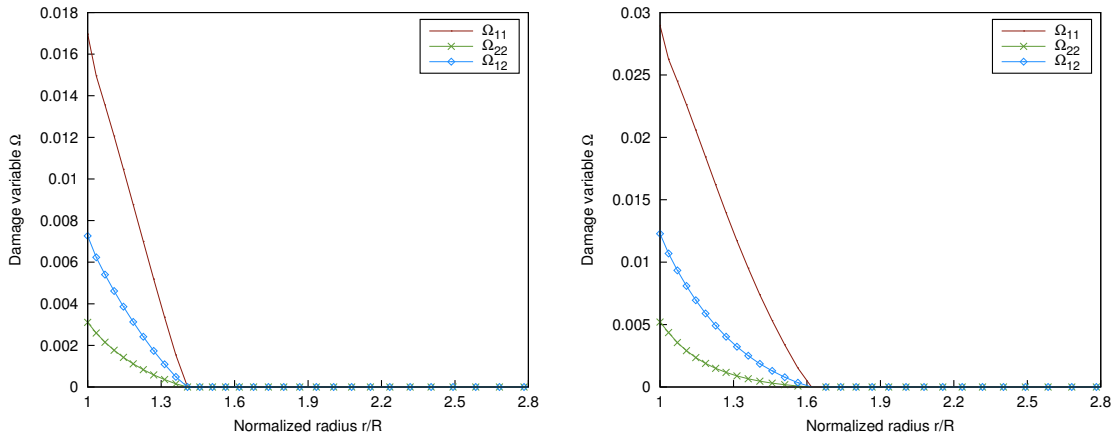

(a) $\Delta\sigma_{22} = 20$ MPa (b) $\Delta\sigma_{22} = 30$ MPa

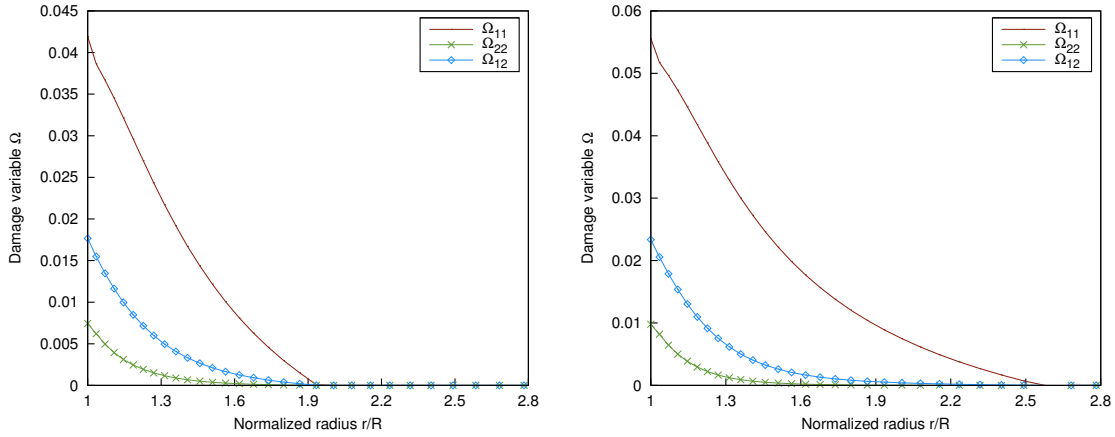

(c) $\Delta\sigma_{22} = 40$ MPa (d) $\Delta\sigma_{22} = 50$ MPa

Figure 74: Radial distribution of damage along an axis oriented by 22.5° to the horizontal, after application of an extra load followed by an excavation, under a confining pressure of $\sigma_0 = 50$ MPa (Sequence 1)

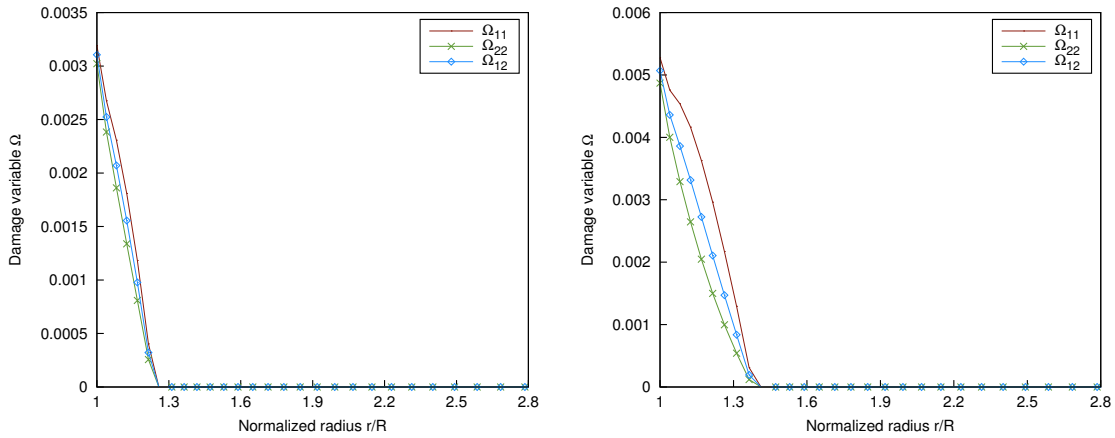

(a) $\Delta\sigma_{22} = 20$ MPa

(b) $\Delta\sigma_{22} = 30$ MPa

(c) $\Delta\sigma_{22} = 40$ MPa

(d) $\Delta\sigma_{22} = 50$ MPa

Figure 75: Radial distribution of damage along an axis oriented by 45° to the horizontal, after application of an extra load followed by an stress relaxation, under a confining pressure of $\sigma_0 = 50$ MPa (Sequence 1).

Effect of Stress Path on Damage Orientation. The simulations of stress relaxation with extra vertical load are repeated for a different sequence of loading (Sequence 2 in Table 15), in which the additional load is applied after the stress relaxation is completed. For $\sigma_0 = \Delta\sigma_{22}$ =50 MPa, the final distributions of stress and damage (shown in Figures 76 and 77) are similar to the ones obtained in the loading sequence in which stress relaxation follows the application of the additional load (Figures 72 and 73). The main difference between the two stress paths lies in the intensity of damage, which is reduced when the extra load is applied after the stress relaxation. The radial distribution of the damage components along an axis oriented by 22.5° to the horizontal indicates in particular that the position of maximum density of vertical cracks (Ω_{11}) is located at the wall of the cavity in sequence 1 (Figure 74), and inside the rock mass in sequence 2 (Figure 78). The value of shear damage in sequence 2 is intermediate between vertical and horizontal damage, like in sequence 1. Differences in the proportions between damage components result in different principal directions of the damage tensor, as can be seen in Figure 80, which displays the orientation of the major principal damage direction relative to the horizontal. Departure from the horizontal is larger for sequence 2 than for sequence 1. In addition, Figure 81 shows that the major damage eigenvalue is less in sequence 2 than in sequence 1 in the vicinity of the cavity.

5.3.1.4 Application: Geomechanical Interpretation of the Damaged Zone around Circular Cavities

The development of an Excavation Damaged Zone (EDZ) under anisotropic stress conditions was investigated by many research groups, e.g. [185, 241, 186, 186, 223, 84, 50]. Acoustic emission tests revealed that fractures propagate along the direction of minimum compression, and that fractures (EDZ) are surrounded by a Excavation disturbed Zone (EdZ), in which rock elastic properties are weakened by the presence of smaller cracks (Table 16, right). It was also found that some tensile cracks developed along the direction of maximum stress. Here, we simulate rock depressurization induced by the excavation of a circular cavity, under isotropic and anisotropic field stress conditions. The simulations presented in the following are a scholar exercise, which would require further refinement

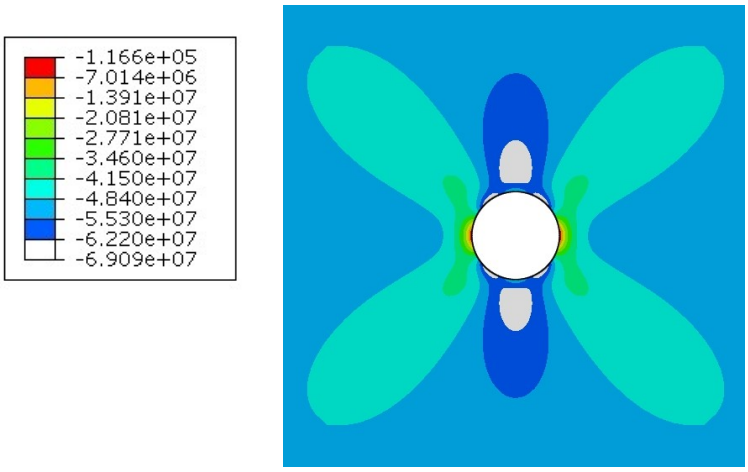

(a) Horizontal stress (σ_{11}, Pa)

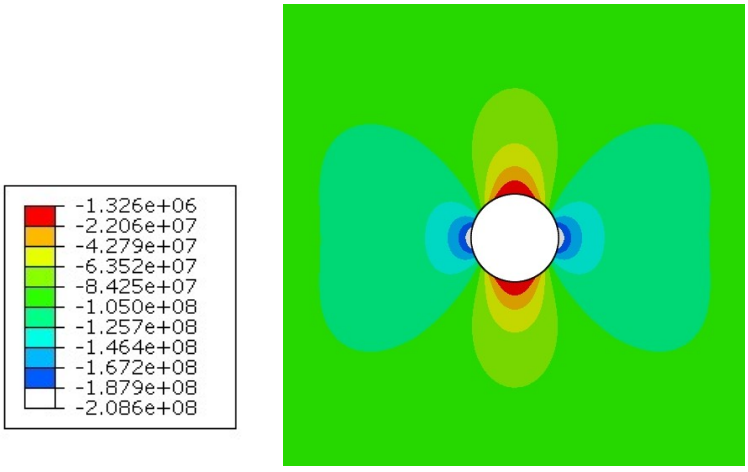

(b) Vertical stress (σ_{22}, Pa)

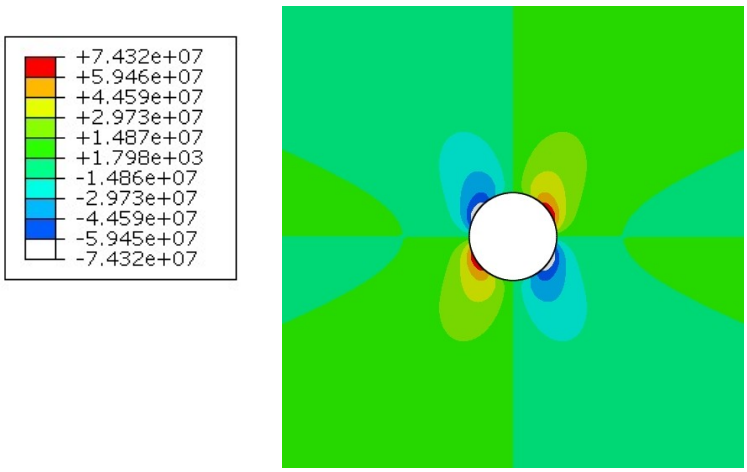

(c) Shear stress (σ_{12}, Pa)

Figure 76: Stress distribution after an stress relaxation followed by the application of an extra load $\Delta\sigma_{22} = 50$ MPa, under a confining pressure of $\sigma_0 = 50$ MPa (Sequence 2). Note: in the FEM program, compression was counted negative and tension was counted positive.

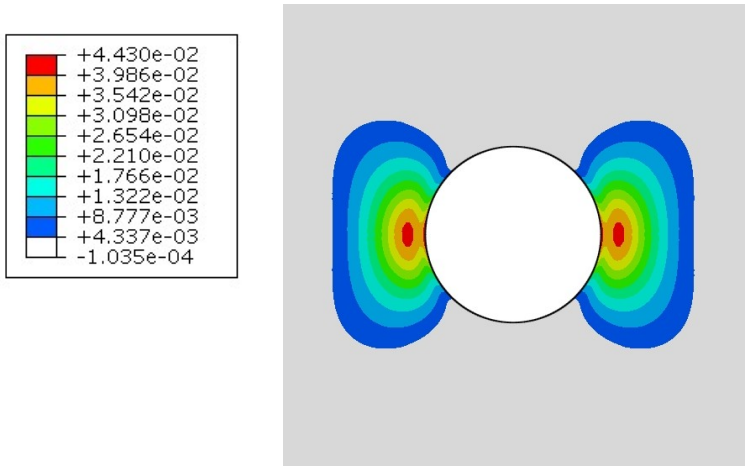

(a) Vertical macro-cracks (Ω_{11})

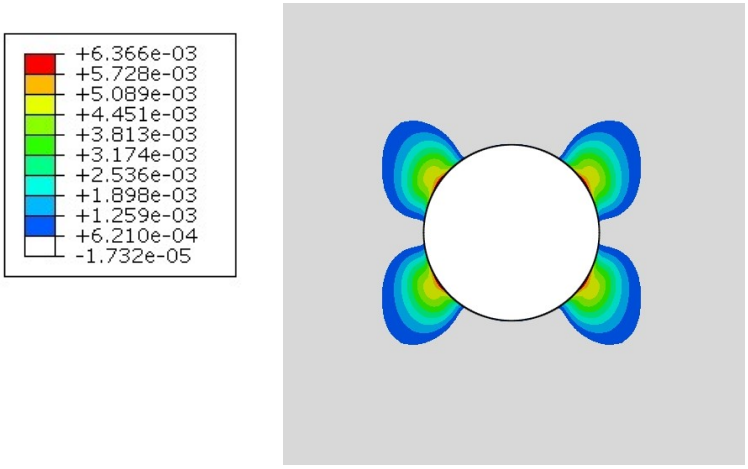

(b) Horizontal macro-cracks (Ω_{22})

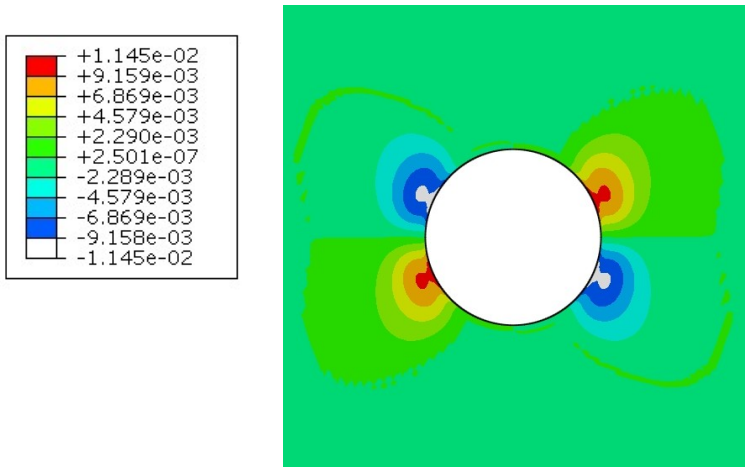

(c) Shear damage (Ω_{12})

Figure 77: Damage distribution after an stress relaxation followed by the application of an extra load $\Delta\sigma_{22} = 50$ MPa, under a confining pressure of $\sigma_0 = 50$ MPa (Sequence 2).

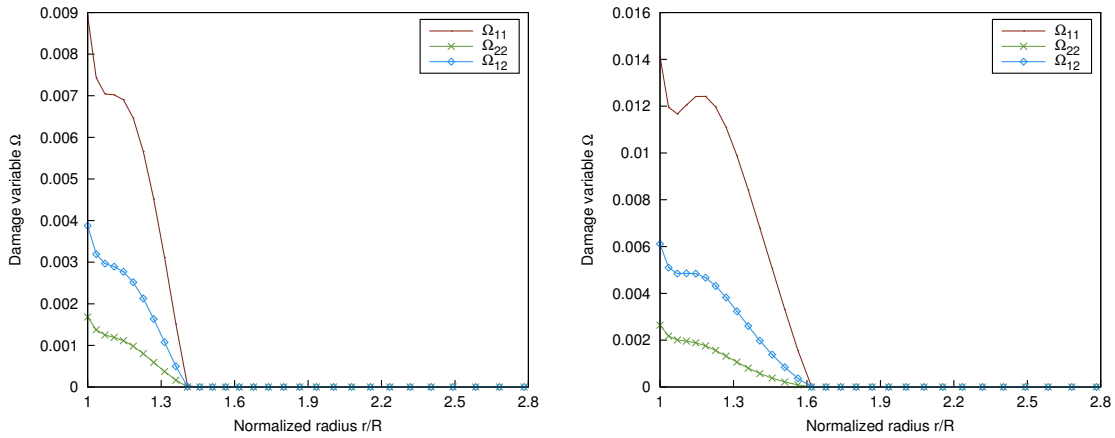

(a) $\Delta\sigma_{22} = 20$ MPa

(b) $\Delta\sigma_{22} = 30$ MPa

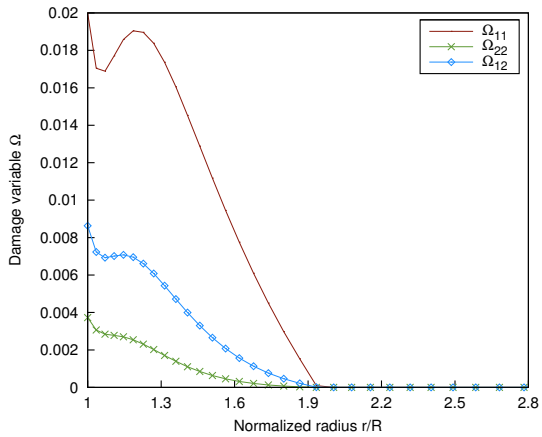

(c) $\Delta\sigma_{22} = 40$ MPa

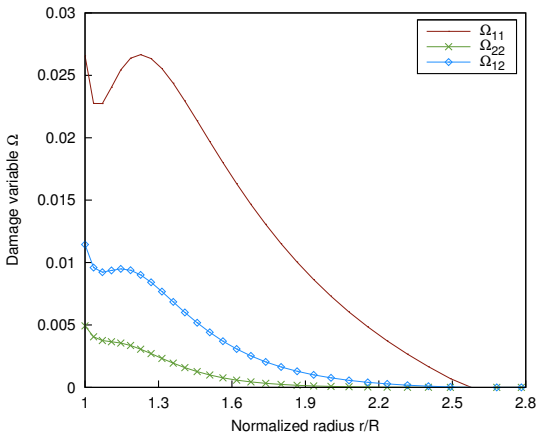

(d) $\Delta\sigma_{22} = 50$ MPa

Figure 78: Radial distribution of damage along an axis oriented by 22.5° to the horizontal, after an stress relaxation followed by the application of an additional load, under a confining pressure of $\sigma_0 = 50$ MPa (Sequence 2).

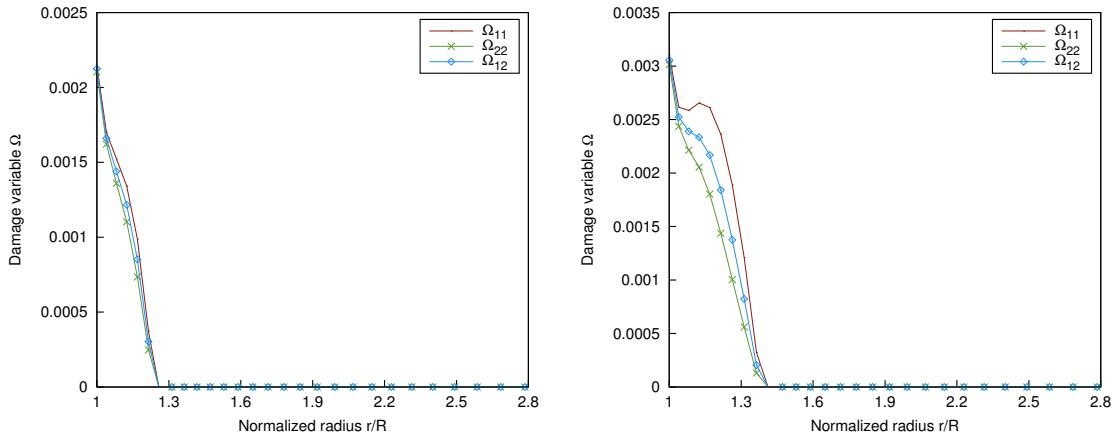

(a) $\Delta\sigma_{22} = 20$ MPa

(b) $\Delta\sigma_{22} = 30$ MPa

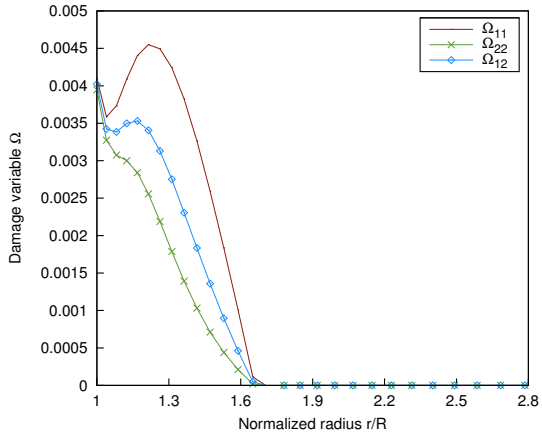

(c) $\Delta\sigma_{22} = 40$ MPa

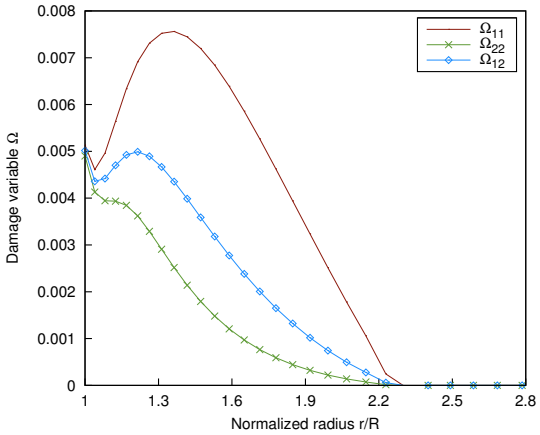

(d) $\Delta\sigma_{22} = 50$ MPa

Figure 79: Radial distribution of damage along an axis oriented by 45° to the horizontal, after an stress relaxation followed by application of an additional load, under a confining pressure of $\sigma_0 = 50$ MPa (Sequence 2).

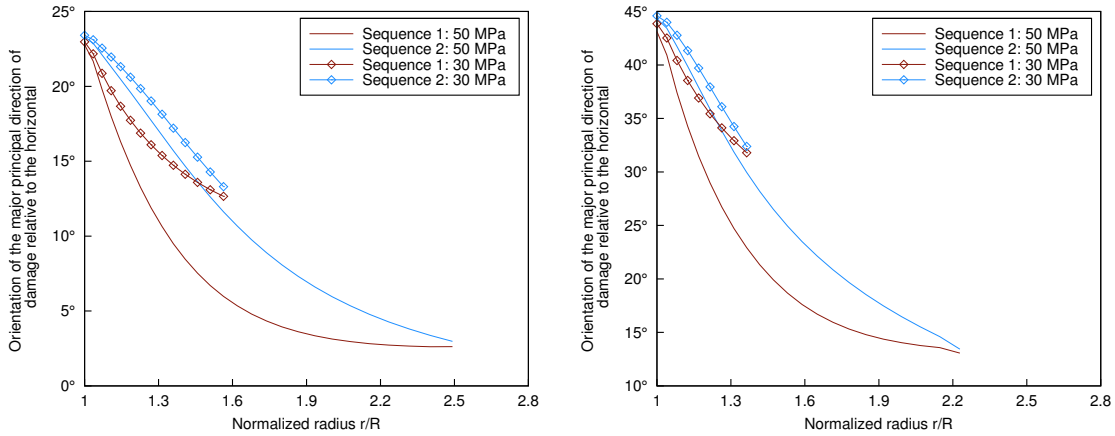

(a) $\theta = 22.5°$ (b) $\theta = 45°$

Figure 80: Orientation of the major principal direction of damage relative to the horizontal, for points located on radial axes oriented by $\theta = 22.5°$ and $\theta = 45°$ to the horizontal. (stress relaxation with $\sigma_0 = 50$ MPa).

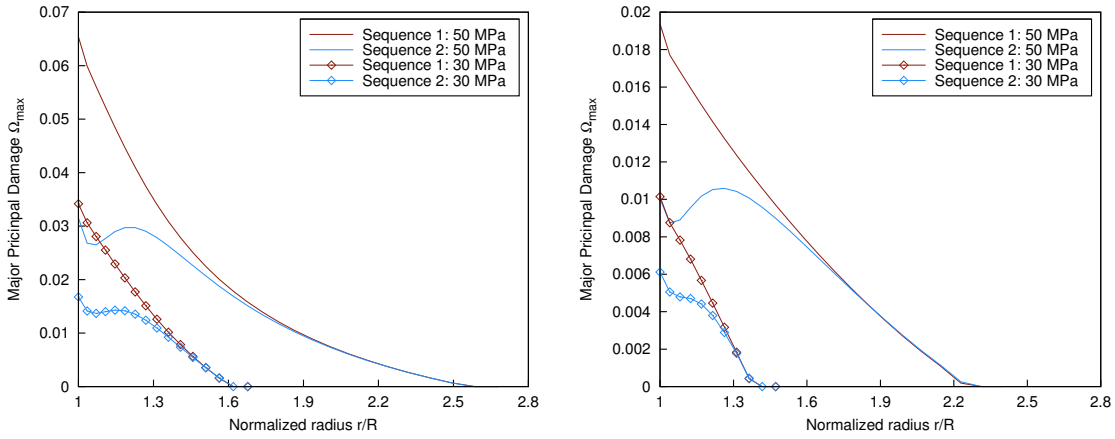

(a) $\theta = 22.5°$ (b) $\theta = 45°$

Figure 81: Maximum eigenvalue of the damage tensor, for points located on radial axes oriented by $\theta = 22.5°$ and $\theta = 45°$ to the horizontal (stress relaxation with $\sigma_0 = 50$ MPa).

to simulate the Excavation Damaged Zone around a cavity for a real tunneling or mining application. However, results discussed herein can be useful to understand the typical shape and extend of the damaged zone in various geological conditions. The simulation results shown in Figures 72 and 73 show that the DSID model captures the characteristics of the EDZ under anisotropic stress conditions. The damaged zone obtained during the simulation of an excavation after application of an extra vertical load is shown in Table 16 (the damaged zone is shown in red, and the distance to the damage threshold increases from blue to red, with green as an intermediate indicator). The numerical results illustrate the development of a weakened zone in the zones where compression is minimum, conform to in situ observations. To the author's best knowledge, no field data is available on EDZ developed under isotropic stress conditions - mainly because in situ stress is scarcely isotropic. However laboratory experiments and numerical studies performed by other research groups [169, 278] (Table 16, left) confirm the predictions obtained with the DSID model (e.g., Figure 66). The damaged zone predicted exhibits the same ring-shape as in the reference studies (Table 16). In a homogeneous rock mass, cracks open in planes parallel to the wall of the cavity, and the EDZ spreads in concentric circles, with zones of higher crack density closer to the cavity. In heterogeneous hosts, the shape of the EDZ can be affected by rock texture (in bedded formations for instance [169]), but in general, the orientation of cracks is not changed significantly (in usual geological conditions, cracks still open in planes parallel to the cavity wall). The comparison of damage distributions obtained with the DSID model under different stress paths can be used as reference cases in order to infer the state of stress or the stress history of the rock in the EDZ. For instance, a symmetric EDZ is typical of an isotropic state of stress. If both the state of damage and the state of stress are known, the DSID model can be used to explain microscopic crack propagation mechanisms driving the damage (e.g. splitting effects vs. crossing effects).

Table 16: Typical Excavation Damage Zones (EDZ) around tunnels.

Isotropy	Anisotropy
Reported numerical analyses	In field detection
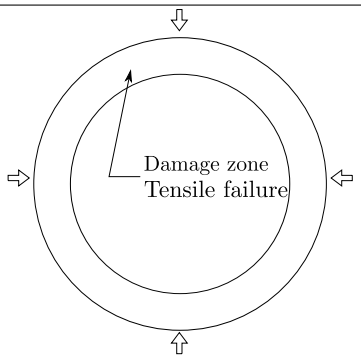	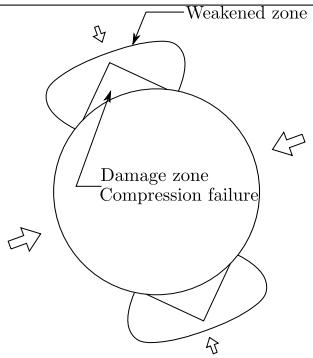
Simulation results	Simulation results
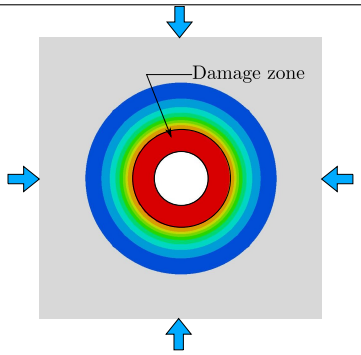	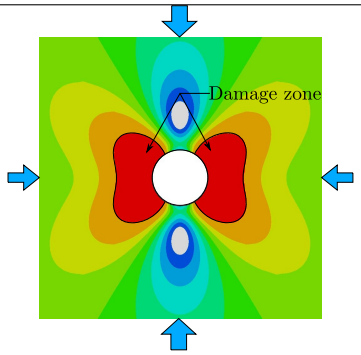
Reference: [169] Hypothesis: brittle failure of horizontally layered rock under isotropic confinement Rock: clay shale Description by numerical analysis: most of cracks are parallel to the surface of hole; some horizontal cracks propagate deeper along the joints.	References: [185, 241, 186, 186, 223, 84, 50] Hypothesis: crack propagation influenced by heterogeneous rock texture Rocks: granite Description from in situ measurements: tensile cracks are generated in planes parallel to the direction of the maximum principal stress (minimum compression); the failure zone spreads along the direction of the minimum principal stress, apart from compressive cracks
Reference: [278] Hypothesis: joints in rock subject to isotropic confinement Rock: jointed rocks Description from numerical analysis and laboratory tests: cracks are parallel to the cavity wall	

5.3.2 Borehole Pressurization in Pre-textured Rock

5.3.2.1 Hydraulic Fracturing in Engineering Mechanics

Hydraulic fracturing is a pressurization process, during which cracks initiate and propagate due to fluid injection. The first research applications were found in petroleum engineering: hydraulic fracturing was used to improve the productivity of oil or gas bearing strata by driving oil and gas flow into the boreholes [282]. Other later applications of hydraulic fracturing were found in dyke maintenance, waste disposal, geothermal reservoirs, and fault reactivation.

Hydraulic fracturing is a complex process. It includes at least three main problems: (1) mechanical deformation induced by the fluid pressure; (2) flow of fluid within the fracture; and (3) fracture propagation [7]. Crack propagation is usually controlled by criteria depending on the energy-release rate. This approach is used in Linear Elastic Fracture Mechanics (LEFM). However, hydraulic fracturing models based on LEFM are scarcely fully coupled to the mechanical behavior of the rock mass, and numerical implementation is not straightforward. Due the heterogeneity of real rock, the effects of temperature gradients, and the possible leak-off of fluids, the fracture propagation condition is necessarily a complex criterion.

That is the reason why hydraulic fracturing problems are generally not solved with the theory of fracture mechanics. Instead, classical models resort to stress analysis. A typical model problem is the determination of the stress field around a circular borehole subjected to compressive stresses at infinity. Such models are fracture-free and neglect the effects of fractures existing prior to borehole pressurization. As a result, the stress solution is mainly dependent on the geometry of the borehole. The rock mass around the hole is assumed to be an elastic, isotropic homogeneous material and the domain of study is assumed to be infinite. Hydraulic fractures are assumed to initiate at the points where the tangential stress reaches the tensile strength of the rock, and the fractures propagate in the direction perpendicular to that tangential stress [282]. Stress analyses can be validated by in situ stress measurements. The Hydraulic Tests on Pre-existing Fractures (HTPF) are based on direct measurement of the normal stress supported by pre-existing fracturing planes.

The Fracture Pressurization (FP) method is an indirect method to determine stress in the absence of pre-existing cracks. In Hayashi's model, two symmetrical notches are considered as starting points of fracture propagation due to injection.

5.3.2.2 Simulation 1: Initiation of Damage

A purely mechanical pressurization process is modeled to simulate the development of damage around boreholes during hydraulic fracturing: it is assumed that a high-pressure gas is injected into the rock mass on a localized portion of a wellbore. The domain under study is a cylinder 20 m in diameter, and 20 m in height. The borehole's diameter is 2 m. External and internal boundaries are subjected to a normal pressure of 4 MPa, except on a localized zone of thickness 0.2 m on the inner surface of the borehole. Former work by Halm and Dragon [115] and Shao et al. [242] is used to get a set of damage constitutive parameters calibrated against experimental rock mechanics test results. The parameters chosen in the simulations are typical of a granite (Table. 13). In the following figures, the value taken by the damage function f_d is displayed for each Finite Element. A non-negative value of f_d indicates that the element is experiencing damage.

First, initiation of damage due to pressurization is simulated by assuming that the rock mass around the borehole is initially undamaged. Figures 82 and 83 indicate that damage propagates into the rock mass within a zone increasing in size along both radial and axial directions. The damaged zone presents several symmetries in three dimensions, which are in agreement with the definition of the damage-driving force controlling the initiation and propagation of damage. A plot of the damage components (not shown here) also indicates that as expected, cracks open in planes perpendicular to the wellbore axis.

5.3.2.3 Simulation 2: Damage Propagation from Notches

In this second example, hydraulic fracturing is simulated under the assumption that notches at the wellbore walls were previously created to enhance fracture propagation during fluid injection. The geometry of the domain is kept unchanged, except for the presence of two conic notches, 0.2m in diameter (at the wellbore wall) and 0.7m in length. Figure 85 shows the geometry of the initial defect.

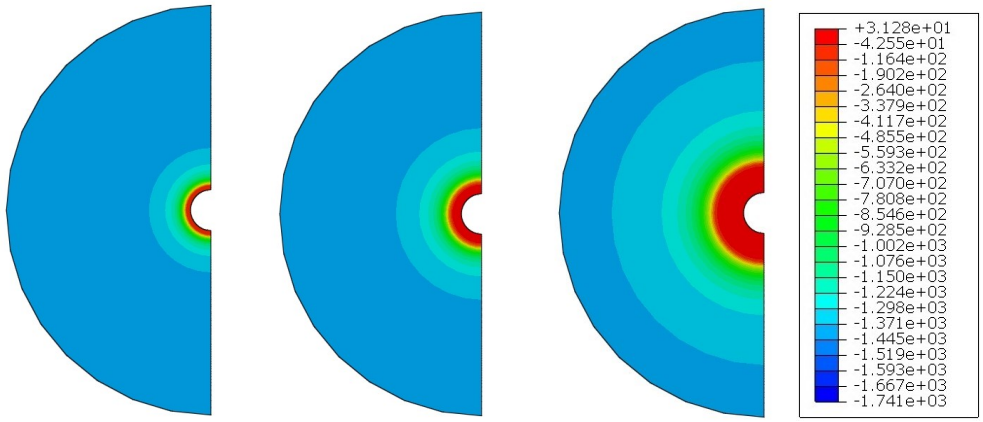

(a) $p = 20$ MPa (b) $p = 50$ MPa (c) $p = 200$ MPa

Figure 82: Damage zone evolution for the pressurization of the cylindrical borehole (transversal cross section). *The contour map shows the values taken by the damage function f_d: a non-negative value indicates that the Finite Element is experiencing damage.*

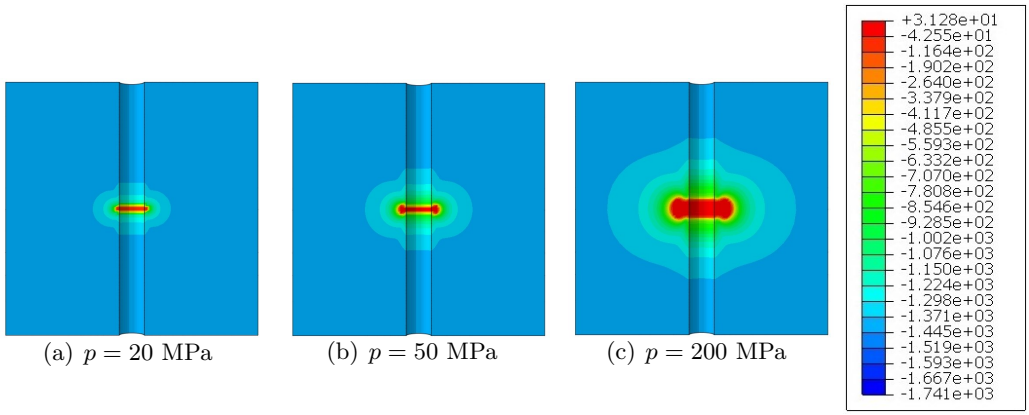

(a) $p = 20$ MPa (b) $p = 50$ MPa (c) $p = 200$ MPa

Figure 83: Damage zone evolution for the pressurization of the cylindrical borehole (axial cross section). *The contour map shows the values taken by the damage function f_d: a non-negative value indicates that the Finite Element is experiencing damage.*

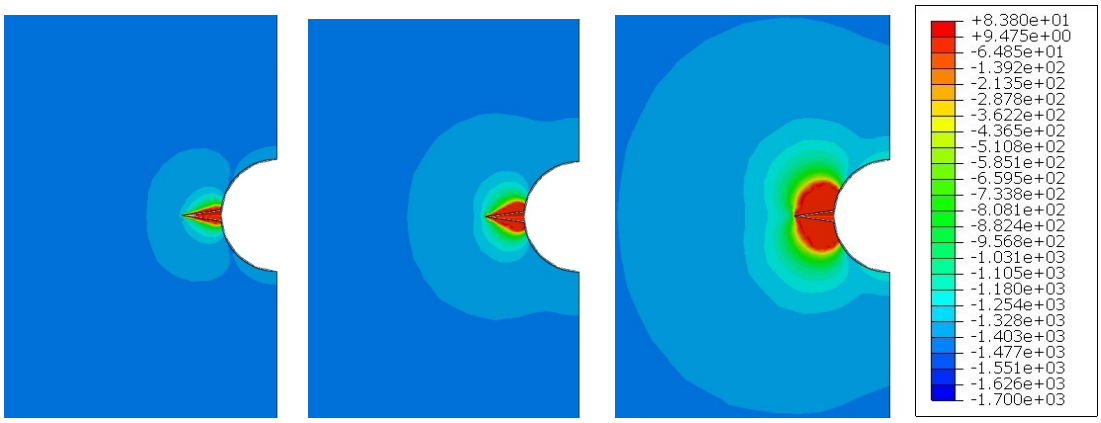

(a) $p = 20$ MPa (b) $p = 50$ MPa (c) $p = 200$ MPa

Figure 84: Damage zone evolution for the notch under pressure (transversal cross section). *The contour map shows the values taken by the damage function f_d: a non-negative value indicates that the Finite Element is experiencing damage.*

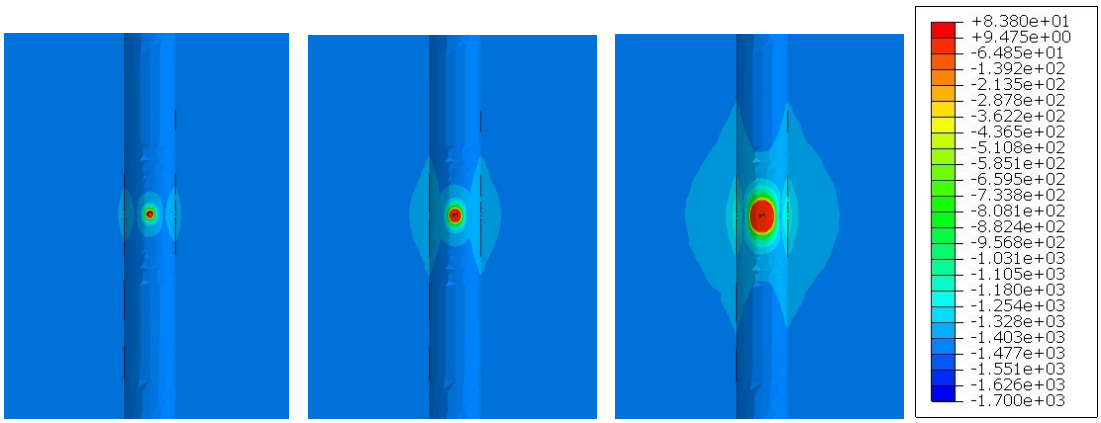

(a) $p = 20$ MPa (b) $p = 50$ MPa (c) $p = 200$ MPa

Figure 85: Damage zone evolution for the notch under pressure (axial cross section). *The contour map shows the values taken by the damage function f_d: a non-negative value indicates that the Finite Element is experiencing damage.*

The damage zone generated during the simulations is almost symmetric and localized near the notch (Figure 84). Damage localizes around the notch (Figure 85(a)), and propagates radially (due to axis-symmetric conditions). For high pressures, damage tends to propagate ahead of the notch tip (Figures 85(b) and 85(c)). In this second set of simulations, the surface of application of the normal pressure is much smaller than in the first set of simulation. The resulting damage driving force is therefore much smaller, so that under similar stress conditions, the extent of the damage zone is much smaller than in the previous set of simulations on damage initiation.

5.3.2.4 Simulation 3: Damage Propagation in a Smeared Damaged Zone

In the last example below, it is assumed that the rock mass has been pre-damaged mechanically (by explosion or by bullet projection for instance) in order to enhance hydraulic fracturing. Crack planes perpendicular to the axis of the wellbore are assumed to exist in the initial state (before fluid injection), in a zone spreading over 0.2m along the wellbore axis, and 0.7m in the radial direction. The initial damage component is set as (y-direction is the vertical direction in Figure 87)

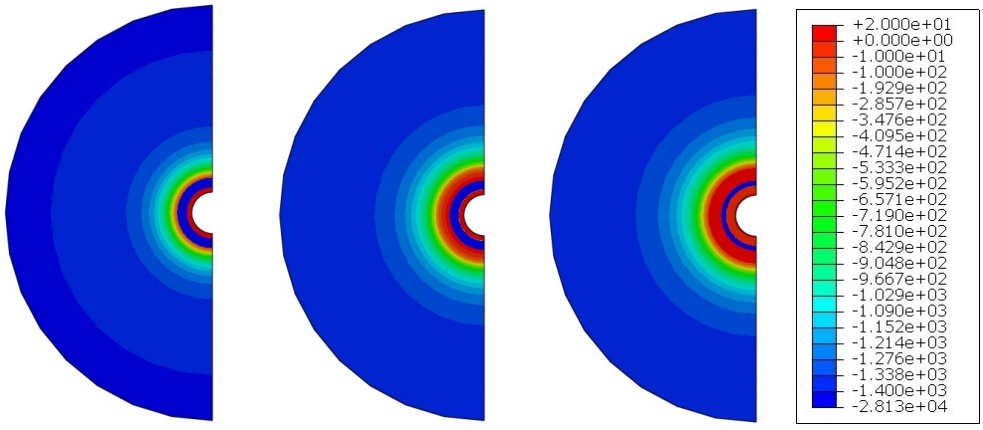

(a) $p = 80$ MPa (b) $p = 150$ MPa (c) $p = 200$ MPa

Figure 86: Damage zone evolution with a smeared damaged zone (transversal cross section). *The contour map shows the values taken by the damage function f_d: a non-negative value indicates that the Finite Element is experiencing damage.*

The shape and extent of the new damage zone during pressurization is very similar to the one obtained in the first example (Figures 86 and 87). However, because of the

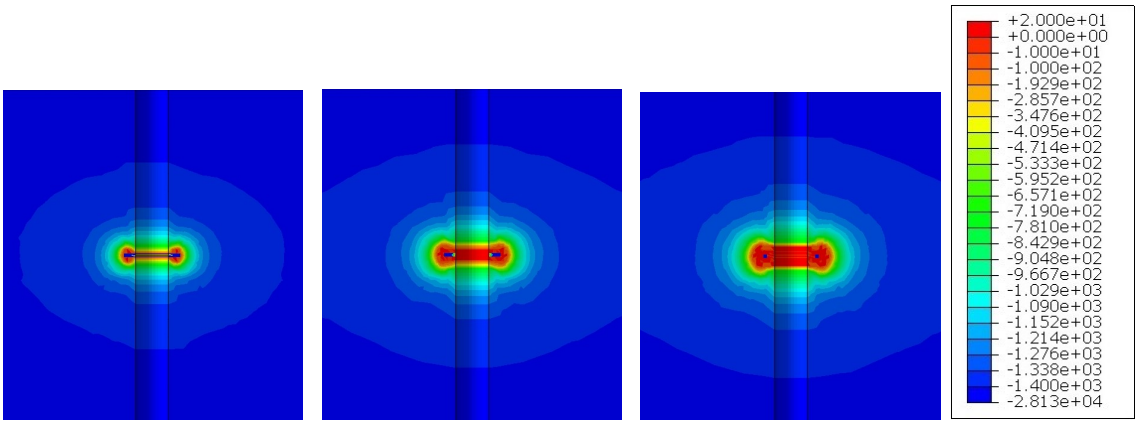

(a) $p = 80$ MPa (b) $p = 150$ MPa (c) $p = 200$ MPa

Figure 87: Damage zone evolution with a smeared damaged zone (axial cross section). *The contour map shows the values taken by the damage function f_d: a non-negative value indicates that the Finite Element is experiencing damage.*

existence of initial cracks, rock mechanical response is different. According to the damage criterion used in the DSID model, initial damage tends to harden the rock. Therefore, it requires more mechanical energy to build up damage on the top of existing cracks. Damage generated during pressurization first concentrates around the initial damage zone (Figure 87(a)). This phenomenon represents well what would happen in the viscosity-dominated propagation regime of hydraulic fractures[231]: pre-existing cracks tend to open without growing. Once damage ahead of the damage zone starts to initiate (Figure 87(b)), damage propagates very rapidly in the radial direction, because the damage threshold (to open new cracks) is low in pristine rock (Figure 87(c)). This part of the simulation reproduces what would occur after the viscosity-dominated propagation regime: once the lag between the fluid propagation front and the fracture tip becomes negligible, rock toughness is the parameter controlling hydraulic fracture propagation. The final damaged zone obtained in this third example is not localized like in the second example. Therefore, it can be concluded that simulating pre-existing damage by setting a non-zero value for the damage tensor is an efficient way to link fracture propagation problems at the borehole and continuum scales.

5.4 Summary

5.4.1 Finite Element analysis of size effects and localization

In this chapter, triaxial compression tests were simulated with the Finite Element (FE) Method, in order to examine size effects and mesh dependence. For similar mesh refinement and external loading conditions, higher stress concentrations were obtained for smaller sample sizes. As expected, the deviation from the ideal stress-strain curve predicted in the one-element simulation was larger for a plug test (sample 1×2 inch. in size) than for a "core" test (sample 4×6 inch. in size). Parametric studies also showed that the anisotropy index of pre-textured rock increases less than that of homogeneous rock in similar loading conditions. Shale delamination planes were modeled with a discrete fracture model and with a smeared damage zone. A lower level of elastic deformation energy was obtained with the smeared damage zone model, because damage propagation in that zone results in stiffness reduction and softening. Energy maps also showed that dissipation due to both crack debonding and crack opening occurs first at the circumference of the sample, and then propagates towards the core of the sample.

5.4.2 Finite Element Analysis of damage propagation in reservoir geomechanics problems

A FE analysis of cavity stress relaxation and cavity pressurization was performed in order to characterize the stress paths leading to shear damage and to compare the orientations of stress and damage for various anisotropic loadings, differential stress intensities and loading sequences. It was verified that in the absence of damage, FE predictions match analytical stress distributions predicted by the theory of elasticity. Damage propagation results in a stress relaxation at the vicinity of the cavity. Damage induced by pressurization under extra vertical pressure results in complex damage distributions, which represent several families of cracks, mainly crossing cracks at the top and bottom of the cavity, and shear cracks in the other radial directions. Competing crossing effects result in damage rotation. Applying an additional vertical load prior to a stress relaxation intensifies damage in the vertical and horizontal directions. The intensity of damage is reduced when the stress relaxation

is performed before the application of the additional load. The presence of an extra load results in significant shear damage, of the same order of magnitude as horizontal and vertical damage. Simulations also highlighted isotropic distribution of damage around pressurized boreholes of circular cross-sections embedded in an isotropic rock mass. As expected, the damage zone is larger in initially damaged rock, and concentrates around discontinuities such as notches.

CHAPTER VI

MODELING OF MULTISCALE CRACK PROPAGATION

6.1 Review of Crack Propagation Models at Different Scales

This chapter presents preliminary work aiming to:

- Model the interaction between discontinuities propagating at different scales simultaneously (e.g., a fracture within a damage process zone),
- Model crack coalescence as a transition between smeared damage zone evolution and discrete fracture propagation.

Tables 17-20 provide an overview of the modeling strategies available at the micro-, meso- and macro- scales.

6.2 Numerical Models at the Macroscale: XFEM vs. FEM

6.2.1 Principle of the EXtended Finite Element Method (XFEM)

Extended Finite Element Methods (XFEM) belong to the family of models based on the local Partition of Unity Finite Element Method (PUFEM). The idea sustaining XFEM is to add discontinuous enrichment functions to the Finite Element approximation to account for the presence of a crack. The geometry of the cracks is explicitly modeled and remeshing is not required. Level set and fast marching methods are used to track moving boundaries.

6.2.1.1 Enrichment

The most general expression of a Finite Element approximate solution is

$$\mathbf{u} = \mathbf{p}^T \mathbf{a} = \sum_{k=1}^{n} p_k \mathbf{a}_k \tag{238}$$

in which the $\mathbf{a}_k$ are degrees of freedom and the p_k are basis functions satisfying differentiability, completeness, independence and boundary condition requirements. Usually, the degrees of freedom used in Finite Element Methods are the nodal values of the dependent

Table 17: Crack propagation models at different scales: Bibliographic References.

Micro-scale 10^{-6}m - 10^{-3}m Micro-cracks **Micromechanics**	**Meso-scale** 0.1m - 1m R.E.V. **CDM**	**Macro-scale** 1m - 10^{3}m Fracture **LEFM**
Fundamentals of micromechanics: Sneddon et al. (Griffith theory) [251, 250, 112], Dormieux et al. (micromechanics and homogenization) [155]	***Definition and evolution of damage:*** Cowin (relationship between fabric tensor and stiffness tensor) [68], Chow & Lu (evolution laws of anisotropic damage) [62], Murakami & Kamiya (thermodynamic framework to model damage evolution in rock) [197]	***Fundamentals of fracture mechanics:*** Whittaker et al. [282], Westergaard (all the concepts of fracture propagation, but at the micro scale) [281], Sih & Liebowitz (mathematical theory of brittle fracture) [246], Perkins & Kern [216] and Norden [205] (PKN model)
Mathematical background of structural geology: Paterson & Weiss (structural geology and fabric tensors) [210], Oda (concept of fabric tensor at the REV scale, and implications of the choice of the order of the fabric tensor) [206], Takemura & Oda (stereology-based fabric analysis of micro-cracks) [265], Lubarda & Krajcinovic (mathematical relationship between crack density distribution and mesoscopic damage tensors of order 2 and 4) [174], Maleki & Pouya (relationship between a microscopic and a mesoscopic fabric tensor to derive a CDM-based mesoscopic damaged permeability model) [183]	***Phenomenological damage models for rock:*** Halm & Dragon [115], Shao et al. [240, 243], Arson et al. [12, 11, 13, 14, 15, 16, 78, 10, 17, 215, 18]	***Theoretical models of hydraulic fracturing:*** Geertsma & de Klerk (model to predict width and extent of hydraulic fracture) [101], Mack & Warpinski (mechanics of hydraulic fracturing) [182], Khristianovic & Zheltov (hydraulic fracture propagation with highly viscous fluids) [147], Ishida et al. (influence of fluid viscosity in hydraulic fracture propagation) [136], Detournay (toughness versus viscosity regime of fracture propagation in a linear elastic rock mass) [231]
Homogenization of media with microscopic pores or cracks: Lydzba & Shao (for poroelasticity) [181], Deudé et al. (for static damage) [76, 75], Kondo et al. (damaged permeability derived from micromechanics and homogenization) [150], Xie, Shao et al. [286], Lu & Elsworth [173]		***Multi-scale models of hydraulic fracturing:*** Wu & Chudnovsky (influence of a static array of micro-cracks on fracture propagation) [285], Valko & Economides (mechanical fracture propagation criterion based on CDM) [80, 273, 274], Suzuki [259] (influence of dynamic anisotropic damage on shear fault slip), Pruess et al. (concept of equivalent permeability upscaled from the REV scale to the reservoir scale for a static fracture network) [219, 218]
Homogenization schemes with multi-scale damage criteria: Homand et al. (mesoscale damage model based on micro-crack toughness, in which only the damage criterion is based on microscopic fracture mechanics) [125], Swoboda & Yang (discrete description of crack geometry and space homogenization of dissipation variables in two steps) [260]		***Numerical simulation of hydraulic fracturing:*** Adachi et al. [7], Busetti [48], Dahi-Taleghani & Olson [70], Lecampion (initiation and propagation of hydraulic fracture using a cohesive zone model coupling BEM for the mechanical problem and FDM for fluid flow) [159], Shen [244] and Smart [249] (damaged zone around the fracture modeled with elasto-plastic deformation) ***Applications of fracture mechanics:*** Rummel & Winter (laboratory applications of the theory of hydraulic fracturing) [228], Germanovich et al. (modeling hydraulic fracturing at the reservoir scale for innovative injection techniques) [284, 108], Zoback et al. (fracture mapping from and micro-seismic events monitored by geophysical methods) [304, 252, 71, 305]

Table 18: Crack propagation models at different scales: Dissipation Variables.

Micro-scale 10^{-6}m - 10^{-3}m Micro-cracks **Micromechanics**	**Meso-scale** 0.1m - 1m R.E.V. **CDM**	**Macro-scale** 1m - 10^{3}m Fracture **LEFM**
N micro-crack planes of area S_α characterized by a length $r_\alpha = 2\sqrt{S_\alpha/\pi}$ and a normal vector $\mathbf{n}_\alpha$	In the most general case, the mesoscopic dissipation variable is the generalized p-order fabric tensor: $\mathbf{F^{(p)}} = \frac{\pi}{4}\frac{N}{V_{REV}}\int_\Omega\int_0^\infty r^3 p(r,\mathbf{n})\,(\mathbf{n}\otimes\mathbf{n}\otimes...\otimes\mathbf{n})\,dr d\mathbf{n}$ or, in a discrete fashion:	PDEs and the non-dimensional toughness $\mathscr{K} = K'\left(\frac{t^2}{\mu'^5 Q_0^3 E'^{13}}\right)^{1/18}$ and non-dimensional viscosity $\mathscr{M} = \mathscr{K}^{-18/5}$ allow to determine in which regime the fracture propagates.
The dissipation variables are: $\xi_\alpha = (r_\alpha, \mathbf{n}_\alpha)$, $\alpha = 1...N$	$\mathbf{F^{(p)}} = \frac{\pi}{4}\frac{1}{V_{REV}}\sum_{\alpha=1}^{N}(r_\alpha)^3\,(\mathbf{n}_\alpha\otimes\mathbf{n}_\alpha\otimes...\otimes\mathbf{n}_\alpha)$ if $p = 2$, the fabric tensor is Kachanov's crack density tensor: $\mathbf{F^{(2)}} = \frac{\pi}{4}\frac{1}{V_{REV}}\sum_{\alpha=1}^{N}(r_\alpha)^3\mathbf{n}_\alpha\otimes\mathbf{n}_\alpha$	There is no "dissipation" variable in the thermodynamic sense. The dissipation variables are the fracture radius $R(t)$ and aperture $w(r,t)$.
	$\mathbf{F^{(2)}} = \sum_{\alpha=1}^{N} d_\alpha \mathbf{n}_\alpha\otimes\mathbf{n}_\alpha = \mathbf{\Omega}$	Coupled PDEs allow solving for the field functions $R(t)$ and $w(r,t)$, as well as for the fluid pressure $p(r,t)$.

variable $\mathbf{u}$ and the Finite Element approximation writes

$$\mathbf{u} = \sum_{j=1}^{n} \mathbf{N}_j \bar{\mathbf{u}}_j \tag{239}$$

in which the $\mathbf{N}_j$ functions are independent approximation functions (usually polynomials or trigonometric functions), satisfying the interpolation property. The most general expression of a Finite Element approximation combines equations 238 and 239

$$\mathbf{u} = \sum_{j=1}^{n} \mathbf{N}_j \bar{\mathbf{u}}_j \; + \sum_{k=1}^{m} f^k(x) p(x) \mathbf{a}_k \tag{240}$$

in which $p_k(x) = f^k(x)p(x)$ and in which the f^k functions satisfy the partition of unity

$$\sum_{k=1}^{m} f^k(x) = 1 \tag{241}$$

In the XFEM, discontinuities induced by crack propagation are described by adding degrees of freedom in the approximation, and consequently by increasing the number of basis functions p_k. In the Partition of Unity Finite Element Method, the basis functions p_k

Table 19: Crack propagation models at different scales: Evolution Laws.

Micro-scale 10^{-6}m - 10^{-3}m Micro-cracks **Micromechanics**	**Meso-scale** 0.1m - 1m R.E.V. **CDM**	**Macro-scale** 1m - 10^{3}m Fracture **LEFM**
Without kinking effects, the micro-crack α propagates if: $\frac{\partial \mathbf{g}_\alpha}{\partial r_\alpha} = \mathscr{G}_\alpha^c$	Using the normality rule: $\dot{\mathbf{\Omega}} = \mathbf{J} : \mathbf{Y}$ in which $\mathbf{J}$ is the damage characteristic tensor (of rank four for a damage variable $\mathbf{\Omega}$ of rank two) and $\mathbf{Y}$ is the thermodynamic force conjugate to damage.	The evolution of the shape of the fracture is governed by coupled PDEs which can be solved for the fracture radius and aperture, which are thermodynamically conjugate to fluid pressure:
Using thermodynamic conjugation relationships: $-\frac{\partial^2 \Psi^*}{\partial r_\alpha \partial \xi_\alpha} = \mathscr{G}_\alpha^c$	By definition: $\mathbf{Y} = -\frac{\partial \Psi^*}{\partial \mathbf{\Omega}}$ and $\dot{\mathbf{\Omega}} = \dot{\lambda} \frac{\partial \mathscr{Q}(\mathbf{\Omega}, \mathbf{Y}, \mathscr{F})}{\partial \mathbf{Y}}$ with the damage potential $\mathscr{Q}(\mathbf{\Omega}, \mathbf{Y}, \mathscr{F}) = \frac{1}{2} \mathbf{Y} : \mathbf{J} : \mathbf{Y}$.	$w = \frac{8R}{\pi E'} \int_{r/R}^{1} \frac{\xi}{\sqrt{\xi^2 - (r/R)^2}} \int_0^1 \frac{xp(x\xi R, t)}{\sqrt{1-x^2}} \mathrm{d}x \mathrm{d}\xi$ $\frac{\partial w}{\partial t} = \frac{1}{12\mu} \frac{1}{r} \frac{\partial}{\partial r} \left(r w^3 \frac{\partial p}{\partial r} \right)$
With kinking effects, a damage criterion needs to be defined as a function of the two components of affinity $\mathbf{g}_\alpha$: $f_\alpha \left(\mathbf{g}_\alpha^n, g_\alpha^t \right) = 0$, in which: $\mathbf{g}_\alpha^n = -\frac{\partial \Psi^*}{\partial \mathbf{n}_\alpha}$, $g_\alpha^t = -\frac{\partial \Psi^*}{\partial r_\alpha}$.	The damage surface is written in the form: $\mathscr{F}(\mathbf{\Omega}, \mathbf{Y}) = \sqrt{\mathscr{G}(\mathbf{\Omega}, \mathbf{Y})} - \mathscr{R}(H(\mathbf{\Omega}, \mathbf{Y}))$ in which $\mathscr{G}(\mathbf{\Omega}, \mathbf{Y})$ is the energy release rate, computed from microscopic variables (microcrack radius and normal vector distributions), and $\mathscr{R}(H(\mathbf{\Omega}, \mathbf{Y}))$ is a damage threshold depending on a hardening variable $H(\mathbf{\Omega}, \mathbf{Y})$ (an additional hardening rule needs to be derived from LEFM principles). In most CDM models however, there is no mathematical proof for the relationship between micro-crack growth and damage increase. In general, the damage evolution law is associate ($\dot{\mathbf{\Omega}} = \dot{\lambda}_d \frac{\partial f_d}{\partial \mathbf{Y}}$) and derives from the expression of a very simple damage surface defined by: $f_d(\mathbf{\Omega}, \mathbf{Y}) = \sqrt{\frac{1}{2} \mathbf{Y} : \mathbf{Y}} - C_0 - C_1 \mathbf{\Omega} : \mathbf{\Omega} = 0$	

Table 20: Crack propagation models at different scales: Model Parameters.

Micro-scale 10^{-6}m - 10^{-3}m Micro-cracks **Micromechanics**	**Meso-scale** 0.1m - 1m R.E.V. **CDM**	**Macro-scale** 1m - 10^{3}m Fracture **LEFM**
In principle, the parameters of the statistical space distribution of cracks ($p(r, \mathbf{n})$) are updated with state variables, but some assumptions can be made to fix them as model parameters. Some statistical relations have to be satisfied, in particular: $\frac{1}{V_{REV}} \int_\Omega \int_0^\infty p(r, \mathbf{n})\, \mathrm{d}r\mathrm{d}\mathbf{n} = 1$ V_{REV} is the scale of observation, chosen to ensure the statistical homogeneity of the sample. In general, it is a fixed parameter of the model. Rigorously speaking, indefinite growth of defects and crack coalescence would require considering the scale of observation as a variable [156]. The damage threshold needs to be characterized in all modeling frameworks. The damage threshold needs to be characterized in all modeling frameworks.		In classical LEFM, coupled PDEs depend on non-dimensional toughness and viscosity, which in turn depend on fracture toughness K_I and fluid dynamic viscosity μ. K_I and μ are thus two mandatory parameters. In the CDM model proposed by Valko & Economides [80, 273, 274], the empirical damage evolution law depends on a coefficient of proportionality between the increment of damage and effective stress. The function determining the state of stress ahead of the crack tip is modified from classical fracture mechanics and depends on two (fixed) scales of observation: the fracture length (L) and the spacing between the micro-cracks ($\widehat{l}$).
Required threshold parameter: critical energy release rate for crack propagation.	For CDM models that do not derive from microscopic LEFM criteria, the required threshold parameters are the initial damage threshold (C_0) and the hardening parameter (C_1).	

are chosen in such a way that the partition of unity requirement be automatically satisfied by the interpolation functions

$$\mathbf{u} = \sum_{j=1}^{n} \mathbf{N}_j(x) \left(\bar{\mathbf{u}}_j + \sum_{k=1}^{m} p_k(x) \mathbf{a}_{kj} \right) \tag{242}$$

$$\forall i = 1..n, \quad \mathbf{u}(x_i) = \bar{\mathbf{u}}_i + \sum_{k=1}^{m} p_k(x_i) \mathbf{a}_{ki} \tag{243}$$

In order to ensure the exactness of the Finite Element approximation at the nodes (i.e. $\mathbf{u}(x_i) = \bar{\mathbf{u}}_i$), the Partition of Unity Finite Element Method approximate solution is expressed as

$$\mathbf{u} = \sum_{j=1}^{n} \mathbf{N}_j(x) \left(\bar{\mathbf{u}}_j + \sum_{k=1}^{m} \left(p_k(x) - p_k(x_j) \right) \mathbf{a}_{kj} \right) \tag{244}$$

The General Finite Element Method (GFEM) approximation writes

$$\mathbf{u}^h(\mathbf{x}) = \sum_{j=1}^{n} N_j(\mathbf{x}) \mathbf{u}_j + \sum_{k=1}^{m} f_k(\mathbf{x}) \psi(\mathbf{x}) \mathbf{a}_k \tag{245}$$

in which ψ is generally a discontinuous function that allows determining on which side of the discontinuity the point considered is (in the solid part or in the crack). The XFEM can be viewed as a particular case of the PUFEM and the GFEM, because the partition of unity required for the enrichment functions are not imposed on the entire domain, but only locally, close to the flaw. The enrichment function $\psi(\mathbf{x})$ can be the Heaviside function:

$$H(\xi) = \begin{cases} 1 & \forall \xi \, 0 \\ 0 & \forall \xi < 0 \end{cases} \tag{246}$$

or signed function:

$$H(\xi) = \text{sign}(\xi) = \begin{cases} 1 & \forall \xi \, 0 \\ -1 & \forall \xi < 0 \end{cases} \tag{247}$$

or the weak discontinuous enrichment function:

$$\chi_k(\mathbf{x}) = |\xi(\mathbf{x})| - |\xi(\mathbf{x}_k)| \tag{248}$$

$$\xi(\mathbf{x}) = \underbrace{\min_{\mathbf{x}_\Gamma \in \Gamma} \|\mathbf{x} - \mathbf{x}_\Gamma\|}_{} \text{sign}(\mathbf{n} \cdot (\mathbf{x} - \mathbf{x}_\Gamma)) \tag{249}$$

6.2.1.2 Level Set Method

The idea is to define signed functions that determine the crack plane and the plane normal to the propagation direction. The surfaces determined by these signed functions define the propagation front. The level set approach takes the original curve and builds it into a surface. A major property of this cone shaped surface is that it intersects the xy plane exactly where the curve sits ([194]).

$$\phi_{,i}\psi_{,i} = 0 \tag{250}$$

with

$$\phi(\mathbf{x}) = \begin{cases} < 0 & \text{behind crack tip} \\ > 0 & \text{in front of crack tip} \\ = 0 & \text{at crack tip} \end{cases} \tag{251}$$

$$\psi(\mathbf{x}) = \begin{cases} < 0 & \text{below crack path} \\ > 0 & \text{above crack path} \\ = 0 & \text{along crack path} \end{cases} \tag{252}$$

6.2.2 The XFEM in ABAQUS

6.2.2.1 Step 1: Introducing nodal enrichment functions

The enrichment functions typically consist of the near-tip asymptotic functions that capture the singularity around the crack tip and a discontinuous function that represents the jump in displacement across the crack surfaces

$$\mathbf{u} = \sum_{i=1}^{n} N_i(x)[\mathbf{u}_i + H(x)\mathbf{a}_i + \sum_{\alpha=1}^{4} F_\alpha(x)\mathbf{b}_i^\alpha] \tag{253}$$

where the $N_i(x)$ are the usual nodal shape functions; $\mathbf{u}_i$ is the usual nodal displacement vector associated with the continuous part of the finite element solution; the second term is the product of the nodal enriched degree of freedom vector, $\mathbf{a}_i$, and the associated discontinuous jump function $H(x)$ across the crack surfaces; and the third term is the product of the nodal enriched degree of freedom vector, $\mathbf{b}_i^\alpha$, and the associated elastic asymptotic crack-tip functions, $F_\alpha(x)$. Figure 88 illustrates the discontinuous jump function across the

crack surfaces, $H(x)$, and the asymptotic crack tip functions in an isotropic elastic material, $F_\alpha(x)$.

$$H(x) = \begin{cases} 1 & \text{if}(\mathbf{x} - \mathbf{x}^*) \cdot \mathbf{n} \geq 0, \\ -1 & \text{otherwise} \end{cases} \tag{254}$$

where $\mathbf{x}$ is a sample (Gauss) point, $\mathbf{x}^*$ is the point on the crack closest to $\mathbf{x}$, and $\mathbf{n}$ is the unit outward normal to the crack at $\mathbf{x}^*$.

$$F_\alpha(x) = [\sqrt{r}\sin\frac{\theta}{2}, \sqrt{r}\cos\frac{\theta}{2}, \sqrt{r}\sin\theta\sin\frac{\theta}{2}, \sqrt{r}\sin\theta\cos\frac{\theta}{2}] \tag{255}$$

where (r, θ) is a polar coordinate system with its origin at the crack tip. These functions span the asymptotic crack-tip function of elasto-statics.

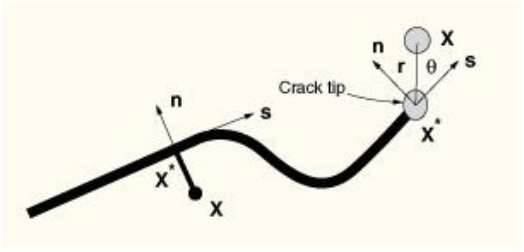

Figure 88: Normal and tangential coordinates for a smooth crack [1]

6.2.2.2 Step 2: Modeling cracks with the cohesive segments method and phantom nodes

This approach is used in Abaqus/Standard to simulate crack initiation and propagation. Unlike the methods that require that the cohesive surfaces align with element boundaries and that the cracks propagate along a set of predefined paths, the XFEM-based cohesive segments method can be used to simulate crack initiation and propagation along an arbitrary, solution-dependent path in the bulk materials. Phantom nodes, which are superposed on the original real nodes, are introduced to represent the discontinuity of the cracked elements, as illustrated in Figure 89. When the element is cut through by a crack, the cracked element splits into two parts. Each part is formed by a combination of some real and phantom nodes depending on the orientation of the crack. Each phantom node and its corresponding real node are no longer tied together and can move apart. The magnitude

of the separation is governed by the cohesive law until the cohesive strength of the cracked element is zero, after which the phantom and the real nodes move independently.

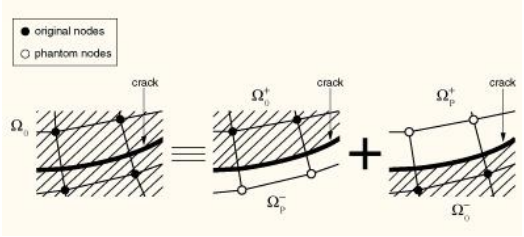

Figure 89: The principle of the phantom node method [1]

6.2.2.3 Step 3: Using the level set method to describe discontinuous geometry

A key development that facilitates treatment of cracks in an extended finite element analysis is the description of crack geometry, because the mesh is not required to conform to the crack geometry. The level set method, which is a powerful numerical technique for analyzing and computing interface motion, fits naturally with the extended finite element method and makes it possible to model arbitrary crack growth without remeshing.

6.2.3 Benchmark of Finite Element models built in ABAQUS

6.2.3.1 Mechanical Benchmark Objectives and Description

The objective of this benchmark is to compare some modeling strategies currently available in ABAQUS software to solve a purely mechanical problem of fracture propagation (Table 21). This study is qualitative and aims to weigh the pros and cons of the models already existing in ABAQUS. Two simple problem geometries are chosen (Figure 90).

- **A circular borehole with one initial fracture tip studied in plane strain.** This can represent an injection problem from an infinitely long vertical well (top view) or from an infinitely long horizontal well (cross-sectional view). Only half of the geometry is meshed (Figure 90(a)), and the domain extent is 6 meters by 6 meters. In the simulations that follow, it is assumed that the well bore is vertical and that the injection is performed at about 200 meters deep. The reasonable fluid pressure injected into the borehole could be as high as 100 MPa. Initially, a 0.4 meter long crack connects to the borehole. The vertical boundary on the left hand-side is an

axis of symmetry, on which the horizontal displacements are fixed. Top and bottom boundaries are constrained in vertical displacement while on the right boundary, there is no horizontal displacement. The stress normal to the wall of the borehole is imposed. The value of that pressure is specified later in this report, for each model tested.

- **A horizontal planar fracture tip studied in plane strain.** This is mainly aimed at predicting the fracture propagation front during injection from a vertical well. The geometry is shown in Figure 90(b). The simulated domain is a 6 m by 24 m rectangle. A 0.6 m long crack is in the mid-depth of the domain. A displacement loading is imposed at the top and bottom surface within 6 m length. The rest of the top and bottom boundaries are free of stress. On both vertical boundaries, shear stress is equal to zero, and horizontal displacements are fixed to zero.

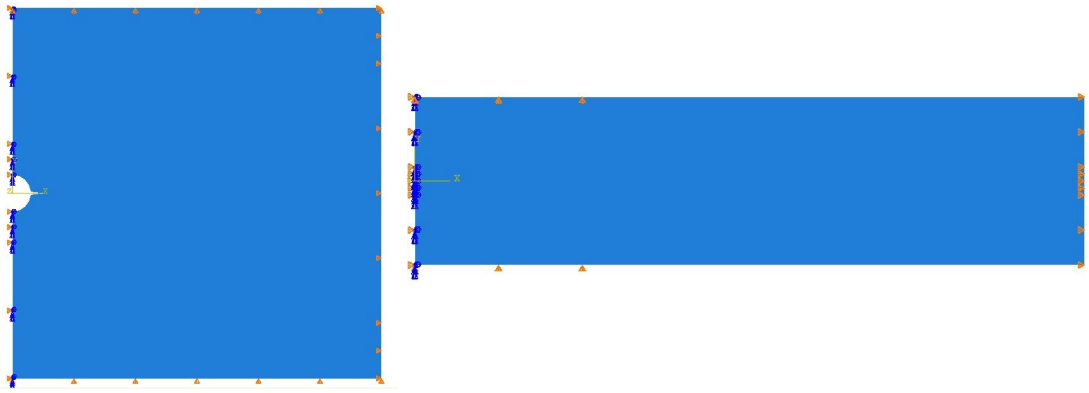

(a) (b)

Figure 90: Geometry of the benchmark problems

The simulation plan is summarized in Table 21. The elastic properties of the rock mass are the same in all simulations, and are given in Table 22.

6.2.3.2 XFEM Results

In XFEM, one initial crack is assumed in the model to define the starting point of propagation. The Virtual Crack Closure Technique (VCCT) criterion is used here to control crack propagation. The VCCT criterion is based on the principles of Linear Elastic Fracture Mechanics (LEFM), and is based on the assumption that the strain energy released when a

Table 21: Summary of the numerical models tested with ABAQUS to simulate a mechanical fracture propagation.

Technique	**Model**	**Benchmark Problems**
XFEM	Fracture propagation in a domain meshed entirely with enriched elements.	Circular borehole embedded in an impermeable intact rock mass and subjected to an isotropic non zero normal stress at the wall.
		Planar fracture tip: initial fracture propagating in impermeable rock due to imposed displacements on both sides of the crack lips.
FEM with Contact Interfaces	Prediction of debonding along element interfaces (the fracture path is known *a priori*).	Planar fracture tip: initial fracture propagating in impermeable rock due to imposed displacements on both sides of the crack lips.
FEM with Elasto-Plasticity: Prediction of a plasticity zone (but not of a fracture front) for the same benchmark problems as in FEM Fracture Mechanics Models.	Mohr-Coulomb Plasticity Model	Circular borehole embedded in an impermeable intact rock mass and subjected to an isotropic non zero normal stress at the wall.
	Drucker-Prager Plasticity Model	

Table 22: Summary of elastic parameters in simulations.

Young's Modulus GPa	Poisson's Ratio -
31.37	0.2

crack is extended by a certain amount is the same as the energy required to close the crack by the same amount. Fracture Mechanics parameters are summarized in Table 23. The simulation results are shown in Figures 91 and 92 for a wall pressure of 100 MPa for the rectangular geometry. The stresses concentrate around the initial crack tip (compression concentration in x-direction and tension concentration in y- direction), so that the crack propagates horizontally (Figure 93 with magnification coefficient of 10). Another example is shown in Figures 94, 95 and 96.

Table 23: Summary of parameters in XFEM simulations.

Damage for Traction Separation Laws and Fracture Criterion			
Max Principal Stress	G_{IC}	G_{IIC}	G_{IIIC}
10.45 MPa	19.58 N/m	19.58 N/m	19.58 N/m
a_m	a_n	a_0	
1	1	1	

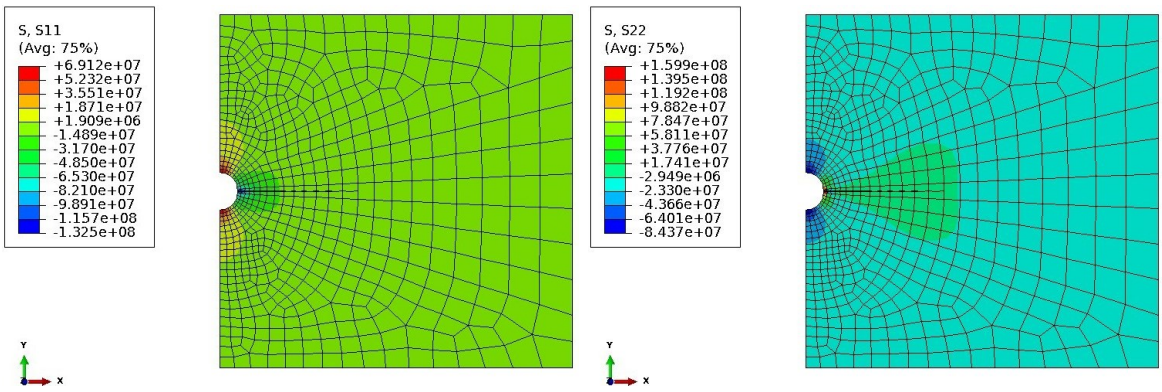

(a) σ_{xx} distribution (b) σ_{yy} distribution

Figure 91: XFEM Simulation: stress distributions.

6.2.3.3 FEM Simulations with Contact Surfaces

In this method, the direction of crack propagation is assumed to be horizontal. Initially, the crack is closed. The crack is modeled as a pair of bonded surfaces. When the fracture criterion is reached, the two surfaces debond from the crack tip node. The crack-tip node actually debonds when the local stress across the interface at a specified distance ahead of the crack tip reaches a critical value. Fracture Mechanics parameters used in the simulations

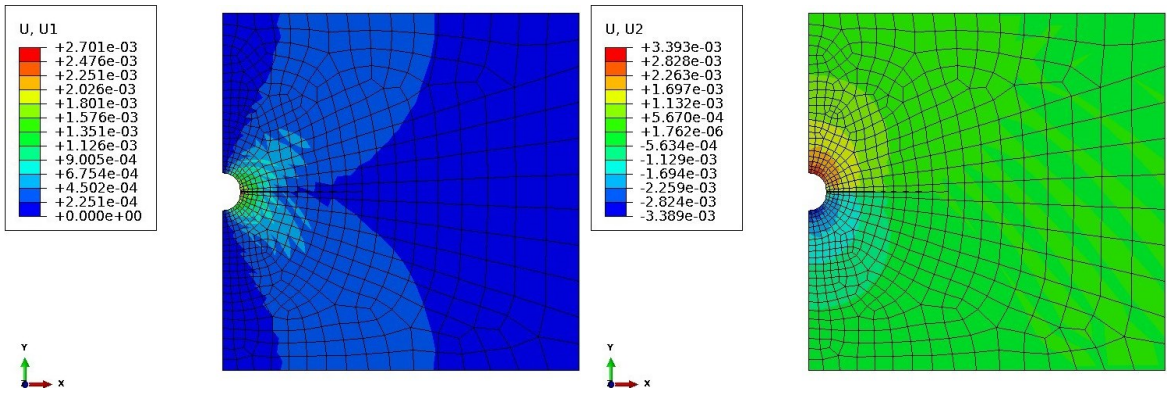

(a) u_x distribution (b) u_y distribution

Figure 92: XFEM Simulation: displacement distributions.

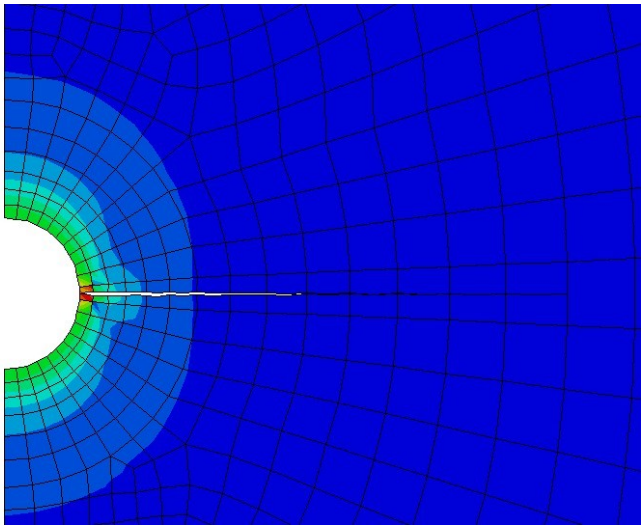

Figure 93: XFEM Simulation: Crack propagation

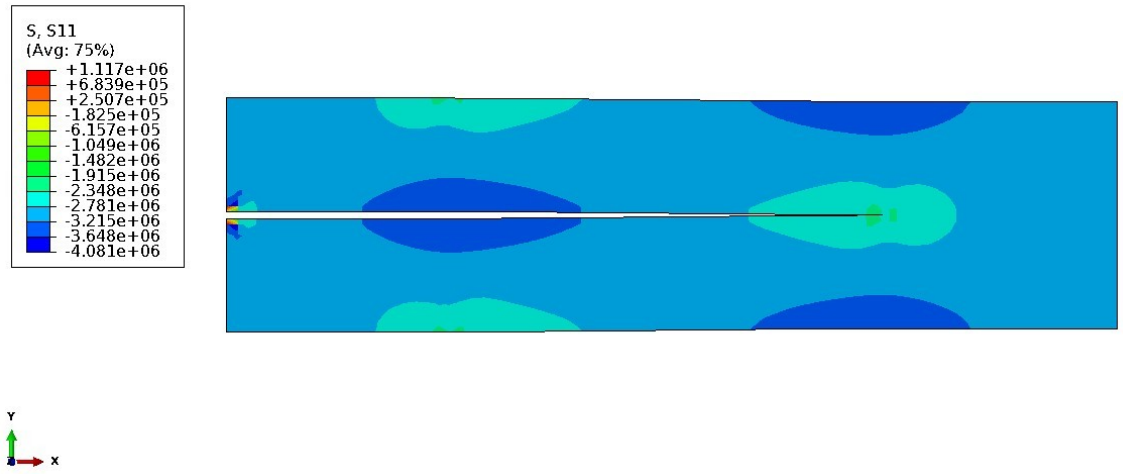

(a) σ_{xx} distribution

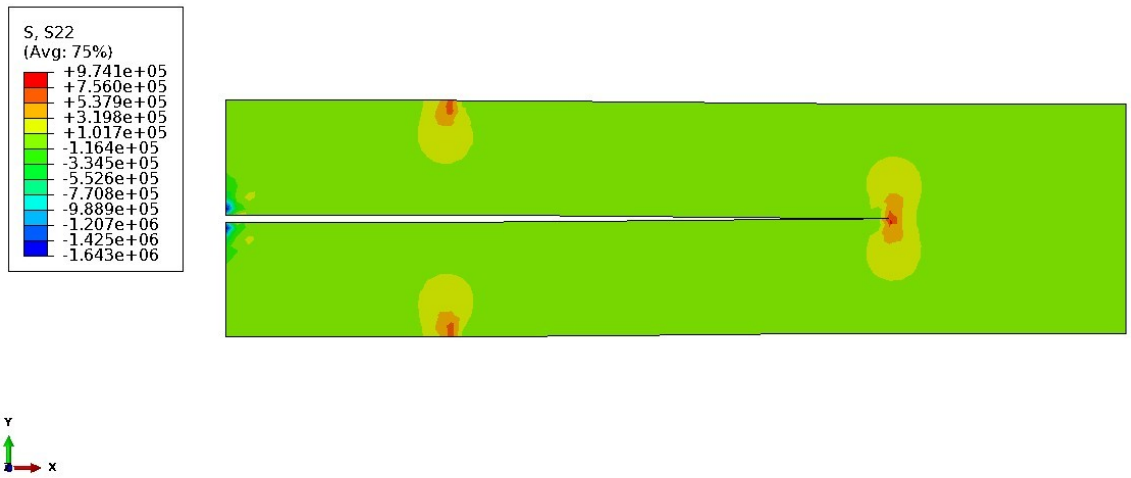

(b) σ_{yy} distribution

Figure 94: XFEM Simulation: stress distributions.

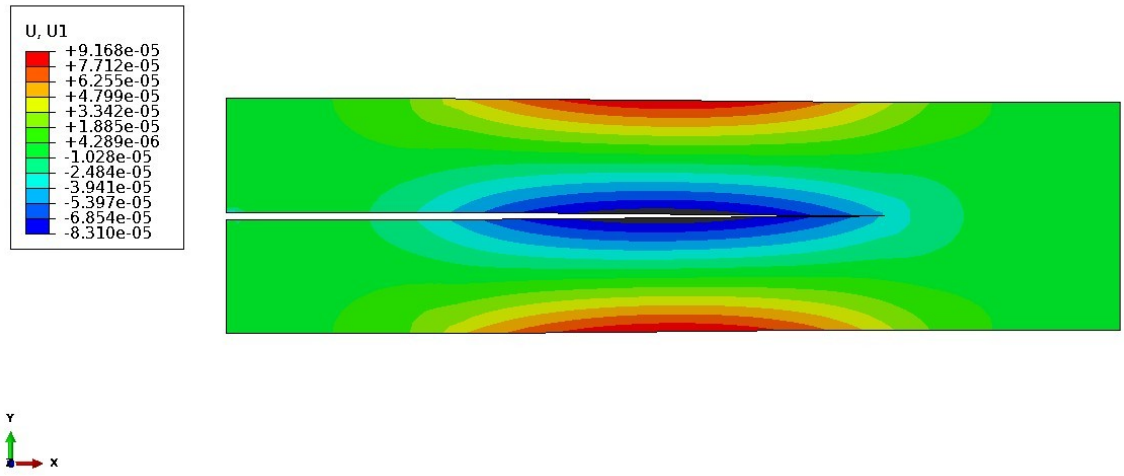

(a) u_x distribution

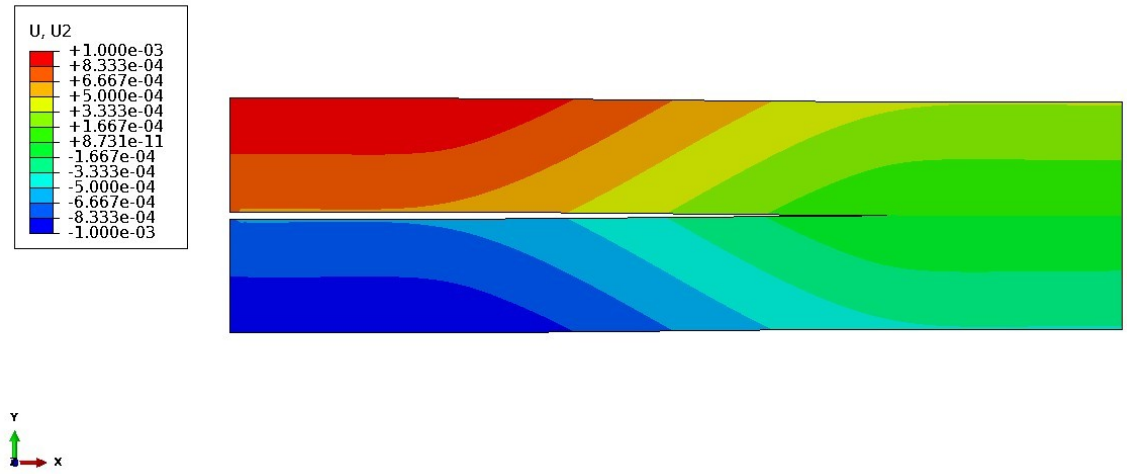

(b) u_y distribution

Figure 95: XFEM Simulation: displacement distributions.

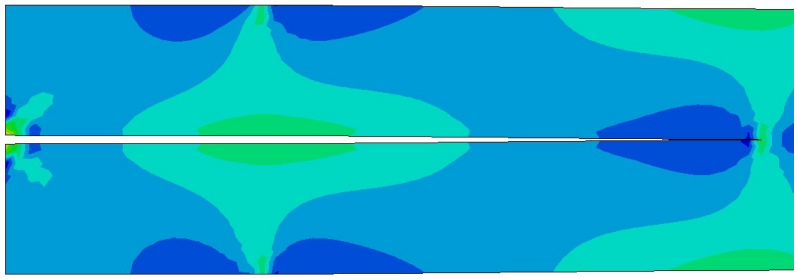

Figure 96: XFEM Simulation: Crack propagation

are summarized in Table 24. The results of simulation are shown in Figures 97 and 98. For simplicity, shear failure stresses are not considered in this simulation. As a result, debonding occurs when normal stress reaches the normal stress limit: this is well illustrated by Figure 97(b), which shows that σ_{yy} reaches the normal failure stress around the crack tip and the surfaces separate in vertical direction.

Table 24: Summary of parameters in FEM with contact surfaces simulations.

Critical stress criterion			
Normal failure stress	Shear failure stress 1	Shear failure stress 2	Tolerance factor
10.45 MPa	0	0	1.0

6.2.3.4 FEM Simulations with Drucker-Prager Plasticity Model

In this problem, it is assumed that a sharp 0.4m-long crack initially extends from the borehole. A pressure of 100 MPAs is imposed at the borehole walls and at the crack surfaces. The yield criterion is based on Drucker-Prager plasticity model. The parameters used in the simulation are given in Table 25. Let us recall that the general form of Drucker-Prager's yield function is the following

$$f(\sigma) = \sqrt{J_2} - \alpha\, I_1 - k \tag{256}$$

where $I_1 = \sigma_{ii}$ is the first stress invariant; $J_2 = \frac{1}{2}(\sigma_{ij} - \frac{2}{3}I_1)(\sigma_{ij} - \frac{2}{3}I_1)$ is the second deviatoric stress invariant; α and k are parameters related to material properties and can be set different values for different yield surfaces. When the Drucker-Prager's yield surface circumscribes the Mohr-Coulomb's yield surface, these two parameters can be obtained

$$\alpha = \frac{2\sin\phi}{\sqrt{3}(3 - \sin\phi)} \tag{257}$$

$$k = \frac{6c\cos\phi}{\sqrt{3}(3 - \sin\phi)} \tag{258}$$

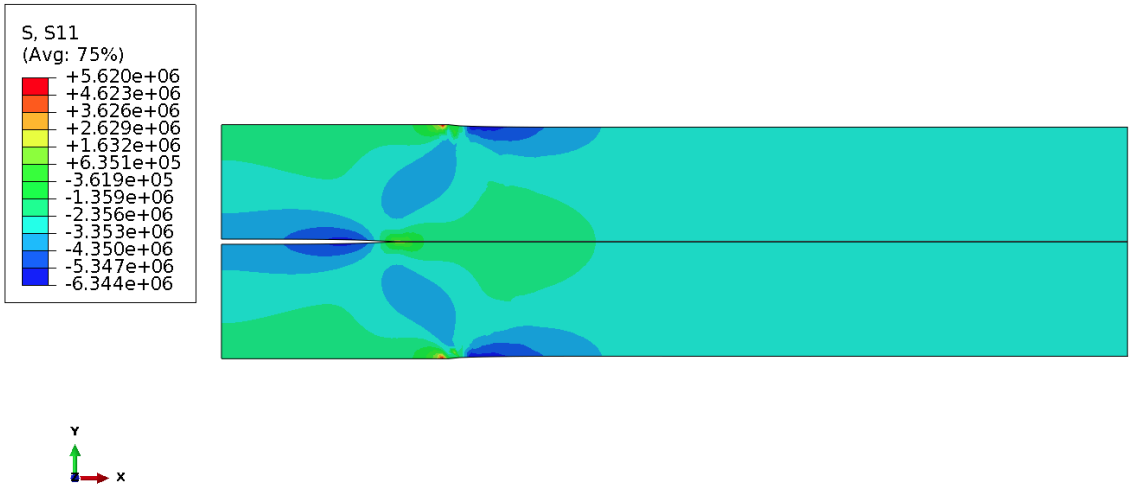

(a) σ_{xx} distribution

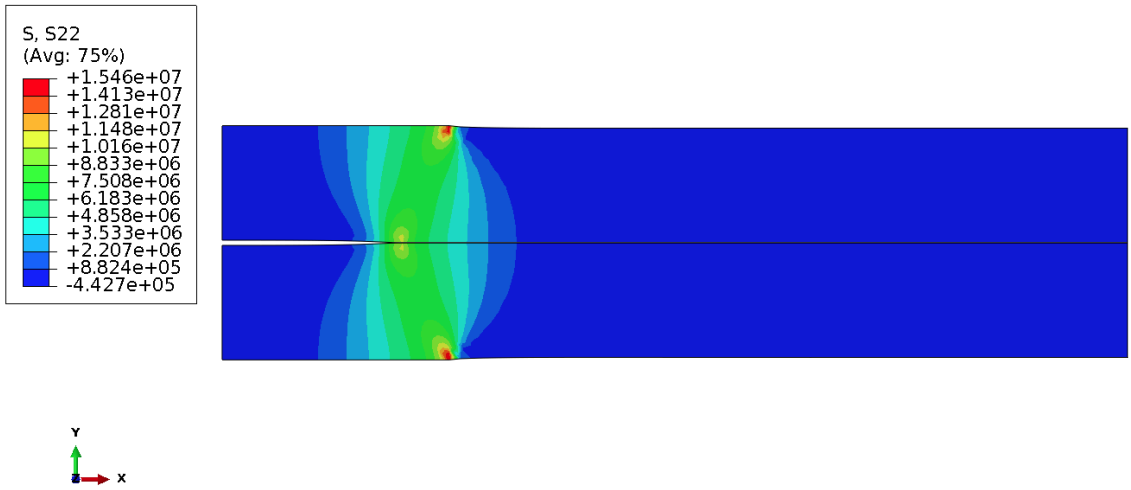

(b) σ_{yy} distribution

Figure 97: Debonding simulation: stress distribution

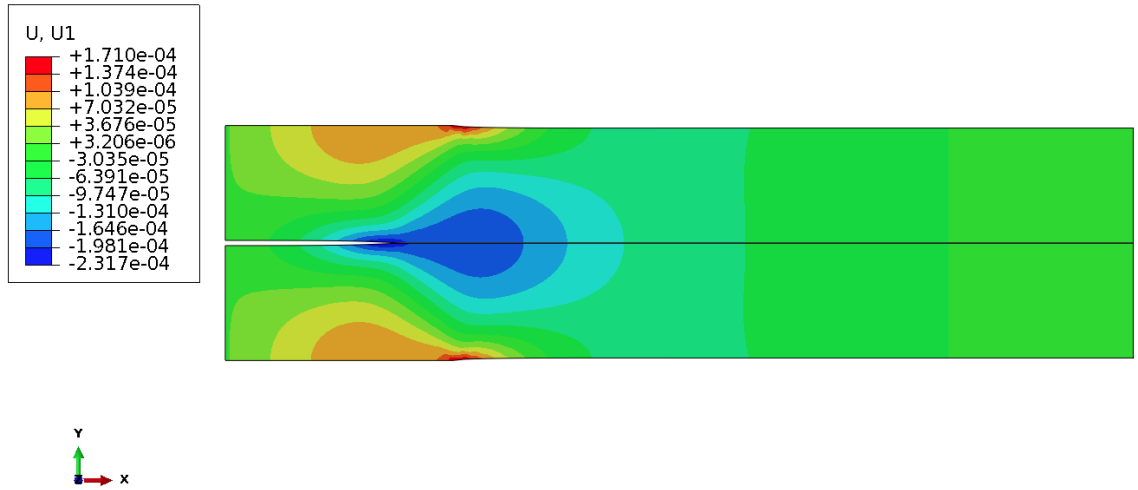

(a) u_x distribution

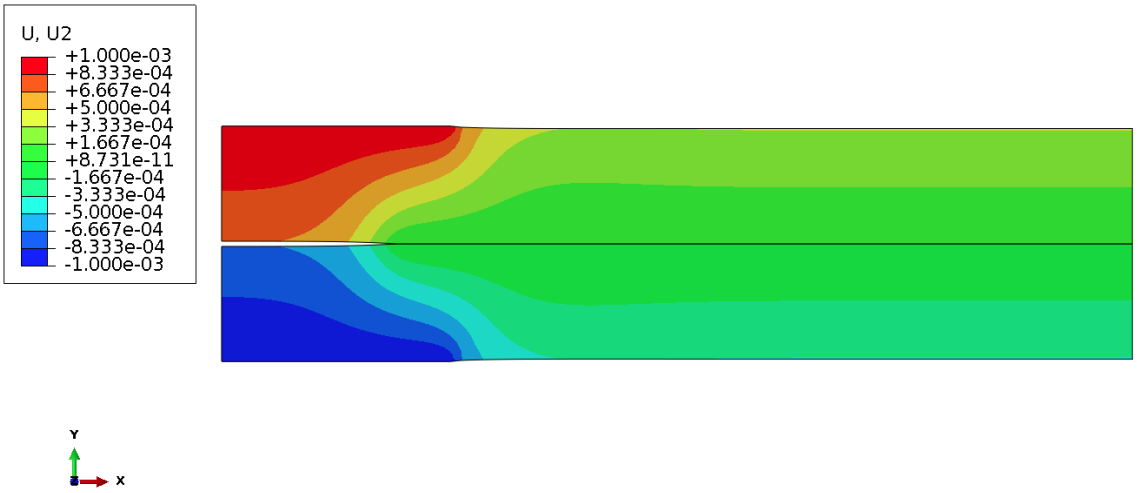

(b) u_y distribution

Figure 98: Debonding simulation: displacement distribution

When the Drucker-Prager's yield surface inscribes the Mohr-Coulomb's yield surface, then

$$\alpha = \frac{\sin\phi}{\sqrt{3(3+\sin^2\phi)}} \tag{259}$$

$$k = \frac{3c\cos\phi}{\sqrt{3(3+\sin^2\phi)}} \tag{260}$$

where c and ϕ are the cohesion and the angle of internal friction, respectively. The governing equation programmed in ABAQUS has a slightly different expression

$$f = \sqrt{3J_2} - 3I_1\tan\phi - c = 0 \tag{261}$$

The distributions of stress and plastic deformation are shown in Figure 99 and 100, respectively. As expected, stress and plastic deformation concentrate around the crack tip. The vertical stress and vertical plastic strain are much larger than the ones in the horizontal direction.

Table 25: Summary of parameters in Drucker-Prager Plasticity Model.

Drucker-Prager Model		
Angle of friction	Flow stress ratio	Dilation angle
30	1	30
Drucker-Prager Hardening		
Yield stress	Absolute plastic strain	
32 MPa	0	
33 Mpa	0.005	
33.5 Mpa	0.08	

6.2.3.5 FEM Simulations with Mohr-Coulomb Plasticity Model

The geometry and boundary conditions are the same as the previous elasto-plasticity problem, but the yield criterion changes from Drucker-Prager Plasticity model to Mohr-Coulomb Plasticity model. The parameters used in the simulation are given in Table 26. Let us recall that the general form of Mohr-Coulomb's yield function is the following

$$f(\sigma) = \sqrt{3J_2} - \sqrt{3}\,m(\theta_l,\phi)\left(\frac{I_1}{3}\sin\phi + c\,\cos\phi\right) \tag{262}$$

The distributions of stress and plastic deformation are shown in Figure 101 and 102, respectively. As expected, stress and plastic deformation concentrates around the crack

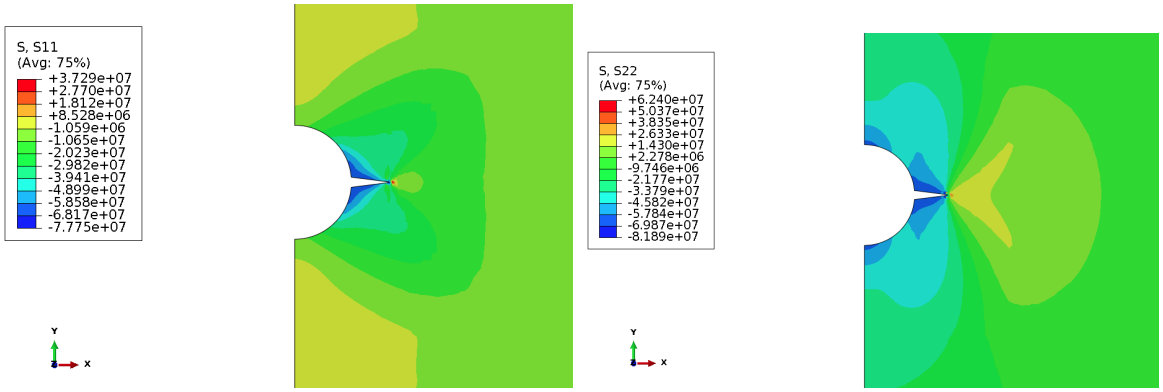

(a) σ_{xx} distribution (b) σ_{yy} distribution

Figure 99: Drucker-Prager Plasticity simulation: stress distribution

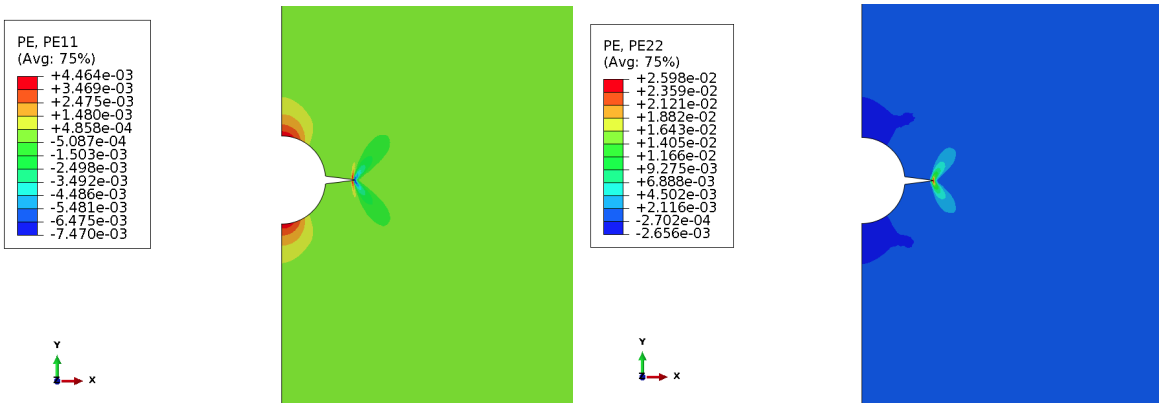

(a) ε_x^p distribution (b) ε_y^p distribution

Figure 100: Drucker-Prager Plasticity simulation: plastic strain distribution

tip. The vertical tensile stress is smaller than the one in horizontal direction. However, the vertical plastic strain is larger than the horizontal one due to the difference of resistance between tension and compression in Mohr-Coulomb model.

Table 26: Summary of parameters in Mohr-Coulomb Plasticity Model.

Mohr-Coulomb Plasticity Model	
Friction angle	Dilation angle
30	20
Cohesion yield stress	Absolute plastic strain
110 kPa	0

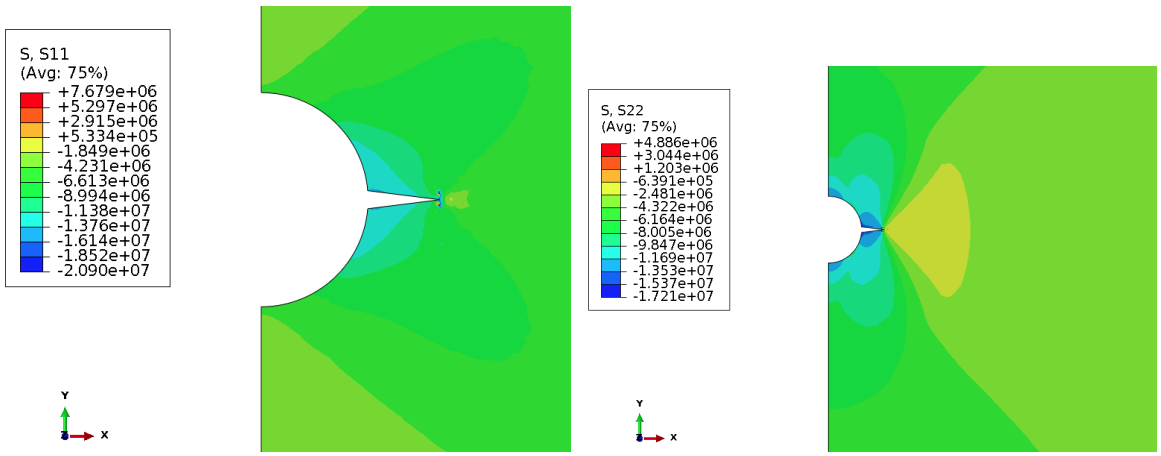

(a) σ_x distribution (b) σ_y distribution

Figure 101: Mohr-Coulomb Plasticity simulation: stress distribution

6.2.4 Stability Problems Encountered in the Benchmark

In the FEM, the evolution of degrees of freedom like displacement is discretized by time steps. The FEM approximation is obtained by summing the increments obtained at each time step. As a result, the error grows at each time step. When the error is not bounded, the scheme is said to be unstable. When the load step generates a lot of plastic deformation, the time step is automatically adjusted by ABAQUS solver in order to satisfy the stability criteria. More iterations are needed in order to reach convergence. When convergence is not reached even for very small time steps, the calculation is aborted. A few cases when the simulation was not terminated are presented below. The geometry of the problem is

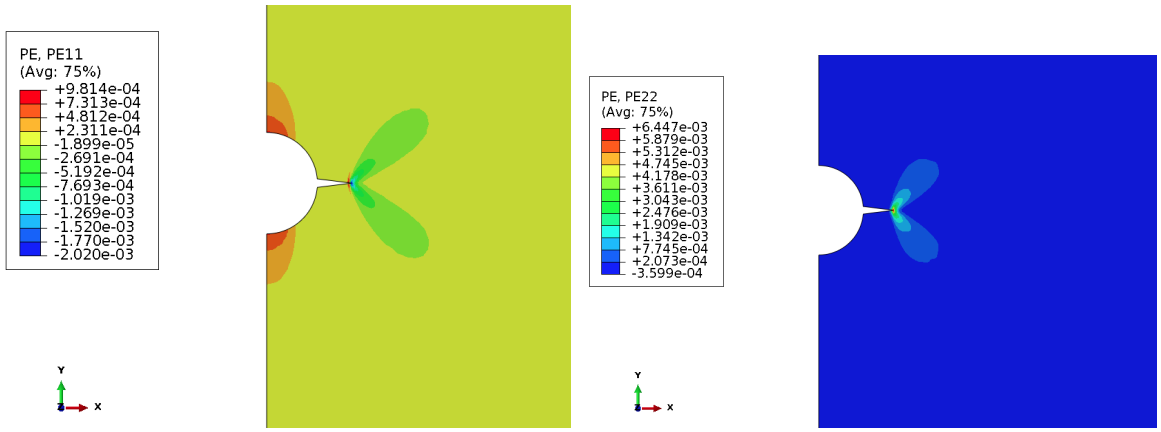

(a) ε_x^p distribution (b) ε_y^p distribution

Figure 102: Mohr-Coulomb Plasticity simulation: plastic strain distribution

the one shown in Figure 90(a). A sharp 0.4m-long static crack is embedded in the wall of the well. A pressure of 100 MPa as the result of water injection is imposed around borehole and at the crack surface. The crack is assumed not to propagate. The simulation results show the development of a plastic zone around the crack tip.

6.2.4.1 Stability Problems with Drucker-Prager Model

The concept of dilation comes from the experimental observation that many materials, especially dense sand, show volume increase under shear stress. The dilation angle is actually the angle between the direction of plastic strain normal to the surface of the plastic potential, and the direction q-axis in p-q plane: see ψ_b in Figure 103. Dilation results in the degradation of stiffness. In general, the dilation angle should be smaller than the friction angle of material, $\psi \leq \phi$. The value of $\psi = 0$ corresponds to no dilatant strain. In practice, the dilation angle tends to decrease as yielding operates. In ABAQUS, the flow rule of linear Drucker-Prager's model is given as

$$G = \sqrt{3J_2} - 3I_1 \tan\psi = 0 \tag{263}$$

As a result, it has to be noted that setting the dilation angle equal to a constant in ABAQUS in unrealistic.

In the simulations presented in the following, the friction angle is set to be 30°, and different simulations were performed for a dilation angle ranging from 15 to 30°. The other

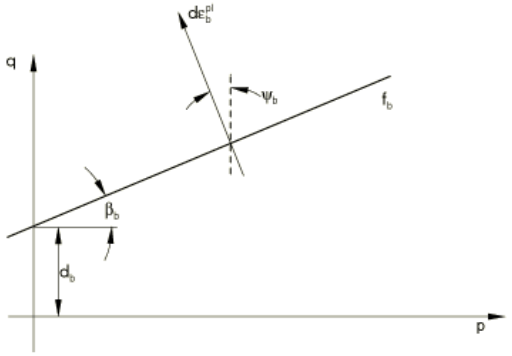

Figure 103: Dilation angle in p-q plane

Table 27: Summary of parameters in Unstable problems with Drucker-Prager Plasticity Model.

Drucker-Prager Model		
Model	Dilation angle	Aborted load (MPa)
I	15	83.77
II	20	81.49
III	25	79.20
IV	30	63.82

parameters were the same as in the preceding benchmark (Table 25). Under the same loading conditions, increasing the dilation angle causes the rate of volumetric strain to increase. For the same boundary conditions (100 MPa applied at the borehole walls and at the lips of the crack), simulations with the highest dilation angle abort at lower load because of difficult convergence (Table 27). Figure 104 shows that for four different values of the dilation angle, plastic deformation starts at the same load substep ($\Delta p = 5.03$MPa), but with different plastic strains: this is because increasing the dilation angle does not change the yield function (i.e.e the threshold at which plasticity occurs), but it affects the plastic potential (controlling hardening). Figure 105 shows that for a given load step, plastic strains are slightly higher for lower dilation angles.

6.2.4.2 Unstable Problems with Mohr-Coulomb Model

In the following simulations done with Mohr-Coulomb model, the friction angle was chosen as 30°, and the dilation angle ranged from 15 to 30°. The other parameters were the same

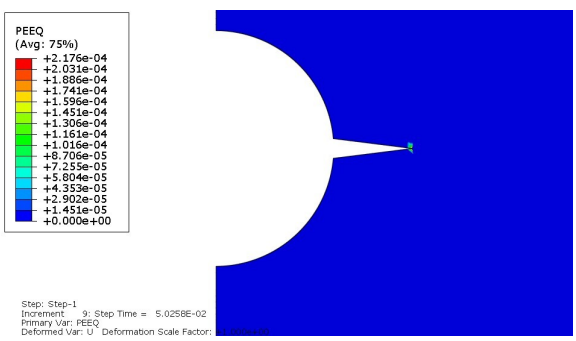

(a) Model I, $\psi = 15°$

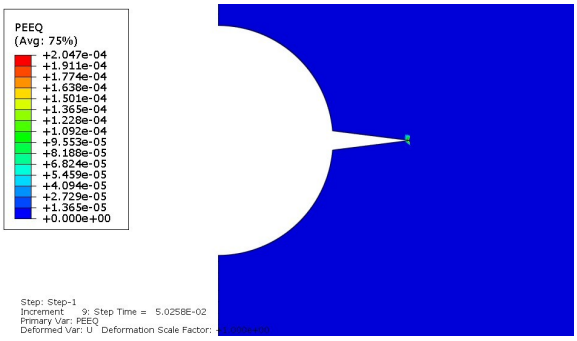

(b) Model II, $\psi = 20°$

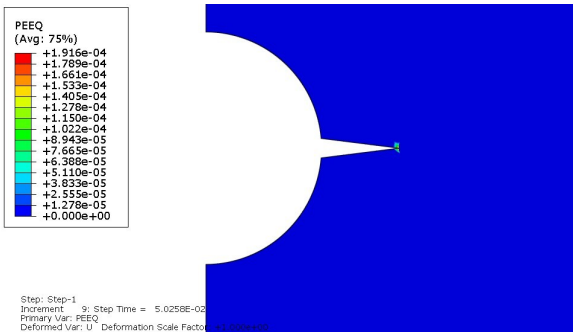

(c) Model III, $\psi = 25°$

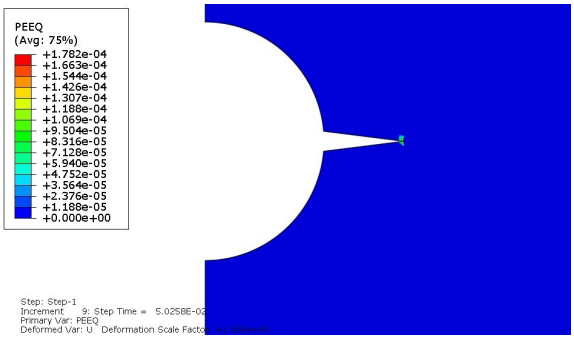

(d) Model IV, $\psi = 30°$

Figure 104: Drucker-Prager Plasticity simulation, for substep $\Delta p = 5.03$MPa.

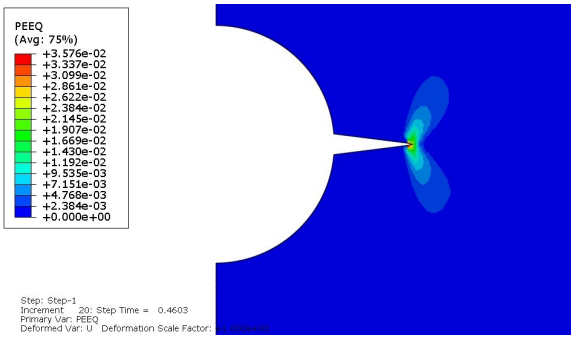

(a) Model I, $\psi = 15°$, $\Delta p = 46.03$MPa

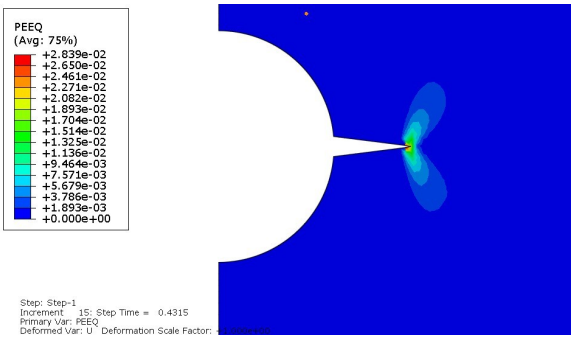

(b) Model II, $\psi = 20°$, $\Delta p = 43.15$MPa

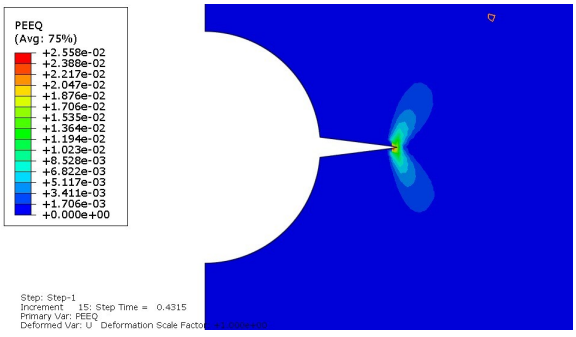

(c) Model III, $\psi = 25°$, $\Delta p = 43.15$MPa

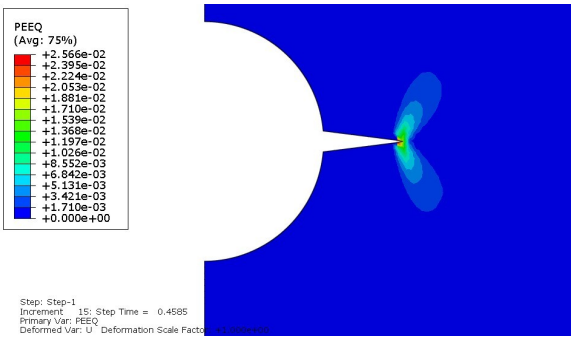

(d) Model IV, $\psi = 30°$, $\Delta p = 45.85$MPa

Figure 105: Drucker-Prager Plasticity simulation, for various substeps.

as precedingly (Table 26). Mohr-Coulomb yield surface and potential surface have sharp corners. Corners are singular points, for which there is no unique flow rule. As a result, the calculation of the increment of plastic strain causes problems. In general, the time needed for the simulations with Mohr-Coulomb model is much longer than with Drucker-Prager model: convergence is more difficult to reach.

$$G = \sqrt{3J_2} - \sqrt{3}\, m(\theta_l, \psi) \left(\frac{I_1}{3} \sin\psi + c \cos\psi \right) \tag{264}$$

All the simulations have aborted before the loading is totally applied, except for the model with a dilation angle of 25°. In the simulation with a dilation angle of 30°, the solver gives a warning message, requesting to set the dilation angle less than 27.452° to ensure stability. Unstable iterations start for a very low load: 0.51MPa before the initiation of plasticity. For lower values of the dilation angle, instability occurs for higher loading (see Table 28). Figure 106 shows that for four different values of the dilation angle, plastic deformation starts at the same load substep ($\Delta p = 0.575$MPa), but with different plastic strains: this is because increasing the dilation angle does not change the yield function (i.e. the threshold at which plasticity occurs), but it affects the plastic potential (controlling hardening). For a given load step, plastic strains are slightly higher for lower dilation angles.

Table 28: Parameters in Unstable problems with Mohr-Coulomb Plasticity Model.

Mohr-Coulomb Model		
Model	Dilation angle	Unstable Load (MPa)
I	15	5.24
II	20	10.11
III	25	Completed
IV	30	0.51

6.3 Towards a Multi-Scale Crack Propagation Model: Energy Dissipated in Mode I with FEM, CZM and XFEM

6.3.1 Scope of the simulations: the need for an energy model

Coupling several models of crack propagation requires determining the fraction of energy dissipated at each scale considered. This issue of "energy budget" is a key towards a better

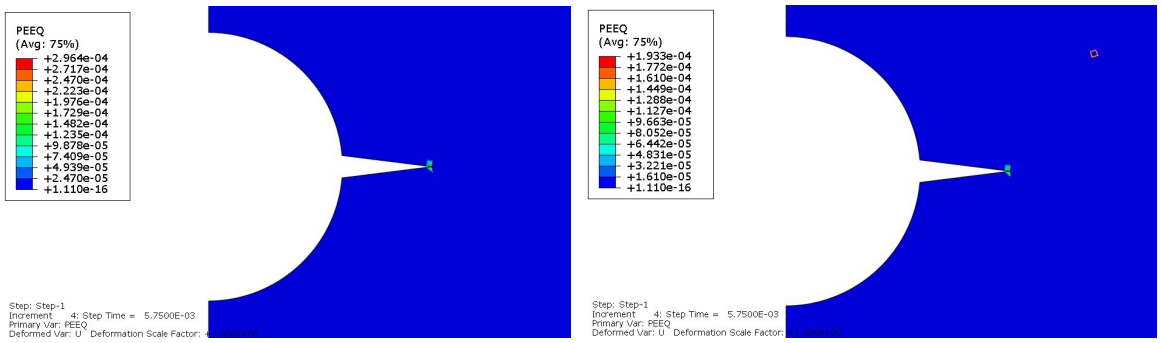

(a) Model I, $\psi = 15°$

(b) Model II, $\psi = 20°$

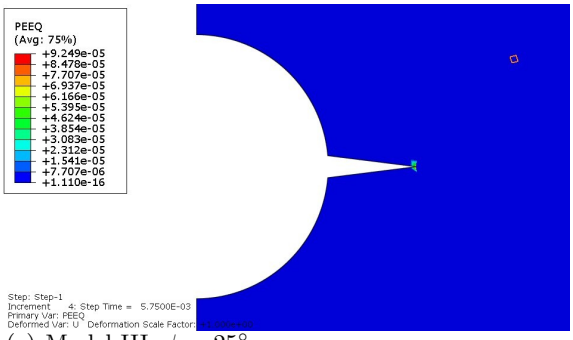

(c) Model III, $\psi = 25°$

Figure 106: Mohr-Coulomb Plasticity simulation

understanding of the inter-play between the propagation of a fracture and the evolution of its damage process zone, which could find applications in geothermal energy exploitation, enhanced oil and gas recovery, and carbon capture. This is also a long-standing problem of fault rupture dynamics. Although micromechanics and fracture mechanics theoretically allow the computation of rock stiffness tensor in fault damaged zones [46, 180], current models fail at predicting the simultaneous and coupled evolution of discontinuities at multiple scales [178, 144]. Valko and Economides [273] used a modified fracture toughness to predict fracture propagation in a damaged rock mass, without mathematical justification. Suzuki [259] proposed a numerical model coupling CDM and shear fault rupture dynamics. Both the microscopic cracks populating the REVs and the fault itself are considered as flat debonded surfaces, which makes it impossible to distinguish isochoric shear deformation from dilatant cracking. Stick-slip predictive models were also proposed to predict faulting (e.g., movement of the tip and rate and state friction at faces) as the result of the propagation of microscopic cracks in a localized zone. Hamiel et al. [117] and Lyakhovsky et al.

[179] linked localized deformation (in the LVFZ for instance) to friction on sliding surfaces, at the price of a simplifying assumption - a linear relationship between the rates of continuum damage rate and visco-elastic strain. Assemblies of springs and dash-pots were used to mimic the rheology resulting from damage accumulating in the LVFZ in the course of several consecutive earthquakes. To avoid the localization problems inherent to this modeling approach, several authors (e.g., [149, 247, 77]) assumed that the structure of the LVFZ is self-organized, i.e., fractal. Mandelbrot [184] designed the fractal distribution to capture the scale-independence of fragmented topologies observed in nature [271], and in earthquake fault systems in particular [229]. For instance, a theoretical CDM model of fractal crack pattern was presented in [270], based on the assumption that the solid fraction of the rock in the LVFZ can be considered as a bundle of fibers. The fractal organization of fibers dictates the form of the damage evolution law. What makes the theoretical framework so powerful also limits the validity of the derivations to one-dimensional problems only. Moreover, the use of the creep law for brittle-elastic solids can actually lead to inconsistencies.

As a matter of fact, modeling the transition from continuum damage to discrete fracture requires not only (1) assessing the size of the REV chosen to compute the energy released due to stress concentrations, but also (2) defining an energy release threshold to replace a highly damaged zone by a portion of macroscopic discontinuity [189]. CDM models used so far in geophysics for this purpose avoid scaling issues (1) by introducing viscous damage evolution laws and/or by assuming fractal distributions of crack patterns, and do not capture the transition in scales in the energy thresholds (2).

In order to couple several numerical models of crack propagation, it is necessary to understand the magnitude and space distribution of energy dissipation predicted by each of these models in similar boundary value problems. As an example, the problem of mode I fracture propagation is analyzed with the DSID model implemented in the FEM, a Cohesive Zone Model (CZM), and the XFEM. The domain under study is a rhomboid (Figure 107). Horizontal displacements along vertical boundaries are all fixed. Vertical displacements are applied on a portion of the top and bottom boundaries. The remainder of the top and bottom boundaries is free of stress. A small defect is embedded in the domain, close to the

left boundary surface. Imposed vertical displacements will open free surfaces in the defect and generate stress concentrations around the crack tip, which will result in the propagation of the crack into the rock mass along the x-direction.

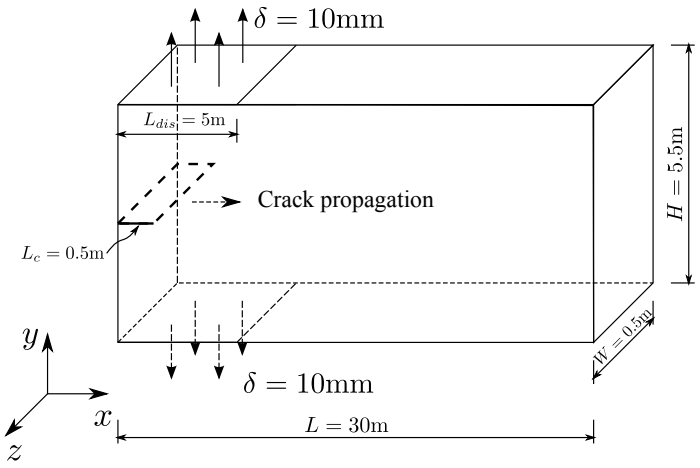

Figure 107: Sketch of the simulation problem.

6.3.2 FEM simulations with the DSID model

The DSID model is employed in a thin layer (two Finite Elements in size) in the middle of the domain. Energy can only be dissipated in the central layer, which will make it possible to compare the DSID model predictions with those of the CZM and XFEM models. The remainder of the domain is assumed to be linear elastic. A tensile zone ahead of the crack tip develops, and stress accumulates in that zone because in CDM, the crack tip cannot move (Figure 108). After damage is induced, the percentage of the elastic energy decreases with the percentage of the irreversible strain energy and crack debonding energy increase (Figure 109). These three energy terms evolve smoothly, which indicates a stable micro-crack propagation around the pre-existing defect. The evolution of the elastic energy density is shown in Figure 110.

6.3.3 CZM simulations

Cohesive Zone Models (CZM), originally proposed by Dugdale [79], were extensively used to simulate fracture and fragmentation processes in concrete, rock and metals. CZM are based on a simplified fracture process zone characterized by a traction-separation law, which

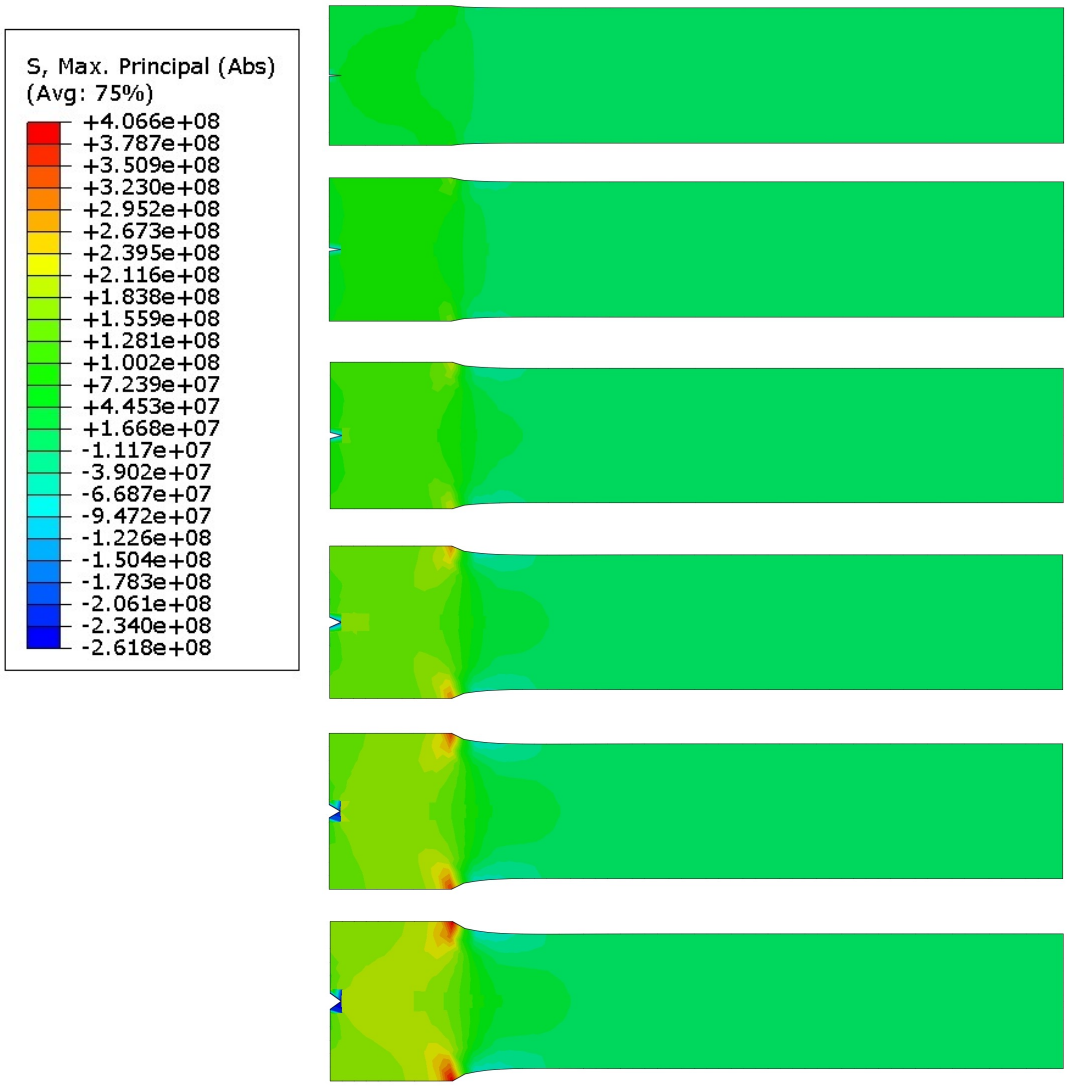

Figure 108: Absolute Maximum Principal Stress distribution during loading processes. Figures correspond to the following the total loading displacements: 3.4, 6.4, 9.8, 14.2, 17, and 20 mm. The figure is displayed with a 50 amplification factor to show the crack opening.

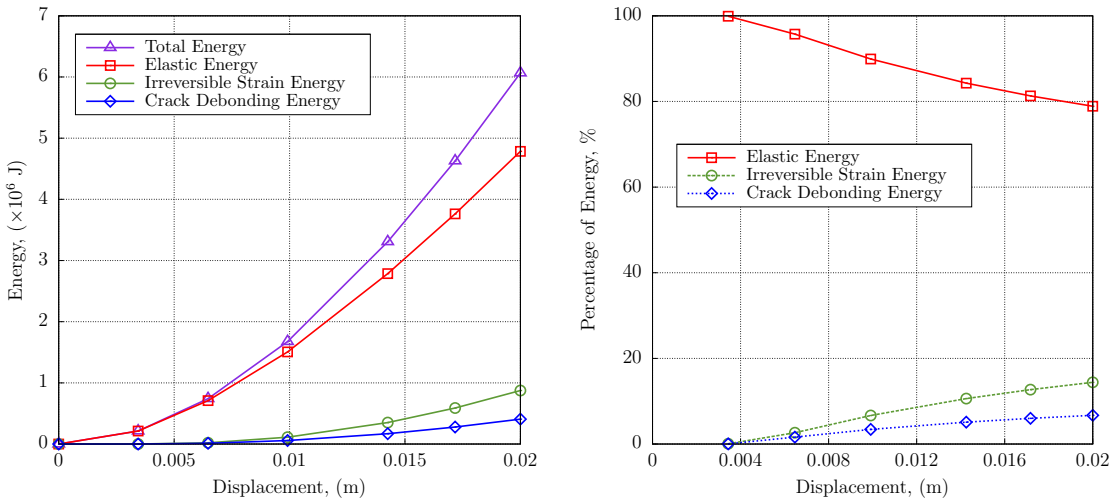

(a) Energy Evolution

(b) Energy fractions

Figure 109: Energy evolution in the problem of mode I fracture propagation simulated with the DSID model.

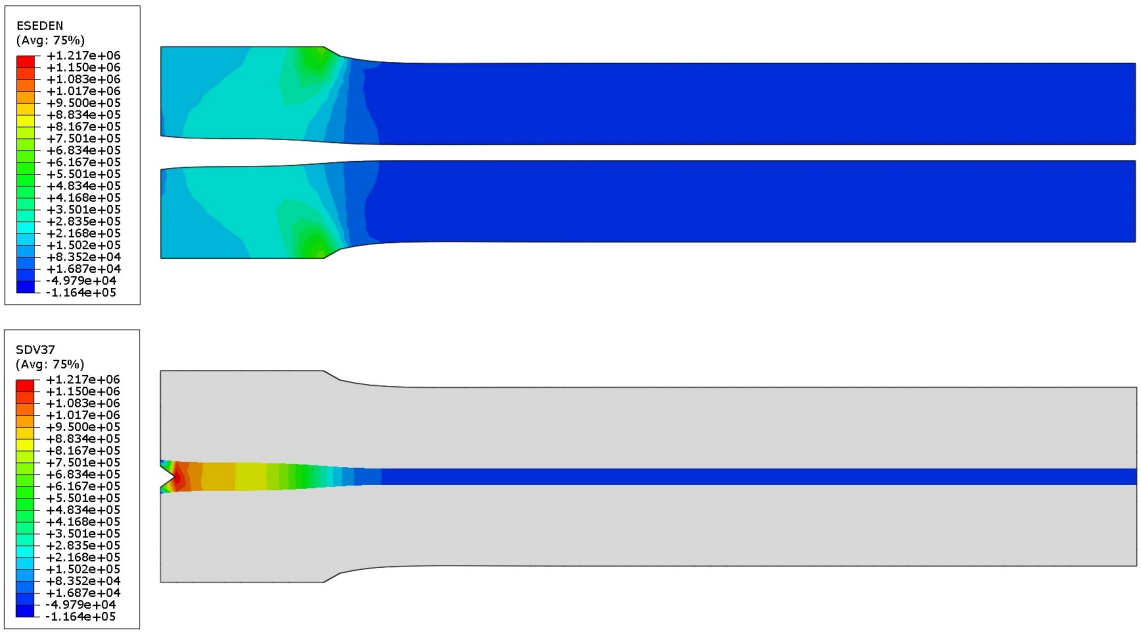

Figure 110: Distribution of the elastic energy density in the DSID model of mode I fracture propagation.

provides an alternative, effective approach for quantitative analysis of fracture behavior through explicit simulation of the fracture processes. In CZM, a traction-displacement relationship across the crack tip represents the degrading mechanisms in the fracture process zone: Figure 111 shows the decohesion relations used for a quasi-brittle fracture. The cohesive crack tip corresponds to the damage initiation point where the traction reaches the cohesive strength t_{max} and where the separation reaches the critical value δ_0. The material crack tip is the complete failure point where the separation reaches the critical value δ_f and the traction or cohesive strength acting across the surfaces are equal to zero. The work of separation, or fracture energy G_c, is the work needed to create a unit area of fully debonded crack. It is formally defined as

$$G_c = \int t \, \mathrm{d}\delta \tag{265}$$

The problem of mode I fracture propagation described above is simulated with the CZM described in Figure 111. For the sake of comparison, the continuum damage model and the discrete fracture models are constructed so as to ensure an equivalent dissipation energy

$$\int \dot{\Phi}_d \, \mathrm{d}t = \int G_c \dot{A} \, \mathrm{d}t \tag{266}$$

The energy dissipated by damage propagation and irreversible deformation in the DSID model is set equal to the fracture energy within the same volume. For a given mesh and for a given continuum damage threshold the fracture energy release rate can be calculated. In the following simulations, the energy equivalence gave $G_c = 120\mathrm{N/m}$. Figure 112 shows the results. Energy dissipated at the beginning of the simulation is less than the elastic energy stored in the sample: this is due to the nature of the decohesion law assumed in the model. When the size of the CZM increases, the surface energy release rate decreases and most of the work provided by the external loading is stored in the form of elastic energy. The rate of elastic energy stored in the sample decreases before CZM propagation, and decreases thereafter. The dissipated energy follows an opposite trend (Figure 113). The final elastic energy density obtained with the CZM is shown in Figure 114, in which the energy density distribution is consistent with the maximum principal distribution shown in Figure 112.

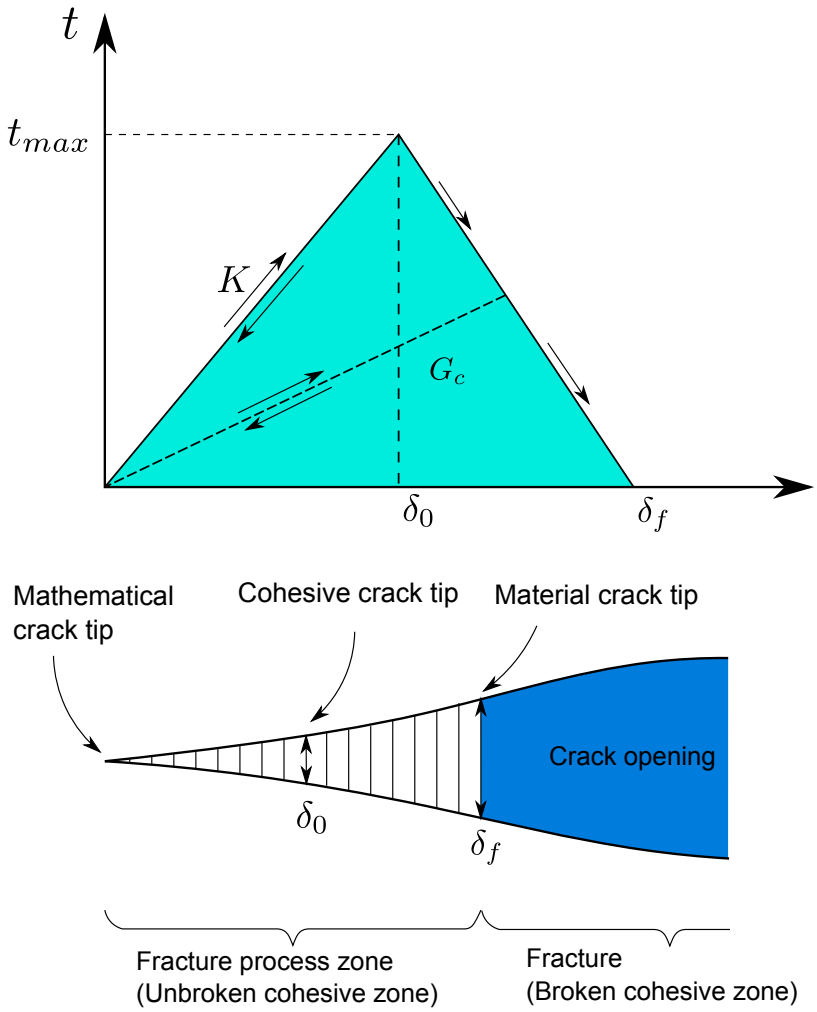

Figure 111: Cohesive Zone Model. Modified from [59, 245].

The high elastic energy density occurs at the position (boundary edge or crack tip) with the higher tensile stress or compressive stress.

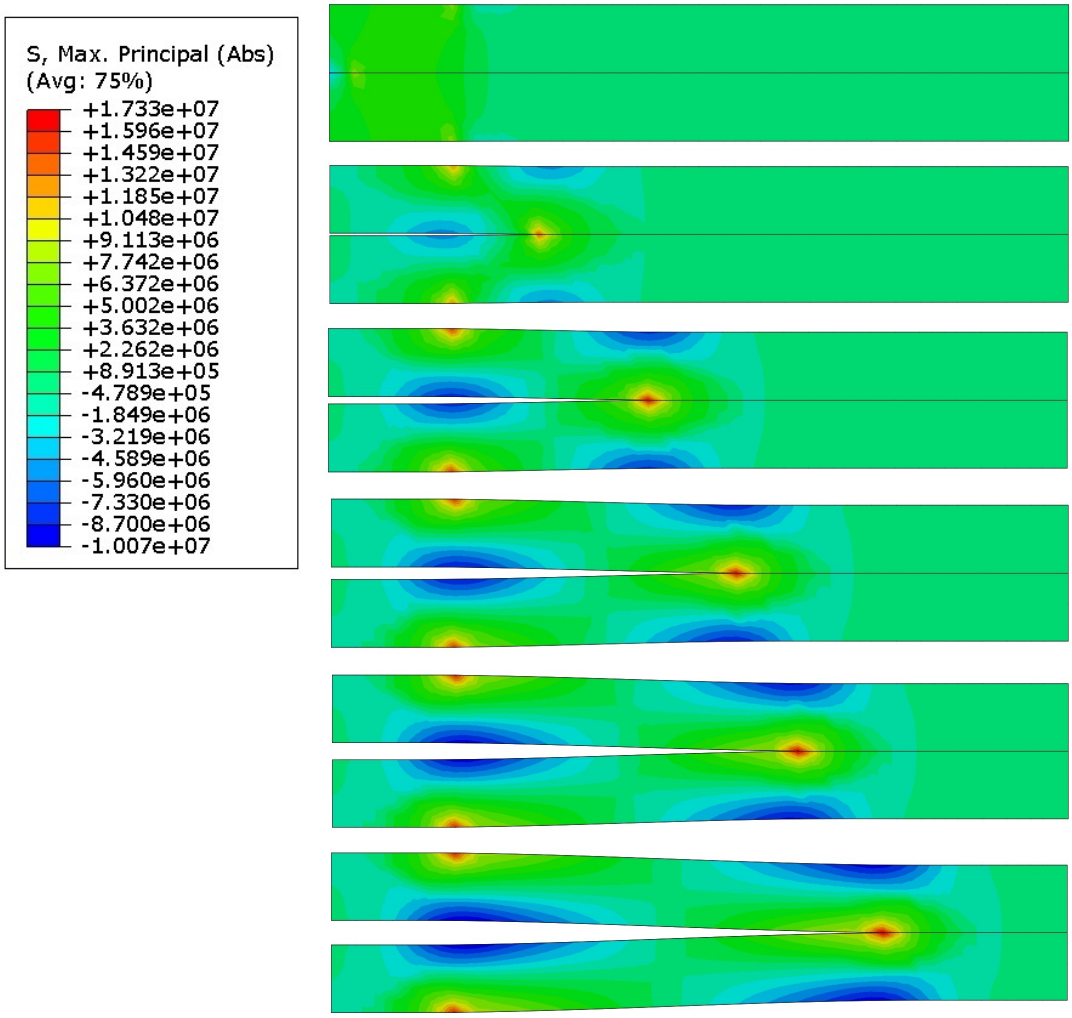

Figure 112: Absolute Maximum Principal Stress distribution during loading processes. Figures correspond to the following the total loading displacements: 0.06, 1.99, 6.00, 9.99, 13.91 and 20 mm. The figure is displayed with a 50 amplification factor to show the crack opening.

6.3.4 XFEM simulations

The problem of mode I fracture propagation described above is simulated with the XFEM, assuming a fracture energy of $G_c = 120\text{N/m}$. The crack is generated within the same plane as initial crack, and propagates along x-direction (figure 115). The maximum tensile stress occurs at the crack tip where high stress concentrations are noted. Figure 116 shows that when the crack propagates at the very early of the loading, the surface energy dissipates

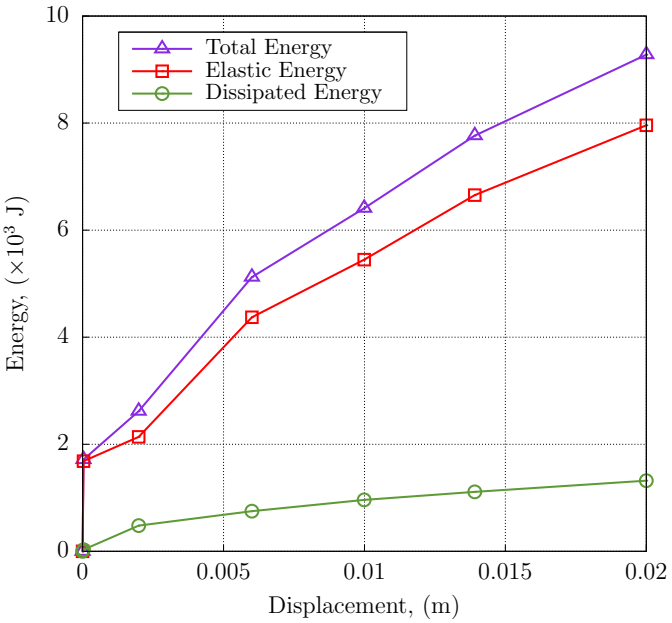

Figure 113: Evolution of the energy stored and the energy dissipated in the CZM model of mode I fracture propagation.

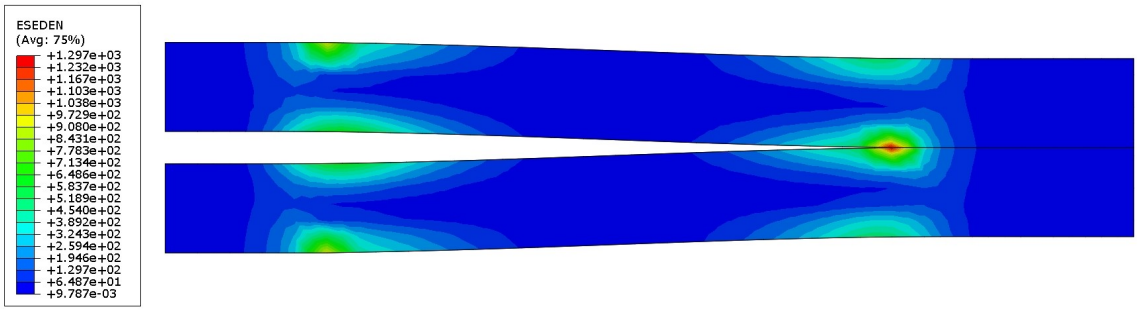

Figure 114: Distribution of the elastic energy density in the CZM model of mode I fracture propagation.

rapidly with the high amount of surface energy released: the dissipated energy exceeds the stored elastic energy. Physically, this corresponds to unstable crack propagation when the initial crack is very small at the beginning; then the crack propagation slows down, and most of the work is stored into the material as strain energy. As a result, the elastic deformation energy rate increases during fracture propagation. Crack propagation becomes stable during the later loading steps. The final elastic energy density is illustrated in Figure 117. The plot is consistent with the maximum principal stress distribution shown in Figure 115: high elastic energy density is obtained where tensile stress or compressive stress is the highest.

6.3.5 Comparison of the three methods and discussion

To compare the energy dissipation predicted in the three numerical models presented above, the evolution of the percentage of the elastic energy stored within the entire study domain is plotted in Figure 118. Although the magnitude of the energy is not in the same order, the plots show energy evolve during the loading. Both XFEM and CZM account for the propagation of the initial defect (macroscale). Until the energy percentage reaches a turning point, the crack extension slows down and opening of crack is dominant. Most of the external work is stored by the material after this turning point, so the percentage of the elastic energy increases. However, this phenomenon cannot be captured by the continuum-based model. The DSID model considers damage propagation at the mesoscale, which smoothens the evolution of dissipation.

6.4 Summary

In this chapter, several strategies to simulate the simultaneous propagation of fractures (at the macro-scale) and the development of a damage process zone (at the meso-scale) are explained and tested. A benchmark was conducted in order to compare continuum and discrete numerical models, including plasticity models, the Cohesive Zone Method (CZM), and the Extended Finite Element Method (XFEM). A mode I fracture propagation problem was simulated with the a smeared damaged zone (with the DSID model), the CZM and

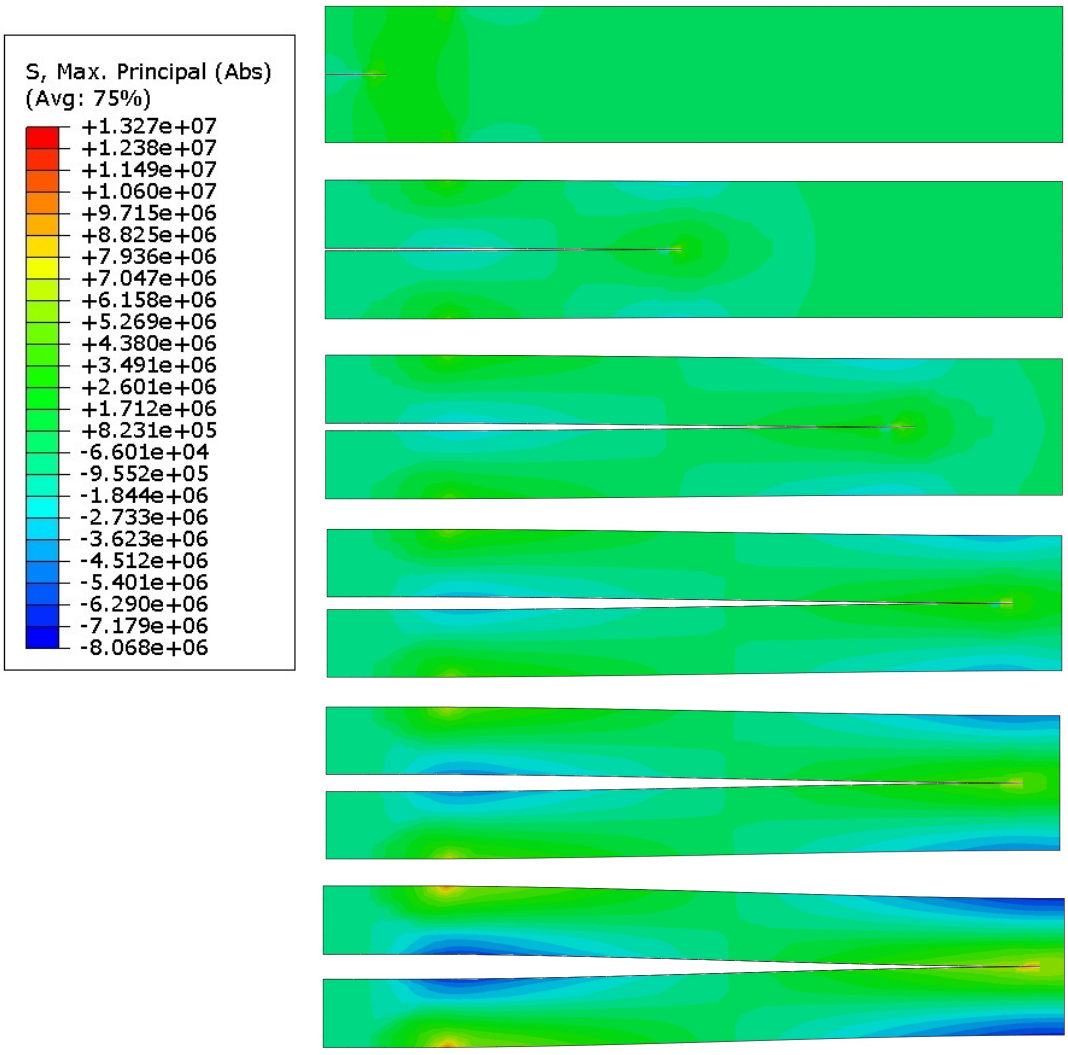

Figure 115: Absolute Maximum Principal Stress distribution during loading processes. Figures correspond to the following the total loading displacements: 0.16, 1.98, 5.98, 10.36, 13.98, and 20 mm. The figure is displayed with 50 amplification factor to show the crack opening.

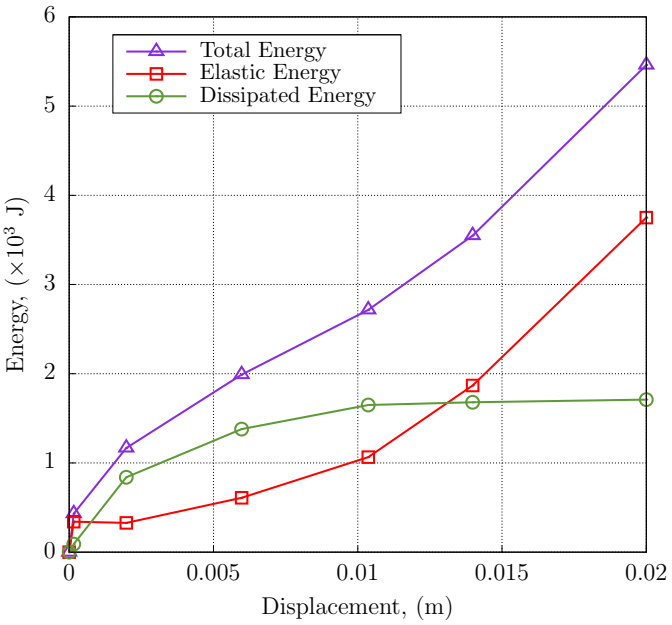

Figure 116: Evolution of the energy stored and the energy dissipated in the XFEM model of mode I fracture propagation.

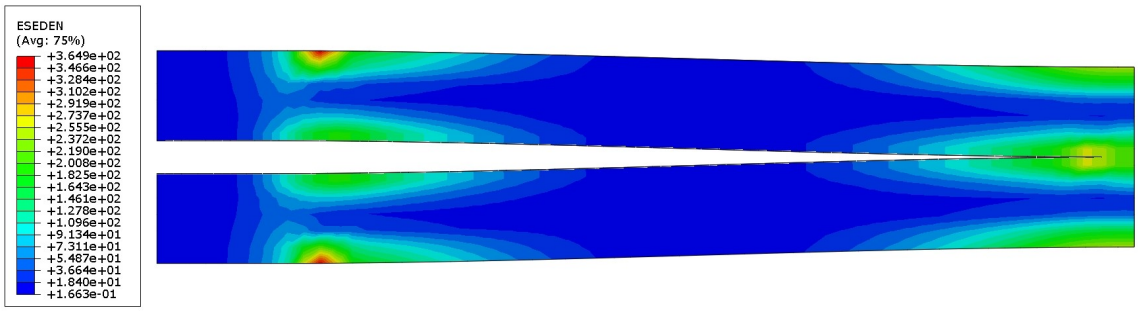

Figure 117: Distribution of the elastic energy density in the XFEM model of mode I fracture propagation.

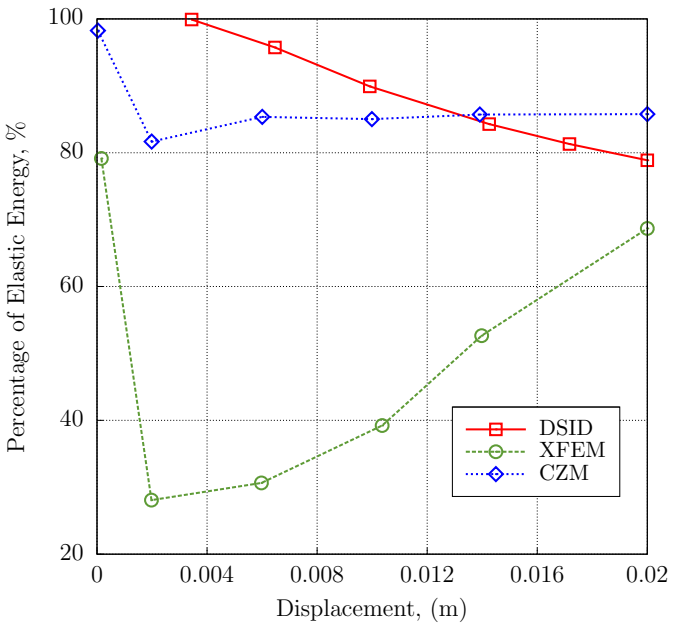

Figure 118: Evolution of the elastic energy stored in the domain upon mode I fracture propagation: comparison of DSID, CZM and XFEM models.

the XFEM. In the CZM and the XFEM models, elastic deformation energy is dissipated abruptly as soon as the fracture propagates. When the the tip reaches a stable position, elastic deformation energy is stored because the fracture opens without propagating. This peak behavior in discrete fracture method (CZM and XFEM) cannot be captured in a continuum approach such as the one employed in the DSID model, because damage propagates continuously, which results in a monotonic decrease of the elastic deformation energy stored in the domain. A coupled multi-scale model remains necessary to close the gap between CDM and discrete fracture mechanics.

CHAPTER VII

CONCLUSIONS AND FUTURE WORK

7.1 Conclusions

This research improved the constitutive descriptions that are required to more realistically simulate fracture propagation in rocks. The proposed damage model considers the degradation of stiffness and the change in rock strength around propagating fractures, which can be used to predict the development of a damaged zone around the fracture tip and around fracture faces. The new damage model is developed at the scale of a Representative Elementary Volume (REV), according to the theory of Continuum Damage Mechanics (CDM). It is assumed that cracks propagate in mode I. Both splitting and crossing effects are considered, in order to account for crack debonding and opening under the influence of a differential stress. This approach allows representing crack-induced orthotropic damage and predicting the rotation of the principal directions of damage due to a change of principal stress directions. The model is constructed to satisfy thermodynamic requirements, physical expectations and differentiability requirements for energy potentials. The flow rules are derived with the energy release rate work-conjugate to damage, which is thermodynamically consistent. The damage criterion is adapted from Drucker-Prager yield function: the function is expressed in terms of damage energy release rate, and a projector is used in order to distinguish between tension and compression damage thresholds. The positivity of dissipation is ensured by computing the damage rate by a non-associate flow rule. The non-elastic deformation due to damage is computed with an associate flow rule in order to maintain the physical meaning of the model trends. The model was calibrated against laboratory data obtained during triaxial compression tests performed on Bakken shale and on claystone, by using an optimization technique to match the stress-strain behavior.

- The triaxial compression test used for model calibration was simulated for different sample sizes with ABAQUS finite element software. The effects of sample size on stress

concentrations and damage localization, and the anisotropy induced by microscopic crack propagation in initially isotropic and anisotropic shale samples is captured by the DSID model. The non uniform state of stress reached after the axial loading stage in elements located in the central zone of the mesh reveals boundary effects.

- Overall, stress-strain curves obtained with the Finite Element Method match the stress-strain curves obtained with the one-element model used for calibration, which justifies the use of the DSID model to study stress-induced anisotropy at multiple scales.

- When considering different states of initial damage representing thin laminae, the anisotropy index grows faster in the plug tests simulated for samples with initial horizontal damage (i.e., initial vertical micro-cracks).

- The influence of a horizontal bedding delamination plane located at mid-height of a linear elastic shale sample was studied by using a discrete fracture model and a smeared damage zone model. The evolution of the energy dissipation rate in the sample illustrates two main differences between the two numerical models. First, the CDM smeared zone model predicts vertical weakening in the damage zone that is not included with the hard normal contact option of the discrete surface model. Second, the discrete fracture model uses a sliding friction threshold that is not exceeded under axial loading, whereas the CDM zone predicts strain localization, gradual energy dissipation and further material weakening at the delamination interface.

Finite Element analyses of damage anisotropy and damage propagation demonstrated the utility of the DSID model to simulate realistic rock deformation using a common laboratory testing configuration. Although simple scenarios were considered, results suggest that the model is suitable for a range of engineering and geologic problems where anisotropic mechanical properties are expected.

- Finite Element simulations of cavity stress relaxation and cavity pressurization were performed in order to characterize the stress paths leading to shear damage and to

compare the orientations of stress and damage for various anisotropic loadings, differential stress intensities and loading sequences. It was verified that in the absence of damage, FE predictions match analytical stress distributions predicted by the theory of elasticity. Damage propagation results in a stress relaxation at the vicinity of the cavity. Damage induced by pressurization under extra vertical pressure results in complex damage distributions, which represent several families of cracks, mainly crossing cracks at the top and bottom of the cavity, and shear cracks in the other radial directions. Competing crossing effects result in damage rotation. Applying an additional load prior to a stress relaxation intensifies damage in the vertical and horizontal directions. The intensity of damage is reduced when the stress relaxation is performed before the application of the extra load. The presence of an additional load results in significant shear damage, of the same order of magnitude as horizontal and vertical damage.

- Localized pressurization from a wellbore was simulated. In a pristine rock mass, the damage zone presents several symmetries in three dimensions, which are in agreement with the definition of the damage-driving force controlling the initiation and propagation of damage. If hydraulic fracturing is enhanced by the presence of initial cracks, the propagation of the damage zone depends on the geometry of the initial defects. The presence of notches tends to reduce the surface of application of the pressure causing damage. As a result the damage driving force stays relatively small and the damage zone localizes around the notch, even under high pressures gradients. In the presence of a smeared damage zone, damage first concentrates around the initial damage zone (analog of the viscosity-dominated propagation regime). Once damage ahead of the damage zone starts to initiate, damage propagates very rapidly in the radial direction, because the damage threshold (to open new cracks) is low in pristine rock (analog of the toughness-dominated propagation regime). Simulating pre-existing damage by setting a non-zero value for the damage tensor turns out to be an efficient way to link fracture propagation problems at the borehole and continuum scales.

7.2 Future Work

Theoretical and numerical model improvements are underway:

- Rigorous calibration techniques are needed in order to optimize the expression of energy potentials to specific rocks and to correlate CDM parameters to geologic characteristics;
- The model needs to be further enhanced by plastic coupling so that the full stress-strain and failure response can be modeled;
- Coupling a fracture propagation model (such as the CZM or the XFEM) with a damage propagation model (such as the DSID FE model) is desirable, in order to allow simulating the simultaneous propagation of fractures and surrounding damage zone;
- A rigorous theory needs to be developed to model the transition between continuum damage and discrete fracture;
- The Continuum Damage model needs to be extended to saturated porous rocks, in order to predict the influence of fluid viscosity and rock permeability on fracture propagation regimes, and conversely, to to predict the evolution of rock hydro-mechanical and physical properties as fractures propagate.

APPENDIX A

PROOF: AN ASSOCIATE DAMAGE FLOW RULE PROVIDES A NON-POSITIVE DAMAGE RATE.

For an associate damage flow rule,

$$\dot{\mathbf{\Omega}} = \dot{\lambda}_d \frac{\partial f_d}{\partial \mathbf{Y}} \tag{267}$$

Equation 267 imposes that $\dot{\mathbf{\Omega}}$ should be parallel to $\frac{\partial f_d}{\partial \mathbf{Y}}$. Lagrange Multiplier $\dot{\lambda}_d$ is a non-negative scalar so that the components of the damage increment should have the same sign as $\frac{\partial f_d}{\partial \mathbf{Y}}$.

Example 1: Triaxial Compression Test.

The stess increment is written as

$$\boldsymbol{\sigma} = \begin{bmatrix} \sigma_1 & 0 & 0 \\ 0 & \sigma_2 & 0 \\ 0 & 0 & \sigma_2 \end{bmatrix} \tag{268}$$

in which, according to the soil mechanics sign convention, all stress eigenvalues are positive. In this particular case, we have $P_1(1,1,1,1) = P_1(2,2,2,2) = P_1(3,3,3,3) = 1$, and all the other components are equal to zero. The thermodynamic damage driving force $\mathbf{Y}$ is calculated from equation 153.

$$\begin{aligned} \mathbf{Y} = a_1(\sigma_1 + 2\sigma_2)^2 \begin{bmatrix} 1 & 0 & 0 \\ 0 & 1 & 0 \\ 0 & 0 & 1 \end{bmatrix} + a_2 \begin{bmatrix} \sigma_1^2 & 0 & 0 \\ 0 & \sigma_2^2 & 0 \\ 0 & 0 & \sigma_2^2 \end{bmatrix} \\ + a_3(\sigma_1 + 2\sigma_2) \begin{bmatrix} \sigma_1 & 0 & 0 \\ 0 & \sigma_2 & 0 \\ 0 & 0 & \sigma_2 \end{bmatrix} + a_4(\sigma_1 + 2\sigma_2)^2 \begin{bmatrix} 1 & 0 & 0 \\ 0 & 1 & 0 \\ 0 & 0 & 1 \end{bmatrix} \end{aligned} \tag{269}$$

$$Y_{11} = a_1(\sigma_1 + 2\sigma_2)^2 + a_2\sigma_1^2 + a_3(\sigma_1 + 2\sigma_2)\sigma_1 + a_4(\sigma_1 + 2\sigma_2)^2 \tag{270}$$

$$Y_{22} = Y_{33} = a_1(\sigma_1 + 2\sigma_2)^2 + a_2\sigma_2^2 + a_3(\sigma_1 + 2\sigma_2)\sigma_2 + a_4(\sigma_1 + 2\sigma_2)^2 \tag{271}$$

Note that for the triaxial compression test, the thermodynamic damage driving force $\mathbf{Y}$ is equal to the physical damage driving force $\mathbb{P}_1 : \mathbf{Y}$,

$$\mathbb{P}_1 : \mathbf{Y} = \mathbf{Y} \tag{272}$$

The terms involved in the damage function are computed below

$$I^* = P_{1_{ijkl}} Y_{kl} \delta_{ij} = (3a_1 + a_3 + 3a_4)(\sigma_1 + 2\sigma_2)^2 + a_2(\sigma_1^2 + 2\sigma_2^2) \tag{273}$$

$$P_{1_{ijkl}} Y_{kl} - \frac{1}{3} I^* \delta_{ij} = \frac{1}{3}[a_2(\sigma_1^2 - \sigma_2^2) + a_3(\sigma_1 + 2\sigma_2)(\sigma_1 - \sigma_2)] \begin{bmatrix} 2 & 0 & 0 \\ 0 & -1 & 0 \\ 0 & 0 & -1 \end{bmatrix} \tag{274}$$

$$P_{1_{klij}} \delta_{kl} = \begin{bmatrix} 1 & 0 & 0 \\ 0 & 1 & 0 \\ 0 & 0 & 1 \end{bmatrix} \tag{275}$$

When the fourth-order tensor $\delta_{ij} P_{1_{pqkl}} \delta_{pq}$ is be expressed in a plane where $k = l$, it becomes a second-order tensor. It turns out that this second-order tensor is identity

$$\left[\delta_{ij} P_{1_{pqkl}} \delta_{pq}\right]_{k=l=1} = \left[\delta \otimes (\delta : P_1)\right]_{i,j,1,1} = \begin{bmatrix} 1 & 0 & 0 \\ 0 & 1 & 0 \\ 0 & 0 & 1 \end{bmatrix} \tag{276}$$

$$\left[\delta_{ij} P_{1_{pqkl}} \delta_{pq}\right]_{k=l=2} = \left[\delta \otimes (\delta : P_1)\right]_{i,j,2,2} = \begin{bmatrix} 1 & 0 & 0 \\ 0 & 1 & 0 \\ 0 & 0 & 1 \end{bmatrix} \tag{277}$$

$$\left[\delta_{ij} P_{1_{pqkl}} \delta_{pq}\right]_{k=l=3} = \left[\delta \otimes (\delta : P_1)\right]_{i,j,3,3} = \begin{bmatrix} 1 & 0 & 0 \\ 0 & 1 & 0 \\ 0 & 0 & 1 \end{bmatrix} \tag{278}$$

Expressions in equations 273 and 276 are used to compute J^*

$$\begin{aligned} 2J^* =&(P_{1_{ijkl}}Y_{kl} - \frac{1}{3}I^*\delta_{ij})(P_{1_{ijpq}}Y_{pq} - \frac{1}{3}I^*\delta_{ij}) \\ &= \frac{1}{9}(\sigma_1 - \sigma_2)^2[a_2(\sigma_1 + \sigma_2) + a_3(\sigma_1 + 2\sigma_2)]^2(2^2 + 2 \times (-1)^2) \\ &= \frac{2}{3}(\sigma_1 - \sigma_2)^2[a_2(\sigma_1 + \sigma_2) + a_3(\sigma_1 + 2\sigma_2)]^2 = A > 0 \end{aligned} \tag{279}$$

Then we can deduce the expression of $\frac{\partial f_d}{\partial \mathbf{Y}}$, in terms of stress components,

$$\begin{aligned} \frac{\partial f_d}{\partial \mathbf{Y}} =&\frac{(P_{1_{efkl}}Y_{kl} - \frac{1}{3}P_{1_{klmn}}Y_{mn}\delta_{kl}\delta_{ef})(P_{1_{efij}} - \frac{1}{3}P_{1_{cdij}}\delta_{cd}\delta_{ef})}{\sqrt{2(P_{1_{pqrs}}Y_{rs} - \frac{1}{3}P_{1_{rstu}}Y_{tu}\delta_{rs}\delta_{pq})(P_{1_{pqvw}}Y_{vw} - \frac{1}{3}P_{1_{vwgh}}Y_{gh}\delta_{vw}\delta_{pq})}} - \alpha P_{1_{klij}}\delta_{kl} \\ =&\frac{1}{\sqrt{2A}}\frac{1}{3}[a_2(\sigma_1^2 - \sigma_2^2) + a_3(\sigma_1 + 2\sigma_2)(\sigma_1 - \sigma_2)] \begin{bmatrix} 2 & 0 & 0 \\ 0 & -1 & 0 \\ 0 & 0 & -1 \end{bmatrix} - \alpha \begin{bmatrix} 1 & 0 & 0 \\ 0 & 1 & 0 \\ 0 & 0 & 1 \end{bmatrix} \end{aligned} \tag{280}$$

$$=\frac{(\sigma_1 - \sigma_2)[a_2(\sigma_1 + \sigma_2) + a_3(\sigma_1 + 2\sigma_2)]}{2\sqrt{3}|\sigma_1 - \sigma_2||a_2(\sigma_1 + \sigma_2) + a_3(\sigma_1 + 2\sigma_2)|} \begin{bmatrix} 2 & 0 & 0 \\ 0 & -1 & 0 \\ 0 & 0 & -1 \end{bmatrix} - \alpha \begin{bmatrix} 1 & 0 & 0 \\ 0 & 1 & 0 \\ 0 & 0 & 1 \end{bmatrix}$$

Equation 280 shows that the sign of the components of $\frac{\partial f_d}{\partial \mathbf{Y}}$ depend on the stress state and on the material parameters a_i. Shao et al. [242] calibrated their model for granite rock with $a_2 = 3.9371 \times 10^{-11}$, and $a_4 = 2.513 \times 10^{-13}$, i.e. $a_2 > 0, \quad a_4 > 0$. Moreover, in the case of the triaxial compression test, which results in $\sigma_1 > \sigma_2 > 0$ and therefore $a_2(\sigma_1 + \sigma_2) + a_3(\sigma_1 + 2\sigma_2) > 0$. In addition, it is assumed that $\alpha > 0$, so that $(\frac{\partial f_d}{\partial \mathbf{Y}})_{22}$ and $(\frac{\partial f_d}{\partial \mathbf{Y}})_{33}$ are non-positive. According to an associate flow rule (equation 267), lateral damage increments will have a negative sign.

Example 2: Uniaxial Compression Test.

This time the test is unconfined, so that lateral stress is not constrained to be a compression

$$\boldsymbol{\sigma} = \begin{bmatrix} \sigma & 0 & 0 \\ 0 & 0 & 0 \\ 0 & 0 & 0 \end{bmatrix} \tag{281}$$

In this particular case, we have $P_1(1,1,1,1) = 1$, and all the other components are equal to zero. The thermodynamic damage driving force $\mathbf{Y}$ is calculated from equation 153

$$\begin{aligned}\mathbf{Y} = & \ a_1\sigma^2 \begin{bmatrix} 1 & 0 & 0 \\ 0 & 1 & 0 \\ 0 & 0 & 1 \end{bmatrix} + a_2 \begin{bmatrix} \sigma^2 & 0 & 0 \\ 0 & 0 & 0 \\ 0 & 0 & 0 \end{bmatrix} + a_3\sigma \begin{bmatrix} \sigma & 0 & 0 \\ 0 & 0 & 0 \\ 0 & 0 & 0 \end{bmatrix} + a_4\sigma^2 \begin{bmatrix} 1 & 0 & 0 \\ 0 & 1 & 0 \\ 0 & 0 & 1 \end{bmatrix} \\ = & \ \sigma^2 \begin{bmatrix} a_1 + a_2 + a_3 + a_4 & 0 & 0 \\ 0 & a_1 + a_4 & 0 \\ 0 & 0 & a_1 + a_4 \end{bmatrix} \end{aligned} \tag{282}$$

Using the projection tensor to calculate the physical damage driving force $\mathbb{P}_1 : \mathbf{Y}$,

$$\mathbb{P}_1 : \mathbf{Y} = \sigma^2 \begin{bmatrix} a_1 + a_2 + a_3 + a_4 & 0 & 0 \\ 0 & 0 & 0 \\ 0 & 0 & 0 \end{bmatrix} \tag{283}$$

The intermediate computations required to determine the damage criterion are provided below

$$I^* = P_{1_{ijkl}} Y_{kl} \delta_{ij} = \sigma^2(a_1 + a_2 + a_3 + a_4) \tag{284}$$

$$P_{1_{ijkl}} Y_{kl} - \frac{1}{3} I^* \delta_{ij} = \frac{1}{3}\sigma^2(a_1 + a_2 + a_3 + a_4) \begin{bmatrix} 2 & 0 & 0 \\ 0 & -1 & 0 \\ 0 & 0 & -1 \end{bmatrix} \tag{285}$$

$$P_{1_{klij}} \delta_{kl} = \begin{bmatrix} 1 & 0 & 0 \\ 0 & 0 & 0 \\ 0 & 0 & 0 \end{bmatrix}, \qquad \delta_{ij} P_{1_{pqkl}} \delta_{pq}(:,:,1,1) = \begin{bmatrix} 1 & 0 & 0 \\ 0 & 1 & 0 \\ 0 & 0 & 1 \end{bmatrix} \tag{286}$$

$$\begin{aligned} 2J^* = & (P_{1_{ijkl}} Y_{kl} - \frac{1}{3} I^* \delta_{ij})(P_{1_{ijpq}} Y_{pq} - \frac{1}{3} I^* \delta_{ij}) \\ = & \frac{1}{9}\sigma^4(a_1 + a_2 + a_3 + a_4)^2(2^2 + 2 \times (-1)^2) \\ = & \frac{2}{3}\sigma^4(a_1 + a_2 + a_3 + a_4)^2 = A > 0 \end{aligned} \tag{287}$$

$$
\begin{aligned}
\frac{\partial f_d}{\partial \mathbf{Y}} =& \frac{(P_{1_{efkl}} Y_{kl} - \frac{1}{3} P_{1_{klmn}} Y_{mn} \delta_{kl} \delta_{ef})(P_{1_{efij}} - \frac{1}{3} P_{1_{cdij}} \delta_{cd} \delta_{ef})}{\sqrt{2(P_{1_{pqrs}} Y_{rs} - \frac{1}{3} P_{1_{rstu}} Y_{tu} \delta_{rs} \delta_{pq})(P_{1_{pqvw}} Y_{vw} - \frac{1}{3} P_{1_{vwgh}} Y_{gh} \delta_{vw} \delta_{pq})}} - \alpha P_{1_{klij}} \delta_{kl} \\
=& \frac{1}{\sqrt{2A}} \frac{1}{3} \sigma^2 (a_1 + a_2 + a_3 + a_4) \begin{bmatrix} 2 & 0 & 0 \\ 0 & 0 & 0 \\ 0 & 0 & 0 \end{bmatrix} - \alpha \begin{bmatrix} 1 & 0 & 0 \\ 0 & 0 & 0 \\ 0 & 0 & 0 \end{bmatrix} \\
=& \frac{(a_1 + a_2 + a_3 + a_4)}{2\sqrt{3}|a_1 + a_2 + a_3 + a_4|} \begin{bmatrix} 2 & 0 & 0 \\ 0 & 0 & 0 \\ 0 & 0 & 0 \end{bmatrix} - \alpha \begin{bmatrix} 1 & 0 & 0 \\ 0 & 0 & 0 \\ 0 & 0 & 0 \end{bmatrix} \\
=& \begin{bmatrix} \frac{(a_1+a_2+a_3+a_4)}{\sqrt{3}|a_1+a_2+a_3+a_4|} - \alpha & 0 & 0 \\ 0 & 0 & 0 \\ 0 & 0 & 0 \end{bmatrix}
\end{aligned}
\tag{288}
$$

According to the calibration performed by Shao et al. [242], the following parameters allow capturing well the behavior of granite: $a_1 = 1.2565 \times 10^{-13}$, $a_2 = 3.9371 \times 10^{-11}$, $a_3 = -1.2565 \times 10^{-12}$, and $a_4 = 2.513 \times 10^{-13}$. We can expect to have to deal with parameters within the same range of values. In the particular case mentioned above, we have $a_1 + a_2 + a_3 + a_4 > 0$. In addition, Shao et al. took $0 < \alpha < \frac{1}{\sqrt{3}}$, which results in a positive damage increment in the direction of the applied compression. In other words and associate flow rule would predict the propagation of cracks perpendicular to the axis of compression. In conclusion, the new damage function defined in equation 156 can not be used as a dissipation potential.

Conclusion

The rate of damage depends on the expression of the free energy (and on the values of the material parameters introduced in that expression) and on the expression of the damage potential. The expression of the free energy chosen in equation 150 satisfies the requirements of the theory of elasticity and proved to give satisfactory predictions for geomaterials [242]. To satisfy the requirement on the positivity of the damage rate [73], it is proposed to resort to a non-associate flow rule, and therefore to introduce a damage potential in the formulation, rather than to change the expression of the free energy.

APPENDIX B

VERIFICATION: POSITIVITY OF THE DAMAGE RATE IN "CROSSING" MODE

The state of stress in a triaxial compression test is given in equation 268. Assuming that a compression is applied in direction 1 under a confining pressure maintained in directions 2 and 3, with $\sigma_1 > \sigma_2 = \sigma_3$, we get: $P_1(2,2,2,2) = P_1(3,3,3,3) = 1$ and all the other components of $\mathbb{P}_2$ are zero. The expression of the thermodynamic damage driving force $\mathbf{Y}$ is given in equation 269. The physical damage driving force defined in the expression of the damage potential can now be computed as

$$(\mathbb{P}_2 : \mathbf{Y})_{22} = (\mathbb{P}_2 : \mathbf{Y})_{33} = a_1(\sigma_1 + 2\sigma_2)^2 + a_2\sigma_2^2 + a_3(\sigma_1 + 2\sigma_2)\sigma_2 + a_4(\sigma_1 + 2\sigma_2)^2 \quad (289)$$

$$\begin{aligned} &\frac{1}{2}P_{1_{ijkl}}Y_{kl}P_{1_{ijpq}}Y_{pq} \\ &= [a_1(\sigma_1 + 2\sigma_2)^2 + a_2\sigma_2^2 + a_3(\sigma_1 + 2\sigma_2)\sigma_2 + a_4(\sigma_1 + 2\sigma_2)^2]^2 = B \end{aligned} \quad (290)$$

$$\begin{aligned} \frac{\partial g}{\partial \mathbf{Y}} =& \frac{P_{2_{rskl}}Y_{kl}P_{2_{rsij}}}{\sqrt{2(P_{2_{pqmn}}Y_{mn})(P_{2_{pquv}}Y_{uv})}} \\ =& \frac{1}{2\sqrt{B}}[a_1(\sigma_1 + 2\sigma_2)^2 + a_2\sigma_2^2 + a_3(\sigma_1 + 2\sigma_2)\sigma_2 + a_4(\sigma_1 + 2\sigma_2)^2] \begin{bmatrix} 0 & 0 & 0 \\ 0 & 1 & 0 \\ 0 & 0 & 1 \end{bmatrix} \end{aligned} \quad (291)$$

First of all, damage propagates in the planes perpendicular to the axis of the major principal stress, which meets the modeling expectations. The sign of above equation depends on the parameters and stress state. In the model calibrated by Shao et al. [242] for granite, $a_1 = 1.2565 \times 10^{-13}$, $a_2 = 3.9371 \times 10^{-11}$, $a_3 = -1.2565 \times 10^{-12}$, and $a_4 = 2.513 \times 10^{-13}$. For the ranges of values of stress in a triaxial compression state, it is possible to calibrate the material parameters a_i to ensure the positiveness of the components of $\frac{\partial g}{\partial \mathbf{Y}}$, which will ensure the positivity of the damage rate.

Similarly for the uniaxial compression test, $P_1(2,2,2,2) = P_1(3,3,3,3) = 1$ and all the other components of $\mathbb{P}_2$ are zero in a triaxial compression test. The physical damage driving force $\mathbb{P}_2 : \mathbf{Y}$ is obtained as follows

$$\mathbb{P}_2 : \mathbf{Y} = \sigma^2(a_1 + a_4) \begin{bmatrix} 0 & 0 & 0 \\ 0 & 1 & 0 \\ 0 & 0 & 1 \end{bmatrix} \tag{292}$$

which provides

$$\frac{1}{2} P_{2_{ijkl}} Y_{kl} P_{2_{ijpq}} Y_{pq} = \sigma^4 (a_1 + a_4)^2 = B \tag{293}$$

$$\begin{aligned} \frac{\partial g}{\partial \mathbf{Y}} =& \frac{P_{2_{rskl}} Y_{kl} P_{2_{rsij}}}{\sqrt{2(P_{2_{pqmn}} Y_{mn})(P_{2_{pquv}} Y_{uv})}} \\ =& \frac{1}{2\sqrt{B}} \sigma^2 (a_1 + a_4) \begin{bmatrix} 0 & 0 & 0 \\ 0 & 1 & 0 \\ 0 & 0 & 1 \end{bmatrix} \end{aligned} \tag{294}$$

Like in the triaxial compression test, damage propagates in the directions perpendicular to the axis where compression is applied, which meets the expectations. For a uniaxial compression test, it is sufficient to take $a_1 + a_4 > 0$ to ensure the positivity of the damage rate. The dissipation potential defined in 160 is suitable to model the propagation of damage in states of uniaxial compression.

APPENDIX C

VERIFICATION: POSITIVITY OF ENERGY DISSIPATION

The positivity of the dissipation related to the irreversible deformation: $\boldsymbol{\sigma} : \dot{\boldsymbol{\varepsilon}}^{id}$ should be greater than 0. Provided that the positivity of the damage dissipation is ensured, that would guarantee that the total dissipation function is positive. The computations below aim to provide the range of values for which the positivity of the dissipation associated to irreversible deformation is ensured.

Example 1: Triaxial Compression Test

Let us define a parameter

$$C = \frac{(\sigma_1 - \sigma_2)[a_2(\sigma_1 + \sigma_2) + a_3(\sigma_1 + 2\sigma_2)]}{|\sigma_1 - \sigma_2||a_2(\sigma_1 + \sigma_2) + a_3(\sigma_1 + 2\sigma_2)|} \tag{295}$$

C's value depends on the stress state and parameter a_i, either $C = 1$ or $C = -1$. The equation 280 gives:

$$\frac{\partial f_d}{\partial \mathbf{Y}} = \begin{bmatrix} \frac{C}{\sqrt{3}} - \alpha & 0 & 0 \\ 0 & -\frac{C}{2\sqrt{3}} - \alpha & 0 \\ 0 & 0 & -\frac{C}{2\sqrt{3}} - \alpha \end{bmatrix}$$

When the fourth-order tensor $\frac{\partial \mathbf{Y}}{\partial \boldsymbol{\sigma}}$ is expressed in a plane where $k = l$, it becomes a

diagonal second-order tensor (off-diagonal components are equal to zero).

$$\left[\frac{\partial \mathbf{Y}}{\partial \boldsymbol{\sigma}}\right]_{1,1,1,1} = 2a_1(\sigma_1 + 2\sigma_2) + 2a_2\sigma_1 + 2a_3(\sigma_1 + \sigma_2) + 2a_4\sigma_1 \tag{296}$$

$$\left[\frac{\partial \mathbf{Y}}{\partial \boldsymbol{\sigma}}\right]_{2,2,1,1} = 2a_1(\sigma_1 + 2\sigma_2) + a_3\sigma_2 + 2a_4\sigma_1 \tag{297}$$

$$\left[\frac{\partial \mathbf{Y}}{\partial \boldsymbol{\sigma}}\right]_{3,3,1,1} = 2a_1(\sigma_1 + 2\sigma_2) + a_3\sigma_2 + 2a_4\sigma_1 \tag{298}$$

$$\left[\frac{\partial \mathbf{Y}}{\partial \boldsymbol{\sigma}}\right]_{1,1,2,2} = 2a_1(\sigma_1 + 2\sigma_2) + a_3\sigma_1 + 2a_4\sigma_2 \tag{299}$$

$$\left[\frac{\partial \mathbf{Y}}{\partial \boldsymbol{\sigma}}\right]_{2,2,2,2} = 2a_1(\sigma_1 + 2\sigma_2) + 2a_2\sigma_2 + a_3(\sigma_1 + 3\sigma_2) + 2a_4\sigma_2 \tag{300}$$

$$\left[\frac{\partial \mathbf{Y}}{\partial \boldsymbol{\sigma}}\right]_{3,3,2,2} = 2a_1(\sigma_1 + 2\sigma_2) + a_3\sigma_1 + 2a_4\sigma_2 \tag{301}$$

$$\left[\frac{\partial \mathbf{Y}}{\partial \boldsymbol{\sigma}}\right]_{1,1,3,3} = 2a_1(\sigma_1 + 2\sigma_2) + a_3\sigma_1 + 2a_4\sigma_2 \tag{302}$$

$$\left[\frac{\partial \mathbf{Y}}{\partial \boldsymbol{\sigma}}\right]_{2,2,3,3} = 2a_1(\sigma_1 + 2\sigma_2) + 2a_2\sigma_2 + a_3(\sigma_1 + 3\sigma_2)a + 2a_4\sigma_2 \tag{303}$$

$$\left[\frac{\partial \mathbf{Y}}{\partial \boldsymbol{\sigma}}\right]_{3,3,3,3} = 2a_1(\sigma_1 + 2\sigma_2) + a_3\sigma_1 + 2a_4\sigma_2 \tag{304}$$

The double contraction between the second order tensor $\frac{\partial f_d}{\partial \mathbf{Y}}$ and fourth order tensor $\frac{\partial \mathbf{Y}}{\partial \boldsymbol{\sigma}}$ can be obtained, so the irreversible strain can be calculated by the associated flow rule (Equation 162) for one loading stress increment:

$$\begin{aligned}
\dot{\boldsymbol{\varepsilon}}^{id}_{11} =& \dot{\lambda}_d \left\{ \frac{C}{\sqrt{3}} \left[4a_2\sigma_1 + 2a_3(2\sigma_1 + \sigma_2)\right] - \alpha \left[6a_1(\sigma_1 + 2\sigma_2) + 2a_2\sigma_1 + a_3(2\sigma_1 + 4\sigma_2) + 6a_4\sigma_1\right] \right\} \\
\dot{\boldsymbol{\varepsilon}}^{id}_{22} =& \dot{\lambda}_d \left\{ \frac{C}{2\sqrt{3}} \left[-2a_2\sigma_1 + a_3(\sigma_1 - 4\sigma_2)\right] - \alpha \left[6a_1(\sigma_1 + 2\sigma_2) + 2a_2\sigma_2 + a_3(2\sigma_1 + 4\sigma_2) + 6a_4\sigma_2\right] \right\} \\
\dot{\boldsymbol{\varepsilon}}^{id}_{33} =& \dot{\lambda}_d \left\{ \frac{C}{2\sqrt{3}} \left[-2a_2\sigma_1 + a_3(\sigma_1 - 4\sigma_2)\right] - \alpha \left[6a_1(\sigma_1 + 2\sigma_2) + 2a_2\sigma_2 + a_3(2\sigma_1 + 4\sigma_2) + 6a_4\sigma_2\right] \right\}
\end{aligned} \tag{305}$$

The dissipation related to the irreversible deformation: $\boldsymbol{\sigma} : \dot{\boldsymbol{\varepsilon}}^{id}$ is determined as follows

$$\begin{aligned}
&\boldsymbol{\sigma} : \dot{\boldsymbol{\varepsilon}}^{id} = \\
&\dot{\lambda}_d\sigma_1 \left\{ \frac{C}{\sqrt{3}} \left[4a_2\sigma_1 + 2a_3(2\sigma_1 + \sigma_2)\right] - \alpha \left[6a_1(\sigma_1 + 2\sigma_2) + 2a_2\sigma_1 + a_3(2\sigma_1 + 4\sigma_2) + 6a_4\sigma_1\right] \right\} - \\
&\dot{\lambda}_d\sigma_2 \left\{ \frac{C}{\sqrt{3}} \left[-2a_2\sigma_1 + a_3(\sigma_1 - 4\sigma_2)\right] - 2\alpha \left[6a_1(\sigma_1 + 2\sigma_2) + 2a_2\sigma_2 + a_3(2\sigma_1 + 4\sigma_2) + 6a_4\sigma_2\right] \right\}
\end{aligned} \tag{306}$$

In equation 306, it is not easy to show that the dissipation will be unconditionally positive $\boldsymbol{\sigma} : \dot{\boldsymbol{\varepsilon}}^{id} > 0$. More work is needed to calibrate the model parameters to ensure

thermodynamic consistency.

Example 2: Uniaxial Compression Test

Let us define another parameter:

$$D = \frac{(a_1 + a_2 + a_3 + a_4)}{|a_1 + a_2 + a_3 + a_4|} \tag{307}$$

The value of parameter D only depends on parameter a_i, either $D = 1$ or $D = -1$. The equation 288

$$\frac{\partial f_d}{\partial \mathbf{Y}} = \begin{bmatrix} \frac{D}{\sqrt{3}} - \alpha & 0 & 0 \\ 0 & 0 & 0 \\ 0 & 0 & 0 \end{bmatrix}$$

When the fourth-order tensor $\frac{\partial \mathbf{Y}}{\partial \boldsymbol{\sigma}}$ is expressed in a plane where $k = l$, it becomes a diagonal second-order tensor (off-diagonal components are equal to zero)

$$\left[\frac{\partial \mathbf{Y}}{\partial \boldsymbol{\sigma}}\right]_{i,j,1,1} = \begin{bmatrix} 2a_1\sigma + 2a_2\sigma + 2a_3\sigma + 2a_4\sigma & 0 & 0 \\ 0 & 2a_1\sigma + 2a_4\sigma & 0 \\ 0 & 0 & 2a_1\sigma + 2a_4\sigma \end{bmatrix} \tag{308}$$

$$\left[\frac{\partial \mathbf{Y}}{\partial \boldsymbol{\sigma}}\right]_{i,j,2,2} = \begin{bmatrix} 2a_1\sigma + a_3\sigma & 0 & 0 \\ 0 & 2a_1\sigma + a_3\sigma & 0 \\ 0 & 0 & 2a_1\sigma \end{bmatrix} \tag{309}$$

$$\left[\frac{\partial \mathbf{Y}}{\partial \boldsymbol{\sigma}}\right]_{i,j,3,3} = \begin{bmatrix} 2a_1\sigma + a_3\sigma & 0 & 0 \\ 0 & 2a_1\sigma & 0 \\ 0 & 0 & 2a_1\sigma + a_3\sigma \end{bmatrix} \tag{310}$$

The double contraction between the second order tensor $\frac{\partial f_d}{\partial \mathbf{Y}}$ and fourth order tensor $\frac{\partial \mathbf{Y}}{\partial \boldsymbol{\sigma}}$ can be obtained, so the irreversible strain can be calculated by the associated flow rule (Equation 162) for one loading stress increment:

$$\dot{\boldsymbol{\varepsilon}}^{id} = \dot{\lambda}_d \left(\frac{D}{\sqrt{3}} - \alpha\right) \sigma \begin{bmatrix} 2a_1 + 2a_2 + 2a_3 + 2a_4 & 0 & 0 \\ 0 & 2a_1 + a_3 & 0 \\ 0 & 0 & 2a_1 + a_3 \end{bmatrix} \tag{311}$$

The dissipation related to the irreversible deformation: $\boldsymbol{\sigma} : \dot{\boldsymbol{\varepsilon}}^{id}$ is determined as follows

$$\boldsymbol{\sigma} : \dot{\boldsymbol{\varepsilon}}^{id} = 2\dot{\lambda}_d \left(\frac{D}{\sqrt{3}} - \alpha \right) \sigma^2 (a_1 + a_2 + a_3 + a_4) \tag{312}$$

Under the condition that

$$\left(\frac{D}{\sqrt{3}} - \alpha \right) (a_1 + a_2 + a_3 + a_4) > 0 \tag{313}$$

In equation 312, it is easy to show that the dissipation associated to the irreversible deformation ($\boldsymbol{\sigma} : \dot{\boldsymbol{\varepsilon}}^{id}$) will be satisfied. For instance, in Shao's model, the parameters are so that $D = 1$, $a_1 + a_2 + a_3 + a_4 > 0$, and we assume $0 < \alpha < \frac{1}{\sqrt{3}}$; thus the dissipation energy related to irreversible strain is positive. The values taken by Shao stem from an experimental calibration, which means that the set of parameters is realistic for the typical simulations the proposed model will be used for.

APPENDIX D

USING MOHR CIRCLES TO REPRESENT DAMAGE ROTATION

Traditionally, Mohr's circle is used as a graphical method for performing coordinate transformations for stress, but the technique applies equally well to any 2×2 tensor matrix. Brannon extended the use of Morhr's Circle to 3-D stress [69], and even in unsymmetrical 3×3 tensor in her unpublished work. Mohr's circle also provides rapid graphical estimations for eigenvalues and eigenvectors, which is extremely useful for verifying analytical results.

The damage tensor represents the net area change due to three dimensional void and microcrack distributions developed during the loading history [26]. The area reduction along the principal directions can be expressed in terms of the eigenvalues of the damage tensor, as

$$(1-d_i)\mathbf{n_i}\mathrm{d}S_i \;=\; \widetilde{\mathbf{n}}_\mathbf{i}\mathrm{d}\widetilde{S}_i, \qquad i=1,2,3 \tag{314}$$

in which d_i is the damage eigenvalue (defining a material area reduction in the plane perpendicular to direction $\mathbf{n_i}$). A graphical representation of the damage tensor is provided in Figure 119. If the damage tensor is not expressed in a principal base, the diagonal components of damage can be seen as area reduction coefficients, and the non-diagonal damage components can be seen as angles of rotation of the planes defining material areas. This representation is similar to that of the deformation tensor in continuum mechanics: diagonal terms define changes of length, and non-diagonal terms define angles of distortion. A 2D representation of the damage tensor, expressed in a non-principal base, is provided in Figure 120.

In a 2-dimensional problem, the damage tensor is expressed as

$$\mathbf{\Omega} = \begin{bmatrix} \Omega_{xx} & \Omega_{xy} \\ \Omega_{xy} & \Omega_{yy} \end{bmatrix} \tag{315}$$

In the following, we assume that $\Omega_{xx} > \Omega_{yy}$. Damage components refer to the coordinate system (x,y). Let us define the coordinate system (x',y') as the coordinate system defined

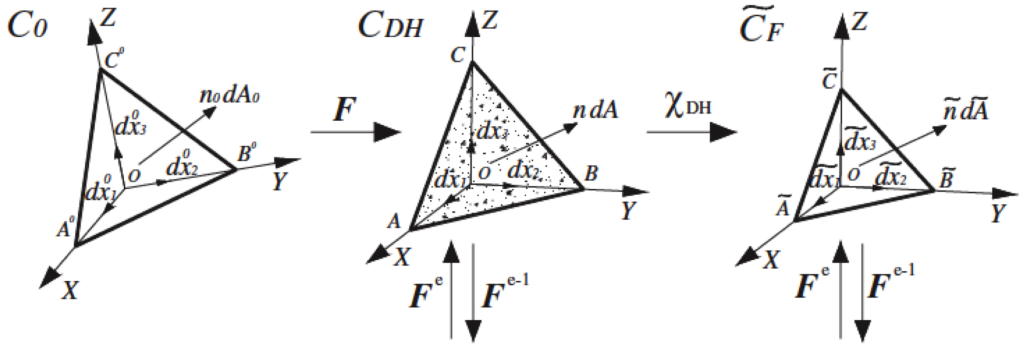

Figure 119: Graphical representation of the 3D damage tensor. Eigenvalues are factors of material area reduction. Taken from [26].

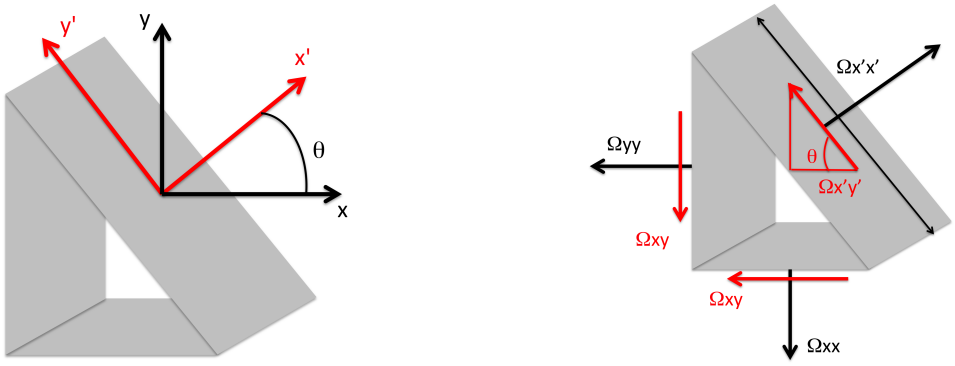

Figure 120: Graphical representation of the 2D damage tensor on a material element that has the shape of an edge in the (x,y) plane, with an infinitesimal thickness in the out-of-plane direction. Diagonal terms are defined as the ratio of degraded material area by total material area in a plane of given orientation. Non-diagonal terms are angles of rotation of the surface planes.

by rotating axes (x,y) about the z-axis by an angle θ. In plane stress conditions, Mohr's circles equations are obtained by writing the balance of forces applying to an edge element similar to that shown in Figure 120. The equations of damage Mohr's circle are obtained in the same way, by projecting the effective material areas represented in the global coordinate system (x,y) onto the plane of damage considered (x',y')

$$\Omega_{x'x'} = \frac{1}{2}(\Omega_{xx} + \Omega_{yy}) + \frac{1}{2}(\Omega_{xx} - \Omega_{yy})\cos 2\theta + \Omega_{xy}\sin 2\theta \tag{316}$$

$$\Omega_{x'y'} = \frac{1}{2}(\Omega_{xx} - \Omega_{yy})\sin 2\theta + \Omega_{xy}\cos 2\theta \tag{317}$$

Classical derivations provide

$$R^2 = (\Omega_{x'x'} - C)^2 + (\Omega_{x'y'})^2 \tag{318}$$

$$R^2 = (\Omega_{y'y'} - C)^2 + (\Omega_{x'y'})^2 \tag{319}$$

$$C = \frac{\Omega_{xx} + \Omega_{yy}}{2} \tag{320}$$

$$R = \sqrt{\left(\frac{\Omega_{xx} - \Omega_{yy}}{2}\right)^2 + (\Omega_{xy})^2} \tag{321}$$

which are the equations of damage Mohr's circle, plotted in figure 121. Note the Mohr Circle's sign convention is different from the general mechanical sign convention for the shear components (off-diagonal components in tensor). Based on geometrical relationships, we can obtain the following result

$$\Omega_c + R_\Omega = \frac{1}{2}(\Omega_{xx} + \Omega_{yy}) + \sqrt{\left[\frac{1}{2}(\Omega_{xx} - \Omega_{yy})\right]^2 + \Omega_{xy}^2} \tag{322}$$

When $\Omega_{x'y'} = 0$, x' and y' are the principal directions of damage. The orientation of damage principal directions is defined by the angle $\theta = (\widehat{x, x'})$

$$\theta = \frac{1}{2}\arctan\frac{\Omega_{xy}}{\frac{1}{2}(\Omega_{xx} - \Omega_{yy})} \tag{323}$$

$$\sin 2\theta = \frac{\Omega_{xy}}{\sqrt{\frac{1}{4}(\Omega_{xx} - \Omega_{yy})^2 + \Omega_{xy}^2}} \tag{324}$$

$$\cos 2\theta = \frac{\frac{1}{2}(\Omega_{xx} - \Omega_{yy})}{\sqrt{\frac{1}{4}(\Omega_{xx} - \Omega_{yy})^2 + \Omega_{xy}^2}} \tag{325}$$

In Figure 121, $\Omega_{x'x'}|_{max}$ is the right intersection between the circle and the horizontal axis. Similarly, the left intersection is the minimum principal damage. Therefore, this damage circle can determine the eigenvalue of the damage graphically. The maximum normal principal damage can be derived.

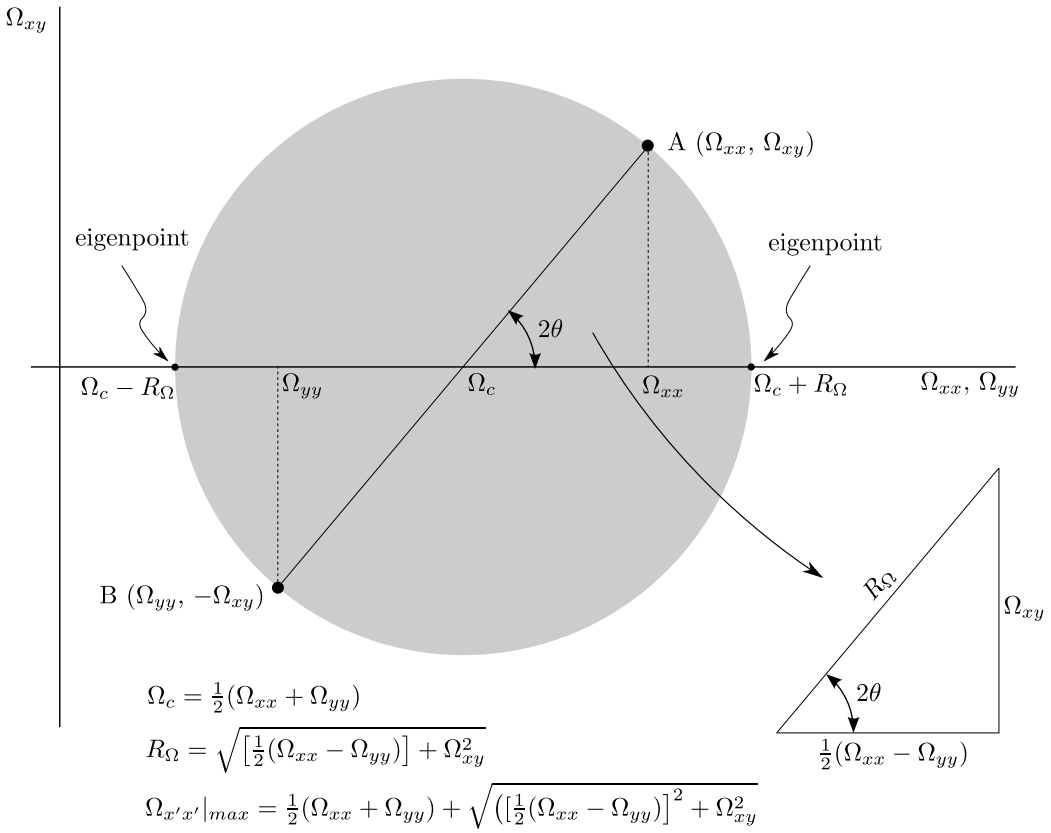

Figure 121: Illustration of the damage tensor represented by Mohr's Circle.

$$\Omega_{x'x'}|_{max} = \frac{1}{2}(\Omega_{xx} + \Omega_{yy}) + \sqrt{\left[\frac{1}{2}(\Omega_{xx} - \Omega_{yy})\right]^2 + \Omega_{xy}^2} \tag{326}$$

Using Mohr's Circle to represent the 2×2 damage tensor can be extended to 3×3 damage tensor, and even for other component such strain or moment of inertia tensors.

APPENDIX E

UMAT SUBROUTINE

E.1 FEM Algorithm with UMAT subroutines in ABAQUS

UMAT is the name given to subroutines written by ABAQUS users to use their own constitutive models. The input parameters will be given either by ABAQUS/CAE or by input files. Because of most of the prevalent commercial FEM in which the computation core is complied by Fortran, UMAT is also written in Fortran format as other subroutines in ABAQUS. All subroutines should follow in Fortran 77 format (which is now also called as fixed-form format). UMAT is used for static problems (small deformation), while VUMAT is used to solve dynamic problems (large deformation).

At the beginning of UMAT, ABAQUS initializes strain, stress and other user-defined state variables calculated from the values stored at the previous time step (t). Then, the strain increment $\Delta\varepsilon$ for the current time step $t + \Delta t$ is computed by ABAQUS solver and is given to UMAT as initial input. In UMAT subroutine, the developer needs to provide the formulas to calculate the stress and other state variables for the current step, $t + \Delta t$. The general flow chart for the proposed anisotropic damage model is illustrated in Figure 41.

The first step is to provide the value of the material parameters to be used in UMAT ("input data"). The user can define as many material constants as required by the model. Like in the models already implemented in ABAQUS, the material parameters to be used in UMAT have to be defined the module of properties in ABAQUS, where the user choses the constitutive model for the simulation (e.g. elastic, plastic or damage model). The material parameters are stored in an array: PROPS(NPROP). An example is given in Tab. 29. The procedure is the following:

Abaqus/CAE Usage: Create Material $\longrightarrow$ General $\longrightarrow$ User Material: User material type: Mechanical

The option *Depvar* is used to specify the number of solution-dependent state variables

(e.g. damage variables defined in UMAT based on continuous damage mechanics). These state variables will be updated and stored at each increment. After running a simulation, the values of the new state variables can be printed out and visualized on the mesh like the other variables (e.g., strains and stresses) already defined in Abaqus (module of Visualization). The procedure is the following:

Abaqus/CAE Usage: Create Material $\longrightarrow$ General $\longrightarrow$ Depvar: Number of solution-dependent state variables

Table 29: Input parameters

Variables	PROPS(1)	PROPS(2)	PROPS(3)	PROPS(4)
	Young's Module E_0	Initial Poisson's ratio ν_0	parameter a_1	parameter a_2
Unit	Pa		Pa^{-1}	Pa^{-1}
Variables	PROPS(5)	PROPS(6)	PROPS(7)	PROPS(8)
	parameter a_3	parameter a_4	Threshold of damage C_0	Hardening variable C_1
Unit	Pa^{-1}	Pa^{-1}	Pa	Pa
Variables	PROPS(9)	PROPS(10)	PROPS(11)	PROPS(12)
	parameter α	Initial damage Ω_{11}	Initial damage Ω_{22}	Initial damage Ω_{33}
Unit	-	-	-	-

E.2 DSID UMAT Subroutines in ABAQUS/CAE

The vectors and matrices storing the DSID parameters and variables are explained in the following.

1. Initialization

   During the ith iteration solving for the kth load increment, Abaqus gives the converged strain increment $\Delta\boldsymbol{\varepsilon}_{k,i}$ from the calculation by stress-strain relationship. The stress $\boldsymbol{\sigma}_{k,i-1}$ and strain $\boldsymbol{\varepsilon}_{k,i-1}$ from the proceeding iteration are stored in variables STRESS(NTENS) and STRAN(NTENS) respectively in the Abaqus solver. Damage

variables $\mathbf{\Omega}_{k,i-1}$ for proceeding iteration is stored in STATEV(1-6).

2. Input of material parameters

   The material parameters are given by the user, and stored in PROPS(NPROPS). The Fortran code is:

```
E0          =  PROPS(1)   ! Initial Young's modulus
ENU0        =  PROPS(2)   ! Initial Poisson's ratio
A1          =  PROPS(3)   ! parameter a_1
A2          =  PROPS(4)   ! parameter a_2
A3          =  PROPS(5)   ! parameter a_3
A4          =  PROPS(6)   ! parameter a_4
C0          =  PROPS(7)   ! Threshold of damage
C1          =  PROPS(8)   ! Hardening variable of damage
ALPHA       =  PROPS(9)   ! parameter α
OMEGA_11    =  PROPS(10)  ! Intial damage Ω_11
OMEGA_22    =  PROPS(11)  ! Intial damage Ω_22
OMEGA_33    =  PROPS(12)  ! Intial damage Ω_33
```

3. Conversion of the stored variables

   Abaqus stores the damage and state variables in STATEV(NSTATV) vector, as shown in Table 30:

   The first step of UMAT is to determine the location of each of components of the damage and state variables of interest in the STATEV vector:

Table 30: State variables

Variables	1	2	3	4	5	6	
Damage variable	Ω_{11}	Ω_{22}	Ω_{33}	Ω_{12}	Ω_{13}	Ω_{23}	
Variables	7	8	9	10	11	12	
Pure elastic strain	ε_{11}^{el}	ε_{22}^{el}	ε_{33}^{el}	$2\varepsilon_{12}^{el}$	$2\varepsilon_{13}^{el}$	$2\varepsilon_{23}^{el}$	
Variables	13	14	15	16	17	18	
Total elastic strain	ε_{11}^{E}	ε_{22}^{E}	ε_{33}^{E}	$2\varepsilon_{12}^{E}$	$2\varepsilon_{13}^{E}$	$2\varepsilon_{23}^{E}$	
Variables	19	20	21	22	23	24	
Irreversibel strain	ε_{11}^{id}	ε_{22}^{id}	ε_{33}^{id}	$2\varepsilon_{12}^{id}$	$2\varepsilon_{13}^{id}$	$2\varepsilon_{23}^{id}$	
Variables	25	26	27	28	29	30	
Damage force	Y_{d111}	Y_{d122}	Y_{d133}	Y_{d112}	Y_{d113}	Y_{d123}	
Variables	31	32	33	34	35	36	37
Energy	Φ_1	Φ_2	Φ_3	Φ_4	Φ_5	Φ_6	Φ_7
	$\sum \boldsymbol{\sigma} : \dot{\boldsymbol{\varepsilon}}$	$\sum \boldsymbol{\sigma} : \dot{\boldsymbol{\varepsilon}}^{E}$	$\sum \boldsymbol{\sigma} : \dot{\boldsymbol{\varepsilon}}^{el}$	$\sum \boldsymbol{\sigma} : \dot{\boldsymbol{\varepsilon}}^{id}$	$\sum \mathbf{Y} : \dot{\boldsymbol{\Omega}}$	$\sum \frac{\partial G_s}{\partial Tr\boldsymbol{\Omega}} : Tr\boldsymbol{\Omega}$	$\frac{1}{2}\boldsymbol{\sigma} : \boldsymbol{\varepsilon}$
Variables	38						
Damage function	f_d						

```
DO I = 1, NTENS
   OMEGA_V(I)    =   STATEV(I)              ! Convert Ω_{k,i-1} to a vector
   EPSEL_V(I)    =   STATEV(I+NTENS)        ! Convert ε^{el}_{k,i-1} to a vector
   EPSE_V(I)     =   STATEV(I+2*NTENS)      ! Convert ε^{E}_{k,i-1} to a vector
   EPSID_V(I)    =   STATEV(I+3*NTENS)      ! Convert ε^{id}_{k,i-1} to a vector
   YD1_V(I)      =   STATEV(I+4*NTENS)      ! Convert Y_{d1k,i-1} to a vector
   ENERGY(I)     =   STATEV(I+5*NTENS)      ! Convert Φ_{k,i-1} to a vector
END DO
ENERGY(7) = STATEV(6*NTENS+1)               ! Convert Φ_7
FD = STATEV(6*NTENS+2)                      ! Convert f_d
```

Then convert these vectors to tensors, which is easy for calculation later.

```
CALL MAT1_MAT2(NTENS,OMEGA_V,OMEGA,ONE)     ! Convert Ω_{k,i-1}
CALL MAT1_MAT2(NTENS,EPSEL_V,EPSEL,HALF)    ! Convert ε^{el}_{k,i-1}
CALL MAT1_MAT2(NTENS,EPSE_V,EPSE,HALF)      ! Convert ε^{E}_{k,i-1}
CALL MAT1_MAT2(NTENS,EPSID_V,EPSID,HALF)    ! Convert ε^{id}_{k,i-1}
CALL MAT1_MAT2(NTENS,YD1_V,YD1,ONE)         ! Convert Y_{d1k,i-1}
CALL MAT1_MAT2(NTENS,DSTRAN,DEPS,HALF)      ! Convert Δε_{k,i}
CALL MAT1_MAT2(NTENS,STRAN,EPS,HALF)        ! Convert ε_{k,i-1}
CALL MAT1_MAT2(NTENS,STRESS,SIGMA,ONE)      ! Convert σ_{k,i}
```

4. Trial computations in the elastic domain

   Based on the previous values of state variables internal variables, the stiffness tensor is updated. Assuming that the material is in the elastic domain, the trial stress increment is calculated, based on the linear elastic constitutive laws.

5. Damage condition

   The damage criterion is checked. If $f_d < 0$, the material is still elastic, the cumulated stress can be computed from the elastic stress increment computed in the previous step. If $f_d \geq 0$, the total strain increment falls into the damage domain, and therefore an iteration is needed to update the damage tensor, the damaged stiffness and the

stress.

6. Storage

   Variables are converted from a tensor form to a vector form, and stored in Abaqus solver so that these state variables can be used in the post-processing module.

```
CALL MAT2_MAT1(NTENS,OMEGA,OMEGA_V,ONE)    ! Convert Ω_{k,i-1}
CALL MAT2_MAT1(NTENS,EPSEL,EPSEL_V,TWO)    ! Convert ε^{el}_{k,i-1}
CALL MAT2_MAT1(NTENS,EPSE,EPSE_V,TWO)      ! Convert ε^{E}_{k,i-1}
CALL MAT2_MAT1(NTENS,EPSID,EPSID_V,TWO)    ! Convert ε^{id}_{k,i-1}
CALL MAT2_MAT1(NTENS,SIGMA,STRESS_V,ONE)   ! Convert σ_{k,i}
CALL MAT2_MAT1(NTENS,YD1,YD1_V,ONE)        ! Convert Y_{d1k,i}
```

   The state variables are stored in the array STATEV(NTENS):

```
DO I = 1, NTENS
  STATEV(I)          =  OMEGA_V(I)                      ! Store Ω_{k,i-1}
  STATEV(I+NTENS)    =  EPSEL_V(I)                      ! Store ε^{el}_{k,i-1}
  STATEV(I+2*NTENS)  =  EPSE_V(I)                       ! Store ε^{E}_{k,i-1}
  STATEV(I+3*NTENS)  =  EPSID_V(I)                      ! Store ε^{id}_{k,i-1}
  STATEV(I+4*NTENS)  =  YD1_V(I)                        ! Store ε^{id}_{k,i-1}
  STATEV(I+5*NTENS)  =  ENERGY(I)+STATEV(I+5*NTENS)     ! Store ε^{id}_{k,i-1}
END DO
STATEV(6*NTENS+2) = ENERGY(6)          ! Store updated Φ_7
STATEV(6*NTENS+1) = FD2                ! Store updated f_d
```

7. Update of the Jacobian matrix

   The Jacobian matrix DDSDDE used in UMAT subroutine provides an approximate stiffness matrix in the algorithm: the elastic stiffness $\mathbb{C}_0$ is used in the Modified Newton-Raphson Method - with a constant stiffness matrix in the entire resolution algorithm. In order to accelerate the convergence, the damaged stiffness $\mathbb{D}_{\mathbb{E}}(\mathbf{\Omega})$ is used: it is updated at each increment. This resolution procedure is based on secant matrices: this is Picard resolution scheme. Picard's method allow accelerating the convergence (compared to the modified Newton-Raphson method), without having to

calculate all the derivatives of the stiffness tensor as would be needed in the original Newton-Raphson method.

```
DO I = 1, NTENS
    DO J = 1, NTENS
        DDSDDE (I, J) = AMATDOM_2 (I, J)      ! DDSDDE=𝕔ₑ(Ω)
    ENDDO
ENDDO
```

The subroutines used in UMAT are used to calculate the damaged stiffness tensor according to the "'Differential Stress Induced Damage Model". In addition, auxiliary subroutines are called for some tensor computations. Subroutines are described in Table 31.

Table 31: Subroutines

Subroutines	Use	Subroutines	Use
MAT1_MAT2	Transfer vector to matrix	DMAT	Calculate stiffness and compliance tensor of material
MAT2_MAT1	Transfer matrix to vector	FDDP	Calculate damage function f_d
MAT2_MAT4	Transfer 4th order tensor to matrix	DIDENTITY_2	Generate identity
MAT4_MAT2	Transfer matrix to 4th order tensor	INVERSE	Calculate inverse of matrix
Aijkl_Bkl	Calculate matrix $C_{ij} = A_{ijkl}B_{kl}$		
Aij_Bij	Calculate scalar $C = A_{ij}B_{ij}$	DY_DSIGFUN	Calculate tensor $\frac{\partial Y_{ij}}{\partial \sigma_{kl}}$
Aij_PLUS_Bij	Calculate matrix $C_{ij} = A_{ij} + B_{ij}$	MATP_1	Calculate projection tensor $\mathbb{P}_1$
Aik_Bkj	Calculate matrix $C_{ij} = A_{ik}B_{kj}$	MATP_2	Calculate projection tensor $\mathbb{P}_2$
Aijkl_Bij	Calculate matrix $C_{kl} = B_{ij}A_{ijkl}$		
Aij_Bkl	Calculate tensor $C_{ijkl} = A_{ij}B_{kl}$		

REFERENCES

[1] *Abaqus 6.9 Documentation*.

[2] Abe, H., keer, L., and Mura, T., "Theoretical study of hydraulic fractured penny-shaped cracks in hot, dry rocks," *International Journal for Numerical and Analytical Methods in Geomechanics*, vol. 3, pp. 79–96, 1979.

[3] Abou-Chakra Guéry, A., Cormery, F., Su, K., Shao, J., and Kondo, D., "A micromechanical model for the elasto-viscoplastic and damage behavior of a cohesive geomaterial," *Physics and Chemistry of the Earth*, vol. 33, pp. S416–S421, 2008.

[4] Abou-Sayed, A. S., "An experimental technique for measuring the fracture toughness of rocks under downhole stress condition," *VDI-Berichte.*, vol. 313, pp. 829–824, 1978.

[5] Abu Al-Rub, R. K. and Kim, S.-M., "Computational applications of a coupled plasticity-damage constitutive model for simulating plain concrete fracture.," *Engineering Fracture Mechanics*, vol. 77, pp. 1577–1603, 2010.

[6] Abu Al-Rub, R. K. and george Z, V., "On the coupling of anisotropic damage and plasticity models for ductile materials," *International Journal of Solids and Structures*, vol. 40, pp. 2611–2643, 2003.

[7] Adachi, J., Siebrits, E., Peirce, A., and Desroches, J., "Computer simulation of hydraulic fractures," *International Journal of Rock Mechanics and Mining Sciences*, vol. 44, pp. 739–757, 2007.

[8] Altmann, J. B., Muller, T. M., Muller, B. I., Tingay, M. R., and Heidbach, O., "Poroelastic contribution to the reservoir stress path," *International Journal of Rock Mechanics & Mining Sciences*, vol. 47, pp. 1104–1113, 2010.

[9] Anderson, T. L., *Fracture Mechanics: Fundamentals and Applications*. CRC Press, 3rd ed., May 2004.

[10] Arson, C., "Using a geo-mechanical damage model to assess permeability in cracked porous media: internal length parameter issues," *Special Topics & Reviews in Porous Media*, vol. 3, pp. 69–77, 2012.

[11] Arson, C. and Gatmiri, B., "Excavation damage in unsaturated porous media," *Key Engineering Materials, Advances in Fracture and Damage Mechanics VII*, vol. 385-387, pp. 137–140, 2008.

[12] Arson, C. and Gatmiri, B., "On damage modelling in unsaturated clay rocks," *Physics and Chemistry of the Earth*, vol. 33, p. S407S415, 2008.

[13] Arson, C. and Gatmiri, B., "A mixed damage model for unsaturated porous media," *Comptes-Rendus de l'Académie des Sciences de Paris, section Mécanique*, vol. 337, pp. 68–74, 2009.

[14] Arson, C. and Gatmiri, B., "Numerical study of a thermo-hydro-mechanical damage model for unsaturated porous media," *Annals of Solid and Structural Mechanics*, vol. 1, pp. 59–78, 2010.

[15] Arson, C. and Gatmiri, B., "Numerical study of damage in unsaturated geological and engineered barriers," *Physics and Chemistry of the Earth*, vol. 36, pp. 1981–1989, 2011.

[16] Arson, C. and Gatmiri, B., "Thermo-hydro-mechanical modeling of damage in unsaturated porous media: Theoretical framework and numerical study of the edz," *International Journal for Numerical and Analytical Methods in Geomechanics*, vol. 36, pp. 272–306, 2012.

[17] Arson, C. and Pereira, J.-M., "Influence of damage on pore size distribution and permeability of rocks," *International Journal for Numerical and Analytical Methods in Geomechanics*, p. DOI: 10.1002/nag.1123, 2012.

[18] Arson, C., Xu, H., and Chester, F., "On the definition of damage in time-dependent healing models for salt rock," *Géotechnique Letters*, p. DOI: 10.1680/geolett.12.00013, 2012.

[19] Arson, C., *Etude théorique et numérique de l'endommagement thermo-hydro-mécanique des milieux poreux non saturés*. PhD thesis, Ecole Nationale des Ponts et Chaussées, Paris, Sep. 2009.

[20] Arson, C., "Proposal of finite element modeling of hydraulic fracturing," 2011.

[21] Ashby, M. F. and Hallam, S. D., "The failure of brittle solids containing small cracks under compressive stress states," *Acta Metallurgica*, vol. 34, no. 3, pp. 497–510, 1986.

[22] Ashby, M. F. and Sammis, C. G., "The damage mehcanics of brittle solids in compression," *Pure and Applied Geophysics*, vol. 133, pp. 489–521, May 1990.

[23] Auqué, L., Acero, P., Gimeno, M., Gómez, J., and Asta, M., "Hydrogeochemical modeling of a thermal system and lessons learned for CO_2 geologic storage," *Chemical Geology*, vol. 268, no. 3–4, pp. 324–336, 2009.

[24] Bae, J.-S. and Bhatia, S., "High-pressure adsorption of methane and carbon dioxide on coal.," *Energy & Fuels*, vol. 20, no. 6, pp. 2599–2607, 2006.

[25] Bakhtiary, E., Xu, H., and Arson, C., "Probabilistic optimization of a continuum mechanics model to predict differential stress-induced damage in claystone," *International Journal of Rock Mechanics & Mining Sciences*, 2014.

[26] Barbero, E. J., Greco, F., and Lonetti, P., "Continuum damage-healing mechanics with application to self-healing composites," *International Journal of Damage Mechanics*, vol. 14, no. 1, pp. 51–81, 2005.

[27] Bažant, Z., "Why continuum damage is nonlocal: Micromechanics arguments," *Journal of Engineering Mechanics*, vol. 117, no. 5, pp. 1070–1087, 1991.

[28] Bažant, Z. and Jirásek, M., "Nonlocal integral formulations of plasticity and damage: Survey of progress," *Journal of Engineering Mechanics*, vol. 128, no. 11, pp. 1119–1149, 2002.

[29] Bear, J., *Dynamics of Fluids in Porous Media*. New York, NY, USA: American Elsevier, 1972.

[30] Belytschko, T. and Black, T., "Elastic crack growth in finite elements with minimal remeshing," *International Journal of Fracture Mechanics*, vol. 45, pp. 601–620, 1999.

[31] Belytschko, T. and Kulkarni, M., *ailure criteria and analysis in dynamic response*, ch. On imperfections and spatial gradient regularization in strain softening viscoplasticity, pp. 1–5. H.E. Lindberg and Aptek (eds), American Society of Mechanical Engineers, 1990.

[32] Bera, B., Mitra, S. K., and Vick, D., "Understanding the micro structure of berea sandstone by the simultaneous use of micro-computed tomography (micro-CT) and focused ion beam-scanning electron microscopy (FIB-SEM)," *Micron*, vol. 42, no. 5, pp. 412–418, 2011.

[33] Bérest, P., Bergues, J., Brouard, B., Durup, J., and Guerber, B., "A salt cavern abandonment test," *International Journal of Rock Mechanics and Mining Sciences*, vol. 38, no. 3, pp. 357–368, 2001.

[34] Berryman, J. G., "Long-wavelength propagation in composite elastic media: Ii. ellipsoidal inclusions," *J. Acoust. Soc. Am.*, vol. 68, pp. 1820–1831, 1980.

[35] Blümling, P., Bernier, F., Lebon, P., and Martin, C. D., "The excavation damaged zone in clay formations time-dependent behaviour and influence on performance assessment," *Physics and Chemistry of the Earth, Parts A/B/C*, vol. 32, no. 8–14, pp. 588–599, 2007.

[36] Bobet, A. and Einstein, H., "Fracture coalescence in rock-type materials under uniaxial and biaxial compression," *International Journal of Rock Mechanics & Mining Sciences*, vol. 35, no. 7, p. October, 1998.

[37] Bobet, A. and Einstein, H., "Numerical modeling of fracture coalescence in a model rock material," *International Journal of Fracture*, vol. 92, pp. 221–252, 1998.

[38] Bonin, B., "Deep geological disposal in argillaceous formations: studies at the tournemire test site," *Journal of Contaminant Hydrology*, vol. 35, no. 1–3, pp. 315–330, 1998.

[39] Borges, J. A. R., Pires, L. F., and Belmont Pereira, A., "Computed tomography to estimate the representative elementary area for soil porosity measurements," *The Scientific World Journal*, vol. 2012, pp. 1–10, 2012.

[40] Bourgeois, F., Shao, J., and Ozanam, O., "An elastoplastic model for unsaturated rocks and concrete," *Mechanics Research Communications*, vol. 29, pp. 383–390, 2002.

[41] Box, G. E. and Cox, D. R., "An analysis of transformations," *Journal of the Royal Statistical Society. Series B (Methodological)*, pp. 211–252, 1964.

[42] Box, G. E. and Tiao, G. C., *Bayesian inference in statistical analysis*, vol. 40. John Wiley & Sons, 2011.

[43] Boyce, L. and Chamis, C., "Probabilistic constitutive relationships for cyclic material strength models," *Journal of Propulsion and Power*, vol. 8, no. 1, pp. 227–232, 1992.

[44] Brady, B. H. and Brown, E., *Rock mechanics: for underground mining*. Springer, 2004.

[45] BRC, "Blue ribbon commission on america's nuclear future draft report to the secretary of energy," tech. rep., Blue Ribbon Commision, JUL 2011.

[46] Budiansky, B. and Oconnell, R. J., "Elastic-moduli of a cracked solid," *International Journal of Solids and Structures*, vol. 12, no. 2, pp. 81–97, 1976.

[47] Bunger, A. P. and Detournay, E., "Early-time solution for a radial hydraulic fracture," *Journal of Engineering Mechanics*, vol. 133, pp. 534–540, May 2007.

[48] Busetti, S., *Fracturing of Layered Reservoir Rocks*. PhD thesis, University of Oklahoma, 2009.

[49] Busetti, S., Mish, K., and Reches, Z., "Damage and plastic deformation of reservoir rocks: Part 1. damage fracturing," *AAPG Bulletin*, vol. 96, no. 9, pp. 1687–1709, 2012.

[50] Cai, M. and Kaiser, P., "In-situ rock spalling strength near excavation boundaries," *Rock Mechanics and Rock Engineering*, vol. 47, no. 2, pp. 659–675, 2014.

[51] Carrier, B. and Granet, S., "Numerical modeling of hydraulic fracture problem in permeable medium using cohesive zone model," *Engineering fracture mechanics*, vol. 79, pp. 312–328, 2012.

[52] Carstensen, C., Hackl, K., and Mielke, A., "Non–convex potentials and microstructures in finite–strain plasticity," *Proceedings of the Royal Society of London. Series A: Mathematical, Physical and Engineering Sciences*, vol. 458, no. 2018, pp. 299–317, 2002.

[53] Carter, N. L. and Hansen, F. D., "Creep of rocksalt," *Tectonophysics*, vol. 92, no. 4, pp. 275–333, 1983.

[54] Chaboche, J.-L., "Damage induced anisotropy: On the difficulties associated with the active/passive unilateral condition," *International Journal of Damage Mechanics*, vol. 1, pp. 148–171, 1992.

[55] Chaboche, J.-L., "Development of continuum damage mechanics for elastic solids sustaining anisotropic and unilateral damage," *International Journal of Damage Mechanics*, vol. 2, pp. 311–329, 1993.

[56] Chan, K. S., Bodner, S. R., and Munson, D. E., "Recovery and healing of damage in wipp salt," *International Journal of Damage Mechanics*, vol. 7, no. 2, pp. 143–166, 1998.

[57] Chan, K., Munson, D., Bodner, S., and Fossum, A., "Cleavage and creep freacture of rock salt," *Acta Materialia*, vol. 44, no. 9, pp. 3553–3565, 1996.

[58] Chan, K. S., Bodner, S. R., and Munson, D. E., "Permeability of wipp salt during damage evolution and healing," *International Journal of Damage Mechanics*, vol. 10, pp. 347–375, Oct. 2001.

[59] Chen, Z., "Finite element modelling of viscosity-dominated hydraulic fractures," *Journal of Petroleum Science and Engineering*, vol. 88–89, pp. 136–144, 2012.

[60] Chiaramonte, L., Zoback, M., Friedmann, J., and Stamp, V., "Seal integrity and feasibility of CO_2 sequestration in the teapot dome eor pilot: geomechanical site characterization," *Environmental Geology*, vol. 54, pp. 1667–1675, 2008.

[61] Chiarelli, A., Shao, J., and Hoteit, H., "Modeling of elastoplastic damage behavior of a claystone," *International Journal of Plasticity*, vol. 19, pp. 23–45, 2003.

[62] Chow, C. and Lu, T., "On Evolution Laws of Anisotropic Damage," *Engineering Fracture Mechanics*, vol. 34, no. 3, pp. 679–701, 1989.

[63] Cicekli, U., Voyiadjis, G. Z., and Abu Al-Rub, R. K., "A plasticity and anisotropic damage model for plain concrete.," *International Journal of Plasticity*, vol. 23, pp. 1874–1900, 2007.

[64] Collins, I. F. and Houlsby, G. T., "Application of thermomechanical principles to the modelling of geotechnical materials.," *Proceedings: Mathematical, Physical and Engineering Sciences*, vol. 453, no. 1964, pp. 1975–2001, 1997.

[65] Cosenza, P., Ghoreychi, M., Bazargan-Sabet, B., and de Marsily, G., "In situ rock salt permeability measurement for long term safety assessment of storage," *International Journal of Rock Mechanics and Mining Sciences*, vol. 36, no. 4, pp. 509–526, 1999.

[66] Coussy, O., *Mechanics of Porous Continua*. John Wiley & Sons, 1995.

[67] Coussy, O., *Poromechanics*. John Wiley & Sons, 2004.

[68] Cowin, S. C., "The relationship between the elasticity tensor and the fabric tensor," *Mechanics of Materials*, vol. 4, pp. 137–147, 1985.

[69] Crossno, P., Rogers, D. H., Brannon, R. M., Coblentz, D., and Fredrich, J. T., "Visualization of geologic stress perturbations using mohr diagrams," *IEEE Transactions on Visualization and Computer Graphics*, vol. 11, no. 5, pp. 508–518, 2005.

[70] Dahi-Taleghani, A. and Olson, J. E., "Numerical modeling of multistranded-hydraulic-fracture propagation: Accounting for the interaction between induced and natural fractures," *SPE journal*, vol. 16, pp. 575–581, September 2011.

[71] Das, I. and Zoback, M. D., "Long-period, long-duration seismic events during hydraulic fracture stimulation of a shale gas reservoir," *The Leading Edge*, pp. 778–786, July 2011.

[72] Deng, H. and Nemat-Nasser, S., "Dynamic damage evolution in brittle solids," *Mechanics of Materials*, vol. 14, pp. 83–103, 1992.

[73] Desmorat, R., "Positivité de la dissipation intrinsèque d'une classe de modèles d'endommagement anisotropes non standards," *Comptes Rendus Mecanique*, 2006.

[74] Detournay, E. and Garagash, D. I., "The near-tip region of a fluid-driven fracture propagating in a permeable elastic solid," *Journal of Fluid Mechanics*, vol. 494, pp. 1–32, 2003.

[75] Deudé, V., Dormieux, L., Kondo, D., and Maghous, S., "Micromechanical Approach to Nonlinear Poroelasticity : Application to Cracked Rocks," *Journal of Engineering Mechanics*, vol. 128, no. 8, pp. 848–855, 2002.

[76] Deudé, V., Dormieux, L., Kondo, D., and Pensée, V., "Propriétés élastiques non linéaires d ' un milieu mésofissuré," *C.R. Mécanique, Acad. Sci. Paris*, vol. 330, pp. 587–592, 2002.

[77] Dieterich, J. and Smith, D., "Non-planar faults: Mechanics of slip and off-fault damage," *Pure Appl. Geophys.*, vol. 166, pp. 1799–1815, 2009.

[78] Dufour, N., Wong, H., Arson, C., Deleruyelle, F., and Pereira, J.-M., "A thermodynamically consistent framework for saturated viscoplastic rock-materials subject to damage," *Mechanics Research Communications*, p. DOI: 10.1016/j.mechrescom.2012.06.009, 2012.

[79] Dugdale, D. S., "Yielding of steel sheets containing slits," *J. Mech. phys. Solids*, vol. 8, pp. 100–104, 1960.

[80] Economides, M. and Valko, P., "Interpretation and modeling of hydraulic frcturing phenomena with continuum damage mechanics - An application to engineering design," in *Computer Methods and Advances in Geomechanics*, pp. 1579–1584, 1994.

[81] Egner, H., "On the full coupling between thermo-plasticity and thermo-damage in thermodynamic modeling of dissipative materials," *International Journal of Solids and Structures*, vol. 49, pp. 279–288, 2012.

[82] Espinoza, D. N., Kim, S. H., and Santamarina, J. C., "CO_2 geological storage geotechnical implications," *KSCE Journal of Civil Engineering*, vol. 15, no. 4, pp. 707–719, 2011.

[83] Espinoza, D. N. and Santamarina, J. C., "Water-CO_2-mineral systems: Interfacial tension, contact angle, and diffusion - Implications to CO_2 geological storage," *Water Resources Research*, vol. 46, 2010.

[84] Everitt, R. and Lajtai, E., "The influence of rock fabric on excavation damage in the lac du bonnett granite," *International Journal of Rock Mechanics & Mining Sciences*, vol. 41, pp. 1277–1303, 2004.

[85] Farias, M. M., Pedroso, D. M., and Nakai, T., "Automatic substepping integration of the subloading tij model with stress path dependent hardening," *Computers and Geotechnics*, vol. 36, pp. 537–548, 2009.

[86] Faulkner, D. R., Mitchell, T. M., Healy, D., and Heap, M. J., "Slip on 'weak' faults by the rotation of regional stress in the fracture damage zone.," *Nature*, vol. 444, pp. 922–5, Dec. 2006.

[87] Fischer, T. and Guest, A., "Shear and tensile earthquakes caused by fluid injection," *Geophysical Research Letters*, vol. 38, 2011.

[88] Florez-Nino, J.-M., Aydin, A., Mavko, G., Antonellini, M., and Ayaviri, A., "Fault and fracture systems in a fold and thrust belt: An example from bolivia," *AAPG Bulletin*, vol. 89, no. 4, pp. 471–493, 2005.

[89] Fouinneteau, M. and Pickett, A., "Shear mechanism modelling of heavy tow braided composites using a meso-mechanical damage model," *Composites: Part A*, vol. 38, pp. 2294–2306, 2007.

[90] Frémond, M. and Nedjar, B., "Damage, gradient of damage and principle of virtual power," *International Journal of Solids and Structures*, vol. 33, pp. 2294–2306, 1996.

[91] Fu, P., Johnson, S. M., and Carrigan, C., "An explicitly coupled hydro-geomechanical model for simulating hydraulic fracturing in complex discrete fracture networks," *International Journal for Numerical and Analytical Methods in Geomechanics*, vol. online, 2012.

[92] Fuenkajorn, K., Phueakphum, D., and Jandakaew, M., "Healing of rock salt fractures.," in *Proceedings of the 38th symposium engineering geology and geotechnical engineering.*, pp. 393–408, 2003.

[93] Fuenkajorn, K. and Phueakphum, D., "Laboratory assessment of healing of fractures in rock salt," *Bulletin of Engineering Geology and the Environment*, pp. 1–8, 2011.

[94] Garcia-Bengoechea, I., Lowell, C., and Altschaeffl, A., "Pore distribution and permeability of silty clays," *J. Geotech. Eng. Div.*, vol. 105, pp. 839–856, 1979.

[95] Gardoni, P., Der Kiureghian, A., and Mosalam, K. M., "Probabilistic capacity models and fragility estimates for reinforced concrete columns based on experimental observations," *Journal of Engineering Mechanics*, vol. 128, no. 10, pp. 1024–1038, 2002.

[96] Gardoni, P., Pillai, R. G., Hueste, M. B. D., Reinschmidt, K., and Trejo, D., "Probabilistic capacity models for corroding posttensioning strands calibrated using laboratory results," *Journal of engineering mechanics*, vol. 135, no. 9, pp. 906–916, 2009.

[97] Gardoni, P., Trejo, D., Vannucci, M., and Bhattacharjee, C., "Probabilistic models for modulus of elasticity of self-consolidated concrete: bayesian approach," *Journal of engineering mechanics*, vol. 135, no. 4, pp. 295–306, 2009.

[98] Gatmiri, B. and Arson, C., "Theta-stock, a powerful tool for thermohydromechanical behaviour and damage modelling of unsaturated porous media," *Computers & Geotechnics*, vol. 35, no. 8, pp. 890–915, 2008.

[99] Gatmiri, B. and Arson, C., "Theta-stock, a powerful tool for thermohydromechanical behaviour and damage modelling of unsaturated porous media," *Computers and Geotechnics*, vol. 35, no. 6, pp. 890–915, 2008.

[100] Gatmiri, B., Hemmati, S., Arson, C., and Emirzehni, E., "A multiphase analysis for environmental impact assessment with theta-stock finite element program," *Journal of Multiscale Modelling*, vol. 2, no. 1-2, pp. 23–68, 2011.

[101] Geertsma, J. and de Klerk, F., "A rapid method of predicting width and extent of hydraulically induced fractures," *J. Pet. Tech.*, vol. 21, pp. 1571–81, 1969.

[102] Gelman, A., Carlin, J. B., Stern, H. S., and Rubin, D. B., *Bayesian data analysis*. CRC press, 2003.

[103] Gens, A., Garcia-Molina, A. J., Olivella, S., Alonso, E. E., and Huertas, F., "Analysis of a full scale in situ test simulating repository conditions," *International Journal for Numerical and Analytical Methods in Geomechanics*, vol. 22, no. 7, pp. 515–548, 1998.

[104] Germain, P., "La méthode des puissances virtuelles en mécanique des milieux continus. première partie : théorie du second gradient," *J. de Mécanique*, vol. 12, no. 2, pp. 235–274, 1973.

[105] Germain, P., "The method of virtual power in continuum mechanics. part 2: Microstructure," *Journal on Applied Mathematics*, vol. 25, no. 3, pp. 556–575, 1973.

[106] Germanovich, L. N., Astakhov, D. K., Mayerhofer, M. J., Shlyapobersky, J., and Ring, L. M., "Hydraulic fracture with multiple segments i. observations and model formulation," *International Journal of Rock Mechanics and Mining Sciences*, vol. 34, no. 3–4, pp. 97.e1–97.e19, 1997.

[107] Germanovich, L. N., Ring, L. M., Astakhov, D. K., Shlyapobersky, J., and Mayerhofer, M. J., "Hydraulic fracture with multiple segments ii. modeling," *International Journal of Rock Mechanics and Mining Sciences*, vol. 34, no. 3–4, pp. 98.e1–98.e15, 1997.

[108] Germanovinch, L. N. and Murdoch, L. C., "Injection of solids to lift coastal areas," *Proceedings of the Royal Society-Mathematical Physical and Engineering Sciences*, vol. 466, pp. 3225–3252, 2010.

[109] Ghabezloo, S., Sulem, J., Gu˜edon, S., Martineau, F., and Sant-Marc, J., "Poromechanical behavior of hardened cement paste under isotropic loading," *Cement and Concrete Research*, vol. 38, pp. 1424–1437, 2008.

[110] Goodman, R. E., *Introduction to Rock Mechanics*. Wiley, 2nd ed., 1989.

[111] Great Bear Petroleum LLC., "Unconventional reservoirs explained." http://greatbearpetro.com/unconventional-reservoirs-explained.html.

[112] Green AE, S. I., "The distribution of stress in the neighbourhood of a flat elliptical crack in an elastic solid," in *Proc. Cambridge Philos. Soc.*, vol. 46, pp. 159–63, 1950.

[113] Guéguen, Y., Gavrilenko, P., and Le Ravalec, M., "Scales of rock permeability," *Surveys in Geophysics*, vol. 17, no. 3, pp. 245–263, 1996.

[114] Guéguen, Y. and Palciauskas, V., *Introduction to the Physics of Rocks*. Princeton University Press, 1994.

[115] Halm, D. and Dragon, A., "An anisotropic model of damage and frictional sliding for brittle materials," *Eur. J. Mech. A/ Solids*, vol. 17, no. 3, pp. 439–460, 1998.

[116] Halm, D. and Dragon, A., "Modelisation de l'endommagement par mesofissuration du granite," *Revue Francaise de Genie Civi.*, vol. 17, pp. 21–33, 2002.

[117] Hamiel, Y., Liu, Y., Lyakhovsky, V., Ben-Zion, Y., and Lockner, D., "A viscoelastic damage model with applications to stable and unstable fracturing," *Geophys. J. Int.*, vol. 25, pp. 729–737, 2004.

[118] Hansen, N. and Schreyer, H., "A thermodynamically consistent framework for theories of elastoplasticity coupled with damage," *International Journal of Solids and Structures*, vol. 31, no. 3, pp. 359–389, 1994.

[119] Hassanzadeh, H., Pooladi-Darvish, M., and Keith, D., "Accelerating CO_2 dissolution in saline aquifers for geological storage s mechanistic and sensitivity studies," *Energy & Fuels*, vol. 23, pp. 3328–3336, 2009.

[120] Hayakawa, K. and Murakami, S., "Thermodynamical modeling of elastic-plastic damage and experimental validation of damage potential," *International Journal of Damage Mechanics*, vol. 6, pp. 333–363, 1997.

[121] Healy, D., "Damage patterns, stress rotations and pore fluid pressures in strike-slip fault zones," *Journal of Geophysical Research*, vol. 113, pp. 1–16, Dec. 2008.

[122] Heap, M. J., Faulkner, D. R., Meredith, P. G., and Vinciguerra, S., "Elastic moduli evolution and accompanying stress changes with increasing crack damage: implications for stress changes around fault zones and volcanoes during deformation," *Geophysical Journal International*, vol. 183, pp. 225–236, Oct. 2010.

[123] Hemminger, J., Crabtree, G., and Kastner, M., "New science for a secure and sustainable energy future," *A Report from the Basic Energy Sciences Advisory Committee, U.S. Department of Energy, December 2008*, 2008.

[124] Homand, F., Chiarelli, A.-S., and Hoxha, D., "Caractéristiques physiques et mécaniques du granite de la vienne et de l'argilite de l'est," *Revue Francaise de Génie Civil*, vol. 6, no. 1, pp. 11–20, 2002.

[125] Homand-Etienne, F., Hoxha, D., and Shao, J. F., "A Continuum Damage Constitutive Law for Brittle Rocks," *Computers and Geotechnics*, vol. 22, no. 2, pp. 135–151, 1998.

[126] Horii, H. and Nemat-Nasser, S., "Brittle failure in compression: splitting, faulting and brittle-ductile transition," *Philosophical Transactions of the Royal Society of London. Series A, MAthematical and Physical Science*, vol. 319, no. 1549, pp. 337–374, 1986.

[127] Horii, H. and Nemet-Nasser, S., "Compression-induced microcrack growth in brittle solids: axial splitting and shear failure," *Journal of Geophysical Research*, vol. 90, no. B4, pp. 3105–3125, 1985.

[128] Hou, Z., "Mechanical and hydraulic behavior of rock salt in the excavation disturbed zone around underground facilities.," *International Journal of Rock Mechanics & Mining Sciences*, vol. 40, pp. 725–738, July 2003.

[129] Houlsby, G. T. and Puzrin, A. M., *Principles of hyperplasticity an approach to plasticity theory based on thermodynamic principles*. London, 2006.

[130] Huang, C., Subhash, G., and Vitton, S. J., "A dynamic damage growth model for uniaxial compressive response of rock aggregates," *Mechanics of Materials*, vol. 34, pp. 267–277, 2002.

[131] Hughes, P., "Geothermal (ground-source) heat pumps: Market status, barriers to adoption, and actions to overcome barriers," *Oak Ridge National Laboratory, Report ORNL/TM-2008/232*, 2008.

[132] Hult, J., "Cdm- capabilities, limitations and promises(continuum damage mechanics)," *Mechanisms of deformation and fracture*, pp. 233–247, 1979.

[133] Hunsche, U. and Hampel, A., "Rock salt - the mechanical properties of the host rock material for a radioactive waste repository.," *Engineering Geology*, vol. 52, pp. 271–291, April 1999.

[134] Hütter, M. and Tervoort, T., "Continuum damage mechanics: combining thermodynamics with a thoughtful characterization of the microstructure," *Acta mechanica*, vol. 201, no. 1-4, pp. 297–312, 2008.

[135] Irawan, Y. S., Hagiwara, Y., and Ohya, S.-I., "Predictions of anisotropy affected fatigue crack propagation paths in pure aluminum sheets," *International Journal of Computational Methods*, vol. 03, no. 01, pp. 83–96, 2006.

[136] Ishida, T., Chen, Q., Mizuta, Y., and Roegiers, J.-C., "Influence of fluid viscosity on the hydraulic fracturing mechanism," *Transactions of the ASME*, vol. 126, pp. 190–200, 2004.

[137] J. Sulem, I. V., *Bifurcation Analysis in Geomechanics*, ch. Second-grade plasticity theory for geomaterials, pp. 282–425. Blackie Academic and Professional, 1995.

[138] Jaeger, J. C., Cook, N. G., and Zimmerman, R. W., *Fundamentals of Rock Mechanics*. Blackwell Publishing, fourth edition ed., 2007.

[139] Jamison, W. R., "Stress spaces and stress paths," *Journal of Structural Geolog*, vol. 14, pp. 1111–1120, 1992.

[140] Jirásek, M., "Nonlocal models for damage and fracture: Comparison of approaches," *International Journal of Solids and Structures*, vol. 35, no. 31–32, pp. 4133–4145, 1998.

[141] Jones, M. E. and Addis, M. A., "The application of stress path and critical state analysis to sediment deformation," *Journal of Structural Geolog*, vol. 8, pp. 575–580, 1986.

[142] Kachanov, L., "Rupture time under creep conditions," *Izvestia Akademii Nauk SSSR, Otdelenie tekhnicheskich nauk*, vol. 8, pp. 26–31, 1958.

[143] Kachanov, M., "Effective elastic properties of cracked solids: critical review of some basic concepts," *Appl. Mech. Rev.*, vol. 45, pp. 304–335, Aug. 1992.

[144] Katz, O. and Reches, Z., "Microfracturing, damage, and failure of brittle granites," *Journal of Geophysical Research: Solid Earth*, vol. 109, no. B1, pp. n/a–n/a, 2004.

[145] Keller, A. and Hutter, K., "On the thermodynamic consistency of the equivalence principle in continuum damage mechanics," *Journal of the Mechanics and Physics of Solids*, vol. 59, no. 5, pp. 1115–1120, 2011.

[146] Keshavarz, M., Pellet, F., and Loret, B., "Damage and changes in mechanical properties of a gabbro thermally loaded up to 1,000 ° c.," *Pure & Applied Geophysics*, vol. 167, pp. 1511–1523, Dec. 2010.

[147] Khristianovic, S. and Zheltov, Y., "Formation of vertical fractures by means of highly viscous liquid," in *Proceedings of the fourth world petroleum congress*, (Rome), pp. 57–86, 1955.

[148] Kim, H.-M., Rutqvist, J., Ryu, D.-W., Choi, B.-H., Sunwoo, C., and Song, W.-K., "Exploring the concept of compressed air energy storage (caes) in lined rock caverns at shallow depth: a modeling study of air tightness and energy balance," *Applied Energy*, vol. 92, pp. 653–667, 2012.

[149] Knopoff, L., J. L. and Abinante, M., "Dynamical model of an earthquake fault with localization," *Physical Review A*, vol. 31, no. 12, pp. 7445–7449, 1992.

[150] Kondo, D. and Dormieux, L., "Approche micro-mécanique du couplage permabilité - endommagement," *Comptes-Rendus de Mécanique, Acad. Sci. Paris*, vol. 332, pp. 135–140, 2004.

[151] Kourepinis, D., Pearce, C., and Bicanic, N., "Higher-order discontinuous modeling or fracturing in concrete using the numerical manifold method," *International Journal of Computational Methods*, vol. 7, no. 1, pp. 83–106, 2010.

[152] Kouznetsova, V., Geers, M. G. D., and Brekelmans, W. A. M., "Multi-scale constitutive modelling of heterogeneous materials with a gradient-enhanced computational homogenization scheme," *International Journal for Numerical Methods in Engineering*, vol. 54, pp. 1235–1260, 2002.

[153] Krajcinovic, D., *Damage Mechanics*. North-Holland, 1996.

[154] Kwon, S. and Wilson, J., "Deformation mechanism of the underground excavations at the WIPP site," *Rock Mechanics and Rock Engineering*, vol. 32, no. 2, pp. 101–122, 1999.

[155] L. Dormieux, D. Kondo, F. U., *Microporomechanics*. John Wiley & Sons, 2006.

[156] Lacy, T. E., McDowell, D. L., and Talreja, R., "Gradient concepts for evolution of damage," *Mechanics of Materials*, vol. 31, pp. 831–860, Dec. 1999.

[157] Lankford, J., "Shear versus dilatational damage mechanisms in the compressive failure of fibre-reinforced composites," *Composites Part A: Applied Science and Manufacturing*, vol. 28, no. 3, pp. 215–222, 1997.

[158] Lasry, D. and Belytschko, T., "Localization limiters in transient problems," *International Journal of Solids and Structures*, vol. 24, no. 6, pp. 581–597, 1988.

[159] Lecampion, B., "Hydraulic fracture initiation from an open-hole : wellbore size , pressurization rate and fluid-solid coupling effects," in *46th Rock Mechanics Geomechanics Symposium*, vol. 2, (Chicago, IL), 2012.

[160] Lee, D.-H., Juang, C., Chen, J.-W., Lin, H.-M., and Shieh, W.-H., "Stress paths and mechanical behavior of a sandstone in hollow cylinder tests," *International Journal of Rock Mechanics and Mining Sciences*, vol. 36, pp. 857–870, 1999.

[161] Lee, J. and Fenves, G., "Plastic-damage model for cyclic loading of concrete structures," *Journal of Engineering Mechanics*, vol. 124, pp. 892–900, 1998.

[162] Lee, J. Y. and Ahn, S. Y., "Interactive visualization of elasto-plastic behavior through stress paths and yield surfaces in finite element analysis," *Finite Elements in Analysis and Design*, vol. 47, pp. 496–510, 2011.

[163] Lemaître, J. and Desmorat, R., *Engineering Damage Mechanics. Ductile, creep, fatigue and brittle failure.* Springer - Verlag, Berlin Heidelberg, 2005.

[164] Lemaître, J., "A continuous damage mechanics model for ductile fracture," *J. Eng. Mater. Technol.*, vol. 107, pp. 83–89, 1985.

[165] Levasseur, S., Collin, F., Charlier, R., and Kondo, D., "A two scale anisotropic damage model accounting for initial stresses in microcracked materials," *Engineering Fracture Mechanics*, vol. 78, pp. 1945–1956, 2011.

[166] Levasseur, S., Collin, F., Charlier, R., and Kondo, D., "On micromechanical damage modeling in geomechanics: Influence of numerical integration scheme," *Journal of Computational and Applied MathematicsJournal of Computational and Applied Mathematics*, vol. 246, pp. 215–224, 2013.

[167] Levasseur, S., Charlier, R., Frieg, B., and Collin, F., "Hydro-mechanical modelling of the excavation damaged zone around an underground excavation at mont terri rock laboratory," *International Journal of Rock Mechanics and Mining Sciences*, vol. 47, no. 3, pp. 414–425, 2010.

[168] Li, S. and Ghosh, S., "Debonding in composite microstructures with morphological variations.," *International Journal of Computational Methods*, vol. 1, no. 1, pp. 121–149, 2004.

[169] Lisjak, A., Grasseli, G., and Vietor, T., "Continuum–discontinuum analysis of failure mechanisms around unsupported circular excavations in anisotropic clay shales," *InternationalJournalof Rock Mechanics & Mining Sciences*, vol. 65, pp. 96–115, 2014.

[170] Liu, H. W., "On the fundamental basis of fracture mechanics," *Engineering Fracture Mechancis*, vol. 17, no. 5, pp. 425–438, 1984.

[171] Loucks, R., Reed, R., Ruppel, S., and Jarvie, D., "Morphology, genesis, and distribution of nanometer-scale pores in siliceous mudstones of the mississippian barnett shale," *Journal of Sedimentary Research*, vol. 79, pp. 848–861, 2009.

[172] Lu, Y. F. and Shao, J. F., "Modelling of anisotropic damage in brittle rocks under compression dominated stresses," *International Journal for Numerical and Analytical Methods in Geomechanics*, vol. 26, pp. 945–961, 2002.

[173] Lu, Y. and Elsworth, D., "Combined Microscopic-Macroscopic Modeling of Rock Damage and Failure," in *46th Rock Mechanics Geomechanics Symposium*, (Chicago, IL), pp. ARMA 12–250, 2012.

[174] Lubarda, V. and Krajcinovic, D., "Damage tensors and the crack density distribution," *International Journal of Solids and Structures*, vol. 30, no. 20, pp. 2659–2677, 1993.

[175] Lubliner, J., Oliver, J., Oller, S., and Onate, E., "A platic-damage model for concrete," *International Journal of Solids and Structures*, vol. 23, no. 3, pp. 299–326, 1989.

[176] Lund, L., "Characteristics, development and utilization of geothermal resources," *GHC Bulletin*, pp. 1–9, June 2007.

[177] Lux, K.-H. and Eberth, S., "Fundamentals and first application of a new healing model for rock salt.," in *Proceedings and Monographs in Engineering, Water and Earth Sciences.*, pp. 129–138, 2007.

[178] Lyakhovsky, V., "Scaling of fracture length and distributed damage," *Geophysical Journal International*, vol. 144, no. 1, pp. 114–122, 2001.

[179] Lyakhovsky, V., Ben-Zion, Y., and Agnon, A., "A viscoelastic damage rheology and rate- and state-dependent friction," *Geophys. J. Int.,*, vol. 161, pp. 179–190, 2005.

[180] Lyakhovsky, V., Podladchikov, Y., and Poliakov, A., "A rheological model of a fractured solid," *Tectonophysics*, vol. 226, no. 1–4, pp. 187–198, 1993.

[181] Lydzba, D. and Shao, J., "Study of poroelasticity material coefficients as response of microstructure," *Mechanics of Cohesive-Frictional Materials*, vol. 5, pp. 149–171, 2000.

[182] Mack, M. and Warpinski, N., *Mechanics of hydraulic fracturing. In: Economides, Nolte, editors. Reservoir stimulation.* Chichester; Wiley, 2000.

[183] Maleki, K. and Pouya, A., "Numerical simulation of damage–Permeability relationship in brittle geomaterials," *Computers and Geotechnics*, vol. 37, pp. 619–628, July 2010.

[184] Mandelbrot, B., *The Fractal Geometry of Nature.* H.B. Fenn and Company, 4th ed., 1989.

[185] Martin, C., Read, R., and Martino, J., "Observation of brittle failure around a circular test tunnel," *International Journal of Rock Mechanics & Mining Sciences*, vol. 34, no. 7, pp. 1065–1073, 1997.

[186] Martino, J. and Chandler, N., "Excavation-induced damage studies at the underground research," *International Journal of Rock Mechanics & Mining Sciences*, vol. 41, pp. 1413–1426, 2004.

[187] Mazars, J., "A description of micro- and macro scale damage of concrete structures," *Engineering Fracture Mechancis*, vol. 25, no. 5–6, pp. 729–737, 1986.

[188] Mazars, J. and Pijaudier-Cabot, G., "Continuum damage theory - application to concrete.," *Journal of Engineering Mechanics*, vol. 115, no. 2, pp. 345–365, 1989.

[189] Mazars, J. and Pijaudier-Cabot, G., "From damage to fracture mechanics and conversely: A combined approach.," *International Journal of Solids and Structures*, vol. 33, no. 22, pp. 3327–3342, 1996.

[190] Meschke, G., Leonhart, D., Timothy, J. J., and Zhou, M.-M., "Computational mechanics of multiphase materials – modeling strategies at different scales," *Computer Assisted Mechanics and Engineering Sciences*, vol. 18, pp. 73–89, 2011.

[191] Miao, S., Wang, M. L., and Schreyer, H. L., "Constitutive models for healing of materials with application of compaction of crushed rock salt.," *Journal of Engineering Mechanics.*, vol. 121, pp. 1122–1129, Oct. 1995.

[192] Miguel Ortiz, E. P. P., "A physical model for the inelasticity of concrete," *Proe. Roy. Soc. Lond. A*, vol. 383, pp. 101–125, September 1982.

[193] Mindlin, R., "Micro-structure in linear elasticity," *Archive for Rational Mechanics and Analysis*, vol. 16, no. 1, pp. 51–78, 1964.

[194] Mohammadi, S., *Extended Finite Element Method for Fracture Analysis of Structures*. Blackwell, 2008.

[195] Montgomery, D. C. and Runger, G. C., *Applied statistics and probability for engineers*. Wiley. com, 2010.

[196] Murakami, S. and Kamiya, K., "Constitutive and damage evolution equations of elastic-brittle materials based on irreversible thermodynamics," *Int. J. Mech. Sci.*, vol. 39, pp. 473–486, 1996.

[197] Murakami, S. and Kamiya, K., "Constitutive and damage evolution equations of elastic-brittle materials based on irreversible thermodynamics," *International Journal of Mechanical Sciences*, vol. 39, pp. 473–486, Apr. 1997.

[198] Murdoch, L. C. and Germanovich, L. N., "Analysis of a deformable fracture in permeable material," *International Journal for Numerical and Analytical Methods in Geomechanics*, vol. 30, no. 6, pp. 529–561, 2006.

[199] Nagashima, T. and Suemasu, H., "Stress analyses of composite laminate with delamination using x-fem.," *International Journal of Computational Methods*, vol. 3, no. 4, pp. 521–543, 2006.

[200] Nayak, G. C. and Zienkiewicz, O. C., "Elasto-plastic stress analysis. a generalization for various constitutive relations including strain softening," *International Journal for Numerical Methods in Engineering*, vol. 5, pp. 113–135, 1972.

[201] Nemat-Nasser, S. and Hori, M., *Micromechanics: Overall Properties of Heterogeneous Materials*. North-Holland, 1993.

[202] Nemat-Nasser, S. and Horii, H., "Compression-induced noplanar crack extension with application to splitting, exfoliation, and rockburst," *Journal of Geophysical Research*, vol. 87, no. B8, pp. 6805–6821, 1982.

[203] Ng, T.-T., "Macro- and micro-behaviors of granular materials under different sample preparation methods and stress paths," *International Journal of Solids and Structures*, vol. 41, pp. 5871–5884, 2004.

[204] Ninth Workshop Geothermal Reservoir Engineering, *Rock failure in compression*, (Stanford University, Stanford, California), December 1983.

[205] Nordren, R., "Propagation of a vertical hydraulic fracture," *SPE. J.*, vol. 12, no. 8, pp. 306–14, 1972.

[206] Oda, M., "Similarity rules of crack geometry in statistically homogeneous rock masses," *Mechanics of Materials*, vol. 3, pp. 119–129, 1984.

[207] Oda, M., "Fabric tensor for discontinuous geological materials," *Soils and Foundations*, vol. 22, no. 4, pp. 96–108, 1982.

[208] Olivella, S. and Gens, A., "Double structure thm analyses of a heating test in a fractured tuff incorporating intrinsic permeability variations," *International Journal of Rock Mechanics and Mining Sciences*, vol. 42, no. 5, pp. 667–679, 2005.

[209] Ortiz, M., "A constitutive theory for the inelastic behaviour of concrete," *Mech. Mater.*, vol. 4, pp. 67–93, 1985.

[210] Paterson, M. and Weiss, L., "Deformed Rocks Symmetry Concepts in the Structural Analysis of Deformed Rocks," *Geological Society of America Bulletin*, vol. 72, no. 6, pp. 841–882, 1961.

[211] Pedroso, D. M., Sheng, D., and Sloan, S. W., "Stress update algorithm for elastoplastic models with nonconvex yield surfaces," *International Journal for Numerical Methods in Engineering*, vol. 76, no. 13, pp. 2029–2062, 2008.

[212] Pellet, F., Hajdu, A., Deleruyelle, F., and Besnus, F., "A viscoplastic model including anisotropic damage for the time dependent behaviour of rock," *International Journal for Numerical and Analytical Methods in Geomechanics*, vol. 29, pp. 941–970, 2005.

[213] Pellet, F. and Keshavarz, M., "Mechanical behavior of a crystalline hard rock subjected to ultra high temperature and consequences for underground opending stability," in *Rock Mechanics in Civil and Environmental Engineering*, (Lausanne, Switzerland), pp. 135–138, Jun 2010.

[214] Pensee, V., Kondo, D., and Dormieux, L., "Micromechanical analysis of anisotropic damage in brittle materials," *Journal of Engineering Mechanics*, vol. 128, no. 8, pp. 889–897, 2002.

[215] Pereira, J.-M. and Arson, C., "Retention and permeability properties of damaged porous rocks," *Computers & Geotechnics (under review)*, 2012.

[216] Perkins, T. and Kern, L., "Widths of hydraulic fractures," *J. Pet. Tech. 1961;13(9):93749 [SPE 89].*, vol. 13, no. 9, pp. 937–49, 1962.

[217] Pouya, A. and Ghoreychi, M., "Determination of rock mass strength properties by homogenization," *International Journal for Numerical and Analytical Methods in Geomechanics*, vol. 25, pp. 1285–1303, 2001.

[218] Pruess, K., Wang, J. S. Y., and Tsang, Y. W., "On Thermohydrologic Conditions Near High-Level Nuclear Wastes Emplaced in Partially Saturated Fractured Tuff 2 . Effective Continuum Approximation," *Water Resources Research*, vol. 26, no. 6, pp. 1249–1261, 1990.

[219] Pruess, K., Wang, J., and Tsang, Y., "On thermohydrologic conditions near high-level nuclear wastes emplaced in partially saturated fractured tuff, 1, Simulation studies with explicit consideration of fracture effects," *Water Resour. Res*, vol. 26, no. 6, pp. 1235–1248, 1990.

[220] Qizhi, Z., Kondo, D., and Jian-fu, S., "An homogenization-based nonlocal damage model for brittle materials and applications," in *Computational Science – ICCS 2007* (Shi, Y., Albada, G., Dongarra, J., and Sloot, P., eds.), vol. 4489 of *Lecture Notes in Computer Science*, pp. 1130–1137, Springer Berlin Heidelberg, 2007.

[221] Rabotnov, Y. N., *Creep Problems in Structural Members, North Holland, Amsterdam.* North Holland, Amsterdam.: Wiley, 1969.

[222] Raj, R., "Creep in polycrystalline aggregates by matter transport through a liquid phase," *Journal of Geophysical Research*, vol. 87, no. B6, pp. 4731–4739, 1982.

[223] Read, R., "20 years of excavation response studies at aecl's underground research laboratory," *International Journal of Rock Mechanics & Mining Sciences*, vol. 41, pp. 1251–1275, 2004.

[224] Reddy, J. N., *An Introduction to Finite Element Method*. McGrill Higher Education, 3rd ed., 2006.

[225] Reddy, J., *An Introduction to Nonlinear Finite Element Analysis*. Oxford University Press, 2004.

[226] Rice, J. R., *Mathematical Analysis in the Mechanics of Fracture*, vol. 2, ch. 3 of Fracture: An Advanced Treatise, pp. 191–311. New York: Academic Press, 1968.

[227] Roudolph, J., kai Bauerbach, and Vormwald, M., "Numerical investigations of phenomena caused by the closure and growth behavior of short cracks under thermal cyclic loading," in *Pressure Vessels and Piping Division of ASME*, vol. 3, pp. 693–700, Jul 2010.

[228] Rummel, F. and Winter, R., "Application of laboratory fracture mechanics data to hydraulic fracturing field tests," in *Proc. 1st japan-USA Symp. on Fracture Mechanics Approach, Hydraulic fracture and Geothermal Energy*, (Sendai, Japan), pp. 495–501, 1982.

[229] Rundle, J. B., Turcotte, D. L., Shcherbakov, R., Klein, W., and Sammis, C., "Statistical physics approach to understanding the multiscale dynamics of earthquake fault systems," *Rev. Geophys.*, vol. 41, no. 4, 2003.

[230] Rutqvist, J., "The Geomechanics of CO_2 Storage in Deep Sedimentary Formations," *Geotechnical and Geological Engineering*, pp. 1–27, 2012.

[231] Savitski, A. and Detournay, E., "Propagation of a penny-shaped fluid-driven fracture in an impermeable rock: asymptotic solutions," *International Journal of Solids and Structures*, vol. 39, pp. 6311–6337, August 2002.

[232] Schulze, O., "Investigations on damage and healing of rock salt.," in *Proceedings and Monographs in Engineering, Water and Earth Sciences*, pp. 33–43, 2007.

[233] Schulze, O., "Thermomechanical properties of irradiated rock salt," *Nuclear Instruments & Methods in Physics research Section B: Beam Interactions with Materials Atoms*, vol. 1, pp. 542–548, Feb. 1984.

[234] Senseny, P. E., Hansen, F. D., Russell, J. E., Carter, N. L., and Handin, J. W., "Mechanical behaviour of rock salt: Phenomenology and micromechanisms," *International Journal of Rock Mechanics and Mining Sciences & Geomechanics Abstracts*, vol. 29, no. 4, pp. 363–378, 1992.

[235] Sethuraman, R. and Reddy, C., "Pseudo-elastic analysis of elastic-plastic crack tip fields using element-free galerkin method," *nternational Journal of Computational Methods*, vol. 5, no. 1, pp. 91–117, 2008.

[236] Shahid, I. and Chang, F.-K., "An accumulative damage model for tensile and shear failures of laminated composite plates," *Journal of composite materials*, vol. 29, no. 7, pp. 926–981, 1995.

[237] Shalev, E. and Lyakhovsky, V., "The processes controlling damage zone propagation induced by wellbore fluid injection," *Geophysical Journal International*, 2013.

[238] Shao, J. F., Chau, K. T., and Feng, X. T., "Modeling of anisotropic damage and creep deformation in brittle rocks," *International Journal of Rock Mechanics & Mining Sciences*, vol. 43, pp. 582–592, 2006.

[239] Shao, J. F. and Rudnicki, J. W., "A microcrack-based continuous damage model for brittle geomaterials," *Mechanics of Materials*, vol. 32, pp. 607–619, 2000.

[240] Shao, J., "Poroelastic behaviour of brittle rock materials with anisotropic damage," *Mechanics of Materials*, vol. 30, pp. 41–53, Sept. 1998.

[241] Shao, J., Hoxha, D., Bart, M., Homand, F., Duveau, G., Souley, M., and Hoteit, N., "Modelling of induced anisotropic damage in granites," *International Journal of Rock Mechanics & Mining Sciences*, vol. 36, pp. 1001–1012, 1999.

[242] Shao, J., Zhou, H., and Chau, K., "Coupling between anisotropic damage and permeability variation in brittle rocks.," *International Journal for Numerical and Analytical Methods in Geomechanics*, vol. 29, no. 12, pp. 1231 – 1247, 2005.

[243] Shao, J.-F. and Lydzba, D., "Un modèle d'endommagement poroélastique pour milieux poreux saturés," *C.R. Acad. Sci. Paris*, vol. 327, pp. 1305–1310, 1999.

[244] Shen, X., "Modeling Fractures with Continuum Damage and Its Numerical Application to Stimulation Estimates," in *46th Rock Mechanics Geomechanics Symposium*, (Chicago, IL), pp. ARMA 12–196, 2012.

[245] Shet, C. and Chandra, N., "Analysis of energy balance when using cohesive zone models to simulate fracture processes," *Journal of Engineering Materials and Technology*, vol. 124, pp. 440–450, 09 2002.

[246] Sih, G. and Liebowitz, H., "Mathematical theories of brittle fracture," *Fracture, An advanced Treatise*, vol. II, 1968.

[247] Silberschmidt, V., "Dynamics and scaling characteristics of shear crack propagation," *Pure and Applied Geophysics*, vol. 157, pp. 523–538, 2000.

[248] Slizowski, J. and Walaszczyk, J., "Long term stability evaluation of natural gas storage caverns," *Mineral Resources Management*, vol. 24, no. 4–1, pp. 83–100, 2008.

[249] Smart, K., Ofoegbu, G., Das, K., and Basu, D., "Geomechanical Modeling of Hydraulic Fracture Initiation and Propagation in a Mechanically Stratified Geologic System," in *46th Rock Mechanics Geomechanics Symposium*, (Chicago, IL), pp. ARMA 12–275, 2012.

[250] Sneddon, I., "The distribution of stress in the neighbourhood of a crack in an elastic solid," in *Proc. R. Soc. London A.*, pp. 229–60, 1946.

[251] Sneddon, I. and Elliot, H., "The opening of a griffith crack under internal pressure," *Q. Appl. Math.*, vol. 4, pp. 262–7, 1946.

[252] Sone, H. and Zoback, M. D., "Strength, creep and frictional properties of gas shale reservoir rocks," (Salt Lake City), 44th U.S. Rock Mechanics Symposium and 5th U.S.-Canada Rock Mechanics Symposium, 2010.

[253] Souley, M., Homand, F., Pepa, S., and Hoxha, D., "Damage-induced permeability changes in granite: a case example at the URL in canada," *International Journal of Rock Mechanics and Mining Sciences*, vol. 38, no. 2, pp. 297–310, 2001.

[254] Souley, M., Armand, G., Su, K., and Ghoreychi, M., "Modeling the viscoplastic and damage behavior in deep argillaceous rocks," *Physics and Chemistry of the Earth*, vol. 36, pp. 1949–1959, 2011.

[255] Stone, C. J., *A course in probability and statistics*. Duxbury Press Belmont:, 1996.

[256] Succar, S. and Williams, R. H., "Compressed air energy storage: Theory, resources, and applications for wind power," *Princeton Environmental Institute Report*, vol. 8, 2008.

[257] Sustainable Cherry Hill, "Shale gas remains controversial and abundant energy source." http://www.sustainablecherryhill.org/shale-gas-remains-controversial-and-abundant-energy-source.

[258] Suvorov, A. P. and Selvadurai, A. P. S., "Effective medium methods and a computational approach for estimating geomaterial properties of porous materials with randomly oriented ellipsoidal pores," *COMPUTERS AND GEOTECHNICS*, vol. 38, pp. 721–730, JUL 2011.

[259] Suzuki, T., "Understanding of dynamic earthquake slip behavior using damage as a tensor variable: Microcrack distribution, orientation, and mode and secondary faulting," *Journal of Geophysical Research*, vol. 117, pp. 1–20, May 2012.

[260] Swoboda, G. and Yang, Q., "An energy-based damage model of geomaterials -II. Deduction of damage evolution laws," *International Journal of Solids and Structures*, vol. 36, pp. 1735–1755, 1999.

[261] Swoboda, G. and Yang, Q., "An energy-based damage model of geomaterials. I. Formulation and numerical results," *International Journal of Solids and Structures*, vol. 36, pp. 1719–1734, Apr. 1999.

[262] Swoboda, G. and Yang, Q., "An energy-based damage model of geomaterials-i. formulation and numerical results," *International Journal of Solids and Structures*, vol. 36, pp. 1719–1734, 1999.

[263] Swoboda, G., Yang, Q., and Ito, F., "Damage Propagation Model and its Application to Rock Engineering Problems," in *Proc. 8th Inernational Congress on Rock Mechanics*, pp. 159–163, 1995.

[264] Swoboda, G., Yang, Q., and Zhou, W., "An energy-based damage model and its engineering application," in *Computer Methods and Advances in Geomechanics*, pp. 1821–1828, 1997.

[265] Takemura, T. and Oda, M., "Stereology-based fabric analysis of microcracks in damaged granite," *Tectonophysics*, vol. 387, pp. 131–150, Aug. 2004.

[266] the 47th US Rock Mechanics/Geomechancis Symposium, *Reduction of macroscale calibration experiments through constraints on anisotropic elastic stiffnesses*, (San Francisco, California), 23-26 June 2013.

[267] the 47th US Rock Mechanics/Geomechancis Symposium, *Relationship between grain size and fracture properties of rock*, (San Francisco, California), 23-26 June 2013.

[268] Tsang, C.-F., Bernier, F., and Davies, C., "Geohydromechanical processes in the excavation damaged zone in crystalline rock, rock salt, and indurated and plastic clays—in the context of radioactive waste disposal," *International Journal of Rock Mechanics & Mining Sciences*, vol. 42, pp. 109—125, 2005.

[269] Tsang, Y. W., Birkholzer, J. T., and Mukhopadhyay, S., "Modling of thermally driven hydrological processes in partially saturated fractured rock," *Reviews of geophysics*, vol. 47, pp. 1–30, 2009.

[270] Turcotte, D. and Scherbakov, R., "Can damage mechanics explain temporal scaling laws in brittle fracture and seismicity?," *Pure Appl. Geophys*, vol. 163, pp. 1031–1045, 2006.

[271] Turcotte, D. L., "Fractals in geology and geophysics," *Pure and Applied Geophysics*, vol. 131, no. 1–2, pp. 171–196, 1989.

[272] Tvergaard, V. and Nielsen, K. L., "Relations between a micro-mechanical model and a damage model for ductile failure in shear," *Journal of the Mechanics and Physics of Solids*, vol. 58, no. 9, pp. 1243–1252, 2010.

[273] Valko, P. and Economides, M., "A Continuum-Damage-Mechanics Model of Hydraulic Fracturing," *Journal of Petroleum Technology*, vol. 45, no. 3, pp. 198–205, 1993.

[274] Valko, P. and Economides, M., "Propagation of Hydraulically Induced Fractures a Continuum Damage Mechanics Approach," *International Journal of Rock Mechanics and Mining Sciences & Geomechanics Abstracts*, vol. 31, no. 3, pp. 221–229, 1994.

[275] Vermylen, J. P. and Zoback, M. D., "Hydraulic fracturing, microseimic magnitudes, and stress evolution in the barnett shale, texas, usa," (Woodlands), the SPE Hydraulic Fracturing Technology Conference and Exhibition, January 2011.

[276] Viatkina, E., Brekelmans, W., and Geers, M., "The role of plastic slip anisotropy in the modelling of strain path change effects," *Journal of materials Processing Technology*, vol. 209, pp. 186–187, 2009.

[277] Voyiadjis, G. Z., Shojaei, A., and Li, G., "A thermodynamic consistent damage and healing model for self healing materials," *International Journal of Plasticity*, vol. 27, no. 7, pp. 1025–1044, 2011.

[278] Wang, T.-T. and Huang, T.-H., "Anisotropic deformation of a circular tunnel excavated in a rock mass containing sets of ubiquitous joints: Theory analysis and numerical modeling," *Rock Mechanics and Rock Engineering*, vol. 47, no. 2, pp. 643–657, 2014.

[279] Wang, Y., Kessler, N., and Santarelli, F. J., "Stress-induced anisotropy and loading path effects on borehole responses," *Int. J, Rock Mech. Min. Sci. d: Geomech. Ab tr.*, vol. 30, pp. 1367–1370, 1993.

[280] Wei, R. P., *Fracture Mechanics: Integration of Mechanics, Materials Science and Chemistry*. Cambridge University Press, 1st ed., February.

[281] Westergaard, H., "Bearing Pressures and Cracks - Bearing Pressures Through a Slightly Waved Surface or Through a Nearly Flat Part of Cylinder, and Related Problems of Cracks," in *Joint Meeting of the Applied Mechancis and Hydraulic Divisions of the American Society of Mechanical Engineers*, (New-York), pp. A49–A53, 1937.

[282] Whittaker, B., Singh, R., and Sun, G., *Rock fracture mehcanics: principles, design, and application*. Elsevier, 1992.

[283] Wong, H.-I., Desroches, E., Hansel, L., Lagrange, M.-H., and Gourram, H., "Trends of edf's fuel core management and consequences on fuel cycle: "cycle impact" analyses," in *Transactions - Fuel Cycles, Proceedings of the European Nuclear Conference (ENC 2012) - published on line in November 2012*, (Manchester, United Kingdom), pp. 22–32, December 9-12 2012.

[284] Wu, R., Germanovich, L. N., Van Dyke, P. E., and Lowell, R. P., "Thermal technique for controlling hydraulic fractures," *Journal of Geophysical Research*, vol. 112, May 2007.

[285] Wu, S. and Chudnovsky, A., "Effect of microcrack array on stress intensity factor of main crack," *International Journal of Fracture*, vol. 59, pp. 41–52, 1993.

[286] Xie, N., Zhu, Q.-Z., Shao, J.-F., and Xu, L.-H., "Micromechanical analysis of damage in saturated quasi brittle materials," *International Journal of Solids and Structures*, vol. 49, pp. 919–928, Mar. 2012.

[287] Xu, H. and Arson, C., "Thermo-mechanical damage in porous rocks: Theoretical framework and modeling considerations.," in *GEOTECHNICAL SPECIAL PUBLICATION*, vol. 4 of *GeoCongress; state of the art and practice in geotechnical engineering*, pp. 2332 – 2341, 2012.

[288] Xu, H. and Arson, C., "Anisotropic damage models for geomaterials: Theoretical and numerical challenges," *International Journal of Computational Methods, Special Issue on Computational Geomechanics*, vol. 11, no. 2, 2014.

[289] Xu, T., Apps, J. A., and Pruess, K., "Numerical simulation of CO_2 disposal by mineral trapping in deep aquifers," *Applied Geochemistry*, vol. 19, no. 6, pp. 917–936, 2004.

[290] Yamashita, T., "Generation of microcracks by dynamic shear rupture and its effects on rupture growth and elastic wave radiation," *Geophysical Journal International*, vol. 143, pp. 395–406, Nov. 2000.

[291] Yang, S.-Y. and Yeh, H.-D., "Modeling heat extraction from hot dry rock in a multi-well system," *Applied Thermal Engineering*, vol. 29, no. 8-9, pp. 1676–1681, 2009.

[292] Yao, Y., Sun, D., and Matsuoka, H., "A unified constitutive model for both clay and sand with hardening parameter independent on stress path," *Computers and Geotechnics*, vol. 35, pp. 210–222, 2008.

[293] Yeh, H.-D., Yang, S.-Y., and Li, K.-Y., "Heat extraction from aquifer geothermal systems," *International Journal for Numerical and Analytical Methods in Geomechanics*, vol. 36, no. 1, pp. 85–99, 2012.

[294] Yow, J. and Hunt, J., "Coupled processes in rock mass performance with emphasis on nuclear waste isolation," *International journal of rock mechanics and mining sciences*, vol. 39, no. 2, pp. 143–150, 2002.

[295] Yu, H., *Plasticity and Geotechnics*. Springer, 2006.

[296] Zhao, J., "Geothermal Testing and Measurements or Rock and Rock Fractures," *Geothermics*, vol. 23, no. 3, pp. 215–231, 1994.

[297] Zhou, H., Hu, D., Zhang, F., and Shao, J., "A thermo-plastic/viscoplastic dmage model for geomaterials," *Acta Mechanica Solida Sinica*, vol. 24, no. 3, pp. 195–208, 2011.

[298] Zhou, J., Shao, J., and Xu, W., "Coupled modeling of damage growth and permeability variation in brittle rocks," *Mechanics Research Communications*, vol. 33, pp. 450–459, July 2006.

[299] Zhu, C. and Arson, C., "A thermo-mechanical damage model for rock stiffness during anisotropic crack opening and closure," *Acta Geotechnica*, pp. DOI: 10.1007/s11440–013–0281–0 (in press), 2014.

[300] Zhu, C. and Arson, C., "A thermo-mechanical damage model for rock stiffness during anisotropic crack opening and closure," *Acta Geotechnica*, pp. 1–21, 2013.

[301] Zienkiewicz, O. and Taylor, R., *The Finite Element Method for Solid and Structural Mechnics*. Elsevier, 6th ed., 2005.

[302] Zienkiewicz, O., Taylor, R., and Zhu, J., *The Finite Element Method: Its Basis and Fundamentals*. Elsevier, 6th ed., 2005.

[303] Zimmermann, G., Burkhardt, H., and Engelhard, L., "Scale dependence of hydraulic and structural parameters in the crystalline rock of the ktb," *Pure and applied geophysics*, vol. 160, no. 5–6, pp. 1067–1085, 2003.

[304] Zoback, M. D. and Pollard, D. D., "Hydraulic fracture propagation and the invterpretation of pressure-time records for in site dterminations," in *Proc. 19th U.S. Symp. on Rock Mech.*, pp. 14–22, 1978.

[305] Zoback, M. D., Kohli, A., Das, I., and McClure, M., "The importance of slow slip on faults during hydraulic fracturing stimulation of shale gas reservoirs," (Pittsburgh), the SPE Hydraulic Fracturing Technology Conference and Exhibition, June 2012.

VITA

Mr. Hao Xu got his Bachelor Degree and Master Degree from Harbin Institute of Technology. He started his Ph.D study at Texas A&M University under the supervision of Dr. Chloé Arson. Then he transferred to Georgia Institute of Technology following Dr. Arson.